Boundary conditions and dynamics of fluvial obstacle mark formation

Dissertation

zur

Erlangung des Doktorgrades (Dr. rer. nat.)

der

Mathematisch-Naturwissenschaftlichen Fakultät

der

Rheinischen Friedrich-Wilhelms-Universität Bonn

vorgelegt von

Oliver Schlömer

aus

Köln

Bonn, Oktober 2024

Angefertigt mit Genehmigung der Mathematisch-Naturwissenschaftlichen Fakultät der
Rheinischen Friedrich-Wilhelms-Universität Bonn

Gutachter/ Betreuer: Prof. Dr. Jürgen Herget
Gutachter: Prof. Dr. Julian Klaus

Tag der Promotion: 30.01.2025
Erscheinungsjahr: 2025

ACKNOWLEDGEMENTS

This thesis would not have been possible without the support and contributions of many people to whom I would like to express my sincere gratitude. First and foremost, I would like to thank my supervisor, Prof. Dr. Jürgen Herget, for his guidance, insightful feedback and support throughout the process. His constructive criticism and encouragement were essential to the completion of this thesis.

I would also like to acknowledge the tremendous help from various institutions and individuals during the laboratory campaigns and fieldwork, for which I am grateful. I am particularly grateful to Paul Grams, Daniel Buscombe, Stephane Rodrigues, Gerardo Benito, Mikel Calle, Theo Bulteau and the people of Gut Frankenforst, who shared their time and knowledge with me and contributed significantly to the empirical basis of this study.

Finally, I would like to express my deepest gratitude to my wife, Lina, whose love, patience and understanding have been my constant source of strength in the most difficult moments.

This dissertation has been a rollercoaster ride with some highs and some lows. It is dedicated to all those who have accompanied and inspired me along the way, especially Lina, Petra, Meggie, Hermann and Aknarf.

CONTENTS

Summary……v

Zusammenfassung……viii

List of publications……xii

List of figures……xiii

List of tables……xviii

List of abbreviations……xix

1. Introduction……1

1.1 General……1

1.2 Problem……2

1.3 Framing the research questions……5

1.4 Research objectives……5

1.5 Addressing the research questions……6

1.6 Thesis outline……7

2. Research on obstacle marks……13

2.1 Obstacle marks as bedforms……13

2.1.1 Research on obstacle marks at man-made obstructions……14

2.1.2 Research on obstacle marks at natural obstructions……15

2.2. Boundary conditions for obstacle mark formation……18

2.3 Hydraulic and sedimentary processes of obstacle mark formation……19

2.4. Usage of obstacle marks for flow reconstruction……22

3. Methods……25

3.1. Physical modelling……25

3.1.1 Modelling approach……26

3.1.2 Principal of experiments……26

3.1.3 Laboratory flume……27

3.1.4 Measurement technique……30

3.1.5 Quality control of measurements……33

3.2. Laboratory campaigns……34

3.3 Field surveys……35

4. Boundary condition control of fluvial obstacle mark formation – a framework from geoscientific perspective……37

Abstract……37

4.1 Introduction……38

4.2 Obstacle marks as sedimentary structures on different spatial scales……40

4.3 Morphodynamic processes at instream obstacles……42

4.4 Review on boundary conditions of morphodynamic processes at instream obstructions……44

4.5 Parameter framework of boundary condition control on morphodynamic processes at natural instream obstacles……50

4.5.1 Categories 50
4.5.2 Hierarchy 52
4.5.3 Impact 53
4.6 Evaluation of submergence ratio and obstacle shape as primary control factors of obstacle mark formation at solid boulder like obstacles 57
4.6.1 Impact of submergence ratio on obstacle mark formation 62
4.6.2 Impact of obstacle shape on obstacle mark formation 65
4.7 Conclusions and perspectives 67
5. Influence of submergence ratio on horseshoe vortex size at boulder obstacles 71
Abstract 71
5.1 Introduction 72
5.2 Material and methods 74
5.3 Results and interpretation 76
5.4 Conclusion 82
6. Geometry of obstacle marks at instream boulders – integration of laboratory investigations and field observations 85
Abstract 85
6.1 Introduction 87
6.2 Geometry of obstacle marks 89
6.3 Morphodynamic processes at instream obstacles 90
6.4 Boundary conditions of obstacle mark formation 91
6.5 Obstacle marks at different spatial scale 92
6.6 Material and methods 93
6.6.1 Facility for laboratory studies 93
6.6.2 Working hypotheses for experimental series 95
6.6.3 Hydraulic boundary conditions of experimental series 96
6.6.4 Experimental procedure 96
6.6.5 Field data 98
6.7 Results 100
6.7.1 Scour Hole evolution at laboratory scale 100
6.7.2 Influence of depth-limited alluvial layer 102
6.7.3 Influence of obstacle mobility 103
6.7.4 Obstacle marks at field scale 104
6.7.5 Frontal scour hole geometry 107
6.7.6 Similitude of frontal scour hole geometry 110
6.7.7 Geometrical relations in time at laboratory scale 112
6.8 Interpretation of laboratory results and field evidence 113
6.8.1 Process dynamics of scour hole enlargement 113
6.8.2 Quantitative models of enlargement 114
6.9 Discussion of laboratory results and field evidence 116
6.9.1 Shortcomings in comparing field evidence and laboratory results 118
6.10 Conclusion and outlook 119

7. Geometry of local scour holes at boulder-like obstacles during unsteady flow conditions and varying submergence 122

Abstract 122
7.1 Introduction 123
7.2 Review on local scouring at boulder-like obstacles 126
7.2.1 Geometry of the local scour holes 126
7.2.2 Flow field 127
7.2.3 Enlargement processes of local scour holes 128
7.2.4 Boundary conditions 128
7.3 Working hypothesis 130
7.4 Experimental design and procedures 131
7.4.1 Flume set-up 131
7.4.2 Laboratory hydrographs 132
7.4.3 Experimental procedure 135
7.5 Results and discussion 137
7.5.1 Local scour evolution 137
7.5.2 Impact of submergence 138
7.5.3 Impact of hydrograph shape 140
7.5.4 Impact of flow intensity 142
7.5.5 Local scour geometry 145
7.5.6 Geometrical relationships over time 148
7.5.7 Impact of hydrograph chronologies 150
7.6 Conclusions 154

8. On the usage of local scour holes at boulders for flow reconstruction in ephemeral streams 157

Abstract 157
8.1 Introduction 158
8.2 Review on obstacle marks at boulders 160
8.2.1 Geometry 160
8.2.2 Formation during flash floods 161
8.3 Study area 163
8.3.1 Rambla de la Viuda 163
8.4 Methods and Data 165
8.4.1 Framework for flow reconstruction 165
8.4.2 Field methods 166
8.5 Results and discussion 169
8.5.1 Obstacle marks at Rambla de la Viuda 169
8.5.2 Estimation of horseshoe vortex size 172
8.6 Estimation of hydraulic boundary conditions 174
8.6.1 Estimation of flow depth 174
8.6.2 Estimation of peak discharge 176
8.7 Shortcomings 177

8.8 Conclusions 178

9. Vegetation-induced sedimentary structures: Porosity of riparian shrubs as control parameter of sedimentary processes during floods 181

Abstract 181

9.1 Introduction 183

9.1.1 Objectives of the study 185
9.1.2 Working hypothesis 186
9.1.3 Flow field at porous obstacles 186
9.1.4 Geometry of the viss 188

9.2 Study and field evidence 189

9.3 Methods and analysis 190

9.3.1 Estimation of porosity at field and laboratory scale 190
9.3.2 Experimental conditions 194
9.3.3 Experimental procedure 198

9.4 Results and discussion 199

9.4.1 VISS at the Loire River 199
9.4.2 Sediment trapping of suspended load at permeable obstacles on laboratory scale 204
9.4.3 Local scouring at permeable obstacles on the laboratory scale 208
9.4.4 Data integration on local scour 211

9.5 Revisiting the working hypothesis and shortcomings 213

10. Synthesis 217

10.1 Recalling the research questions 217

10.2 Open questions in relation to the research questions 226

References 232

SUMMARY

Obstacles such as boulders, riparian vegetation and man-made engineering infrastructure such as bridge piers are ubiquitous elements of fluvial environments. When exposed to flow, these obstacles can induce the formation of specific geomorphological and sedimentary structures known as “obstacle marks”. These bedforms typically consist of a conical depression upstream of the obstacle, called a “local scour hole”, and an adjacent depositional region downstream of the obstacle, called a “sediment ridge”, both of which can be characterised by specific geometric length scales (i.e. depth, length, width). The formation and temporal evolution of obstacle ridges are initiated by three-dimensional turbulent eddy systems in the vicinity of the obstacle. These eddies increase the flow velocity and turbulent shear stress in the vicinity of the obstacle, inducing sediment mobilisation even when the upstream flow velocity is below the critical threshold for general bedload movement. The hydraulic and sedimentary processes involved in the formation of obstacle marks are influenced by a variety of environmental conditions that affect the characteristics of the approaching flow, the characteristics of the sediment and the characteristics of the obstacle itself. Much of the knowledge on the influence of boundary conditions on obstacle mark formation has been gained in the hydraulic engineering community, particularly in relation to localised scour holes on engineering infrastructure such as bridge piers and pipelines. However, boundary conditions that are important for the formation of obstacle marks at natural obstacles, such as isolated solid boulders or porous riparian vegetation elements, have not been considered in this context. Furthermore, process-related geoscientific research on obstacle mark formation at natural obstacles is surprisingly rare. This is particularly relevant in the context of the unknown effects of varying submergence on local scouring of boulder-like obstacles of different shapes during a flood event, as well as the effect of permeability on eddy formation at a shrubby obstacle.

The use of flume studies allows the systematic variation of individual boundary conditions of flow and obstacle characteristics, and thus the analysis of their effects on the processes of obstacle mark formation, while keeping other boundary conditions constant. This approach allows the simulation and measurement of rare or varied environmental boundary conditions that cannot be measured in the natural world. In addition, physical experiments provide an essential link between field observations and theoretical models.

This thesis presents the results of four experimental campaigns, comprising a total of over 190 experimental runs (including test runs). Each experimental campaign was designed to focus on a specific control parameter, which was systematically varied to quantify the dynamics of obstacle marking and to describe the associated thresholds. The laboratory results on obstacle mark geometries will be compared with in-situ obstacle marks on boulders in the Colorado River, Arizona, USA, and vegetation-induced sedimentary structures on permeable *Populus nigra* L shrubs in the Loire River, France, at different spatial scales. In addition to its academic relevance, a refined understanding of the control of boundary conditions and thresholds for obstacle mark formation is expected to be beneficial for application in field sites, where persistent obstacle marks are expected to be suitable indicators for estimating the magnitude of past flood events.

In addition, this thesis presents a novel framework for reconstructing the most likely flow conditions in terms of flow depth, velocity and duration during formation from preserved local scour hole geometries on boulders. The framework is based on an empirical approach combining laboratory and field data. The framework is tested on preserved local scour hole geometries on individual boulders in the ephemeral stream Rambla de la Viuda, Spain, using the bedforms as indicators of the boundary conditions during their formation.

The main results of the paper can be summarised as follows:

- A novel parameter framework is presented that includes 13 non-dimensional control parameters of boundary conditions that influence the formation of obstacle marks at instream obstacles. The framework is based on two hierarchical levels, which are threshold based and distinguish boundary conditions where (i) the geometric length scales of obstacle marks are maximised, (ii) conditions where the spatial extent of the geometric length scales is limited relative to the maximum level, and (iii) conditions where the formation of obstacle marks is completely inhibited.
- The primary control parameters determine the geometric scale of the flow field at the obstacle and thus control the potential maximum size of the obstacle mark. The secondary control parameters affect the dynamics of the flow field within the geometric scale and limit the potential maximum size of the emerging obstacle mark when certain thresholds are exceeded.

- The flow depth in relation to the obstacle size is a primary control parameter for obstacle mark formation at natural obstacles such as boulders. Consequently, geometric length scales are maximised at a flow depth comparable to the obstacle size. Conversely, increasing the flow depth beyond this value limits the spatial extent of the obstacle mark.
- A number of boundary conditions, including the depth of the alluvial layer and the property that a boulder-like object can tilt into the local scour hole as a result of local scour, limit the spatial extent of the geometric length scales and their evolution with time. In the case of a permeable obstacle, such as shrubby riparian vegetation, a threshold value has been identified through experimental observation. This value represents the point at which obstacle mark formation and sediment trapping cease to occur due to the excessive porosity of the obstacle. This allows the approaching flow to "pass through" the obstacle. In addition, a method for quantifying the optical porosity of vegetation elements under field conditions has been refined and successfully applied to riparian *Populus nigra* L. shrubs on the Loire River in France.
- A quantitative model is presented that assesses local scour hole expansion over time for steady and unsteady flow conditions. The in-situ obstacle mark geometries at the field site and at different spatial scales show similarities with the laboratory results, suggesting that the observed processes and shapes are scale-invariant.
- The size of the dominant vortex at the obstacle base can be determined from the persistent geometric characteristics of the local scour hole. A re-evaluation of the laboratory and field data indicates that there is a correlation between vortex size and flow depth during the formation of the obstacle mark. An empirical model was formulated to estimate the most likely flow depth during obstacle mark formation. The approach was applied to persistent obstacle marks on boulders in the ephemeral stream Rambla de la Viuda, Spain, and gave results that were considered plausible. This is the first case where the geometric characteristics of preserved local scour holes on boulders have been used as a quantitative indicator of flow depth during their formation.

ZUSAMMENFASSUNG

Hindernisse wie Felsbrocken, Ufervegetation und technische Infrastrukturen wie Brückenpfeiler sind allgegenwärtige Elemente von Flusslandschaften. Wenn diese Hindernisse einer Strömung ausgesetzt sind, können sie zur Bildung spezifischer geomorphologischer und sedimentärer Strukturen führen, die als „fluviale Hindernismarken“ bezeichnet werden. Diese Gerinnebettformen bestehen in der Regel aus einer konischen Vertiefung stromaufwärts des Hindernisses, die als „Kolk“ bezeichnet wird, und einem angrenzenden Ablagerungsbereich stromabwärts des Hindernisses, der als „Sedimentrücken“ bezeichnet wird. Die Bildung und zeitliche Entwicklung von fluvialen Hindernismarken wird durch turbulente Wirbelsysteme in der Nähe des Hindernisses ausgelöst. Diese Wirbel erhöhen die Strömungsgeschwindigkeit und die turbulente Schubspannung im Umfeld des Hindernisses und bewirken eine Sedimentmobilisierung, selbst wenn die Strömungsgeschwindigkeit stromaufwärts unterhalb der kritischen Schwelle für eine allgemeine Geschiebebewegung liegt. Die hydraulischen und sedimentären Prozesse der Hindernismarkenbildung werden durch eine Vielzahl von Rahmenbedingungen beeinflusst, die sich aus den Eigenschaften der anströmenden Strömung, den Eigenschaften des Sediments und den Eigenschaften des Hindernisses selbst zusammensetzten. Die meisten Erkenntnisse über den Einfluss verschiedener Rahmenbedingungen auf die Bildung von fluvialen Hindernismarken stammen aus dem Wasserbau, vor allem im Hinblick auf die Kolkung an technischen Infrastrukturen wie Brückenpfeilern.

Dabei werden jedoch Rahmenbedingungen, die für die Bildung von fluvialen Hindernismarken an natürlichen Hindernissen (Felsblöcke, Ufervegetation) wichtig sind, nicht berücksichtigt. Die prozessbezogene geowissenschaftliche Forschung zur Entstehung von fluvialen Hindernismarken an natürlichen Hindernissen fällt zudem erstaunlich überschaubar aus. Dies gilt insbesondere im Hinblick auf die unbekannte Auswirkung unterschiedlicher Überflutungstiefen auf die Kolkung an Felsblöcken unterschiedlicher Form während eines Hochwasserereignisses sowie die Auswirkung der Durchlässigkeit auf die Wirbelbildung an einem strauchartigen Hindernis.

Die experimentelle Forschung in hydraulischen Versuchskanälen erlaubt die systematische Variation einzelner Rahmenbedingungen während andere Rahmenbedingungen konstant gehalten werden und ermöglicht so die Analyse ihrer Auswirkungen auf die Prozesse der Bildung von fluvialen Hindernismarken.

Experimentelle Forschung ermöglicht somit die Simulation und Messung von Rahmenbedingungen, die während der Hindernismarken-Entstehung im Gelände nicht, oder nur mit sehr großem technischen Aufwand gemessen werden können. Darüber hinaus stellen Experimente eine wesentliche Verbindung zwischen Feldbeobachtungen und theoretischen Modellen dar.

In dieser Dissertationsschrift werden die Ergebnisse von vier experimentellen Versuchskampagnen vorgestellt, die insgesamt über 190 Versuchsdurchläufe (einschließlich Testläufe) umfassten. Jede Versuchskampagne war auf ein bis zwei Rahmenbedingungen ausgerichtet, die systematisch variiert wurden, um die Dynamik der Bildung fluvialer Hindernismarken zu quantifizieren und die damit verbundenen Schwellenwerte zu beschreiben. Die vorliegende Studie vergleicht Laborergebnisse zu Geometrie fluvialer Hindernismarken auf verschiedenen räumlichen Skalen. Dazu wurde die Geometrie fluvialer Hindernismarken an Felsblöcken im Colorado River, Arizona, Vereinigte Staaten von Amerika, und vegetationsbedingten Sedimentstrukturen an durchlässigen *Populus nigra* L.-Sträuchern an der Loire, Frankreich, erfasst und mit den Laborergebnissen verglichen. Abgesehen von der rein akademischen Relevanz dürfte ein verfeinertes Verständnis der Kontrolle der Rahmenbedingungen und Schwellenwerte für die Bildung von Hindernismarken auch für die Anwendung in der Praxis von Nutzen sein, wo persistente Hindernismarken als geeignete Indikatoren für die Abschätzung des Ausmaßes vergangener Hochwasserereignisse gelten.

In dieser Dissertationsschrift wird auf Grundlage erhaltener fluvialer Hindernismarken Geometrien an Felsblöcken ein weiterentwickeltes Konzept für die Rekonstruktion der wahrscheinlichsten Strömungsbedingungen in Bezug auf Strömungstiefe, -geschwindigkeit und -dauer während der Bildung vorgestellt. Dieses Konzept basiert auf einem empirischen Ansatz, der Labor- und Felddaten kombiniert. Das Konzept wird für persistente lokale Kolkgeometrien an solitären Felsblöcken im ephemeren Fluss Rambla de la Viuda, Spanien, getestet, wobei die Sohlenformen als Indikatoren für die Rahmenbedingungen während ihrer Entstehung verwendet werden.
Die wichtigsten Erkenntnisse des Beitrags lassen sich wie folgt zusammenfassen:

- Es wird ein Konzept vorgestellt, das 13 nichtdimensionale Kontrollparameter von Rahmenbedingunegn umfasst, die sich auf die Bildung von Hindernismarken an Fließgewässerhindernissen auswirken. Das Konzept basiert auf zwei

hierarchischen Ebenen, die schwellenbasiert sind und Rahmenbedingungen enthalten, für die die (i) geometrischen Längenskalen von fluvialen Hindernismarken maximiert werden; (ii) Rahmenbedingungen, die dazu beitragen, dass die maximalen Ausmaße einer fluvialen Hindernismarke nicht erreicht werden; und (iii) Bedingungen, bei denen die Bildung von Hindernismarken vollständig verhindert wird.

- Die primären Kontrollparameter bestimmen die Größe der Verwirbelungen am Hindernis und damit auch die potenzielle Maximalgröße der fluvialen Hindernismarke. Die sekundären Kontrollparameter beeinflussen die Dynamik der Verwirbelungen und begrenzen die potenzielle maximale Größe der entstehenden Hindernismarke, wenn bestimmte Schwellenwerte überschritten werden.
- Die Fließtiefe in Relation zur Hindernisgröße stellt einen primären Kontrollparameter für die Hindernismarkenbildung an natürlichen Hindernissen, wie z.B. Felsblöcken, dar. Folglich werden die geometrischen Längenskalen bei einer Fließtiefe, die mit der Hindernisgröße vergleichbar ist, maximiert. Umgekehrt begrenzt eine Erhöhung der Fließtiefe über diesen Wert hinaus die räumliche Ausdehnung der Hindernismarke.
- Die räumliche Ausdehnung einer fluvialen Hindernismarke und ihre zeitliche Entwicklung werden durch eine Reihe von Rahmenbedingungen eingeschränkt, darunter die Mächtigkeit der Sedimentablagerungen in denen sich das Hindernis befindet und die Eigenschaft, dass ein Geröll- /Felsblock infolge der Kolkung in den Kolk kippen kann. Im Falle eines durchlässigen Hindernisses, wie z. B. strauchartiger Ufervegetation, wurde durch experimentelle Versuche ein Schwellenwert ermittelt. Dieser Wert stellt den Punkt dar, an dem aufgrund der übermäßigen Porosität des Hindernisses die Entstehung fluvialer Hindernismarken und die Ablagerung von Sedimenten im Strömungsschatten nicht mehr möglich sind. Dadurch kann die ankommende Strömung das Hindernis „passieren“. Außerdem wurde eine Methode zur Quantifizierung der optischen Porosität von Vegetationselementen unter Feldbedingungen weiterentwickelt und erfolgreich auf *Populus nigra* L.-Sträucher an der Loire in Frankreich angewendet.
- Es wird ein quantitatives Modell vorgestellt, das die Vergrößerung des Kolks im Laufe der Zeit für stationäre und instationäre Strömungsbedingungen bewertet. Der Vergleich der Modellergebnisse mit *in-situ*-Hindernisgeometrien im Gelände

und auf unterschiedlicher räumlicher Skala zeigen Ähnlichkeiten mit den Laborergebnissen, was impliziert, dass die beobachteten Prozesse und Formen skaleninvariant sind.

- Die Größe der dominanten Verwirbelung an der Hindernismarke kann auf der Grundlage von persistenten geometrischen Merkmalen des lokalen Kolks bestimmt werden. Eine Auswertung von Labor- und Geländedaten zeigt, dass es eine Korrelation zwischen der Wirbelgröße und der Strömungstiefe während der Bildung der Hindernismarke gibt. Daraufaufbauend wurde ein empirisches Modell formuliert, um die wahrscheinlichste Strömungstiefe während der Bildung der Hindernismarke zu bestimmen. Das empirische Modell wurde auf persistente Hindernismarken an Felsblöcken im ephemeren Fluss Rambla de la Viuda, Spanien, angewendet und führte zu Ergebnissen, deren Plausibilität mit etablierten Methoden der paläohydrologischen Forschung überprüft wurde. Dies ist der erste Fall, in dem die geometrischen Merkmale erhaltener Kolke an Felsblöcken als quantitativer Indikator für die Fließtiefe während ihrer Entstehung verwendet wurden.

LIST OF PUBLICATIONS

Schlömer, O., Herget, J. & Euler, T. (2020) Boundary condition control of fluvial obstacle mark formation – framework from a geoscientific perspective. *Earth Surface Processes and Landforms* 45(1), 189–206.
DOI: https://doi.org/10.1002/esp.4793
The published version is reproduced in Chapter 4 of this thesis

Schlömer, O., Grams, P. E., Buscombe, D. & Herget, J. (2021) Geometry of obstacle marks at instream boulders—integration of laboratory investigations and field observations. *Earth Surface Processes and Landforms* 46(3), 659–679.
DOI: https://doi.org/10.1002/esp.5055
The published version is reproduced in Chapter 6 of this thesis

Schlömer, O., & Reimann, A. (2021) Wenn Büsche Flussbaumeister werden: Der Einfluss von Vegetation auf die Flussbettformung. *Geographische Rundschau* (7–8), 20–25.

Schlömer, O. & Herget, J. (2023) Geometry of local scour holes at boulder-like obstacles during unsteady flow conditions and varying submergence. *Water* 15(5), 958.
DOI: https://doi.org/10.3390/w15050958
The published version is reproduced in Chapter 7 of this thesis

Schlömer, O., Luneau, S., Rodrigues, S. & Herget, J. (2024) Vegetation-induced sedimentary structures: porosity of riparian shrubs as control parameter of sedimentary processes during floods. *International Journal of Sediment Research* 39, 497–513.
DOI: https://doi.org/10.1016/j.ijsrc.2024.05.006
The published version is reproduced in Chapter 9 of this thesis

*Schlömer, O. & Herget, J. (2025) Influence of submergence ratio on horseshoe vortex size at boulder obstacles. Submitted to *Journal of Hydraulic Research*.

*Schlömer, O., Herget, J., & Benito, G. (2025) On the usage of local scour holes at boulders for flow reconstruction in ephemeral streams. Submitted to *River*.

*) Manuscripts were submitted during the course of the assessment of the thesis.

LIST OF FIGURES

Figure 1. Obstacle marks at natural obstacles of various spatial scales. Dashed lines indicate the extent of the local scour hole; doted lines the extent of the sediment ridge. (a) Obstacle mark at a rectangular boulder in Rambla de la Viuda (Spain). (b) VISS in the wake of a *Populus nigra* L. sprout at Amboise, Loire River (France). (c) Local scour at a mussel shell at a beach resulting from bi-directional flow (copyright Paul Davies | Dreamstime). Arrows indicate direction of flow. 2

Figure 2. Thematic relationship and interrelation between the different analysis chapters. 10

Figure 3. Obstacle marks at different obstacle types at field scale from various locations. Dashed lines indicate the extent of the local scour hole. (a) Large solitary boulder at Anapodaris gorge, Crete (Greece) (copyright Jürgen Herget). (b) Matured tree with entangled driftwood at the Loire River near Port Charbonnier (France). (c) Power pole at the Tagliamento River near Spilimbergo (Italy) (copyright Jürgen Herget). Arrows indicate direction of flow. 14

Figure 4. Schematic plan view of an obstacle mark generated at a laboratory flume indicating characteristic geometric length scales. Arrow indicates direction of flow. 17

Figure 5. (a) Flow field at a cube at full submerged conditions and back-flow mode of the HV1. (b) Flow field at a porous vegetal element including bled flow through the obstacle. 20

Figure 6. Cross sectional profile of the upstream local scour hole slope indicating internal differentiation and positions of primary horseshoe vortex (HV1) and secondary horseshoe vortex (HV2) (not to scale).ls and ds indicate local scour hole length (l_s) and local scour hole depth (d_s) as shown in Figure 3. 21

Figure 7. Local scour hole at a bedrock hill near the village of Chagan Uzun, Altai Mountains, Siberia. Arrow indicates direction of flow. Dashed line indicates the approximate extent of the local scour hole. Man to scale (copyright Jürgen Herget) 23

Figure 8. Scheme on different physical modelling approaches modified after Baynes *et al*. (2018) and Peakall *et al*. (2009). 25

Figure 9. Diagram of the laboratory flume. (a) Pump and cone valves for flow control. (b) Slide gate at the end of the working section to adjust the flume depth. (c) Flow straightener in the flume inlet. (d) Cross section of the working section. (e) Technical sketch of the flume. Blue arrows indicate flow direction. 28

Figure 10. Photographs of obstacles used in laboratory flume studies. (a) Solid obstacles of various shapes. (b) Permeable brushes of different porosity (increasing from left to right). .30

Figure 11. Laboratory flume instrumentation for topography and flow measurements. 32

Figure 12. Sedimentary structures at obstacles in the ephemeral Rambla de la Viuda, Spain. (A) Obstacle mark on a boulder (~ 1 m height). The black dotted line indicates the upper edge of the scour hole and the dashed white line indicates the sediment accumulation in the wake. (B) Tapered accumulation of fine gravel in the wake of an instream vegetation element. Rod (1.5 m) for scale. Arrows indicate flow direction. 38

Figure 13. Time evolution of scour depth at a rectangular obstacle for test run A9. 44

Figure 14. Block chart on boundary condition control of obstacle mark formation at natural instream obstacles. It should be noted that the equilibrium time (t_e) is a function of d_w/L_o, U_m/U_c and L_o/D_{50} and is not displayed. 51

Figure 15. Water surface profiles for series A experiments at a cuboid obstacle. (A) Slightly submerged conditions ($1 < d_w/L_o < 2$). (B) Non-submerged conditions ($0 > d_w/L_o < 1$). For fully submerged conditions ($d_w/L_o > 2$) no disturbance of the water surface could be detected. Flow direction is from left to right. Point measurements are interpolated using piecewise cubic Hermite interpolation polynomials. 62

Figure 16. (A) Normalized scour volumes ($Vol_s^{1/3}/L_o$) of runs A1-11 and A17-22. Squares = cuboid obstacle, circles = spherical obstacle. (B) Normalized scour volumes ($Vol_s^{1/3}/L_o$) of

runs B34-44. (C) Comparison of (A) and (B) for different d_w/L_o and U_m/U_c. The indications of $U_m/U_c = 0.72$ and $U_m/U_c = 0.67$ are valid for the data point marked by the vertical arrows. 64

Figure 17. Obstacle mark topography at a spherical obstacle after 24 h runtime for different submergence ratios (d_w/L_o). (A) Inverse obstacle mark, (B) Transitional obstacle mark, (C) Typical obstacle mark. Flow direction from left to right. 66

Figure 18. Flow field in the vicinity of (A) elliptical pebble and (B) spherical obstacle for runs A13 an A24. TKE = turbulent kinetic energy (Nm^{-2}). Estimates critical bed shear stress for used sediment is 0.20 N/m^{-2}. 67

Figure 19. Normalized local scour hole volume over submergence ratio.....77

Figure 20. Normalized diameter of HV1 over normalized local scour hole volume. (a) For different experimental series and (b) for different extent of submergence ratio within experimental series.....79

Figure 21. Normalized diameter of HV1 over submergence ratio. 81

Figure 22. (a) Side view of experimental setups within the working section of the flume; FB = flume bottom. (b) Definition of subsequent cross-sections for the estimation of the sediment transport rate (q^b) exemplified for the upstream cross-section of the frontal scour hole in non-dimensional form. (c) Point measurements of upstream horizontal cross-section in non-dimensional form for run A6 displaying calibrated measurements while flume was operating (cyan) and drained (red). 94

Figure 23. Map of Colorado River in the upstream portion of Grand Canyon National Park (shaded in grey) highlighting extent of bathymetric and topographic survey in lower Marble Canyon in 2009 (Kaplinski *et al*., 2017 a). Distance between black dots in the study segment is 5 river miles. GIS data is provided by the U.S. Geological Survey and the Grand Canyon Monitoring & Research Center (GCMRC), while illustration is inspired by Figure 1 published in Grams *et al*., (2019).....100

Figure 25. Scaled sediment transport rate over scaled time-scale of all experimental series estimated form (a) upstream longitudinal profiles of the frontal scour hole and (b) upstream horizontal profiles of the frontal scour hole. 102

Figure 26. Plan view of frontal scour holes modelled at different stages of evolution and different experimental setups. (a) Frontal scour hole at a mounted cube (b) Frontal scour hole at a moveable cube partially buried in the frontal scour hole and tilted into upstream direction. (c) Frontal scour hole at an alluvial layer of reduced thickness after 5 min runtime indicating that scour incision reached flume bottom and (d) after 1440 min indicating ongoing enlargement of frontal scour hole in length, width as well as in the extent of scour hole bottom. (e) Frontal scour hole at a moveable sphere partially buried in the frontal scour hole and tilted into upstream direction. (f) Wake scour at a moveable sphere. 103

Figure 27. Movement (self-burial and upstream tilting) at a cuboid obstacle (run C1) for (a) initial phase of experiments ($t/te \leq 0.05$) and (b) for final phase of experiments ($t/t_e \geq 0.42$). (c) Trajectory of non-dimensional obstacle movement and scour depth evolution over non-dimensional time observed at run C4 (spherical obstacle). 104

Figure 28. (a) Histogram of absolute scour hole dimensions (d_s, l_s, w_s) at field evidence. (b) Histogram of morphometric relation (d_s/l_s) including kernel density estimation. (c) Histogram of morphometric relation (d_s/w_s) including kernel density estimation.....106

Figure 29. Examples of obstacle mark morphologies at boulders of different size identified within the study area. (a), (c), and (d) represent typical obstacle mark morphologies, while (b) depicts a wake scour pattern. Isoline-interval is 1 m and arrows indicate direction of flow. Boulders are highlighted in black. 107

Figure 30. Linear relationships of non- dimensional morphometric variables of the frontal scour hole. (a) l_s/L_o against d_s/L_o for series A, slope (ß1) of the relationship is depicted in Table 7. (b) w_s/L_o against d_s/L_o for series A, slope (ß1) of the relationship is depicted in Table 7. (c) l_s/L_o against d_s/L_o for series B. (d) w_s/L_o against d_s/L_o for series B. (e) l_s/L_o against d_s/L_o for

series C. (f) w_s/L_o against d_s/L_o for series C. (g) l_s/L_o against d_s/L_o for field evidence, slope (ß1) of the relationship is depicted in Table 7. (h) w_s/L_o against d_s/L_o for field evidence, slope (ß1) of the relationship is depicted in Table 7. 109

Figure 31. (a) Scaled longitudinal frontal scour hole profiles exemplified for runs A1, A6, and A9 at indicated times (a), runs B2 and B6 (c), and runs C1 and C4 (e). Scaled horizontal frontal scour hole profiles of runs A1, A6, and A9 (b), runs B2 and B6 (d), and runs C1 and C4 (f). (g) Scaled longitudinal frontal scour hole profiles at boulders of different size. (h) Scaled horizontal frontal scour hole profiles at boulders of different size. (i) Inclination of longitudinal and horizontal scour hole slopes for all field evidence (n = 89).....111

Figure 32. Geometrical relations of the frontal scour hole over non-dimensional time in $\log_{10}$-scale for all experimental series (a) d_s/l_s and (b) d_s/w_s. 112

Figure 33. (a) Scaled scour bottom against non-dimensional time (1: $t/t_e < 0.003$; 2: = $0.003 < 0.04$; 3: ≥ 0.04. (b) Scaled scour bottom against scaled scour depth. (c) Inclination of upper slope segment (n= 174) of the frontal scour hole estimated from longitudinal profiles grouped by non-dimensional time (1: $t/t_e < 0.003$; 2: = $0.003 < 0.04$; 3: ≥ 0.04). (d) From horizontal scour hole profiles (n=176). (e) Inclination of lower slope segment (n=157) of the frontal scour hole estimated from longitudinal profiles grouped by non-dimensional time. (f) From horizontal profiles (n=109).....114

Figure 34. (a) Log-transformed l_s of laboratory data and field evidence against log-transformed model values. (b) Log-transformed l_s against log-transformed d_s for laboratory data and field evidence. 115

Figure 35. Linear relationships of l_s against w_s for (a) laboratory data and (b) for field evidence. (c) Log-transformed w_s of laboratory data and field evidence against log-transformed model values. (d) Log-transformed w_s against log-transformed d_s for laboratory data and field evidence. 116

Figure 36. (a) Local scour hole at a boulder in ephemeral Rambla de la Viuda, NE Spain, 2019 . (b) Local scour hole at a cube generated in a flume. 125

Figure 37. Laboratory hydrographs and indication of discharge intervals (n) and duration of rising limb (tr) and falling limb (tf): (a) symmetrical, (b) positively skewed, (c) negatively skewed, and (d) flash flood. 133

Figure 38. Extent of submergence of the obstacle and indication of discharge interval (n): (a) unsubmerged, (b) shallowly submerged, and (c) fully submerged. 134

Figure 39. Evolution of normalized scour depth (d_s/L_o) over non-dimensional time (t/t_e) for different hydrograph shapes in Series A experiments: (a) symmetrical, (b) left-skewed, (c) right-skewed, (d) flash flood. 137

Figure 40. Dimensionless flow work (W*) of Series A experiments: (a) scenario 1 (clear water), (b) scenario 2 (transitional), and (c) scenario 3 (channel degradation). 139

Figure 41. Dimensionless scour hole depth (d_s/L_o) versus dimensionless flow work (W*) observed in symmetrical hydrographs of different durations in clear-water conditions.....140

Figure 42. Trajectory of dimensionless scour hole depth (d_s/L_o) versus dimensionless time (t/t_e) for general sediment transport and clear-water conditions in Series A experiments and for different hydrograph shapes: (a) symmetrical, (b) positively skewed, (c) flash flood, and (d) negatively skewed. 142

Figure 43. Estimation of bedload transported out of the local scour hole along its longitudinal axis. 143

Figure 44. Dimensionless bedload (q*) versus dimensionless time scale of experiments (t/t_{end}): (a) clear water and (b) general sediment transport. 144

Figure 45. Hysteresis pattern: (a) clear water and (b) channel degradation. 145

Figure 46. Dependence of non-dimensional geometrical length scales on non-dimensional scour hole depth in different experimental series: (a) scour hole length and (b) scour hole width. 146

Figure 47. Scaled scour hole cross sections at different time intervals: (a) longitudinal (l_s to d_s) and (b) horizontal (w_s to d_s). 147
Figure 48. Normalized local scour hole volume of present experimental results versus model of local scour hole enlargement by Schlömer *et al*. (2021).....148
Figure 49. Geometrical relationship of d_s/l_s vs. non-dimensional time in clear-water conditions and for different hydrograph shapes: (a) symmetrical, (b) positively skewed, (c) flash flood, and (d) negatively skewed. 149
Figure 50. Geometrical relationship of d_s/w_s vs. non-dimensional time in clear-water conditions and for different hydrograph shapes: (a) symmetrical, (b) positively skewed, (c) flash flood, and (d) negatively skewed. 149
Figure 51. Modeled DEMs (a–d) and associated DoDs (e–g) for flash flood hydrographs in clear-water conditions: (a) Flood 1, (b) Flood 2, (c) Flood 3, (d) Flood 4, (e) DoD 1, (f) DoD 2, and (g) DoD 3. Arrows indicate direction of flow.....153
Figure 52. Obstacle mark at a boulder in the Rambla de la Viuda (OM5). Arrow indicates direction of flow. The width of the boulder perpendicular to the flow is 2.7 m.....160
Figure 53. Map of the study area at Rambla de la Viuda (Spain) View in the study reaches is downstream. 164
Figure 54. The registered daily mean discharge at the Maria Christina Reservoir from 2013 to 2018. The data was sampled by the Júcar River Basin Authority (Confederación Hidrográfica del Júcar). 165
Figure 55. DEM of OM2 (a) and OM8 (b). The distance between isolines is 0.25 m. Arrow indicates direction of flow. 170
Figure 56. Morphometric relationship of the geometrical length scales of the local scour holes at boulders in Rambla de la Viuda.....172
Figure 57. Persistent segmentation of local scour hole slope at a boulder in Rambla de la Viuda (OM13). Arrow indicates direction of flow. Scale bar is 2 metres.....173
Figure 58. Longitudinal cross-section of the local scour hole (OM7) indicating position for axis estimation of D_v (a and b). Flow is from left to right. Scale is in metres. Points are measurements that are connected through interpolated line. 174
Figure 59. Channel cross-sectional profiles in Rambla de la Viuda with estimated flow depth from jetsam deposits. (a) Reach I. (b) Reach. (c), (d) woody jetsam deposits as indicators for maximum flow depth during peak flow.....176
Figure 60. Vegetation-induced sedimentary structures on *P. nigra* L. shrubs in the Loire River. Local scour hole (solid line) and sediment ridge (dashed line) on a shrub at two different seasonal stages (a) full foliage, (b) leafless. (c) Sediment ridge in the wake of a shrub without a local scour hole. Arrows indicate flow direction. 185
Figure 61. Schematic map and photographs of the study area at the Loire River. 190
Figure 62. Definition of representative length scales of field evidence) (Rodrigues *et al*., 2007). 191
Figure 63. Workflow of optical porosity estimation exemplified for artificial obstacles. 193
Figure 64. Relation between optical porosity (V_p) and volumetric porosity (Vol_p) for artificial obstacles used in the laboratory study. 194
Figure 65. (a) Results of sieving analysis for sediment used in series A experiments where d_x is the diameter for which x percent of the sediment is finer); (b) suspended sediment concentration (SSC) approaching the obstacle for Series A experiments; and (c) results of sieving analysis for sediments used in Series B experiments).....195
Figure 66. Workflow for estimating optical porosity in field conditions. (a), (c), and (e) display measurements taken during full foliage in May 2018, while (b), (d), and (f) exhibit measurements taken during leafless conditions in January 2019. The scale bar is 0.2 m. ...200

Figure 67. Results of sieving analysis of field evidence. (a) VISS composed of local scour hole and adjacent sediment ridge, and (b) VISS from sediment alone in the wake. 202
Figure 68. Sediment ridge outcrop reveals herbaceous vegetation root network as depicted in images (a) and (b). Muddy layers are visible in the uniform medium sand deposition shown in images (c) and (d). 203
Figure 69. Dependence local scour hole (a–c) and sediment ridge (d–f) geometrical length scales on the surface exposed to flow. 204
Figure 70. (a) Estimated normalized sediment ridge volume ($Vol_r^{1/3}/w_o$) as a function of normalized sediment ridge volume from weighed sediment samples ($Vol_w^{1/3}/w_o$). (b) Dependence of estimated normalized sediment ridge volume ($Vol_r^{1/3}/w_o$) on optical porosity (V_p). Error bars represent standard errors and means. 205
Figure 71. Flow field quantification near porous obstruction for d_w = 0.006 m, 0.015 m, and 0.03 m: (a-c); streamwise flow component normalization (d-f) of turbulence intensity (TI); and (g-i) vertical flow component. 207
Figure. 72. Estimated normalized bed load (q*) exiting the local scour hole during the normalized experimental duration for longitudinal cross-sections (a, b) and horizontal cross-sections (c, d). This is for hydraulic scenario 3 (a, c) and hydraulic scenario 2 (b, d). 210
Figure 73. Dependence of geometric length scales on optical porosity (V_p). (a-c) Local scour hole. (d-f). Sediment ridge. 211
Figure 74. Dependence scoured volume ($Vol_s^{1/3}$) (a) and normalized deposited volume ($Vol_r^{1/3}$) (b) on proposed empirical model. 212

LIST OF TABLES

Table 1. Brief summary of the methods of the analyses in Chapters 4 to 9: Laboratory study, field study, combined study. 11

Table 2. Experimental campaigns, focal control parameters, and number of laboratory runs. ... 34

Table 3. Primary and secondary control parameters of obstacle mark formation at solid and permeable instream obstructions. 56

Table 4. Boundary conditions of the experiments and results. C = cube, Sp = sphere, P = pebble. Values are in m, m/s and m³. Uc is estimated by equations (14) and (15). ‡ denotes scour holes in the wake. 61

Table 5. Non-dimensional hydraulic boundary conditions of all experimental series. C = Cube, S = Sphere. † Uc = 5.75 log (5.53 d_w/D_{50}) u_c*, with u_c* = 0.015+0.0125 D_{50}1.4 (0.1 < D_{50} < 1mm). 98

Table 6. Statistical properties of absolute values of morphometric variables at field evidence (n = 89). IQR = interquartile range, MAD = median absolute deviation. 106

Table 7. Statistical properties of linear regression (y = ß1 x) for laboratory (n=231) and field results (n = 89) on non-dimensional morphometric variables. ‡ bootstrapped estimates. ... 110

Table 8. Statistical properties of model fits (linear regressions (y = ß1 x)) on-dimensional morphometric variables (n = 320). 116

Table 9. Duration of discharge intervals in experimental hydrographs in Series A/B/C. 135

Table 10. Hydraulic boundary conditions of flow intervals used to design hydrographs. 135

Table 11. Surveyed obstacle marks in Rambla de la Viuda. † Coordinates in WGS 84. 170

Table 12. Measured geometrical length scales of obstacle marks and estimated flow depth during formation.† estimated by equation (47) ‡ estimated by equation (48) 175

Table 13. Hydraulic conditions of Series B experiments. 197

LIST OF ABBREVIATIONS

B	Channel cross section (L)
b_p	Number of black pixels
c^b	Depth-integrated frontal scour hole area (L^2)
d_s	Local scour hole depth at the obstacle front (L)
d_s/L_o	Nondimensional local scour hole depth (-)
d_{sed}	Thickness of the bed layer (L)
d_{sed}/L_o	Relative thickness of the bed layer (-)
d_w	Flow depth (L)
d_w/L_o	Submergence ratio (-)
D_{16}	16th percentile grain size (L)
D_{50}	Median grain diameter of the bed sediment (L)
D_{84}	84th percentile grain size (L)
Fr	Froude number (-)
g	Gravitational acceleration (L/T^2)
h_d	Deflected height of a flexible vegetation element exposed to a current (L)
h_o	Height of the obstacle (L)
h_r	Height of sediment ridge (L)
HV	Horseshoe vortex system
HV1	Primary horseshoe vortex
HV2	Secondary horseshoe vortex
I_o	Inclination of the obstacle in streamwise direction (-)
I_v	Perpendicular alignment of the obstacle to the streambed (90°) (-)
L_o	Effective obstacle size ($h_o^{2/3}\ w_o^{1/3}$) (-)
L_o/D_{50}	Relative sediment coarseness (-)
L_o/B	Blockage ratio (-)
le_o	Length of obstacle (L)
L_o/B	Blockage ratio (-)
L_o/D_{50}	Relative sediment coarseness (-)
l_s	Local scour hole frontal length (L)
l_s/L_o	Nondimensional local scour hole frontal length (-)
l_r	Length of sediment ridge (L)
Mb	Indicator for the mobility of a boulder-like obstruction due to tilting (-)
Q	Discharge (L^3/T)

q	Discharge per unit width (L^2/T)
q^b	Bedload flux out of the local scour hole (L^2/T)
q_p	Unit discharge at peak flow (L^2/T)
q^*	Dimensionless bedload flux (-)
Re	Reynolds number (-)
S_b	Scour hole bottom (-)
Sh	Hydrodynamic shape of a body (L_o/le_o) (-)
SOF	Surface exposed to flow (L^2)
t	Time (T)
t_e	Time scale to reach equilibrium (T)
t_{end}	Overall runtime of experimental hydrographs
t_f	Duration of the rising limb of experimental hydrographs
TI	Turbulence intensities
t_p	Total number of pixels
t_r	Duration of the falling limb of experimental hydrographs
u	Instantaneous flow velocity in streamwise direction (L/T)
$\bar{u}$	Time-averaged flow velocity in streamwise direction (L/T)
$\bar{u}'$	Time-averaged derivation of flow velocity in streamwise direction (L/T)
U_c	Critical flow velocity for the entrainment of bed sediment (LT−1)
u_c^*	Critical shear velocity (L/T)
U_m	Mean approach flow velocity (L/T)
U_m/U_c	Flow intensity
$U_m/gL_o^{1/2}$	Obstacle Froude number (Fr_o) (-)
U_mL_o/ν	Obstacle Reynolds number (Reo) (-)
$\bar{u}'_{rms}$	Root mean square of the fluctuating velocity component in streamwise direction (L/T)
v	Instantaneous flow velocity in lateral direction (L/T)
$\bar{v}$	Time-averaged flow velocity in lateral direction (L/T)
$\bar{v}'$	Time-averaged derivation of flow velocity in lateral direction (L/T)
$\bar{v}'_{rms}$	Root mean square of the fluctuating velocity component in lateral direction (L/T)
V_p	Optical porosity
Vol_p	Volumetric porosity
Vol_r	Volume of sediment ridge (L^3)

Vol_s	Volume of local scour hole (L^3)
Vol_w	Volume of sediment ridge from weighed sediment samples (L^3)
V_s or Vol_s	Volume of the local scour hole (L^3)
W*	Dimensionless effective flow work (-)
w	Instantaneous flow velocity in vertical direction (L/T)
$\bar{w}$	Time-averaged flow velocity in vertical direction (L/T)
$\bar{w}$'	Time-averaged derivation of flow velocity in vertical direction (L/T)
w_o	Obstacle width (L)
w_p	Number of white pixels
w_r	Width of sediment ridge (L)
$\bar{w}'_{rms}$	Root mean square of the fluctuating velocity component in vertical direction (L/T)
w_s	Local scour hole frontal width (L)
w_s/L_o	Nondimensional local scour hole frontal width (-)
w_{set}	Settling velocity of grain size fraction (L/T)
x	Longitudinal streamwise direction in a local Cartesian coordinate system
y	Perpendicular to streamwise direction in a local Cartesian coordinate system
z	Vertical direction in a local Cartesian coordinate system
Φ	Angle of slopes (-)
Φ_{crit}	Critical angle of repose (-)
ν	Kinematic viscosity (L^2/T)
ρ	Water density (M/L^3)
ρ_s	Sediment density (M/L^3)
σ_G	Gradation coefficient of sediment ($D_{84}/D_{16}^{1/2}$ (-))

1. INTRODUCTION

1.1 GENERAL

Obstacles such as boulders, woody debris, trees and shrubs, as well as man-made structures such as bridge piers, have a profound effect on the dynamics of water flow and sediment movement in alluvial streams and rivers. It is important to recognise that these changes can have a significant impact on the surrounding environment due to the formation of three-dimensional vortex structures in the vicinity of the obstacle caused by local pressure gradients. This results in an increase in turbulent bed shear stresses which have a significant impact on the river bed, leading to sediment mobilisation and erosion which causes the formation of a "local scour hole" upstream and lateral to the obstacle. As a result, sediment is mobilised even when there is no general sediment transport in the undisturbed upstream flow, i.e. when clear water conditions prevail. The eroded sediment is transported downstream where it accumulates in the wake zone, creating a tapered leeward "sediment ridge". In summary, a distinctive bedform is created around the obstacle, commonly referred to as a "fluvial obstacle mark" (Richardson, 1968; Allen, 1984; Paola *et al*., 1986) (Fig. 1). In the case of a vegetation element, the term "vegetation induced sedimentary structure (VISS)" is commonly used, where a sediment ridge and sometimes a local scour hole are present in the vicinity of riparian vegetation (Rygel *et al*., 2004).

Either way, fluvial riffles are sedimentary structures that create unique microhabitats in streams. They are also known to be the primary cause of fluvial island formation, which is critical for providing ecological services and supporting biodiversity. As such, riffles are of paramount importance to the discipline of biogeomorphology (Osterkamp, 1998; Wu *et al*., 2024). Fluvial obstacle marks have been documented in the field at fixed obstructions at a range of spatial scales. These scales range from overland flow at rock fragments (Poesen *et al*., 1994; Niu *et al*., 2019) to large boulders, bedrock mounds and icebergs affected by large glacier outburst floods (jökulhlaups) (Herget, 2005; Wells *et al*., 2022). The consistent macroscopic pattern persists across all spatial scales, for which characteristic geometric length scales (i.e. depth/height, length, width) are defined to describe geometry (Euler & Herget 2011, 2012). However, in the disciplines of fluvial geomorphology and biogeomorphology, there is surprisingly little quantitative knowledge of how hydraulic and sedimentary processes of obstacle formation at natural obstacles, such as isolated boulders or riparian vegetation elements, are influenced by environmental boundary conditions.

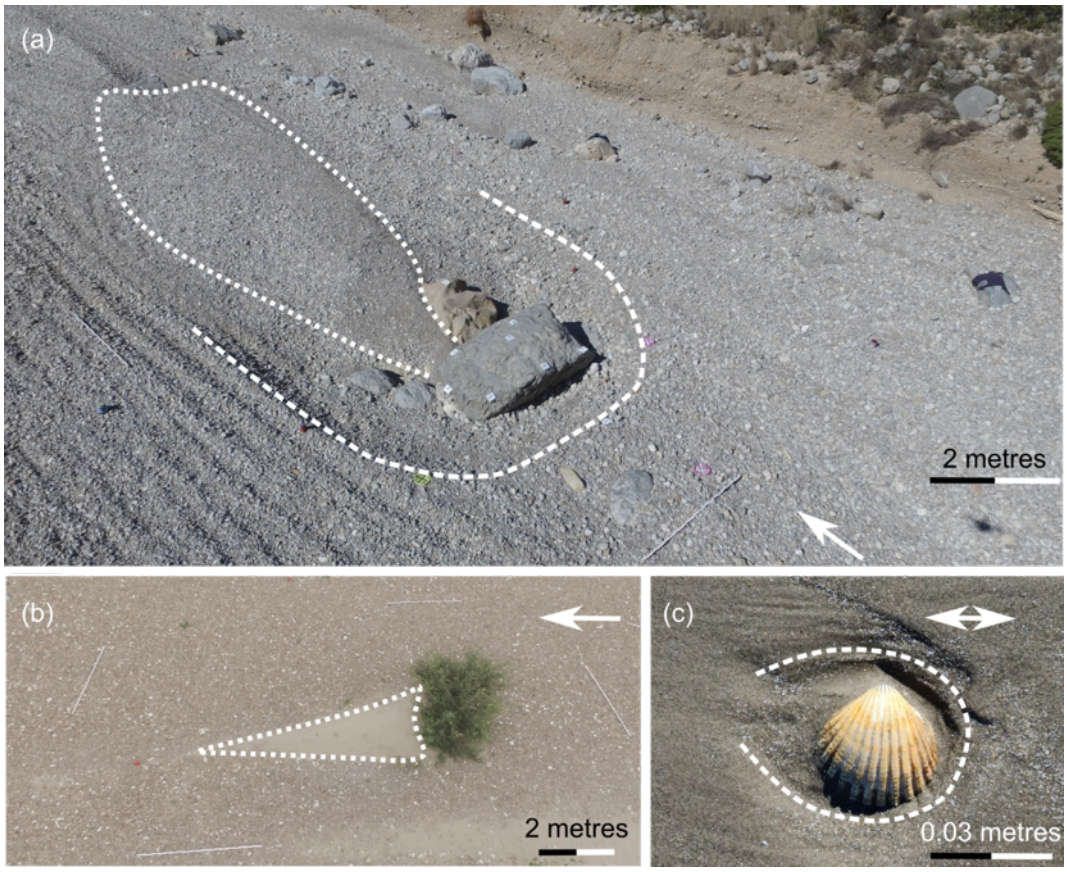


Figure 1. Obstacle marks at natural obstacles of different spatial scales. Dashed lines indicate the extent of the local scour hole; dotted lines indicate the extent of the sediment ridge. (a) Obstacle mark on a rectangular boulder at Rambla de la Viuda (Spain). (b) VISS in the wake of a *Populus nigra* L. shoot at Amboise, Loire River (France). (c) Local scour on a mussel shell on a beach resulting from bidirectional flow (copyright Paul Davies | Dreamstime). The arrows indicate the direction of flow.

1.2 PROBLEM

Boundary conditions compromise the conditions of the approaching flow, the properties of the sediment and the properties of the obstacle itself. From this perspective, environmental boundary conditions determine the shape and dimension of the developing bedform. The formation of obstacle marks is therefore interpreted as a geomorphic system of interrelated influences that trigger positive and negative feedback loops when thresholds are crossed (Murray *et al*., 2014; Phillips, 2002).

Over the past decades, the vast majority of knowledge on the control of boundary conditions on processes at river barriers has been gained by the hydraulic engineering community, particularly with regard to the phenomenon of local scour at engineering infrastructure such as bridge piers, groynes and pipelines (Breusers & Raudkivi, 1991; Melville & Coleman, 2000). However, the formation of fluvial scarps at natural obstacles, such as isolated boulders or porous riparian vegetation, is influenced by

boundary conditions that have not been the subject of hydraulic engineering research. Furthermore, process-related geoscientific research on this topic is surprisingly limited. For example, boulders are mobile in the sense that they are likely to tilt into the emerging local scour hole when the underlying sediment layer is eroded (Inman & Jenkins, 2019). The impact of this self-burial on hydraulic and sedimentary processes has not been systematically investigated (Friedrich *et al*., 2016; Rennie *et al*., 2017). In addition, shrubby riparian vegetation has a unique effect on hydraulic processes that is different from that of solid obstacle. Flow is able to penetrate the voids not occupied by stems, branches, twigs and leaves, resulting in different hydraulic processes that have not been investigated in the context of obstacle mark formation.

Furthermore, during a flood event, natural obstacles such as boulders are affected by flow conditions that are different from those affecting engineered infrastructure such as bridge piers. The presence of a boulder in a stream can result from a number of factors, including natural processes such as rockfall and debris flows, or human activities such as stream restoration (Euler *et al*., 2017). In the case of a boulder in a stream, depending on its size and shape, it may remain submerged during periods of low flow, with part of it protruding above the water surface. As the flow depth increases, for example due to a flood event, the boulder becomes submerged and occupies only the lower part of the flow depth. Thus, the submergence ratio of the obstacle, i.e. the ratio of the approaching flow depth to the size of the obstacle, is likely to be an important boundary condition that has not yet been systematically investigated. Substantial basic research on the control of boundary conditions on obstacle marks is therefore essential in order to identify conditions that enhance formation processes or boundary conditions that limit the formation of obstacle marks at natural flow obstacles.

Physical experiments in a laboratory flume offer the advantage of controllable boundary conditions and the ability to reset the system as often as necessary. In addition, process quantification is much more feasible than under field conditions. Experiments also have advantages over numerical modelling because the materials and processes in experiments are real, unlike those in numerical models, which are virtual (Burkow & Griebel, 2016; Liao *et al*., 2021). The physical modelling approach used is interpreted as a 1:1 model that does not apply formal scaling principles, but replicates the flow and sediment transport processes of focal interest. Starting from basic assumptions and boundary conditions, the experimental setups will be gradually and systematically refined with newly obtained results. In order to achieve an approximation

to natural boundary conditions, it is necessary to refine and adapt the procedure in the presence of unsteady flow and sediment movement (i.e. live-bed conditions), which affect the formation of obstacle marks over time.

In addition to the purely academic relevance, a refined knowledge of the control of boundary conditions and thresholds for fluvial obstacle mark formation is expected to be beneficial for application in field sites, where persistent obstacle marks are expected to be suitable indicators for estimating the magnitude of past flood events (Herget, 2005; Herget *et al*., 2014). However, Herget's (2005) attempt to use obstacle marks on large boulders and bedrock outcrops in the Altai Mountains (Siberia) as indicators of flow depth during Pleistocene high-magnitude glacial outburst floods was unsuccessful. The semi-empirical relationship derived from hydraulic engineering research to determine flow depth from the geometry of a local scour hole and the width of the obstacle gave implausible results. This was because the relationship was originally derived from laboratory studies of local scour on bridge piers, which did not take into account the effect of submergence. The resulting flow depth relative to the local scour hole would have resulted in overtopping of the nearby mountain ranges. In addition, Herget *et al*. (2013) have described fluvial obstacle mark geometries in the field that deviate from the "typical" obstacle mark pattern previously described. These deviations include the presence of a local scour hole in the wake (i.e. downstream) of a large boulder, or the formation of depressions only on the lateral edges of the obstacle. However, the boundary conditions that lead to these variations in obstacle mark geometry remain largely unknown.

It has therefore been suggested that further, more comprehensive studies of flumes are required to investigate the local scouring phenomenon at natural obstacles such as boulders, and to determine the extent to which different environmental boundary conditions influence this phenomenon. This would allow an evaluation of the dependence and possible indicator function of obstacle mark geometries to assess the magnitude of responsible floods.

1.3 FRAMING THE RESEARCH QUESTIONS

Based on the outlined problems and the unknown effects of boundary condition control on obstacle mark formation at natural instream obstructions, the central research questions of this thesis are

Q1: What are the boundary conditions that enhance or limit the formative processes of fluvial obstacle mark evolution at natural instream obstructions, and how can they be operationalised as physical control parameters?

Q2: Can control parameter thresholds be identified that modify hydraulic and sedimentary processes and regulate transitions in the spatial pattern and geometric relationship of fluvial obstacle marks?

Q3: What is the effect of changing time-dependent boundary conditions on the evolution of fluvial obstacle geometry?

Q4: Can the geometry of fluvial obstacle marks be used as hydraulic indicators to improve procedures for estimating the magnitude of past flood events?

1.4 RESEARCH OBJECTIVES

Based on the research questions formulated above, the main objectives of this thesis are as follows:

I. To develop a theoretical framework for controlling the evolution of fluvial obstacle marks at natural river obstructions using scale-invariant physical control parameters.

II. Conducting systematic laboratory physical modelling studies of control parameters (sensu stricto parameter studies) to quantify control parameter thresholds affecting the formation and expansion of fluvial obstacle marks.

III. Comparison of laboratory results on obstacle mark formation and enlargement with field evidence on obstacle marks at different spatial scales.

IV. Evaluate the usability of fluvial obstacle mark geometry on isolated boulders as a hydraulic indicator of the magnitude of past flood events.

1.5 ADDRESSING THE RESEARCH QUESTIONS

The thesis consists of several analysis chapters, each of which is self-contained. Each chapter represents an experimental campaign that provides valuable information for operationalising and parameterising key research questions. Each analysis chapter contains methodically tested and evaluated working hypotheses. Boundary conditions and derived control parameters for obstacle mark formation are systematically varied from simple to more complex conditions. In addition, each analysis chapter provides a concise review of the relevant literature. The structure of the central research questions is explained in detail below.

> **Q1** *What are the boundary conditions that enhance or limit the formative processes of fluvial obstacle mark evolution at natural instream obstructions, and how can they be operationalised as physical control parameters*?

To answer Q1, an interdisciplinary literature review was conducted to identify the boundary conditions for obstacle mark formation at natural instream objects. Boundary conditions are operationalised as non-dimensional control parameters by performing a dimensional analysis based on the principle of the Buckingham Π-theorem (Barenblatt, 2012). The framework integrates control parameters and classifies their significance based on two hierarchical levels for the size of geometric length scales of an obstacle mark. The purpose of the systematisation is to identify the conditions that maximise, limit or completely inhibit the formation of fluvial obstacle marks in relation to characteristic geometric length scales. This framework provides the basis for quantification and threshold setting.

> **Q2** *Can control parameter thresholds be identified that modify hydraulic and sedimentary processes and regulate transitions in the spatial pattern and geometric relationship of fluvial obstacle marks*?

The framework established in Q1 quantifies unknown control parameter thresholds. Q2 is answered by laboratory parameter studies that systematically vary a single control parameter of interest within the constraints of the laboratory facility, while holding other variables constant. This type of sensitivity analysis provides a comprehensive understanding of the effect of each control parameter. Submergence ratio, unsteady flow

effects, the minimum thickness of the alluvial layer to develop an obstacle mark, and obstacle boundary conditions including obstacle shape, mobility and obstacle porosity have been analysed through laboratory studies and sensitivity analysis.

> **Q3** *What is the effect of changing time-dependent boundary conditions on the evolution of fluvial obstacle geometry*?

For a range of control parameters established in Q1 and within empirical thresholds of flow conditions established in Q2, the temporal evolution of river obstacle marks will be investigated by two laboratory campaigns. First, fluvial obstacle mark evolution was experimentally modelled for long duration steady flow (over 4 days) to assess its temporal characteristics. Second, unsteady flow conditions, i.e. temporally varying flow conditions, operationalised by hydrographs for clear water and live bed conditions, are modelled to assess the temporal consistency of the obstacle mark evolution.

> **Q4** *Can the geometry of fluvial obstacle marks be used as hydraulic indicators to improve procedures for estimating the magnitude of past flood events*?

The theoretical and laboratory results derived from Q1 to Q3 are used to establish an application framework for reconstructing the most likely flow conditions in terms of flow depth, velocity and duration during formation based on preserved local scour hole geometries on boulders. The framework was applied to preserved local scour holes on individual boulders in an ungauged ephemeral river in Rambla de la Viuda (Spain), characterised by the occurrence of flash floods.

1.6 THESIS OUTLINE

Chapter 2 of this thesis presents a comprehensive review of obstacle marks as geomorphological structures, including the hydraulic and sedimentary processes that trigger them. In Chapter 3, the methodology for physical experiments and laboratory flume used for parameter studies is outlined and thoroughly characterized. Additionally, Chapter 3 provides an overview of the experimental runs and the parameters of interest in tabular form. Chapters 2 and 3 provide an introduction to the analysis chapters that follow.

Chapters 4 to 8 represent individual analysis that has undergone rigorous peer-review and has been published as journal articles or is currently undergoing revision. The Introduction and Methods-section of each analysis chapter presents a comprehensive version of the content of Chapter 2 and 3. The scheme in Figure 2 and Table 1 illustrate the overall thematic relationship between the different analysis chapters in regard to main research objectives.

Chapter 4 confidently establishes a framework of 13 non-dimensional control parameters to address **Q1**. Additionally, **Q2** is tackled by confidently identifying a threshold in submergence ratio and obstacle shape that maximises the dimensions of the local scour hole. Chapter 4 is aimed at research objectives **I** and **II**.

Chapter 5 addresses **Q2** by comparing experiment results from Chapter 4 to external laboratory datasets on fluvial obstacle mark formation at different degrees of submergence ratio at solid solitary obstacles. A multiple linear regression shows that the size of a vortical structure in the local scour hole is influenced by flow depth, obstacle size, and local scour hole depth. The size of the vortical structure can be assessed based on geometrical characteristics of the local scour hole slopes. Chapter 5 is aimed at research objective **II**.

Chapter 6 addresses **Q3** and presents a laboratory dataset on the temporal evolution of local scour hole geometry at solitary solid obstacles. The geometrical relations of the local scour hole are used to formulate the phases of temporal evolution. A mechanistic model of local scour hole enlargement is established and the shape similitude of local scour holes and scale invariance of the enlargement model is evaluated by comparing laboratory results to an independent field dataset on fluvial obstacle marks at solitary boulders in the Colorado River. Chapter 6 is aimed at research objectives **II** and **III**.

Chapters 7 confidently address **Q3** by conducting experimental runs on fluvial obstacle mark formation at solid solitary obstacles at unsteady discharge. The mechanistic enlargement model is successfully validated for changing hydraulic conditions over time, while the characteristics of the temporal evolution based on geometrical relations over time are firmly confirmed for repetitive discharge events. Chapter 7 is aimed at research objective **II**.

Chapter 8 addresses **Q4** and presents a synthesis to evaluate obstacle marks at boulders, as an indicator of flood magnitude in ephemeral Rambla de la Viuda (Spain). Based on an empirical approach combining laboratory and field data, a novel framework for reconstructing the most likely flow conditions in terms of flow depth, velocity, and duration during formation based on preserved local scour hole geometries at boulders is presented. The reliability of these reconstructions is confirmed by plausibility checks of other reconstruction approaches at the same location. Chapter 8 is aimed at research objective **IV**.

Chapter 9 focuses on the formation of obstacle marks and sediment ridges at porous shrubby vegetation elements in order to address **Q2**. A refined procedure for estimating optical porosity under laboratory and field conditions presented, and a threshold in porosity of the obstacle is experimentally determines that inhibits obstacle mark formation. Field evidence of obstacle marks at *Populus nigra* L. shrubs in floodplain areas of the Loire River (France) is investigated and compared to laboratory observations. An empirical model is presented that assesses the volumes of sediment erosion and deposition at porous obstacles. Chapter 9 is aimed at research objectives **II** and **III**.

In Chapter 10, the results are synthesized and discussed in relation to the main research questions. The final chapter confidently presents a comprehensive conclusion and provides recommendations for future research on obstacle mark formation at natural obstacles.

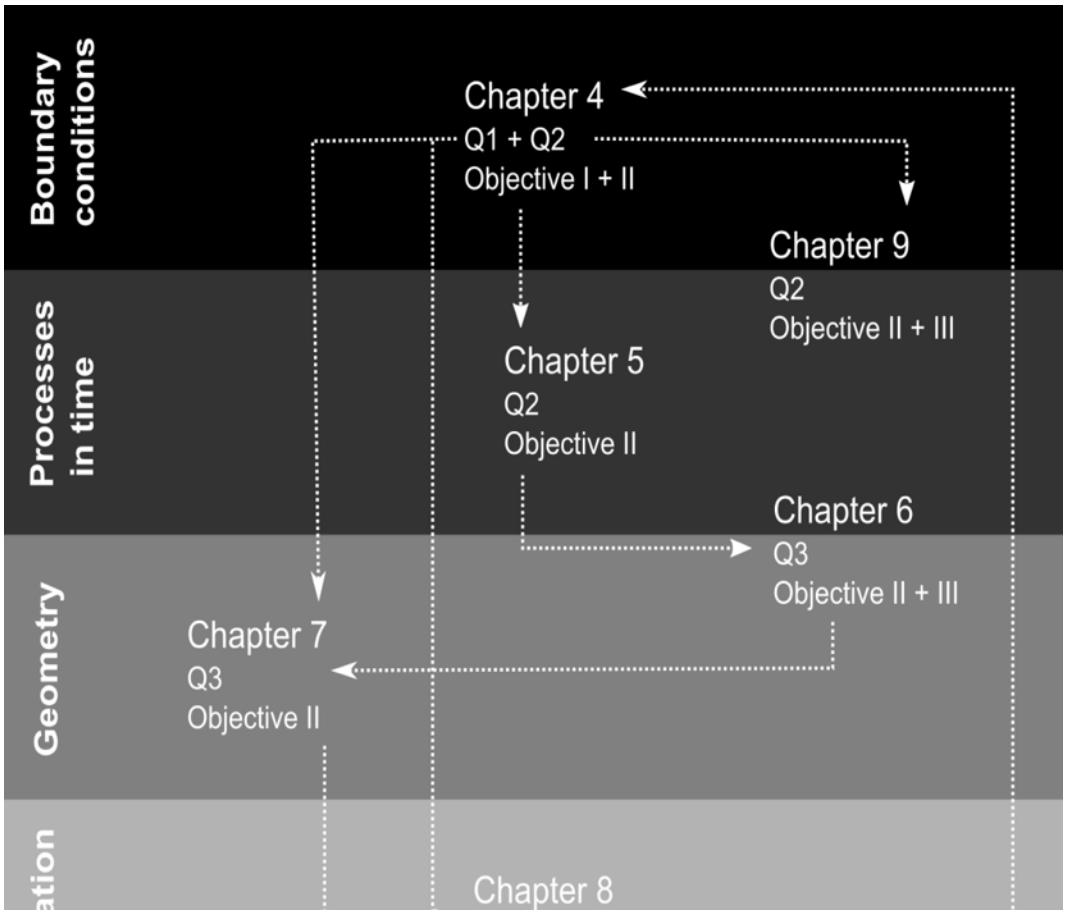


Figure 2. Thematic relationship and interrelationship between the different analysis chapters.

Table 1. Brief summary of the methods of the analyses in Chapters 4 to 9: Laboratory study, field study, combined study.

Chapter	Methods
4 **Q1 Objective I/II**	• Operationalisation of scale-invariant experimental control parameters using the Buckingham Π-theorem (Barenblatt, 2012) • 44 flume runs in two different test series on solid boulder-like obstacles of different shapes exposed to different flow depths and degrees of submergence (emergent to submerged) at subcritical, clear-water conditions and steady discharge for 24 hours experimental runtime
5 **Q2 Objective II**	• Meta-analysis of experiments from Chapter 4 and integration of external laboratory datasets from Euler & Herget (2011) and Euler *et al*. (2017) for a total of 74 experiments to analyse the geometry of local scour holes at boulder-like obstacles and their dependence on flow depth at steady discharge for experimental runtime ranging between 20 and 72 hours
6 **Q3 Objective II/III**	• 33 long duration flume runs (runtime more than four days) on local scouring at solid obstacles at a range of flows (subcritical, clear-water conditions, emergent and submerged water levels) and boundary conditions designed to represent the field setting (i.e. obstacle tilting, and limited thickness of the alluvial layer) at steady discharge • Geometric study of 90 *in-situ* obstacle marks at boulder obstacles in the Colorado River, Marble Canyon, Arizona based on a 1 m-resolution digital elevation model (DEM), (Kaplinski *et al*., 2017b) in a Geographical Information System (GIS)
7 **Q3 Objective II**	• 48 flume runs on local scouring at solid obstacles at unsteady flow conditions and laboratory flood hydrographs of various shapes and durations at clear-water conditions and live-bed conditions for experimental runtimes ranging between two and eight hours
8 **Q4 Objective IV**	• Geometrical measurement of 14 preserved obstacle marks at boulders located in Rambla de la Viuda, Spain, using a Zeiss Elta C30 geodetic total station and in particular Structure-from-Motion Stereo Photogrammetry (SfM-MVS).
9 **Q2 Objective II/III**	• 21 flume experiments on sediment trapping from suspended transport at emergent obstacles of different porosity a live-bed conditions for a experimental runtime of around 25 minutes • 24 flume experiments on local scouring at emergent porous obstacles at clear-water conditions for a experimental runtime of eight hours • Geometric study of vegetation induced sedimentary structures at *Populus nigra L* sprouts at the Loire River, France

2. RESEARCH ON OBSTACLE MARKS

2.1 OBSTACLE MARKS AS BEDFORMS

Obstacle mark are geomorphological and sedimentary structures created by the interaction of a fluid and the topographic obstacles in the flow path. The obstacle alters the flow field, leading to the creation of complex three-dimensional eddies and turbulence in the surrounding area. This results in areas of erosion in front of and to the side of the obstacle and areas of deposition in its wake. These typically consist of a crescent-shaped local scour hole running upstream and surrounding the obstacle laterally downstream, and a dune-like sediment accumulation in the downstream wake of the obstacle, the so-called "sediment ridge". Studies from various geoscience disciplines lead to synonymous terms for erosional and depositional bed features induced by obstacles, including obstacle scour marks (Dżułyński, 1965), current crescents and shadows (Peabody, 1947; Allen, 1984), comet marks (Werner *et al*., 1980), obstruction-formed pool (Buffington *et al*., 2002; Hassan & Woodsmith, 2004; Comiti *et al*., 2005) and vegetation-induced sediment structure (Nakayama *et al*., 2002; Rygel *et al*., 2004).

Although fluvial obstacle marks are considered here as geomorphological structures of the fluvial environment (hereafter referred to as obstacle marks), similar morphologies at different spatial scales have been reported from shipwreck sites on the seafloor (Garlan *et al*, 2015; Quinn & Smyth, 2018; Jiménez-Romero *et al*., 2022), sandy surfaces in the aeolian environment (Luo *et al*., 2012; McKenna Neuman *et al*., 2013; van Dijk *et al*., 2021) and snow (Allen, 1965; Filhol & Sturm, 2015; Zuhr *et al*., 2021). A distinctive feature of obstacle marks is that they are composed of sediments of different textural types, including gravel, sand, and mud. The obstacle is an integral part of the structure and is typically a large bed obstacle with a diameter greater than the grain size of the surrounding alluvium (Shobe *et al*., 2021). In the fluvial environment, many natural obstructions are capable of acting as an obstacle, such as isolated boulders, woody debris and vegetative elements. In addition, man-made structures in rivers such as bridge piers, groynes and weirs can act as obstacles (Fig. 3). These structures have been the focus of engineering research for decades due to safety concerns.



Figure 3. Field scale obstacle marks for different obstacle types from different locations. Dashed lines indicate the extent of local scour. (a) Large single boulder in the Anapodaris gorge, Crete (Greece) (copyright Jürgen Herget). (b) Mature tree with tangled driftwood on the Loire River near Port Charbonnier (France). (c) Electricity pylon on the Tagliamento River near Spilimbergo (Italy) (copyright Jürgen Herget). Arrows indicate the direction of flow.

2.1.1 Research on obstacle marks at man-made obstructions

In engineering, research has focused on the formation of local scour holes at engineering infrastructure. Local scour holes on bridge piers and abutments in fluvial environments can seriously compromise their integrity. Therefore, a large body of knowledge on the phenomenon of local scour at bridge piers in fluvial environments has been built up over the last decades (Breusers & Raudkivi, 1991; Hoffmans & Verheij, 1997; Melville & Coleman, 2000; Ettema *et al*., 2011). Local scouring has also been studied in the marine environment (Sumer & Fredsøe, 2005), for example in the case of local scour hole formation at pipelines (Chiew, 1990; Wu & Chiew, 2012; Drumond e*t al*., 2018; Hu *et al*., 2023), offshore wind farm foundations (Qi & Gao, 2020; Guan *et al*., 2022) and submarine cables (Li *et al*., 2023). Traditionally, the motivation for this research is to estimate the potential maximum local scour depth at the engineering

infrastructure, which is then used as a design parameter for foundation depth or as a proxy for risk assessment procedures during the lifetime of the engineering infrastructure.

The temporal evolution of local scour depth towards a near steady state (i.e. a maximum value) is an asymptotic process in time. It is known from laboratory research that almost 80% of the near steady state local scour depth is reached within only 5 to 40% of the total experimental duration, which is typically of the order of days (Melville & Chiew, 1999). The time scale of local scour under laboratory conditions is mainly dependent on flow velocity and grain size (Lee & Sturm, 2009; Manes & Brocchini, 2015). The engineering community has not focused on the evolution of the whole structure. Most approaches rely on semi-empirical equations that account for key control parameters, including hydraulic and sedimentary boundary conditions and obstacle characteristics (Sheppard *et al*., 2014; Shahriar *et al*., 2021; Tubaldi *et al*., 2022). These control parameters are calibrated in laboratory flume studies to a range that is "more than sufficient" to induce local scour (Ettema *et al*., 2011). Consequently, this introduces a reasonable level of conservatism into design estimates and predictions. Although prediction equations can become more accurate by including more control parameters, the large number of parameters may make them impractical for real-world applications. For example, hydraulic engineering approaches do not take into account boundary conditions that may result in shallower local scour hole depths. Applying design equations to field sites may also result in overpredictions due to conservatism and uncertainty regarding overlooked boundary conditions (Johnson, 1995; Johnson *et al*., 2015).

2.1.2 RESEARCH ON OBSTACLE MARKS AT NATURAL OBSTRUCTIONS

Obstacle marks have been reported qualitatively on solid natural obstructions at various spatial scales. These marks result from overland flow at rock fragments (Poesen *et al*., 1994), at boulders as remnants of flood events in ephemeral streams (Karcz, 1968, 1972; Euler *et al*., 2017), and at icebergs during glacier outburst floods (jökulhlaups) (Russel, 1993; Høgaas & Longva, 2016; Beebee, 2022). Obstacle marks of varying spatial extent are also observed on permeable riparian vegetation elements. Rygel *et al*. (2004) introduced the term "vegetation-induced sedimentary structures" (VISS) to describe ancient sedimentary structures found in floodplain layers. Tooth and Nanson, (2000); Nakayama *et al*. (2002), Rodrigues *et al*. (2007), Euler *et al*., (2014),

Corenblit *et al*. (2016), Schulze *et al*. (2022) and Schalko and Nepf (2024) report *in situ* evidence of such structures in grass colonies, shrubs, shoots, mature trees and dead wood logs. According to the authors, shrubs and shoots tend to cause leeward deposition of sediment in their wake, resulting in sediment ridges. In contrast, mature single trunk trees are known to cause significant local scour holes.

Despite the abundance of documented field evidence for natural obstacles, there is limited research on the formation processes and controlling boundary conditions for obstacle mark formation in channel studies. Laboratory research on solid obstacles, such as boulders, has primarily focused on investigating the flow field (Shamloo *et al*., 2001; Polvi, 2021; Wyssmann *et al*., 2024) and the ability of the boulder to trap incoming sediment in its wake (Thompson, 2008; Papanicolaou *et al*, 2018; Golpira *et al*., 2023), as solitary boulders are often used in stream restoration to improve aquatic habitat availability and quality (Branco *et al*., 2013; Golpira *et al*., 2022). From this research, it is known that the submergence ratio of the boulder, which expresses the relationship between the approaching flow depth and the size of the obstacle, is a particularly important control parameter affecting the flow field and sediment transport processes. At lower flow rates, the obstacle may be emergent, with a portion protruding above the water surface. This affects the flow with localised flow structures, such as hydraulic jumps, which become a function of the Froude number. In contrast, at higher flows, the obstacle occupies only the lower part of the flow depth and is completely submerged, while the flow is subcritical (Papanicolaou *et al*., 2010; Papanicolaou *et al*., 2012). The formation of obstacle marks at boulder-like obstacles has been studied experimentally either under non-submerged conditions (Fisher & Klingman, 1984; Boyer & Roy, 1991) or under fully submerged conditions (Euler & Herget, 2011, 2012; Euler *et al*., 2017), while a systematic evaluation of the effect of different submergence ratios on obstacle mark formation is lacking.

However, based on the work of Euler & Herget (2011, 2012), characteristic geometrical length scales have been defined to describe the geometry of the local scour hole in front of cylindrical obstacles and the sediment ridge in their wake in a near-steady state. The definition of the characteristic geometric length scales was based on what is referred to here as a “typical” obstacle pattern, i.e. a frontal local scour hole and an adjacent sediment ridge in the wake of the obstacle (Fig. 4). This typical pattern differs from a pattern where local scour holes are present in the downstream wake, but a frontal local scour hole is absent. Such a morphology has been described for boulders in

high gradient rivers or rock sills (Comiti *et al*., 2005; Pagliara & Palermo, 2018). However, beyond the description, there is no further explanation based on dominant boundary conditions to explain this type of "inverted" obstacle mark.

Considering a typical obstacle mark pattern, the characteristic geometric length scales include the scour hole depth at the obstacle front (d_s), measured from the undisturbed upstream bed; the scour hole frontal length (l_s) in the plane of symmetry to the incoming flow, measured from the obstacle front to the upstream edge of the scour hole; and the scour hole frontal width (w_s), measured perpendicular to the incoming flow direction from the lateral edges of the scour hole at the obstacle front. The geometry of a local scour hole can be interpreted as an inverted truncated cone with an elliptical shape in plan view ($l_s < w_s$) (Mia & Nago, 2003), whereas the longitudinal shape (i.e. in the direction of flow) is quite symmetrical. A similar definition can be applied to the sediment ridge, including sediment ridge height (h_r), sediment ridge width (w_r) and sediment ridge length (l_r), measured from the downstream end of the obstacle.

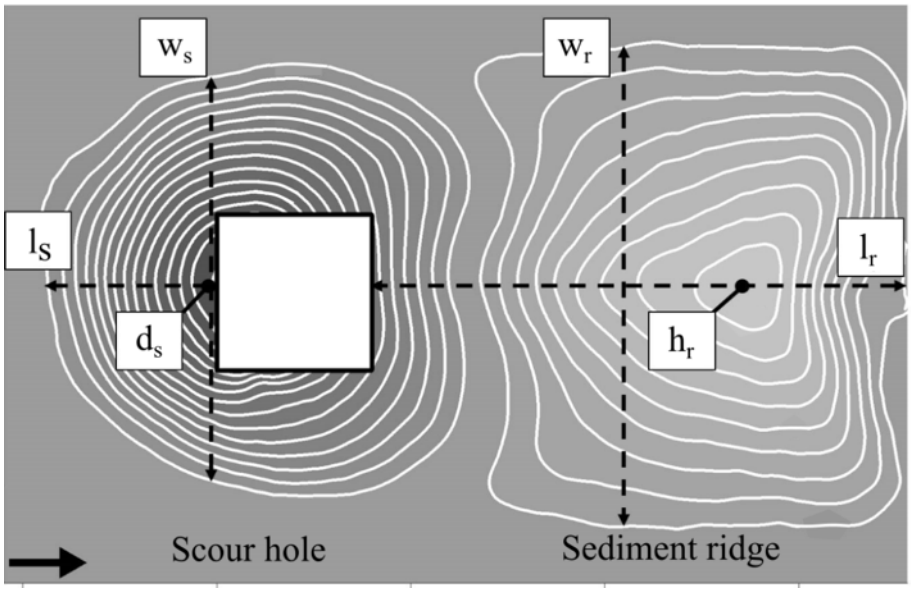


Figure 4. Schematic plan view of an obstacle mark generated on a laboratory flume, showing characteristic geometric length scales. The arrow indicates the direction of flow.

Recent studies in hydraulic engineering have examined the temporal evolution of local scour hole geometry for different types of obstacles and sediment sizes using a range of measurement methods (Bouratsis *et al*., 2017; Poggi & Kudryavtseva, 2019; Rogers *et al*., 2020). However, these studies have focused exclusively on the evolution of local scour depth (d_s), ignoring the formation of other geometric length scales over

time. Therefore, our understanding of the evolution of geometric length scales in boulder-like obstacles over time is limited. The same principles apply to non-solid obstacles in flood channels, such as shrubs and shoots. Local scour holes can form at these porous obstacles (Chen *et al*., 2012; Yagci *et al*., 2016; Yagci *et al*., 2024). However, a comprehensive experimental evaluation of the effect of obstacle permeability on hydraulic and sedimentary processes is lacking.

2.2. BOUNDARY CONDITIONS FOR OBSTACLE MARK FORMATION

The formation of obstacle marks at upstream obstacles can be interpreted as a complex two-phase flow involving water and sediment. Therefore, the hydraulic and sedimentary processes of obstacle mark formation are influenced by environmental boundary conditions. With reference to the advanced knowledge of the hydraulic engineering community on the phenomenon of local scour at engineering infrastructure, the environmental boundary conditions of local scour can be grouped into

Flow conditions, sediment characteristics, geometric characteristics of the obstacle and time (Melville & Coleman, 2000; Sumer & Fredsøe, 2005; Ettema *et al*., 2011). Within these categories, different independent variables operationalise the boundary conditions (i.e. “flow conditions”) into measurable quantities (i.e. mean flow velocity and depth). Some of these quantities are variables, while others are fixed values. They include:

Flow depth (d_w), mean approach velocity (U_m), fluid density (ρ), kinematic viscosity (ν), gravity acceleration (g), mean size (D_{50}) and geometric standard deviation of sediment particle size distribution (σ_G), sediment density (ρ_s), critical mean approach velocity for sediment entrainment (U_c), obstacle size (typically obstacle width, w_o) and time (t).

In engineering approaches to local scour, a functional relationship of boundary condition control on local scour, i.e. the local scour hole depth (d_s), is typically presented:

$$d_s = f\,(d_w, U_m, \rho, \nu, g, \rho_s, U_c, w_o, t)$$

(Eq. 1)

However, the classification only provides a categorisation and does not provide any further hierarchy on the impact of obstacle mark formation. In addition, the classification does not take into account certain boundary conditions that are crucial for

the formation of obstacle marks around natural obstacles such as rocks or vegetation. These conditions include the height and shape of the obstacle, as well as its porosity and other variables.

In this context, obstacle mark formation is interpreted as a system of interrelated influences, whereas obstacle mark formation does not belong to the class of linear cause and effect systems. Rather, they are multi-component complex geomorphic systems characterised by dynamic process interactions that induce positive and negative feedback loops when thresholds are exceeded. There is currently no systematic framework for analysing and evaluating the control of boundary conditions, particularly in relation to the formation of obstacle marks on instream boulders or vegetation elements. When considering the formation of obstacle marks, it is important to consider both the conditions that trigger and enhance their formation as well as those that may limit their formation under natural conditions. This framework can therefore be seen as a basis for the systematic evaluation of individual boundary conditions and control factors under laboratory conditions.

2.3 HYDRAULIC AND SEDIMENTARY PROCESSES OF OBSTACLE MARK FORMATION

Obstacle marks at solid obstacles such as boulders are caused by deformations of the approaching flow in the vicinity of the obstacle, resulting in the following processes: (1) contraction of the streamlines lateral to the obstacle, resulting in higher flow velocities; (2) vertical jet-like downflow towards the bed, resulting from the pressure gradient at the front of the obstacle; (3) formation of an unstable turbulent necklace-like vortex structure at the base of the obstacle, commonly referred to as a horseshoe vortex system (HV); (3) formation of an unstable turbulent necklace-like vortex structure at the base of the obstacle, commonly referred to as a horseshoe vortex system (HV) - because the vortex structure wraps laterally around the sides of the obstacle in the downstream direction; and (4) a decelerated region of flow in the wake of the obstacle, including a wake vortex system of detached shear layers with a vertical axis of rotation (Fig. 5 a), (Dargahi, 1989; Kirkil & Constantinescu, 2015; Pizarro *et al*., 2020)

Processes (1) to (4) are common for the case where the boulder is not submerged, a condition analogous to local scouring at bridge piers. However, under fully submerged conditions, additional eddies are generated at the obstacle (Okamoto & Sunabashiri, 1992; Pattenden *et al*., 2005). In fully submerged conditions, an arched vortex consisting of two lateral vortices at the sides of the obstacle has been reported due to

flow separation at the obstacle, and a vortex is located at the crest of the obstacle (Dey *et al*., 2011; Hajimirzaie *et al*., 2014). As shown by Euler and Herget (2011), this recirculation zone can cause local scouring in the wake of the obstacle instead of frontal local scouring (Fig. 5 a).

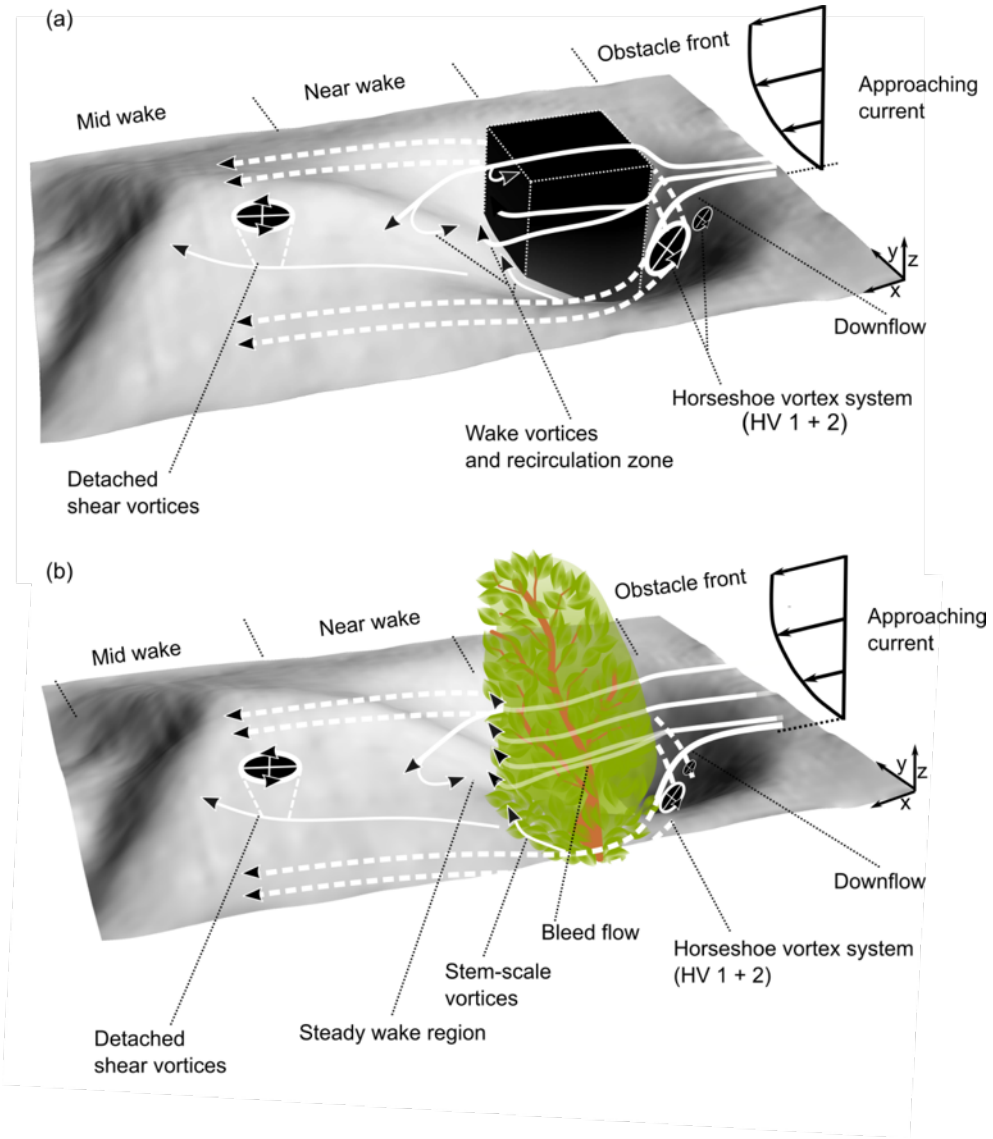


Figure 5. (a) Flow field at a cube at full submergence and backflow mode of the HV1. (b) Flow field at a porous vegetation element including bled flow through the obstacle.

For a non-solid and porous obstacle such as a shrub, a fraction of the approaching flow is forced to pass through the voids (Chen *et al.*, 2012). This not only reduces the flow velocity in the wake of the porous obstacle, but also weakens the pressure gradient in front of the obstacle and conversely reduces the downflow. As a result, only weak HV is present at the base of the obstacle (Fig. 5 b). Considering local scouring at the front of a

solid obstacle processes (1) to (4) increase the bed shear stress relative to the undisturbed upstream flow and induce sediment mobilisation in the vicinity of the obstacle, leading to the formation of an obstacle mark, even if the threshold velocity for general sediment transport in the approaching flow is not exceeded.

The enlargement of the local scour hole is largely closely related to the HV as the main driver of sediment mobilisation (Radice & Tran, 2012; Chen *et al*., 2019). The HV is actually composed of several interacting and unsteady eddies. The largest and most stable eddy is called the primary horseshoe eddy (HV1) and is located near the base of the obstacle (Guan *et al*., 2019). During incision, HV1 sinks into the local scour hole where it promotes sediment mobilisation through saltation and rolling (Dargahi, 1989; Chen *et al*., 2017). Upstream of HV1, a smaller and less coherent eddy (HV2) is located in the outer region of the frontal scour hole. The HV system is an unsteady vortex system that oscillates randomly in time, causing transient weakening. It is known from laboratory fluid dynamics studies that HV2 can lose coherence completely, while HV1 exhibits aperiodic bimodal oscillations that cause changes in the position and shape of the vortex core, from the more common elliptical shape (backflow mode) with the core away from the obstacle, to a circular shape (zero-flow mode) closely aligned with the obstacle (Paik *et al*., 2007; Kirkil & Constantinescu, 2015; Qi *et al*., 2022).

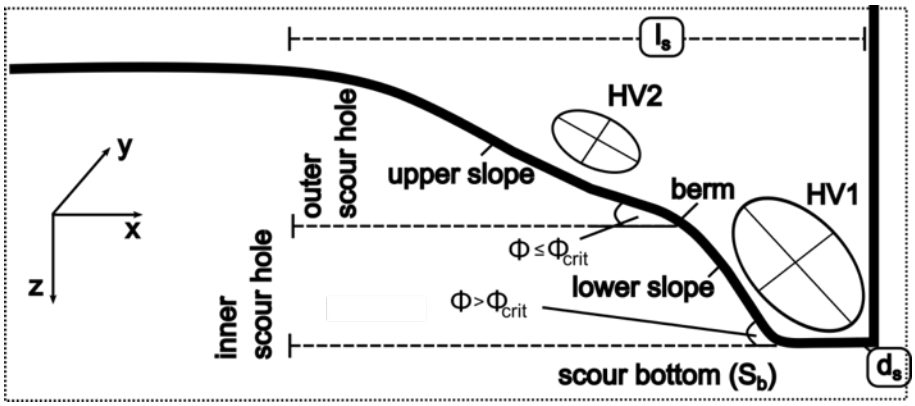


Figure 6. Cross-sectional profile of upstream local scour hole slope showing internal differentiation and positions of primary horseshoe vortex (HV1) and secondary horseshoe vortex (HV2) (not to scale). l_s and d_s indicate local scour hole length (l_s) and local scour hole depth (d_s) as in Figure 3.

In experiments on solidified local scour holes in non-cohesive sediments (sand to gravel), it was observed that the vertical extent of the HV1 in backflow mode coincides with the kink in the upstream local scour hole slope, distinguishing the outer and inner frontal scour holes and a flat semicircular local scour hole bottom (Fig. 6) (Muzzammil

& Gangadhariah, 2003; Muzzammil *et al*., 2004; Unger & Hager, 2006). The steeper inner scour hole is shaped by the HSV and the rotation of the HV1 generally stabilises the lower slope at an angle greater than the angle of repose (Hoffmans, 1993; Link *et al*., 2008). The aforementioned temporal oscillations (HV1) and occasional disappearances (HV2) destabilise the slopes and result in collapses characterised by gravitational movements into the local scour hole bottom, causing an increase in the frontal length and width of the local scour hole. As a result of the collapses, sediment grains slide into the scour bed where they are picked up by HV1 and transported downstream as bedload under its expanding legs. In the mid to far wake region, sediment is deposited as a sediment ridge due to decreasing bed shear stress. Sediment transport on the ridge is also a combination of rolling and sliding.

2.4. USAGE OF OBSTACLE MARKS FOR FLOW RECONSTRUCTION

In contrast to other sedimentary structures where geometric features have been used to reconstruct the most likely flow conditions during their formation, such as dunes (Carling, 1996; Bradley & Venditti, 2017) and antidunes (Shaw, 1977; Froude *et al*., 2017), obstacle marks have not been commonly used to quantitatively reconstruct flow conditions during their formation. A first approach was presented by Herget (2005) on obstacle marks on large boulders and bedrock outcrops in the Altai Mountains (Siberia), which are remnants of Pleistocene large glacier outburst floods (jökulhlaups). A semi-empirical relationship from the engineering community was used to assess flow depth during formation, which describes the presence of a local scour hole for the condition that the ratio of obstacle width to approaching flow depth is equal to or less than 0.5. However, when applied to a local scour hole on a wide bedrock hill (392 metres wide) near the village of Chagan Uzun (Fig. 7), the resulting minimum flow depth during the formation of the local scour hole must have been close to 800 metres, which would have caused the water to overflow the adjacent mountain ranges. This is because the original empirical relationship was established in the engineering community to describe the dependence of local scour holes at bridge piers on the width of the pier and the approaching mean flow depth. The relationship was calibrated solely on the basis of non-submerged conditions of the bridge pier and does not take into account the effects of submergence on local scour, even though the top of the obstacle is underwater. Such conditions were indeed present for the rock mound at Chagan Uzun, as it was located at the bottom of a glacial lake.

Later, Herget *et al*. (2013) were able to present a refined procedure for using obstacle mark geometry to reconstruct the most likely flow velocities during formation. The framework was based on laboratory research focusing on hydraulic and sedimentary processes at submerged obstacles, and showed a consistency of correlations between obstacle mark morphometries over a wide spatial scale. To the author's knowledge, this is the only approach to use obstacle mark geometry quantitatively for flow reconstruction in terms of flow velocity and discharge. Flow velocity and discharge estimates are therefore considered to be minimum values during obstacle mark formation. However, despite significant advances, the approach does not take into account the effects of varying flow depths, which are typical of natural unsteady flood events. Thus, it remains an open question whether flow depths can be inferred from the geometric characteristics of the emerging obstacle mark.



Figure 7. Local scour hole in a bedrock hill near the village of Chagan Uzun, Altai Mountains, Siberia. Arrow indicates direction of flow. Dashed line indicates approximate extent of local scour hole. Man to scale (copyright Jürgen Herget).

3. METHODS

3.1. PHYSICAL MODELLING

For several decades, physical models have been used as a tool in fluvial geomorphology to simulate and study the interaction between flow, sediment transport and morphology (Yalin, 1971; Schumm *et al*., 1987; Bennett *et al*., 2015). The technique is also well established in hydraulic engineering for the design and testing of hydraulic structures (Vittal *et al*., 1993; Xiong *et al*., 2022). Physical modelling offers a significant advantage in terms of experimental control. It allows the simulation and measurement of rare or variable environmental boundary conditions that cannot be measured in their natural counterparts (Peakall *et al*., 1996; Paola *et al*., 2009; Baynes *et al*., 2018). They thus provide an essential link between field observations and theoretical models, allowing for intensive parameter analyses and scenario expansion (Thomas *et al*., 2014). It is important to note that the use of physical models does not necessarily imply the use of an upscaled or downscaled prototype of the studied phenomenon. In a basic sense, they are simple representations of reality and a simplification of a complex system to approximate a real situation. The degree of fidelity achieved is determined by (i) the spatial and temporal scale of the phenomenon under study and (ii) the modelling approach used. Physical modelling approaches can be classified based on their specificity, which refers to the degree to which the model is replicable, and the spatial scale at which they are most applicable (Fig. 8) (Peakall *et al*., 1996; Baynes *et al*., 2018).

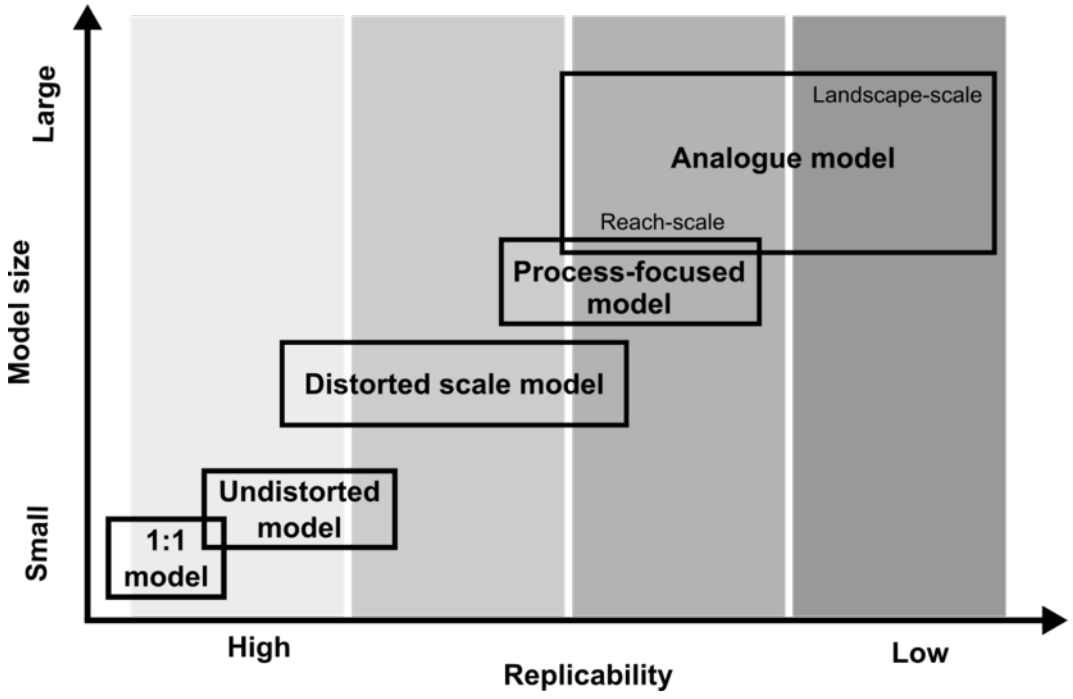


Figure 8. Scheme of different physical modelling approaches, modified from Baynes *et al*. (2018) and Peakall *et al*. (2009).

3.1.1 MODELLING APPROACH

The current work is a 1:1 model and does not aim to formally scale the experimental conditions to the target natural system. This approach is justified when focusing on well-defined, scale-independent features of interest (Novak & Čábelka, 1981). The 1:1 model replicates the flow and transport processes of interest. It does not apply formal scaling principles based on geometric, dynamic and kinematic similarity criteria. However, it is important to consider laboratory scale effects (Heller, 2011; Pfister & Chanson, 2014) in the experimental setup. These effects are often caused by the laboratory infrastructure, which introduces geometric scale effects. Hydraulic models often exhibit scale effects, such as wall-driven secondary flows (Nezu & Nakagawa, 2017), which create unrealistic flow conditions at the model boundaries. Excessive scaling of flow and sediment properties can also introduce laboratory scale effects, resulting in the dominance of surface tension over turbulent flow. Avoiding laboratory scale effects is therefore based on a "rule of thumb" and is not an exact science (Heller, 2011). Compromises will also depend on the size of the laboratory infrastructure. In the previous example, to avoid surface tension effects and establish turbulent flow, the minimum flow depth in physical experiments should be at least five times greater than the median diameter of the sediment used (D_{50}). Sediment size is also a limiting factor in experimental setups, as sediments smaller than the sand fraction (i.e. $D_{50} < 0.063$ mm) (Wentworth, 1922) introduce detrimental cohesive effects into the experimental setup. To avoid geometric effects at the laboratory scale, limits for flow, sediment and obstacle characteristics were considered (Muste, 2017). According to Frostick *et al*. (2011), time scale effects are insignificant in physical experiments on local scour, as the temporal evolution is identical in both experiments and their natural counterparts.

3.1.2 PRINCIPAL OF EXPERIMENTS

The experiments were based on non-dimensional parameters that parameterise the most dominant environmental boundary conditions for obstacle mark formation at natural obstacles. This dimensional analysis was performed by applying the principle of the Buckingham-Π theorem (Barenblatt, 2012), which is a precise mathematical framework for assembling non-dimensional parameters from meaningful variables of the studied phenomenon. The procedure produces a dimensional homogeneity functional relationship that describes the formation of obstacle marks at natural solid and permeable obstacles located in a straight, moderately sloped channel with non-cohesive alluvial sediment. The experiments were conducted in hydraulically rough, subcritical and turbulent flow so that the

dimensionless parameters accurately describe the underlying processes of obstacle mark formation at different spatial scales. Details of the dimensionless analysis procedure are presented in Chapter 4.4 of this paper. However, it should be noted that physical hydraulic modelling is largely controlled by the available laboratory infrastructure, which often leads to simplifications and compromises in the experimental setup. The experimental setup was therefore designed as a type of parameter study in which a single non-dimensional parameter of interest is systematically varied within the constraints of the laboratory facility, while all other parameters are held constant. The experimental design is a type of sensitivity analysis (Hall *et al*., 2009). It examines how changes in the size and geometry of the obstacle mark can be quantitatively attributed to a variation in a non-dimensional parameter.

The rationale for conducting physical experiments as parameter studies and sensitivity analysis is that thresholds can be quantified and boundary conditions can be identified that have the most influence on the resulting obstacle marks. Therefore, functional relationships were established based on regression analysis. Suitable external datasets on obstacle mark formation at natural obstacles were included. The flow properties and the boundary conditions of the obstacle characteristics were systematically modified during the different experimental series. The complexity of the laboratory campaigns was increased to adequately approximate natural conditions.

3.1.3 LABORATORY FLUME

The physical experiments were carried out in a laboratory flume measuring 5 metres in length, 0.32 metres in width and 0.27 metres in depth. The flume has a straight planform and a rectangular cross-sectional profile. The flume side walls and bottom are made of acrylic glass (Fig. 9). The bottom slope of the flume was not adjustable as it was fixed at a moderate slope (0.003 m/m) to ensure water flow in the flume. The flume discharge was regulated by a manually controlled recirculation pump (Lowara FCE Series®, Langenhagen, Germany) and two cone valves (Fig. 9 a). The adjustable flow rates range from 0.5 to 10.5 litres per second. The flow is measured using a magnetic-inductive flowmeter (Schwing MS 1000®, Neukirchen-Vluyn, Germany) with an accuracy of ±1% of the actual flow. Water was stored in two reservoirs, each with a capacity of approximately 1 cubic metre. Flow depth was controlled by a tailgate at the downstream end of the flume outlet (Fig. 9 b). Flow depths in the flume ranged from 0.02 to 0.20 metres, depending on flow velocity. A flow straightener consisting of bundled pipes (approximately 100 pipes, each 3 cm in diameter and 40 cm long) was installed at the inlet of the flume to reduce turbulence and condition the flow to a typical

boundary layer flow profile under pseudo-uniform flow conditions (Fig. 9 c) (Hager & Hutter, 1984).

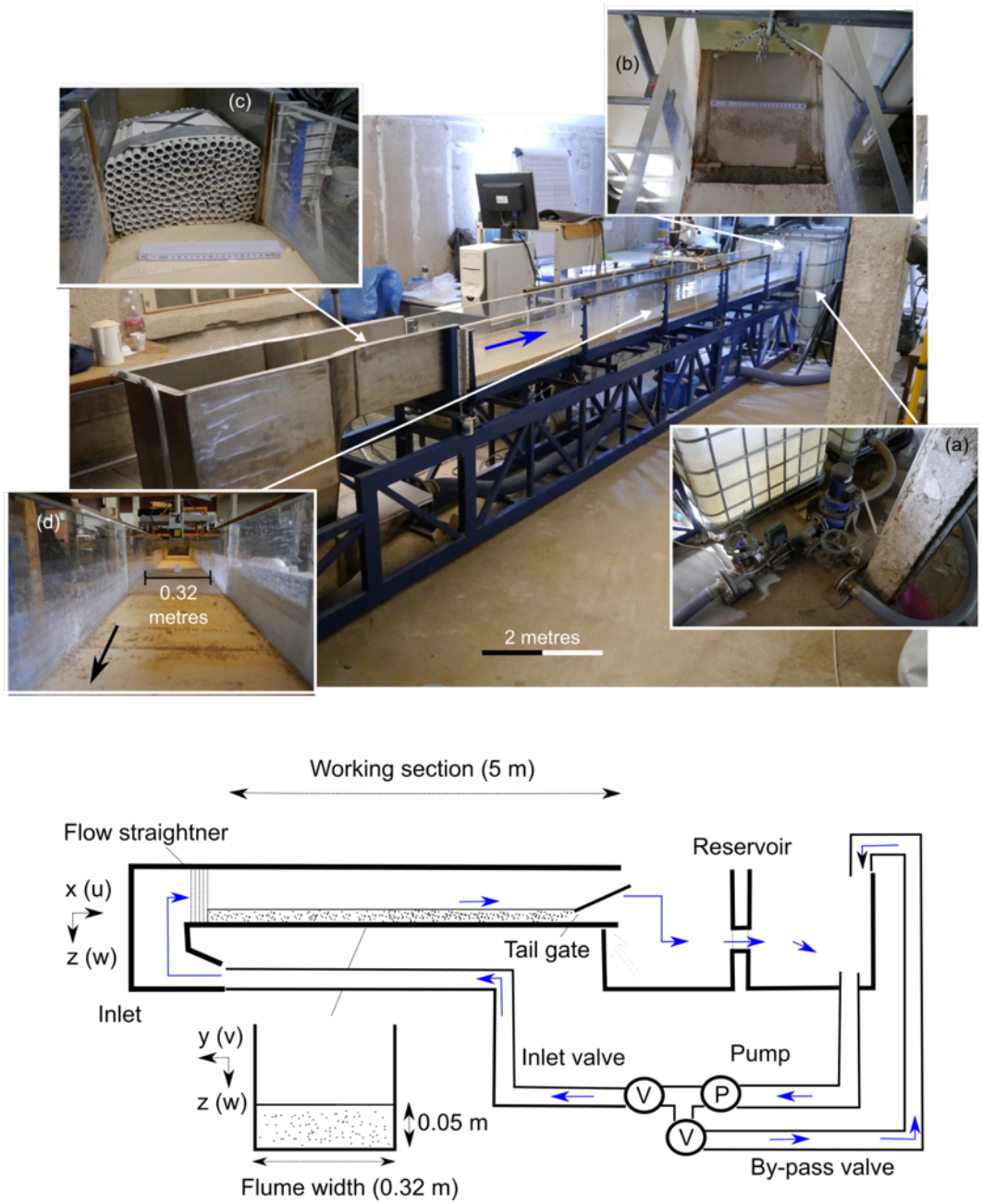


Figure 9. Diagram of the laboratory flume. (a) Pump and cone valves for flow control. (b) Slide gate at the end of the working section to adjust the flume depth. (c) Flow straightener in the flume inlet. (d) Cross section of working section. (e) Technical sketch of the flume. Blue arrows indicate direction of flow.

The working section was positioned 2.7 metres downstream of the flume inlet and was 1.3 metres long. The obstacle was installed in the plane of symmetry to prevent the effects of wall-driven currents on the flume boundaries from affecting the formation of the obstacle mark (Fig. 9 d). A technical design of the flume layout is shown in Figure 9 e.

The obstacles used had a maximum width of 0.04 metres when measured perpendicular to the approaching flow. The ratio of obstacle width to flume width was 0.125, which is below the threshold for over-proportional blocking effects to be introduced in the experimental setup (when obstacle width to flume width > 0.15) (Wu & Balachandar, 2016). Solid boulder-like obstacles were represented by a glass cube and a glass sphere, as well as an elliptical sandstone pebble. The height and width of the obstacles ranged from 3 to 4.5 cm (Fig. 10 a). Depending on the test series, the obstacle was either fixed to the bottom of the channel or freely movable. Cylindrical dish brushes were used to represent a porous barrier. The brushes consisted of a central metal body with plastic bristles over the entire height and were not flexible or inclined in the downstream direction when exposed to flow (Fig. 10 b).

For most of the test series, the flume was filled with a layer of uniform medium-grain sand (σ_G = 1.3, D_{50} = 0.75 mm). For the series of experiments on obstacle mark formation at porous obstacles presented in Chapter 9, a finer uniform sediment size was used (σ_G = 1.5, D_{50} = 0.2 mm) and the flume bottom was modified by installing polystyrene boards to ensure sediment suspension.

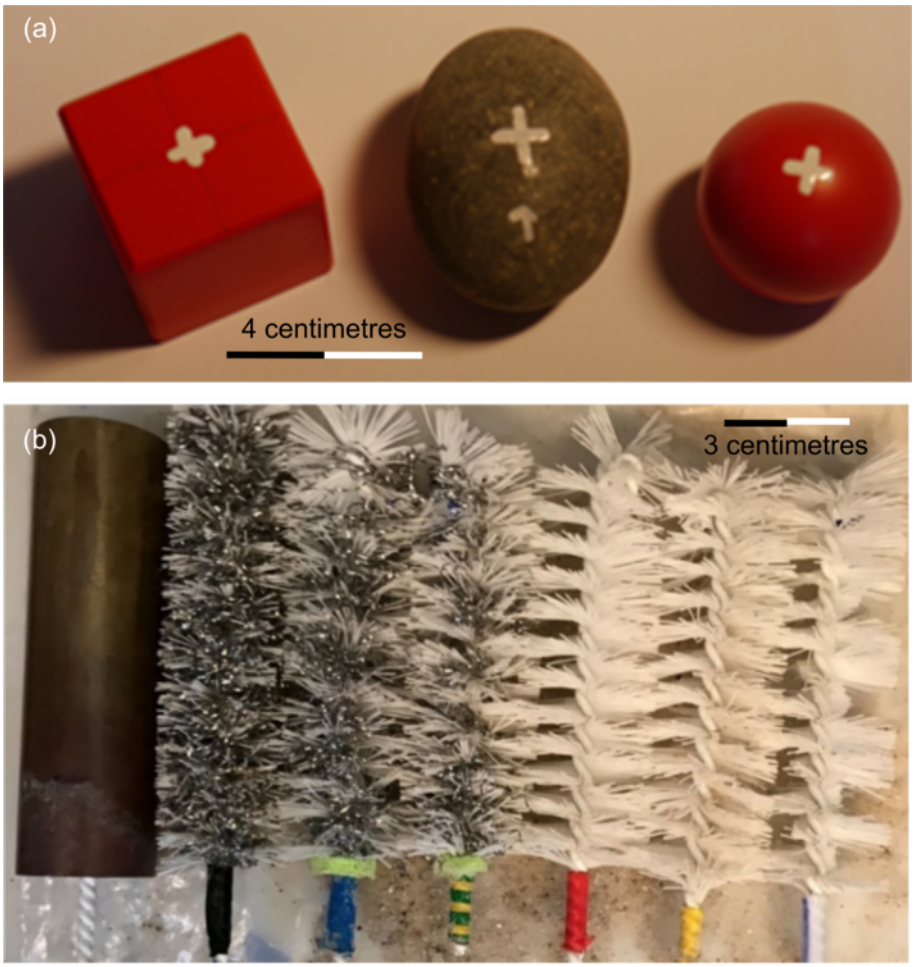


Figure 10. Photographs of obstacles used in laboratory flume studies. (a) Solid obstacles of different shapes. (b) Permeable brushes of varying porosity (increasing from left to right).

3.1.4 MEASUREMENT TECHNIQUE

Several instruments were available for hydraulic or topographic surveys of the channel. These instruments were mounted on a traversing system at the top of the flume, operating both in the longitudinal and flow directions, as well as horizontally, perpendicular to the flow direction. Two LED distance meters (Welotec® OWRB series, Laer, Germany) measured the position of the traversing system to an accuracy of ± 0.5 millimetres. A laser rangefinder (Baumer Electric® ODAM S14C, Frauenfeld, Switzerland, Fig. 11 a, b and c) was used to measure the bed elevation to an accuracy of ± 1.5 millimetres. The instruments were used to measure coordinates in a local Cartesian coordinate system, i.e. x /y /z. Topographic measurements were taken either as a time series during the development of the obstacle mark, where the size of the geometric length scales was measured, or at the end of the experimental runs, where the entire morphology was measured. The topographic measurements were read out and stored using an Orbit Controls OC 7052 data logger (Orbit Controls®, Schlieren, Switzerland, Fig. 11 d). The storage interval was 1 second.

During the experimental runs, the water surface profile in the working section was measured using a Mic + 25 ultrasonic distance meter (Microsonic®, Dortmund, Germany) with an accuracy of ± 0.1 mm (Fig. 11 a). Flow velocity was measured with two instruments. A Streamflow 403 miniature velocity probe (Nixon Flowmeter®, Cheltenham, United Kingdom) was used to measure the streamwise velocity component (u) in vertical velocity profiles from the bed to near the water surface (Fig. 11 e). The accuracy of the instrument is ±1.5% of the actual velocity. The velocity probe was used to ensure that the boundary layer in the test section was fully developed and followed a logarithmic distribution upstream of the obstacle. A downward-looking Vectrino Acoustic Doppler Velocimeter (ADV) (Nortek AS®) was used to measure the three-dimensional velocity components (u = streamwise; v = perpendicular to the streamwise direction; w = vertical to the streamwise direction) and turbulence (u', v', w') in the vicinity of the obstacle, also using vertical profiles (Fig. 11 c). The sampling volume of the ADV was located 4.7 cm below the emitting sensor, making the measurement procedure contactless. However, the ADV was not suitable for flow depths less than 4.7 centimetres. The sampling volume remained constant at a height of 7 millimetres and a width of 6 millimetres, while the sampling frequency was 25 hertz. Flow velocity and turbulence were measured for 60-120 seconds at each vertical measurement point to ensure a statistically significant time series (Fig. 11 f).

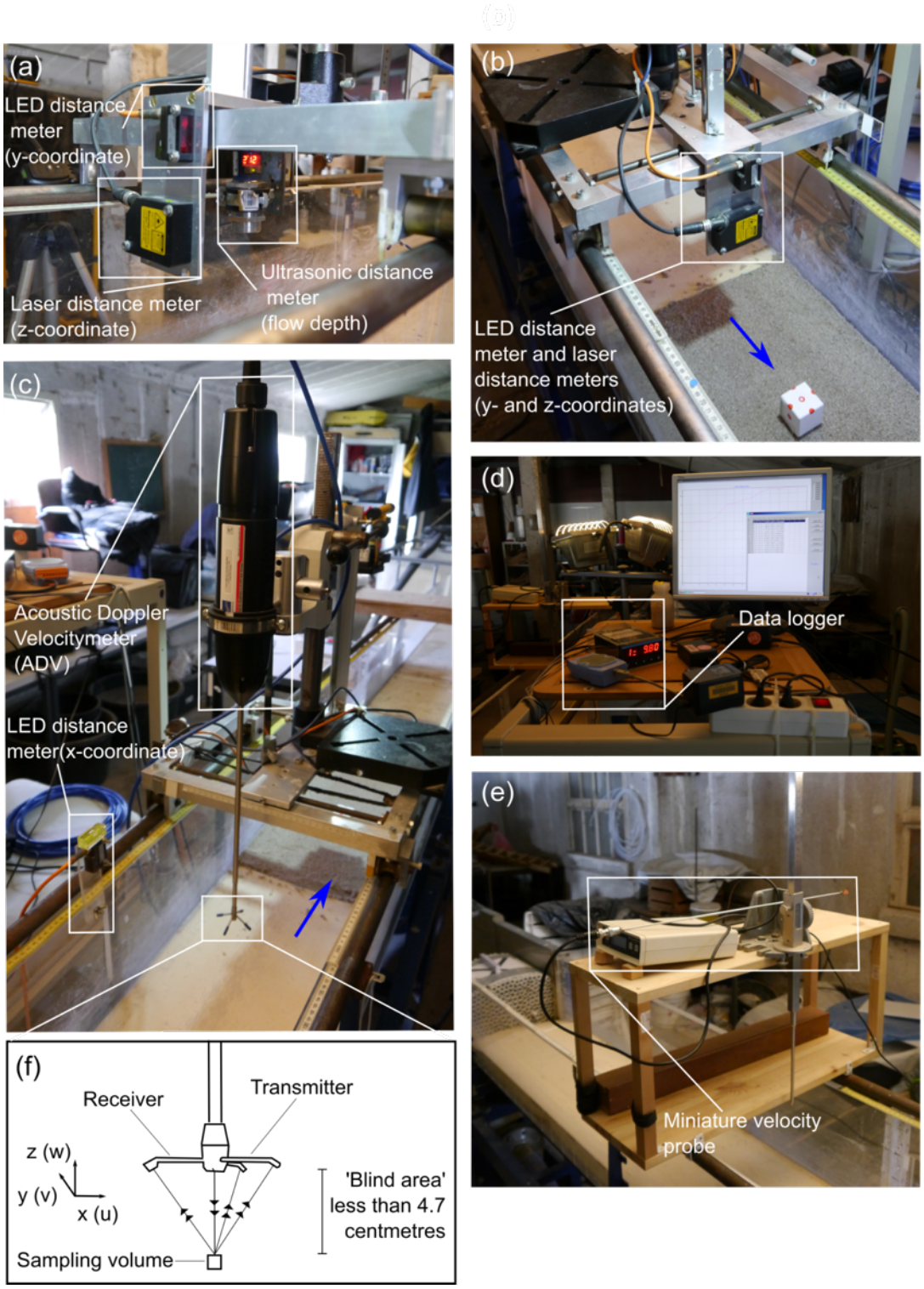


Figure 11. Laboratory flume instrumentation for topography and flow measurements.

For the series of experiments presented in Chapter 7, DEMs were generated using the structure-from-motion multiview stereo photogrammetry (SfM-MVS) technique. This method can resolve a 3D structure from overlapping images acquired from different camera positions (Westoby *et al*., 2012; Smith *et al*., 2016; Morgan *et al*., 2017). Images were captured using a Panasonic® Lumix DMC-G5 (DSLM) camera with a 4/3" (17.3 × 13.0 mm) 16-megapixel image sensor and a Lumix G-Vario 14-42 mm zoom lens set at 21 mm focal length for minimal image distortion (35 mm full frame equivalent). Images were captured at a resolution of 4608 × 3072 pixels with a field of view of 52°. The camera was mounted on the traverse system approximately 60 centimetres above the channel. Several ground control points (GCPs) were distributed throughout the area of interest to serve as reference points for the modelling process. PhotoScan software (version 1.2.6) was used for image processing and DEM modelling.

3.1.5 QUALITY CONTROL OF MEASUREMENTS

All components of the aforementioned measurement system were calibrated prior to the experimental campaigns in order to eliminate systematic measurement errors from the raw data. Such a systematic error was present in the measurements of the bed elevation with the laser distance meter during the experimental runs when the flume was filled with water. This error is due to the refraction of the laser beam within the water column. A simple calibration was used to compensate for the propagation time of light in water. The compensation procedure gave sufficiently accurate results when compared to bed elevation measurements taken with the same measurement system in a drained condition. The raw data collected by the ADV were post-processed using WinADV® (version 2.031) (Wahl, 2000). A spike removal filter and a correlation filter (Goring & Nikora, 2002) were applied to the velocity data.

Multiple experiments were replicated for each experimental series. Repetitive runs were conducted with the same measurement system and multiple measurements of hydraulic and topographic data were taken. This allowed an indication of reasonable environmental scatter and a successful assessment of reproducibility, while excluding randomness. The raw data from the topographic and hydraulic measurements were subjected to statistical analysis and spatial interpolation using MATLAB® 2016a. The software was also used to generate the figures in this paper.

3.2. LABORATORY CAMPAIGNS

Four experimental campaigns, comprising a total of over 190 experimental runs (including test runs), were conducted for this thesis. Each campaign was designed to focus on several specific control parameters, which were systematically varied in order to quantify the dynamics of obstacle mark formation and to describe the associated thresholds. Table 2 provides an overview of the experimental series and the focal control parameters of interest, as well as the number of laboratory runs conducted.

Table 2. Experimental campaigns, focal control parameters, and number of laboratory runs.

Laboratory campaign	Focal control parameters	Number of experimental runs‡	Experimental design	Chapter
1	Submergence ratio, obstacle shape	44	Steady discharge at clear water-conditions for 24 hours	4
2	Time, obstacle mobility, limited thickness of alluvial layer	33	Steady discharge at clear water-conditions for 96 hours	6
3	Submergence, hydrograph shape, flow intensity	48	Unsteady discharge at clear-water and live-bed conditions; sediment transport as bedload; duration 2 to 8 hours	7
4	Obstacle porosity, flow intensity	45	Steady discharge at clear-water and live-bed conditions; sediment transport as suspension, duration 25 minutes to 4 hours	9

‡ Only experimental runs that were quantitatively analysed; test runs not included.

3.3 FIELD SURVEYS

During two field campaigns, persistent obstacle marks were measured in the field for comparison with laboratory observations and for upscaling purposes. In the ephemeral Mediterranean gravel stream Rambla de la Viuda (Region of Valencia, eastern Spain), obstacle marks on solid boulders were studied. In the floodplain of the Loire River (Amboise and Tour region, France), where the sediment consists mainly of siliceous sands and gravels, obstacle marks were studied in detail in porous and shrubby riparian pioneer vegetation (*Populus nigra* L.) at different seasonal stages (leafless and fully leafed). Further details of the sites and field settings are given in Chapters 8 and 9.

The geometric length scales of the obstacle marks were measured during the field surveys using a handheld laser distance meter, DISTO 5 (Leica Geosystems®, Heerbrugg, Switzerland). A Zeiss Elta C30 geodetic total station (Leica Geosystems®, Heerbrugg, Switzerland) was used when personal assistance was required. In the case of the ephemeral Rambla de la Viuda (Spain), the instrument was used to measure cross-sectional profiles of the local scour hole and the channel. A Phantom II Advanced drone (DJI®, Nanshan, China) was used to take aerial photographs of the structure in order to survey the overall morphology of the obstacle mark. Overlapping aerial photographs taken from different camera positions were used for structure-from-motion multiview stereo photogrammetry (SfM-MVS) to derive digital elevation models (DEM) (Westoby *et al*., 2012; Smith *et al*., 2016; Morgan *et al*., 2017; Eltner & Sofia, 2020). Sediment analysis was performed either by sieve analysis of sandy sediment samples (Loire River) or by photogrammetric approaches for gravel-bed surfaces (Rambla de la Viuda, Spain). The measurement procedure for the field sites is described in more detail in the relevant chapters of this thesis.

4. BOUNDARY CONDITION CONTROL OF FLUVIAL OBSTACLE MARK FORMATION – A FRAMEWORK FROM GEOSCIENTIFIC PERSPECTIVE

ABSTRACT

Obstacle marks are sedimentary bedforms, typically composed of an upstream local scour hole and a downstream sediment accumulation in the vicinity of an obstruction that is exposed to a current. However, specific morphologies are variable in fluvial, coastal and submarine environments. Although obstacle marks and the phenomenon of local scouring are the subject of different scientific disciplines, the objectives of the investigations are rather incoherent and there is no systematic framework for the analysis and evaluation of boundary condition control, especially in view of the limited knowledge of the cause and effect relationship of obstacle mark formation at instream boulders or vegetation elements at variable environmental conditions. Therefore, a parameter framework is developed which identifies a spectrum of extrinsic and intrinsic boundary conditions that control the main process dynamics of obstacle mark formation. The framework consists of dimensionless control parameters that are separated by a hierarchical order regarding their significance for obstacle mark formation. Primary control parameters determine the geometric scale of the flow field at the obstacle, and therefore control the potential maximum size of the obstacle. Secondary control parameters affect the dynamics of flow field within the geometric scale and limit the potential maximum size of the resulting sedimentary structure when thresholds are exceeded. The framework is intended to provide a basis for subsequent quantification and determination of thresholds by systematic laboratory studies. To illustrate this, flume based research is presented, which evaluates the influence of different flow levels at boulder-like obstacles of different shapes. Results show that obstacle marks dimensions were maximised at shallow flow depths compared to obstacle dimensions, while deep flows at submerged boulder-like obstructions caused considerably smaller obstacle marks. In combination with a rounded and more streamlined obstacle shape deep flows even cause a deviation of morphology, when the flow depth above obstacle exceeded 1.6 times the obstacle dimensions.

This chapter has been published as:

Schlömer, O., Herget, J. and Euler, Th. (2020) Boundary condition control of fluvial obstacle mark formation – a framework from geoscientific perspective. *Earth Surfaces Processes and Landforms*, 45(1), 189-206. DOI: https://doi.org/10.1002/esp.4793

4.1 INTRODUCTION

In general, obstacle marks are morphological features formed by coherent vortex structures induced by obstacles exposed to a current (Karcz, 1968; Richardson, 1968; Allen, 1984; Paola *et al.*, 1986). The presence of an obstruction initially confines the approaching flow field and leads to areas of potential scouring in front of and around the obstacle, as well as depositional areas in the wake of the obstacle, due to local acceleration and deceleration of the flow around the obstacle. Although obstacle marks are considered here as a bed feature of the fluvial environment, similar morphologies are reported from seabed at shipwreck sites (Quinn, 2006; Garlan *et al*., 2015; Quinn & Smyth, 2018), in the aeolian environment at sandy surfaces (Leenders *et al.*, 2007; Bishop, 2011; Luo *et al.*, 2012; McKenna Neuman *et al.*, 2013) and snow (Allen, 1965; Filhol & Sturm, 2015). In the fluvial environment, numerous natural elements are capable of acting as obstacles (boulders, deadwood and vegetation elements), (Fig. 12). Studies from different scientific disciplines in Earth-science lead to synonymous expressions of erosional and depositional bed features induced by obstructions, including obstacle scour mark (Dżułyński, 1965), current crescent and current shadow (Peabody, 1947; Allen, 1984), comet mark (Werner *et al.*, 1980), obstruction formed pool (Buffington *et al.*, 2002; Hassan & Woodsmith, 2004; Comiti *et al.*, 2005) and vegetation-induced sedimentary structure (Nakayama *et al.*, 2002; Rygel *et al.*, 2004).

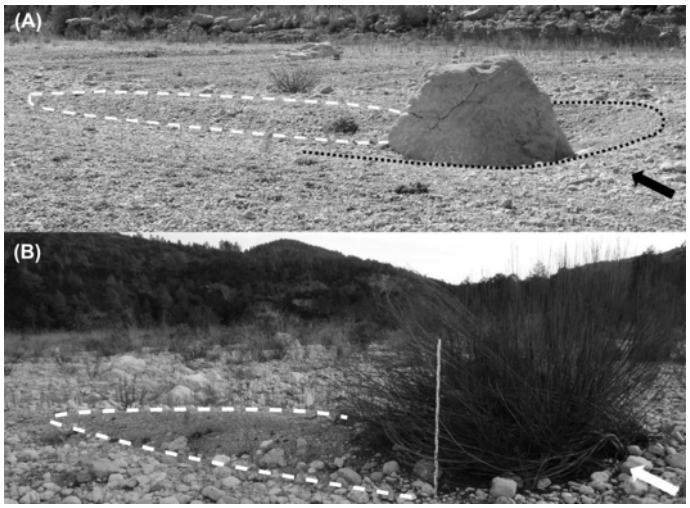


Figure 12. Sedimentary structures at obstacles in the ephemeral Rambla de la Viuda, Spain. (A) Obstacle mark on a boulder (~ 1 m height). The black dotted line indicates the upper edge of the scour hole and the dashed white line indicates the sediment accumulation in the wake. (B) Tapered accumulation of fine gravel in the wake of an instream vegetation element. Rod (1.5 m) for scale. Arrows indicate flow direction.

In engineering, the term local scour is used to describe morphodynamic processes at man-made structures such as bridge piers, river training structures and pipelines. Safety problems

at these structures due to the local scour phenomenon lead to numerous physical modelling studies and deterministic approaches to evaluate the importance of different boundary conditions, including flow conditions, sediment characteristics, geometric characteristics of the obstruction and time (Breusers & Raudkivi, 1991; Hoffmans & Verheij, 1997; Melville & Coleman, 2000; Sumer & Fredsøe, 2005; Ettema *et al.*, 2011). Traditionally, the motivation for this research has been to estimate the potential maximum scour depth on engineering infrastructure exposed to flood events as a design parameter for foundation depth or as a proxy for risk assessment procedures (Melville & Sutherland, 1988; Chang *et al.*, 2004; Sheppard *et al.*, 2014). Most equations are derived using empirical approaches and rely on independent, dimensionless control parameters that represent boundary conditions. Unsurprisingly, these approaches do not take into account the specific properties of natural instream obstructions (boulders and vegetation elements) (Shamloo *et al.*, 2001; Euler & Herget, 2012; Euler *et al.*, 2017).

For example, the influence of many non-dimensional parameters on local scour at engineered infrastructure has been identified and isolated by the hydraulic engineering community, while knowledge of the boundary condition control of obstacle mark formation at natural river obstructions is rather scarce. In particular, there is a lack of a systematic framework that analyses obstacle marks as complex and self-organising bedforms (Werner, 1999, 2010) and not only as components of it (i.e. potential maximum scour depth). In this perspective, environmental boundary conditions and derived control parameters govern the shape and dimensions of the evolving bedform (Ewing & Kocurek, 2010; Kocurek *et al.*, 2010; Chojnacki *et al.*, 2019). The formation of obstacle marks is interpreted as a system of interconnected influences that induce positive and negative feedback loops when thresholds of control parameters are exceeded.

We propose a systematic parameter framework that sorts control parameters into different categories and classifies them based on two hierarchical levels. The influence of each control parameter is quantified by critical thresholds derived from different literature on the subject. In order to assess the complexity of boundary condition control on obstacle mark formation at natural in-stream obstructions, specific control factors are introduced that have not been considered previously. The framework is established as a means to investigate the interplay of environmental conditions on erosional and depositional processes at obstructions within the fluvial system, and to identify sensitivity through systematic laboratory parameter studies. It synthesises knowledge from the extensive literature on local scour at artificial structures and identifies gaps where the effects of individual control parameters have not yet

been adequately explained. In addition to the pure academic relevance in the course of basic research on obstacle formation, the growing knowledge on boundary condition control is expected to be beneficial for application perspectives at field sites (Fig. 12):

(1) Persistent obstacle marks are suitable indicators for estimating past local flow conditions (e.g., Herget *et al.*, 2013). However, a systematic framework for controlling boundary conditions on obstacle mark formation can refine existing procedures for using obstacle marks as hydraulic indicators.

(2) Instream solid and permeable obstacles have significant effects on river structural dynamics through sediment mobilisation, sediment trapping and pioneer island formation, and are often used to improve habitat quality in degraded rivers (Radspinner *et al*., 2010).

The extent of these effects is controlled by boundary condition thresholds and further knowledge would be beneficial in the course of valuable and sustainable river restoration practices. The aims of this paper are:

(i) To review obstructions as sedimentary structures, combining knowledge and experience from different disciplines;

(ii) To provide a comprehensive overview of the morphodynamic processes that leading to the formation of these structures;

(iii) To review the existing knowledge on the boundary conditions and control factors of obstacle mark formation across different scientific disciplines;

(iv) To sort the boundary conditions and control parameters of obstacle mark formation at natural in-stream obstacles into different categories and hierarchies in a novel parameter framework;

(v) Evaluate the effects of different water levels at the obstacle and obstacle shape on obstacle mark formation based on a laboratory flume study to support the relevance of the parameter framework.

4.2 Obstacle marks as sedimentary structures on different spatial scales

Typically, obstacle marks are considered as sedimentary structures that develop in non-cohesive and cohesive sediments (Briaud *et al.*, 1999; Brandimarte *et al.*, 2006; Debnath & Chaudhuri, 2010) and also in bedrock channels (Richardson & Carling, 2005; Yin *et al.*, 2016). Obstacle marks are composite structures, typically consisting of an upstream conical depression that wraps laterally around an obstacle in the downstream direction, termed a scour hole, and a contiguous depositional region in the wake of the obstacle, termed a sediment

ridge. The obstacle itself is considered an integral part of the structure and consists of a large bed obstruction, typically with a diameter greater than the grain size of the surrounding alluvium (Judd & Peterson, 1969; Lisle, 1981; Thompson, 2008). The overall pattern can be characterised by certain morphometric variables that characterise the length values of the scour hole, including scour depth (d_s), scour width (w_s) and scour length (l_s), as well as the length values of the sediment ridge, including ridge height (h_r), ridge width (w_r) and ridge length (l_r) (Fig. 4), (Euler & Herget, 2012). Scour hole and sediment ridge volumes (Vol_s and Vol_r) can be estimated by multiplying the morphometric variables, although this procedure does not take into account the specific shape of the structures and may lead to overestimation (Euler & Herget, 2012). The upstream scour slopes in front of the obstacle, both in the plane of symmetry and perpendicular to it, can be separated into upper and lower slopes. The transition is characterised by a berm or rim as a kind of "knickpoint" separating the steeper inner scour hole from the outer scour hole (Fig. 6) (Dargahi, 1990; Hoffmans, 1993; Link *et al.*, 2008). A shallow semicircular scour hole is located close to the obstacle front.

Field evidence of obstacle marks at solid obstacles has been reported at different spatial scales, resulting from overland flow at rock fragments (Poesen *et al.*, 1994), at boulders as remnants of flood events in ephemeral streams (Karcz, 1968; Euler *et al.*, 2017), and at icebergs during glacier outburst floods (jökulhlaups) (Russell, 1993; Russell *et al.*, 2006; Høgaas & Longva, 2016). Among the largest obstacle marks (dimensions up to 10^2 m) are reported as evidence of Quaternary megafloods (peak discharge $>10^6$ m^3 s^{-1}) on large boulders and bedrock hills (Baker & Bunker, 1985; Carling *et al.*, 2002b; Herget, 2005; Baker, 2009). Their macroscopic pattern is thus consistent across different spatial scales (Fig. 1). However, Nakayama (1992) describes scour holes in the wake of large boulders, whereas a frontal scour hole is missing. A connection can be drawn with the impact of boulders in high gradient streams or rock sills, which are able to induce local scour formation in their wake due to overtopping and jet stream motion on their wake side (Buffington *et al.*, 2002; Comiti *et al.*, 2005; Endreny *et al.*, 2011; Pagliara & Palermo, 2018). However, beyond description, there is no further explanation based on dominant boundary conditions to explain this type of "inverted" obstacle mark.

For solid roughness elements, such as boulders in the upper segments of gravel bed rivers, similar sedimentary structures called particle clusters are well documented as small-scale bedforms (Cin, 1968; Storm & Papanicolaou, 2007; Papanicolaou & Tsakiris, 2017) . In contrast to obstacle marks, no local scour hole is formed on the face of the obstruction (stoss side). Instead, the obstacle acts as an anchor particle that traps incoming finer sediments either

on its stoss side or in its wake, depending on the relative submergence ratio (i.e. ratio of flow depth to anchor particle diameter) of the obstacles as these bedforms evolve during the rising or falling limp of a hydrograph (Laronne *et al.*, 2001; Papanicolaou *et al.*, 2011; Ghilardi *et al.*, 2014b; Papanicolaou *et al.*, 2018).

Obstacle marks of varying spatial extent are also reported at permeable riparian vegetation elements. Rygel *et al.* (2004) introduced the term "vegetation-induced sedimentary structures (VISS)" to describe ancient sedimentary structures at fossil forests in floodplain layers, while Tooth and Nanson (2000), Nakayama *et al.* (2002), Rodrigues *et al.* (2007), Euler *et al.* (2014) and Corenblit *et al.* (2016) report *in situ* evidence at grass colonies, shrubs, sprouts and mature trees. As reported by these authors, shrubs and sprouts tend to favour leeward deposition of sediments in their wake (i.e. sediment ridges, Fig.12 B), while scour holes are significantly small or even absent. On the contrary, mature trees with a single trunk are also documented with significant scour holes. The formation of obstacle marks at the individual plant scale has also been investigated in laboratory studies to assess the influence of permeability and porosity on the flow field around vegetation elements (Chen *et al.*, 2012; Kim *et al.*, 2015; Yagci *et al.*, 2016).

4.3 MORPHODYNAMIC PROCESSES AT INSTREAM OBSTACLES

Large bed obstacles exposed to a steady current are capable to modify the flow field in their vicinity, resulting in the following processes: (1) contradiction of streamline lateral to the obstacle, causing higher flow velocities; (2) a vertical jet-like down-flow towards the sediment bed at the obstacle front as consequence of a vertical pressure gradient at the obstacle frontal face; (3) formation of a horseshoe-vortex system (abbreviated: HV) at the obstacle base, resulting from the deflection of the down-flow against the main flow direction; the HV extents downstream, past of the sides of the obstacle, and (4) a decelerated region of flow in the wake region of the obstacle including a wake vortex system of detached shear layers with vertical axis of rotation (cf. Fig. 5 a) (Allen, 1984; Dargahi, 1989; Shamloo *et al.*, 2001; Sumner *et al.*, 2004; Pattenden *et al.*, 2005; Euler & Herget, 2012; Papanicolaou *et al.*, 2012; Sumner, 2013; Hajimirzaie *et al.*, 2014; Bauri & Sarkar, 2016; Launay *et al.*, 2017) .

Processes (1) to (4) are capable of amplifying the bed shear stress above the critical bed shear stress for sediment mobilisation, inducing local scouring in front of and lateral to the obstacle, even in the absence of general sediment movement in the vicinity. The main driver of sediment mobilisation and local scouring is the HV (Dargahi, 1990; Radice *et al.*, 2009; Link *et al.*, 2012; Bouratsis *et al.*, 2017). The HV is located in the inner scour hole close to the bottom of the scour hole, where sediment is picked up below the HV by the particle

transport modes of saltation and rolling (Dey, 1996; Unger & Hager, 2006). The steeper inner scour hole is shaped by the HV. Rotation of the HV generally stabilises the lower slope at an angle greater than the angle of repose (Hoffmans, 1993b; Dey *et al.*, 1995). However, the HV is an unsteady eddy system that randomly oscillates in time and thus temporarily weakens (Unger & Hager, 2006). Thus, the ongoing depth incision and occasional weakening of the HV destabilise the scour slopes and result in gravitational mass movements, causing an increase in the frontal length and width of the scour hole (cf. Fig. 2 A). As a result of the collapses, sediment grains slide into the scour bed where they are picked up by the HV and transported downstream as bedload under its expanding legs. In the mid to far wake region, sediments are deposited as dune-like sediment ridges due to decreasing bed shear stress (Oliveto & Hager, 2014). Sediment transport on the sediment ridge consists of rolling and sliding (Euler *et al.*, 2017).

Deposition of finer material in the low-energy wake of large bed obstructions (boulders) also occurs without evidence of local scouring in front of the obstruction (Thompson, 2008; Papanicolaou *et al.*, 2011; Papanicolaou *et al.*, 2012). Here, fine sediments are transported as sheets or in suspension and form a conical sediment ridge or sand shadow (Werner *et al.*, 1980). However, the unique aspect of obstacle marks is that they can develop even when the threshold for general sediment movement is not exceeded (Euler & Herget, 2012). The development of the scour depth is characterised by a non-linear evolution until a state of equilibrium is reached. The scour depth is then referred to as the equilibrium scour depth and is determined as the maximum depth of the scour hole measured from the undisturbed bed level. The equilibrium scour depth is reached asymptotically in time (Fig. 13).

As reported from laboratory flume studies, the initial scour incision is characterised by positive feedback mechanisms as the HV sinks into the developing scour hole (Dey, 1996; Dey, 1999; Muzzammil & Gangadhariah, 2003; Dey & Raikar, 2007a). As the scour hole evolves over time and increases in size, the cross-sectional area of the vortex increases and the shear stress under the HV decreases because less energy is available per unit mass (Kothyari *et al.*, 1992; Mia & Nago, 2003; Li *et al.*, 2018). Thus, the feedback mechanism becomes negative and dampens the further development of scouring (Muzzammil & Gangadhariah, 2003; Muzzammil *et al.*, 2004). Once the shear stress induced by the HV is well below the critical shear stress, an equilibrium condition of scour incision is reached while the gravitational movements on the upper slope also relax. If the alluvial material is not uniform, an armour layer of coarser sediments develops at the bottom of the scour hole, which has a reducing effect on the scour depth incision and the equilibrium condition is reached

more quickly (Dey & Raikar, 2007b). From laboratory data it is known that almost 80% of the equilibrium scour depth is developed in only 5 to 40% of the duration of experimental runs, while the time scale for reaching equilibrium scour depth depends on flow conditions and sediment characteristics (Melville & Chiew, 1999).

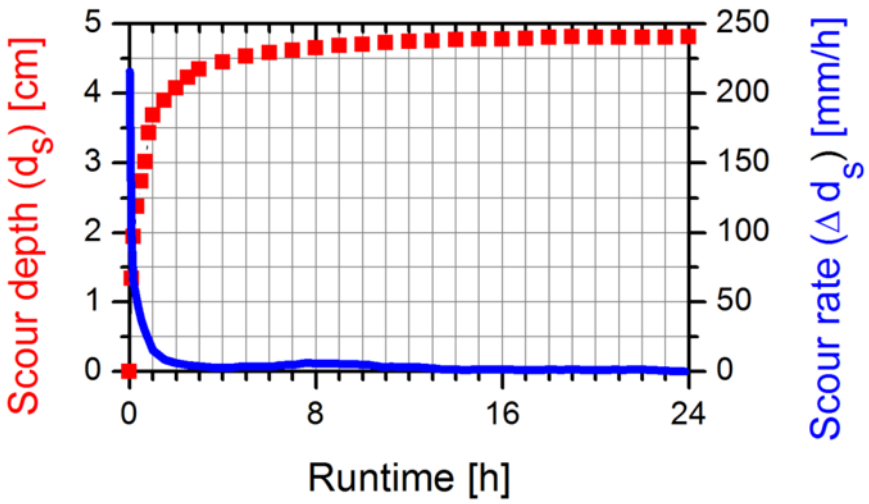


Figure 13. Time evolution of scour depth at a rectangular obstacle for test run A9.

At equilibrium, scour hole morphometric characteristics show a clear relationship where wide and long frontal scour holes belong to deeply incised scour holes, while sediment ridge width also has a linear relationship with scour depth (Euler & Herget, 2012; Euler *et al.*, 2017). Laboratory observations suggest that feedback loops resulting from dynamic interactions between hydraulic and sedimentary processes lead to a non-linear temporal evolution towards equilibrium, despite a constant external energy input (discharge) (Euler *et al.*, 2017). This behaviour is commonly known as self-organisation (Coco & Murray, 2007), which depends on thresholds of external environmental boundary conditions as a type of cause and effect relationship (Murray *et al.*, 2014).

4.4 Review on boundary conditions of morphodynamic processes at instream obstructions

With reference to the advanced knowledge from hydraulic engineering on the phenomenon of bridge pier scour, the environmental boundary conditions of local scour are grouped into: (1) flow conditions, (2) sediment characteristics, (3) geometric characteristics of the bridge pier and (4) time, indicating the multidimensional complexity of the phenomenon (Breusers & Raudkivi, 1991; Hoffmans & Verheij, 1997; Melville & Coleman, 2000; Sumer & Fredsøe, 2005; Ettema *et al.*, 2006; Ettema *et al.*, 2011; Williams *et al.*, 2017). Boundary

conditions are composed of various influencing factors that operationalise conditions (i.e. "flow conditions") into measurable quantities (i.e. mean flow velocity and depth). By applying dimensional analysis and Buckingham's π-theorem (Barenblatt, 2012), these influence factors are transformed into non-dimensional, scale-invariant control parameters and represented as functional relationships that can be meaningfully analysed in physical modelling studies (Ettema *et al.*, 1998; Williams *et al*., 2017). Local scour depth is basically controlled by flow depth (dw has dimension L) relative to pier/obstacle width (w_o [L]), mean approach velocity (U_m [LT^{-1}]) relative to critical mean approach velocity for sediment entrainment (U_c [LT^{-1}]), obstacle Reynolds number ($Re_o = U_m\, w_o/\nu$ [$M^0L^0T^0$,] where ν = kinematic viscosity [L^2T^{-1}]), obstacle Froude number ($Fr_o = U_m/g\, w_o^{1/2}$ [$M^0L^0T^0$], where g = gravitational acceleration [LT^{-2}]), pier/obstacle width relative to mean grain diameter (D_{50} [L]), sediment gradation coefficient ($\sigma_G = (D_{84}/D_{16})^{1/2}$ [$M^0L^0T^0$]), pier/obstacle shape, pier/obstacle orientation and time (t [T]) (e. g. Breusers & Raudkivi, 1991; Hoffmans & Verheij, 1997; Melville & Chiew, 1999; Melville & Coleman, 2000; Sumer & Fredsøe, 2005¸ Ettema *et al*, 2011). Detailed descriptions of the influence of parameters, including envelope curves and empirically determined thresholds, can be found in the aforementioned references.

Obviously, hydraulic engineers' research on local scour has a technical background, as the potential failure of technical infrastructure due to local scour is the motive for studying the phenomenon. In this context, the height of the obstacle is neglected, as the obstacle (i.e. bridge piers) protrudes above the water surface. Thus, the height of the obstruction (h_o [L]) is always greater than the depth of the flow (i.e. emergent flow prevails, $d_w \leq h_o$). This perspective may be inadequate for natural large bed elements, such as isolated boulders on the stream bed, as it neglects flow over the obstacle (i.e. submergence, $d_w \geq h_o$). The formation of obstacle marks on submerged obstructions such as pipelines has been investigated in laboratory studies by Dey *et al.* (2008) and Sarkar, (2014), while Euler and Herget (2011) related obstacle mark formation on submerged cylinders to an adjusted obstacle Reynolds number incorporating the obstacle height (h_o). Euler and Herget (2011) defined the effective obstacle size (L_o) as a length value ($h_o^{2/3}w_o^{1/3}$), resulting in an adapted obstacle Reynolds number ($Re_o = U_mL_o/\nu$). The exponents were chosen to account for the impact of obstacle height (h_o) on local scouring at submerged obstacles and derived from a data analysis on pier and abutment scouring reported in Oliveto and Hager (2002). Re_o expresses the ratio between turbulent and viscous stresses at the obstacle (Euler & Herget, 2011; Lança *et al.*, 2016; Manes *et al.*, 2018) and thresholds for the initiation of obstacle mark formation based on the Reo number are formulated (Euler & Herget, 2012). The product of U_m and L_o thereby

controls the turbulence and the erosive energy of the HV as it determines flow separation and adverse pressure gradients at the obstacle frontal face (Muzzammil & Gangadhariah, 2003; Muzzammil *et al*., 2004). However, the size of the HV also depends on flow depth (d_w) and the structure of the approaching boundary layer (Sumer & Fredsøe, 2005, Fig.3.3 therein). Although, the flow over the obstruction ($d_w > h_o$) is a common feature at boulder-like obstacle, its implication for local scouring and obstacle mark formation is considered only by a few empirical studies so far (Fisher & Klingman, 1984; Shamloo *et al*. 2001, Tominga, 2014). As opposed to this the influence of emergent ($d_w < h_o$) and submerged ($d_w \geq h_o$) flow has been analysed sufficiently in course of bed load transport around large roughness elements and pebble cluster formation in gravel bed rivers, identifying submergence ratio (d_w/h_o) as dominant control parameter for deposition of incoming sediments (Kramer & Papanicolaou, 2006; Papanicolaou & Kramer, 2006; Papanicolaou *et al*., 2010); Ghilardi *et al.*, 2014a), while boundary conditions of the surrounding alluvial bed material in relation to the diameter of the roughness element inhibit the formation of a local scour hole in front of the obstruction. Considering a solitary solid boulder-like obstructions located in a straight, moderately sloped channel with sub-critical (Fr < 1) flow conditions and cohesion less alluvial sediment (i.e. plane-bed type streams, Simons & Richardson, 1966) local scour incision can be functionally determined by:

$$d_s = f(d_w, U_m, \rho, \nu, g, B, h_o, w_o, le_o, M_b, D_{50}, \rho_s, \sigma_G, U_c, d_{sed}, t)$$

(Eq. 2)

where d_s is local scour depth [L], ρ is water density [ML-³] B is channel cross section [L], le_o is length of obstacle in streamwise direction [L], Mb is an indicator for the mobility of an boulder-like obstruction, due to tilting into the scoured depression which limits further evolution of local scouring and induces equilibrium more quickly (Truelsen *et al*., 2005; Friedrich *et al*., 2016; Euler *et al*., 2017; Rennie *et al*., 2017), ρ_s is sediment density and d_{sed} is the thickness of the alluvial layer [L].

Considering a solitary riparian vegetation element (i.e. mature tree or shrub) exposed to a current, local scouring is anticipated to be functionally determined as:

$$d_s = f(d_w, U_m, \rho, \nu, g, B, h_o, w_o, I_o, V_p, h_d, D_{50}, \rho_s, \sigma_G, U_c, d_{sed}, t)$$

(Eq. 3)

where I_o is the inclination of the stem in streamwise direction [$M^0L^0T^0$], V_p is porosity of a permeable obstruction [$M^0L^0T^0$] which triggers bleed-flow (i.e. flow through the obstruction) instead of downflow and HV formation (Schnauder & Moggridge, 2009), and h_d is the deflected height of a flexible vegetation element exposed to a current [L].

Equations (2) and (3) indicate that the dependent variable, d_s, is a function of 16, respectively 17 independent variables (denoted n) in three basic dimensions (denoted m), which define the inherent degrees of freedom inherent to the problem (Sonin, 2004). Assuming a constant relative sediment density $(\rho s-\rho)/\rho$, that is to say, neglecting both ρ and ρs and introducing Lo ($= h_o^{2/3}\ w_o^{1/3}$) as a reference length (Euler & Herget, 2011), results in a reduction of the degrees of freedom in both equations. Moreover, the application of the π-theorem (Barenblatt, 2012) to equations (1) and (2) reveals n-m non-dimensional control parameters. Among other expressions, we obtain:

$$d_s/L_o = f\,(d_w/L_o,\ U_m/g\,L_o^{1/2}\ U_m/U_c,\ U_mL_o/\nu,\ L_o/B,\ Sh,\ Mb,\ L_o/D_{50},\ \sigma_G,\ d_{sed}/L_o,\ t/t_e)$$

(Eq. 4)

where $U_m/g\,L_o^{1/2}$ is Obstacle-Froude number (Fr_o), U_mL_o/ν is Obstacle-Reynolds number (Re_o), L_o/B is blockage ratio, Sh (L_o/le_o) describes the hydrodynamic shape of a body, generally differing between streamlined obstructions which cross-flow dimensions are smaller than its stream-wise dimensions ($Sh \leq 0.5$) and bluff obstructions which cross-flow dimensions are comparable to its stream-wise dimensions ($Sh \geq 0.8$), (Douglas *et al*., 2001), and t_e is time scale to reach equilibrium [T] that is a function of d_w/L_o, U_m/U_c and L_o/D_{50} (Melville & Chiew, 1999).

Considering a permeable vegetation element equation (2) can be expressed as:

$$d_s/L_o = f\,(d_w/L_o,\ Fr_o,\ U_m/U_c,\ Re_o,\ L_o/B,\ I_o/I_v,\ V_p,\ h_d/h_o,\ L_o/D_{50},\ \sigma_G,\ d_{sed}/L_o,\ t/t_e)$$

(Eq. 5)

where I_v is perpendicular alignment of the obstruction to the streambed (= 90°).

As posited by Manes *et al*. (2018) and Manes and Brocchini (2015), the inclusion of flow intensity (U_m/U_c) in the dimensional analysis of local scouring is often somewhat artificial. This is due to the fact that U_m/U_c has the important physical meaning of discerning between The approach flow can be classified as either clear water ($U_m/U_c < 1$) or live bed condition ($U_m/U_c > 1$) (Melville & Coleman, 2000; Ettema *et al*., 2011). For the latter, sediment mobilisation is not only occurring in the vicinity of the obstruction, but also in the undisturbed

flow upstream. However, as Simarro *et al*. (2007) have highlighted, the usage of U_c (i.e. U_m/U_c) introduces technical difficulties in the analysis, namely:

$$U_c = f(D_{50}, \nu, g, d_w)$$

(Eq. 6)

which can be expressed as non-dimensional equation, applying dimensional analysis by:

$$f(d_w/D_{50}, U_c/gD_{50}^{1/2}, gD_{50}^3/\nu^2) = 0$$

(Eq. 7)

Comparison of equations (4), (5) and (7) indicates analogy of several control parameters although different reference length (L_o and D_{50}) are used. It becomes obvious that control parameters d_w/L_o, Re_o and Fr_o are linked due to the consideration of U_c/U_m, because = (U_m/U_c) $(U_c/gD_{50}^{1/2})$ generates a derivative of Fr_o and g D_{50}^3/ν^2 can be rearranged to a derivative of Re_o (cf. Lanca *et al*., 2016). Thus, technical speaking the right hand side of equations (4) and (5) are not independent and one of the control parameters (i.e. d_w/L_o, Re_o or Fr_o) has to be excluded (Simarro *et al*., 2007, Lanca *et al*., 2016). As it is preferred to keep U_m/U_c, Fr_o is excluded and the functional relationships reduce to:

$$d_s/L_o = f(d_w/L_o, U_m/U_c, Re_o, L_o/B, Sh, Mb, L_o/D_{50}, \sigma_G, d_{sed}/L_o, t/t_e)$$

(Eq. 8), (solid boulder-like obstruction)

$$d_s/L_o = f(d_w/L_o, U_m/U_c, Re_o, L_o/B, I_o/I_v, V_p, h_d/h_o, L_o/D_{50}, \sigma_G, d_{sed}/L_o, t/t_e)$$

(Eq. 9) (permeable vegetation element)

Furthermore, due to shape similitude of the local scour hole (Euler & Herget, 2012) it is possible to replace d_s/L_o in equations (6) and (7) by any characteristic length of the scour hole (Fig. 4), i.e.:

$$w_s/L_o \text{ and } l_s/L_o = f(d_w/L_o, U_m/U_c, Re_o, L_o/B, I_o/I_v, Sh, Mb, L_o/D_{50}, \sigma_G, d_{sed}/L_o, t/t_e)$$

(Eq. 10)

$$w_s/L_o \text{ and } l_s/L_o = f(d_w/L_o, U_m/U_c, Re_o, L_o/B, I_o/I_v, V_p, h_d/h_o, L_o/D_{50}, \sigma_G, d_{sed}/L_o, t/t_e)$$

(Eq. 11)

A comparison of equations (8), (9) and (10), (11) reveals that d_s/L_o can be used to substitute any of the non-dimensional parameters on the right side of equations (6) and (7) (cf. Chreties

et al., 2008). This emphasises the dependence of scour depth incision on the evolution of the scour hole width (w_s) and length (l_s), as well as other control parameters.

Equations (8) and (9) comprise control parameters pertaining to the formation of obstacle marks at natural obstructions. They incorporate well-established parameters from the field of hydraulic engineering research on this topic, as well as parameters that account for the specific properties and characteristics of natural obstacles. However, technical considerations indicate that the control parameters d_w/L_o and U_m/U_c in equations (8) and (9) are linked due to the variables d_w and U_c (cf. equation 6). Consequently, a change in one control parameter along an axis of influence often results in a change in another parameter, which then affects the morphodynamic processes and the size of the emerging obstacle mark (Ettema *et al*., 2011). A further systematization of the control parameters included in equations (8) and (9) is proposed. This classification is based on two different hierarchical levels and quantifies the impact of the control parameters on the formation and size of the emerging structure, with the use of defined thresholds.

4.5 Parameter framework of boundary condition control on morphodynamic processes at natural instream obstacles

Obstacle marks are complex geomorphic systems (Werner, 1999, 2003) that are characterised by feedback loops of hydraulic and sedimentary processes and demonstrate a non-linear evolution in time towards an equilibrium condition. In particular, this phenomenon is frequently referred to as self-organisation (Coco & Murray, 2007), which is contingent upon the attainment of specific control parameter thresholds. It is hypothesised that the impact of control parameters on obstacle mark formation and dynamics can be assessed by thresholds of two distinct categories: (1) The thresholds of control parameters that must be surpassed to initiate local scouring and (2) the thresholds of control parameters that demarcate the conditions under which obstacle marks are spatially maximised. Consequently, between these control parameter thresholds, the size of the obstacle and its characteristic morphometric variables (Fig. 4) are reduced in comparison to the potential maximum. From this perspective, the control factors of equations (8) and (9) can be classified into hierarchical levels regarding their significance for obstacle mark formation and the size of the emerging structure, while also considering the interconnections.

It can thus be seen that the typical obstacle mark pattern resulting from the erosive action of the HV and scour depth incision serves as the target of the parameter framework. In this context, the control factors are classified into two categories: extrinsic and intrinsic. These are further distinguished into two levels of effectiveness, namely (1) hierarchy and (2) impact. Figure 14 presents a graphical representation that succinctly illustrates the dimensional influence factors and non-dimensional control parameters associated with obstacle mark formation at natural instream obstacles. These are subsequently elaborated upon in greater detail.

4.5.1 Categories

Control parameters are classified into two principal categories: intrinsic and extrinsic. The extrinsic control parameter cluster encompasses hydraulic conditions and alluvial characteristics, in addition to time. Intrinsic control parameters, on the other hand, characterise the properties of the obstacle, including its geometrical definable roughness and its status as an integral component of the emerging obstacle mark. In terms of the characteristics of natural in-stream obstacles, there is a distinction between solid obstacles, which are boulder-like, and permeable obstacles, which are composed of vegetation. This is illustrated in Fig. 14. In the case of solid, boulder-like obstructions, the parameters Sh and Mb

can be classified as intrinsic control parameters. In such cases, bluff obstructions (Sh ≥ 0.8) offer greater resistance to the approaching flow, resulting in higher pressure gradients at the obstacle's frontal face. This leads to a stronger HV and more intense local scouring processes. Furthermore, boulder-like obstructions are also classified as mobile (Mb). In the context of high-energy flows (i.e. Fr ≥ 1), this may result in the mobilisation of the obstacle itself and its subsequent transport downstream (Carling *et al*., 2002a; Alexander & Cooker, 2016; Bressan *et al*., 2018). In the process of obstacle marking formation, the mobile obstacle is not transported downstream; rather, it tilts into the evolving scour hole when a critical scour depth is reached. This process of self-burial limits further incision of the scour hole and induces equilibrium more quickly (Euler *et al*., 2017).

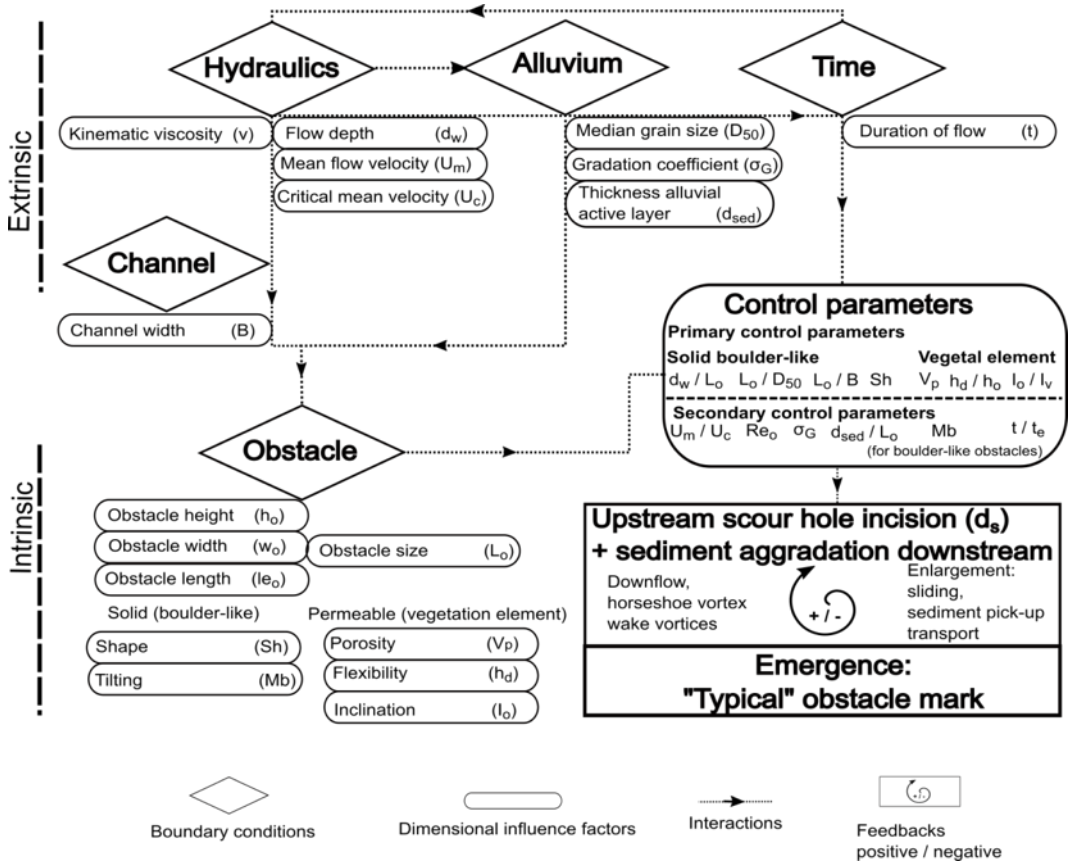


Figure 14. Block chart on boundary condition control of obstacle mark formation at natural instream obstacles. It should be noted that the equilibrium time (t_e) is a function of d_w/L_o, U_m/U_c and L_o/D_{50} and is not displayed.

In contrast shrubs are permeable obstacle. The porosity of the frontal area leads to flow penetrating the obstruction irrespective of water level (i.e. emergent or submerged), (Lee *et al*., 2018). Vegetation porosity (V_p) represents the fraction of void spaces in relation to the total body volume and is commonly expressed as dimensionless quantity between 0 and 1 (Grant & Nickling, 1998, Montakhab *et al*., 2013). Indeed, porosity is not a fixed value as it

depends on number and size of stems and leaves per unit area which vary during the annual growth cycle due to exfoliation (Schnauder & Moggridge, 2009). If the obstacle is too porous, frontal scouring is inhibited due to absent downflow. Nevertheless, sediment trapping of incoming sediments is still observable (Leenders *et al*., 2007). No systematically investigation on the influence of V_p as intrinsic control parameter of obstacle mark formation is conducted so far. In addition, shrub stems and leaves are flexible and tend to bend in the direction of the flow in response to the flow passing over or through them (Nikora *et al*., 2008; Nikora, 2010). According to Okamoto and Nezu, (2010) the deflected height (hd) is an appropriate measure of flexibility, which depends primarily on the stiffness of the vegetation element. The stiffness of a vegetation element determines the extent to which a vegetation element provides resistance to flow and generates pressure resistance to induce local scour incision (Nikora, 2010). Thus, if the deflected height (h_d) relative to the obstacle height (h_o) (without deflection) exceeds a critical threshold, local scour is inhibited, although trapping of incoming sediment may still be possible (Nikora, 2010). Again, no critical threshold of h_d/h_o has been formulated so far. However, the effect of streamwise slope (I_o) is similar to the deflected height (h_d) described for logs of mature riparian vegetation due to local scouring (Nakayama *et al*., 2002).

4.5.2 HIERARCHY

Intrinsic and extrinsic control parameters are divided into two hierarchical levels with respect to their importance for the magnitude of the morphometric parameters. The hierarchical levels consider the relationships of the control parameters shown in equations (8) and (9). Primary control parameters define the geometric scale of the HV at the obstacle and determine the potential maximum size of morphometric variables (scour depth). It is assumed that the size of an obstacle mark is maximised at certain values or within small ranges of the primary control parameters, which can be interpreted as thresholds. From these thresholds, an increase or decrease of a primary control factor affects the geometric scale of the HV and limits the spatial extent of an obstacle mark (expressed by the size of the morphometric variables). For given primary control parameters, the actual size of the morphometric variable is further influenced by the secondary control parameters, as they affect the dynamics of the flow field at the obstacle. In general, they characterise the limits of scour hole incision and sediment ridge accumulation and limit the potential maximum size of the obstacle mark below or above a certain threshold (Ettema *et al*., 2011).

The control parameters L_o/D_{50}, L_o/B, d_w/L_o and Sh are considered as primary control parameters for obstacle mark formation at solid boulder-like obstacles, as they influence the geometric scale of the HV at the obstacle, while for vegetation elements porosity (V_p), relative stem inclination in flow direction (I_o/I_v) and relative deflected height of flexible parts (h_d/h_o) are additional primary control parameters. Within the geometric scale, the control parameters U_m/U_c, Re_o, σ_G, d_{sed}/L_o, t/t_e and Mb (only for solid boulder-like obstacles) are considered as secondary control parameters that, above or below certain thresholds, influence the potential maximum size of the morphometric variables for given primary control parameters.

4.5.3 IMPACT

The influence of primary and secondary control parameters on the magnitude of morphometric variables is quantified in terms of thresholds, i.e. different conditions where morphometric variables are potentially maximised, conditions where morphometric variables are limited compared to a potential maximum, and conditions where obstacle mark formation is completely inhibited. As a synthesis, these thresholds are gathered from empirical evidence reported in various references on local scour, with scour depth (d_s) chosen as the target morphometric variable. Table 3 gives a comprehensive overview of the known threshold ranges of the primary and secondary control parameters used for the present framework, which can be summarised as follows:

(1) Relative coarseness (D_{50}/w_o or D_{50}/L_o): d_s is maximised for relative coarseness $w_o/D_{50} \approx$ 25-50 (Lee & Sturm 2009). For $w_o/D_{50} >$ 60-10000, d_s is reduced because in non-cohesive alluvial sediments, ripple formation at sub-threshold motion conditions ($U_m/U_c <1$) can cause sediment transport into the scour hole. When $w_o/D_{50} < 8$, alluvial sediment particles are too coarse for the obstacle size and completely inhibit local scouring due to the dissipative effects of large sediment particles on the HV (Firat & Gungor, 2009). Under these conditions, the obstacle is more likely to act as an anchor particle for pebble cluster formation when $U_m/U_c > 1$. For the framework, w_o is replaced by L_o.

(2) Blocking ratio (w_o/B or L_o/B): for $L_o/B < 0.1$, the effect of blockage on the magnitude of d_s is negligible (e.g., Wu & Balachandar, 2015), whereas for increasing blockage (i.e., $L_o/B > 0.15$), d_s scales with the blocking ratio (e.g., Mazumder *et al.*, 2011). However, it is crucial to determine a threshold where d_s is maximised.

Nevertheless, Chou and Chao (2000) reported that for $L_o/B > 0.6$, no connected HV persists in front of the obstacle because the HV branches into several smaller vortices at the lateral edges of the obstacle.

(3) Shape (Sh): for $Sh \geq 0.8$, d_s is maximised for bluff obstructions, while for more streamlined obstructions ($Sh \leq 0.6$) limitations of d_s are documented (Euler *et al*., 2017). For $Sh \leq 0.4$, the formation of a HV and frontal scouring should be completely alleviated.

(4) Relative stream inclination of the stem (I_o/I_v): d_s is maximised when $I_o/I_v = 1$, so that the obstacle is perpendicular to the stream bed. For $I_o/I_v \geq 1.3$, HV ceases to prevail due to the streamwise tilt (Euler *et al*. 2014). Here, wake eddies create a zone of recirculating currents in the wake of the obstacle, causing wake scouring as a kind of "inverse" obstacle marker. For $I_o/I_v >> 1.3$ there is no frontal scour hole.

(5) Porosity (V_p): d_s should be maximised when $V_p = 0$ so that no bleed flow occurs. Unfortunately, no empirical data are available, nor have thresholds for $V_p > 0$ been formulated to limit d_s.

(6) Relative deflection height of flexible parts (h_d/h_o): no thresholds have yet been described.

(7) Flow intensity (U_m/U_c): for $U_m/U > 1$, ds is reduced by the passage of bedforms such as ripples or dunes (Melville & Coleman, 2000; Hong *et al*., 2017). For $U_m/U_c \leq 0.3$, no local scour is initiated at the obstacle front, regardless of flow depth (d_w) and obstacle size (L_o) (Chiew, 1995).

(8) Obstacle Reynolds number (Re_o): for $Re_o < 3000$, viscous stresses dominate at the obstacle, inhibiting the formation of an HV and the emergence of a frontal scour hole irrespective of flow depth (d_w) and obstacle size (L_o) (Euler & Herget, 2012).

(9) Gradation coefficient (σ_G): For $\sigma_G > 1.3$ and non-uniform alluvial sediment, d_s is limited (Raudkivi & Ettema, 1985). Frontal scour should be prevented when D_{84}/L_o is <

8. As reported by Sheppard and Miller (2006), d_s is largely independent of σ_G under live-bed conditions ($U_m/U_c > 1$).

(10) Mobility (Mb): If an obstacle is considered mobile, local scouring can undermine the obstacle and cause it to tilt into the scour hole, limiting further ds incision. Clearly, the tilting of a mobile obstacle depends on ds, so the identification of different thresholds is crucial. Nevertheless, Euler *et al*. (2017) experimentally determined the onset of tilting at $d_s/le_o > 0.6$.

(11) Relative sediment thickness (d_{sed}/L_o): If an obstacle is located in a thin alluvial sediment layer above the bedrock (i.e. $d_{sed}/L_o < 1$) (Hodge *et al*., 2011, Church & Haschenburger, 2017), the d_s incision is significantly limited, while a slight enlargement of w_s and l_s could be observed (Schlömer & Herget, 2016). When $d_{sed}/L_o = 0$, the formation of obstacle marks as a sedimentary structure is inhibited.

(12) Time scale (t/t_e): ds is potentially maximised under equilibrium conditions ($t/t_e = 1$). It is known from laboratory studies on bridge piers that t_e is reached after several days depending on flow conditions and sediment characteristics (Melville & Chiew, 1999). The scour depth (d_s) will not reach equilibrium if $t/t_e < 1$.

(13) Submergence ratio (d_w/L_o): d_w/L_o is considered to be the primary control factor and thresholds are quantified below by a laboratory study.

Table 3. Primary and secondary control parameters of obstacle mark formation at solid and permeable instream obstructions.

Primary parameter	**Maximization of d_s/L_o**	**Limitation of d_s/L_o**	**No scouring**	**References**
d_w/L_o	0.8 - 1	$0.7 < d_w/L_o > 1.1$	> 1.6 (for Sh ≤ 0.6)	within this contribution
L_o/D_{50}	~ 25 – 50	$20 < L_o/D_{50} > 60$ – 10000	< 8	Lee & Sturm (2009), Melville & Coleman (2000)
L_o/B	> 0.15	< 0.1	≥ 0.6	Chou & Chao (2000), Wu & Balachandar (2015)
Sh	≥ 0.8	≤ 0.6	≤ 0.4	within this contribution
I_o/I_v	1	≥ 1.3	>> 1.3	Euler *et al*. (2014)
V_p	0	?	?	-
h_d/h_o	0	?	?	-
Secondary parameter	**Upper envelope**	**Limitation of d_s/L_o**	**Lower envelope**	**References**
U_m/U_c	1	> 1	< 0.3	Chiew (1995), Simarro *et al*., (2007)
Re_o	> 4500	< 4500	≤ 3000	Euler & Herget (2012) Manes & Brocchini (2015)
σ_G	< 1.3	> 1.3	if $D_{84}/L_o < 8$	Raudkivi & Ettema (1985)
Mb	-	if $d_s/l_{eo} > 0.6$	-	Euler *et al*. (2017)
d_{sed}/L_o	> 1	< 1	0†	Schlömer & Herget (2016)
$t/_{te}$	1	< 1	-	Melville & Chiew (1999)

4.6 Evaluation of submergence ratio and obstacle shape as primary control factors of obstacle mark formation at solid boulder like obstacles

The submergence ratio (d_w/L_o) and the shape of the obstacle (Sh) are considered as the primary control parameters defining the geometric scale of the HV, as they control the unfavourable pressure gradients formed at the front of the obstacle and determine the potential maximum size of the obstacle mark. Considering a solid boulder-like river obstacle, the variable d_w is the key determinant to achieve different d_w/L_o ratios, because the height and width (i.e. $L_o = h_o^{2/3}w_o^{1/3}$) of the boulder-like obstacle are not expected to change during a flood event (Lacey & Rennie 2012). This perspective contrasts with previous investigations of local scour at submerged structures, where different d_w/L_o ratios were modelled by varying the obstruction height (h_o) of a cylinder protruding into the flow while keeping the flow depth (d_w) constant (Dey *et al*., 2008; Sarkar, 2014). This resulted in relatively slender obstacles ($h_o > w_o$) at relatively shallow submergence ($d_w \approx h_o$), whereas obstacles were relatively squat ($h_o \leq w_o$) at fully submerged conditions ($d_w > h_o$).

Therefore, in order to quantitatively describe d_w/L_o as the primary control parameter of obstacle mark formation, a flume study is presented in which d_w/L_o was varied by changing the approach flow depth (d_w). Three solid obstacles of almost identical size (h_o = 0.037-0.04 m and w_o = 0.04-0.045 m, i.e. L_o = 0.036 to 0.037 m) but different shape (Sh) (glass cube (Sh ≥ 0.8), glass sphere (Sh ≤ 0.6) and elliptical sandstone pebble (Sh ≤ 0.4)) were used to mimic boulder-like obstacles. The aim of the study was to identify the threshold condition of d_w/L_o at which obstacle markings are maximised.The experiments were conducted in a 5 m long, 0.32 m wide and 0.27 m deep rectangular channel with a fixed slope (0.003 m/m), filled with a 0.055 m thick layer of uniform medium-grained sand ($\sigma_G < 1.3$, $D_{50} = 7.5\ 10^{-4}$ m).

In a first set of experiments (series A), individual trials were designed to represent steady state flow conditions with a constant mean approach velocity (U_m = 0.2 m/s), while d_w was varied from 0.02 m to 0.14 m for individual runs at different intervals (0.005 to 0.02 m) by adjusting a sluice gate at the end of the flume. The procedure resulted in submergence ratios (d_w/L_o) ranging from 0.55 to 3.83, indicating emergent conditions (top of obstacle protruding above the water surface, $d_w < L_o$) to fully submerged conditions ($d_w >> L_o$) to adequately mimic natural conditions at instream boulders.

The depth of flow (d_w) in the working section (~ 2.7 m downstream of the inlet) was measured by punctual measurements of the water surface profile along the plane of symmetry using an ultrasonic distance meter (Mic +25, Microsonic®, accuracy ± 0.1 mm). By applying the principles of continuity ($Q = U_mB$), different discharges (Q) were calculated to ensure

constant U_m at different d_w, based on the fixed cross section of the channel (B). The water flow was provided by a recirculation pump (Lowara FCE series®) and the discharge measured by a magnetic-inductive discharge meter (Schwing MS 1000®, accuracy ± 1%).
For a given D_{50}, varying d_w while keeping U_m constant impacts the shear velocity (u* [LT^{-1}]) at the undisturbed bed which can be explained by Keugelan's restistance law for dynamical rough beds (Muste *et al*. 2017):

$$U_m/u^* = 2.5 \ln (11\ d_w/D_{50})$$

(Eq. 12)

Here, u* decreases with rising d_w, if U_m is kept constant (Breusers & Raudkivi, 1991). Recalling equation (6) and the interdependence of hydraulic control parameters, a variation of d_w for a given D_{50} yields different U_c:

$$U_c/u_c^* = 5.75 \log (5.53\ d_w/D_{50})$$

(Eq. 13)

for which u_c* is the critical shear velocity [LT^{-1}], that can be estimated by a procedure given by Melville and Coleman (2000: p. 194):

$$u_c^* = 0.0115 + 0.0125\ D_{50}^{1.4} \text{ (valid for 0.1 mm} < D50 < \text{1mm)}$$

(Eq. 14)

so that:

$$U_c = 5.75 \log (5.53\ d_w/D_{50})\ u_c^*$$

(Eq. 15)

Applying equations (14) and (15) to the conditions of series A experiments, it is clear that the secondary control parameter U_m/U_c was varied for different submergence ratios (d_w/L_o), ranging from 0.65 (for d_w/L_o = 3.83) to 0.89 (for d_w/L_o = 0.55), which could have been compensated by changing the slope of the flume. Unfortunately, it is not possible to change the slope of the flume used. However, recalling the underlying assumptions of the parameter framework, d_w/L_o controls the potential maximum size of the morphometric variables as it determines the geometric scale of the HV, while the secondary control parameter U_m/U_c controls the dynamics of the HV within this geometric scale and affects the actual size of the morphometric variables.

Series A experiments were designed to determine threshold conditions of d_w/L_o at which morphometric variables are maximised and to analyse the implications for the size of the

morphometric variable below or above this threshold condition. In the present investigation, morphometric variables of the scour hole and its simplified volume $Vols = d_s\ w_s\ l_s$, normalised to $Vols^{1/3}/L_o$, were analysed.

Series B experiments were repeated on the rectangular obstacle ($Sh \geq 0.8$) for the same d_w/L_o ratios, keeping U_m/U_c constant ($U_m/U_c = 0.72$). In this way, the thresholds observed in the A series of experiments are evaluated. In order to keep U_m/U_c constant at different flow depths (d_w), U_m had to be varied (0.162 - 0.22 m/s). This procedure also affected the secondary control parameter Re_o, which was varied for different ratios of d_w/L_o, ranging from 5928 (at $d_w/L_o = 0.55$) to 8050 (at $d_w/L_o = 3.83$).

For the present study, the following primary and secondary control parameters were kept constant $L_o/D_{50} = 66.5$, $L_o/B = 0.11$, $\sigma_G < 1.3$, $d_{sed}/L_o > 1$, $t/t_e \geq 1$ and Mb is neglected, thus Eq. (8) reduces to:

$$d_s/L_o = f\,(d_w/L_o,\ U_m/U_c,\ Sh)$$

Eq. (16)

for series A and

$$d_s/L_o = f\,(d_w/L_o,\ Re_o)$$

Eq. (17)

for series B. Table 4 shows the conditions and results of all 44 test runs (series A and B).

The obstacles were placed in the test section of the flume (~ 2.7 downstream of the inlet) in the plane of symmetry to minimise sidewall effects (Nezu & Nakagawa, 2017). The obstacles were buried 0.005 m deep in the sediment layer and mounted on a plate attached to the flume bottom to prevent tipping. The elliptical sandstone pebble was oriented with its longest axis parallel to the flow direction. For most experiments, one-dimensional vertical velocity profiles of the undisturbed approaching boundary layer were measured 0.10 m upstream of the obstacle using a miniature velocity probe (Streamflow 403, Nixon Flowmeter®, accuracy ± 1.5%) to ensure that the boundary layer was fully developed in the test section and followed a logarithmic distribution. During selected runs under fully submerged conditions (i.e. flow depth = 0.12 m), a down-looking acoustic Doppler velocimeter (ADV) (Vectrino, Nortek AS®, accuracy ± 1%) was used to measure three-dimensional velocities and turbulence in the vicinity of the obstacles along two-dimensional profiles in the plane of symmetry. The sampling frequency was 25 Hz and flow velocity and turbulence were sampled for 60 to 90 s at each measurement point. Intervals were 0.01 - 0.05 m in the longitudinal direction and

0.005 - 0.01 m in the vertical direction. Data were collected near the end of each experimental run (> 22 h) and the raw data were post-processed using WinADV (version 2.031) (Wahl, 2000) with a peak removal and correlation filter (Goring & Nikora, 2002; Chanson *et al*., 2008). The turbulent kinetic energy (TKE) method (Kim *et al*., 2000; Biron *et al*., 2004) was used to calculate the shear stress, taking into account the variance of the streamwise, cross-channel and vertical flow components. A run time of 24 hours was chosen to ensure that the obstacle marks were close to equilibrium (see Fig. 13) (Melville & Chiew, 1999). After 24 hours, the flume was drained and the characteristic morphometric variables of the obstacle mark were measured using point measurements from a laser distance meter (ODAM S14C, Baumer Electric®, accuracy ± 1.5 mm) mounted on a carriage on top of the flume.

Table 4. Boundary conditions of the experiments and results. C = cube, Sp = sphere, P = pebble. Values are in m, m/s and m³. Uc is estimated by equations (14) and (15). ‡ denotes scour holes in the wake.

Run	Series	Type	h_o	w_o	L_o	d_w	U_m	U_c	Re_o	d_s	w_s	l_s	Vol_S
1	A	C	0.035	0.04	0.037	0.14	0.20	0.306	7319	0.022	0.105	0.04	$9.24\ 10^{-5}$
2	A	C	0.035	0.04	0.037	0.12	0.20	0.3	7319	0.023	0.108	0.049	$1.22\ 10^{-4}$
3	A	C	0.035	0.04	0.037	0.10	0.20	0.292	7319	0.026	0.113	0.052	1.5310^{-4}
4	A	C	0.035	0.04	0.037	0.08	0.20	0.283	7319	0.031	0.137	0.066	$2.8\ 10^{-4}$
5	A	C	0.035	0.04	0.037	0.06	0.20	0.27	7319	0.042	0.182	0.078	$5.96\ 10^{-4}$
6	A	C	0.035	0.04	0.037	0.05	0.20	0.263	7319	0.038	0.173	0.077	$5.06\ 10^{-4}$
7	A	C	0.035	0.04	0.037	0.04	0.20	0.253	7319	0.047	0.189	0.075	$6.66\ 10^{-4}$
8	A	C	0.035	0.04	0.037	0.035	0.20	0.248	7319	0.047	0.195	0.081	$7.42\ 10^{-4}$
10	A	C	0.035	0.04	0.037	0.025	0.20	0.233	7319	0.047	0.192	0.079	$7.13\ 10^{-4}$
11	A	C	0.035	0.04	0.037	0.02	0.20	0.224	7319	0.042	0.181	0.075	$5.7\ 10^{-4}$
12	A	Sp	0.035	0.04	0.037	0.14	0.20	0.306	7319	‡0.01	‡0.109	‡0.06	$6.54\ 10^{-5}$
13	A	Sp	0.035	0.04	0.037	0.12	0.20	0.3	7319	‡0.009	‡0.107	‡0.064	$6.16\ 10^{-4}$
14	A	Sp	0.035	0.04	0.037	0.10	0.20	0.292	7319	‡0.009	‡0.102	‡0.065	$5.97\ 10^{-5}$
15	A	Sp	0.035	0.04	0.037	0.08	0.20	0.283	7319	‡0.008	‡0.12	‡0.065	$6{,}24\ 10^{-5}$
16	A	Sp	0.035	0.04	0.037	0.06	0.20	0.27	7319	‡0.009	‡0.126	‡0.085	$9.64\ 10^{-5}$
17	A	Sp	0.035	0.04	0.037	0.05	0.20	0.263	7319	0.002	0.03	0.004	$2.4\ 10^{-7}$
18	A	Sp	0.035	0.04	0.037	0.04	0.20	0.253	7319	0.002	0.032	0.003	$1.92\ 10^{-7}$
19	A	Sp	0.035	0.04	0.037	0.035	0.20	0.248	7319	0.003	0.041	0.006	$7.8\ 10^{-7}$
20	A	Sp	0.035	0.04	0.037	0.03	0.20	0.241	7319	0.037	0.146	0.06	$3.24\ 10^{-4}$
21	A	Sp	0.035	0.04	0.037	0.025	0.20	0.233	7319	0.038	0.158	0.063	$3.78\ 10^{-4}$
22	A	Sp	0.035	0.04	0.037	0.02	0.20	0.224	7319	0.035	0.139	0.059	$2.87\ 10^{-4}$
23	A	P	0.032	0.045	0.036	0.14	0.20	0.306	7170	‡0.004	‡0.109	‡0.048	$2.09\ 10^{-5}$
24	A	P	0.032	0.045	0.036	0.12	0.20	0.3	7170	‡0.007	‡0.108	‡0.06	$4.54\ 10^{-5}$
25	A	P	0.032	0.045	0.036	0.10	0.20	0.292	7170	‡0.005	‡0.116	‡0.068	$3.94\ 10^{-5}$
26	A	P	0.032	0.045	0.036	0.08	0.20	0.283	7170	‡0.007	‡0.126	‡0.071	$6{,}26\ 10^{-5}$
27	A	P	0.032	0.045	0.036	0.06	0.20	0.27	7170	‡0.012	‡0.163	‡0.105	$2.05\ 10^{-4}$
28	A	P	0.032	0.045	0.036	0.05	0.20	0.263	7170	‡0.01	‡0.164	‡0.12	$1.97\ 10^{-4}$
29	A	P	0.032	0.045	0.036	0.04	0.20	0.253	7170	‡0.014	‡0.181	‡0.134	$3.4\ 10^{-4}$
30	A	P	0.032	0.045	0.036	0.035	0.20	0.248	7170	‡0.026	‡0.267	‡0.223	$1.55\ 10^{-3}$
31	A	P	0.032	0.045	0.036	0.03	0.20	0.241	7170	‡0.024	‡0.3	‡0.248	$1.79\ 10^{-3}$
32	A	P	0.032	0.045	0.036	0.025	0.20	0.233	7170	‡0.004	‡0.104	‡0.05	$2.08\ 10^{-5}$
33	A	P	0.032	0.045	0.036	0.02	0.20	0.224	7170	‡0.017	‡0.201	‡0.13	$4.44\ 10^{-4}$
34	B	C	0.035	0.04	0.037	0.14	0.22	0.306	8050	0.034	0.148	0.063	$3.17\ 10^{-4}$
35	B	C	0.035	0.04	0.037	0.12	0.215	0.3	7868	0.034	0.145	0.065	$3.20\ 10^{-4}$
36	B	C	0.035	0.04	0.037	0.10	0.21	0.292	7685	0.034	0.145	0.062	$3.06\ 10^{-4}$
37	B	C	0.035	0.04	0.037	0.08	0.205	0.283	7502	0.034	0.145	0.065	$3.20\ 10^{-4}$
38	B	C	0.035	0.04	0.037	0.06	0.195	0.27	7136	0.034	0.142	0.064	$3.09\ 10^{-4}$
39	B	C	0.035	0.04	0.037	0.05	0.19	0.263	6953	0.041	0.178	0.077	$5.62\ 10^{-4}$
40	B	C	0.035	0.04	0.037	0.04	0.183	0.253	6697	0.044	0.178	0.077	$6.03\ 10^{-4}$
41	B	C	0.035	0.04	0.037	0.035	0.179	0.248	6550	0.047	0.185	0.078	$6.78\ 10^{-4}$
42	B	C	0.035	0.04	0.037	0.03	0.173	0.241	6331	0.042	0.176	0.078	$5.77\ 10^{-4}$

43	B	C	0.035	0.04	0.037	0.025	0.168	0.233	6148	0.041	0.169	0.077	$5.34\ 10^{-4}$
44	B	C	0.035	0.04	0.037	0.02	0.162	0.224	5928	0.037	0.158	0.064	$3.74\ 10^{-4}$

4.6.1 IMPACT OF SUBMERGENCE RATIO ON OBSTACLE MARK FORMATION

The submergence ratio is classified based on the perturbation of the water surface profile due to the presence of the obstacle (Shamloo *et al*., 2001). At fully submerged conditions ($d_w/L_o > 2$), no disturbance of the water surface profile was observed, indicating free flow of the approaching boundary layer over the top of the obstacle. At shallow submerged conditions ($1 < d_w/L_o < 2$) the obstacle top was only slightly below the water surface, causing the water level above the obstacle top to drop. In addition, a bow wave accumulates at the front of the obstacle. In unsubmerged conditions ($0 < d_w/L_o < 1$), the obstacle top was above the water surface and a bow wave was also detected at the obstacle front, while in the mid to far wake irregularities of the water surface indicate the presence of trailing vortices due to detached shear layers. The perturbations of the water surface profiles were similar for the different obstacle shapes and for both sets of experiments (Fig. 15).

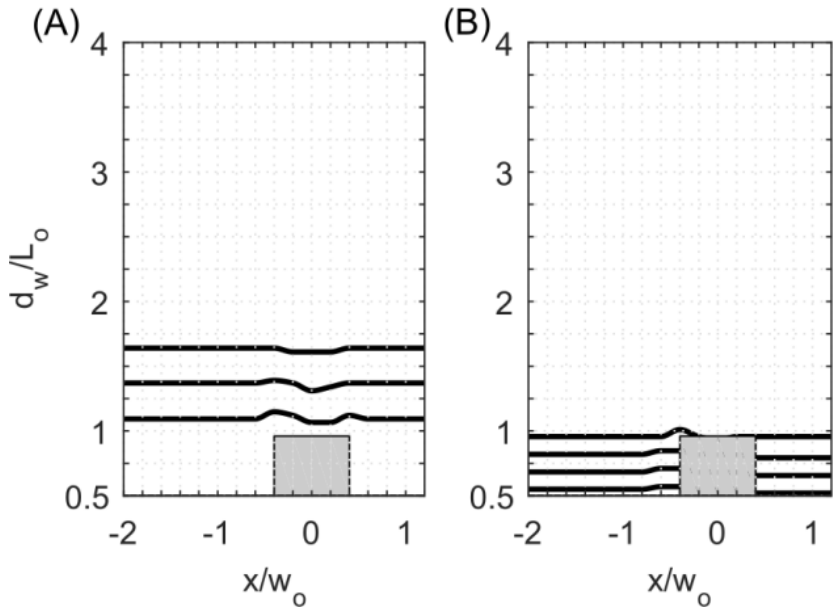


Figure 15. Water surface profiles for series A experiments at a cuboid obstacle. (A) Slightly submerged conditions ($1 < d_w/L_o < 2$). (B) Non-submerged conditions ($0 > d_w/L_o < 1$). For fully submerged conditions ($d_w/L_o > 2$) no disturbance of the water surface could be detected. Flow direction is from left to right. Point measurements are interpolated using piecewise cubic Hermite interpolation polynomials.

For series A experiments, the typical obstacle mark pattern controlled by the action of the HV developed at the bluff cuboid obstacle ($Sh \geq 0.8$) for all ratios of d_w/L_o, while this was not true for the spherical obstacle ($Sh \leq 0.4$) and the streamlined pebble ($Sh \leq 0.4$), (see following

section). With respect to the typical obstacle mark morphology, the morphometric variables d_s, w_s and l_s and the normalised scour hole volume ($Vol_s^{1/3}/L_o$) are maximised at d_w/L_o = 0.8 to 1.0 (experimental runs A8, 9 and 21). An increase or decrease of d_w/L_o from this threshold causes a limitation of $Vol_s^{1/3}/L_o$ (Fig. 16 A). At the threshold condition, d_w is comparable to L_o, thus a high vertical pressure gradient is present at the obstacle front, creating an intensive downflow and an efficient HV system at the obstacle base. In the threshold condition, the secondary control parameters U_m/U_c were 0.83 and 0.81, respectively. It is noteworthy that although U_m/U_c was higher in unsubmerged conditions (i.e. U_m/U_c = 0.86 and 0.89 at d_w/L_o = 0.68 and 0.55), $Vol_s^{1/3}/L_o$ is reduced compared to the observed maximum in shallow submerged conditions ($1 < d_w/L_o < 2$), indicating that within the range of constant primary control parameters (L_o/D_{50} = 66.5, L_o/B = 0.11), the maximum size of the obstacle mark is determined by d_w/L_o alone. A significant limitation of $Vol_s^{1/3}/L_o$ is also evident for $d_w/L_o > 1.1$ (U_m/U_c = 0.79) up to the experimental limit of d_w/L_o = 3.83 (U_m/U_c = 0.65). The limitation of $Vol_s^{1/3}/L_o$ for both cases can be explained as follows:

(a) for $d_w/L_o < 0.7$, boulder-like obstacles are exposed to rather shallow flow (i.e. horizontal length scale of flow > vertical scale of flow). For this unsubmerged condition, the formation of a bow wave at the obstacle front is observed (Fig. 15 B). The bow wave interferes with the HV due to the opposite direction of rotation (cf. Melville and Coleman, 2000), which limits the spatial extent of the HV. For d_w/L_o = 0.55, obstacle mark formation could be observed in the present study. Unfortunately, $d_w/L_o < 0.55$ could not be physically modelled in the laboratory setup. Therefore, the threshold of d_w/L_o where the HV ceases to persist due to bow wave interference could not be determined.

b) For $d_w/L_o > 1.1$, increasing flow depth at the boulder-like obstacles leads to a weakening of the vertical pressure gradient in front of the obstacle and eases the downflow at the obstacle front. As a result, a lower HV prevails, as much of the approaching current flows over the top of the obstacle. The weaker downflow and HV-system dampens the incision of ds and the enlargement of w_s and l_s. As a result, $Vol_s^{1/3}/L_o$ at fully submerged conditions ($d_w/L_o > 2$) is 60% smaller than the maximum $Vol_s^{1/3}/L_o$ at d_w/L_o = 0.8 - 1.

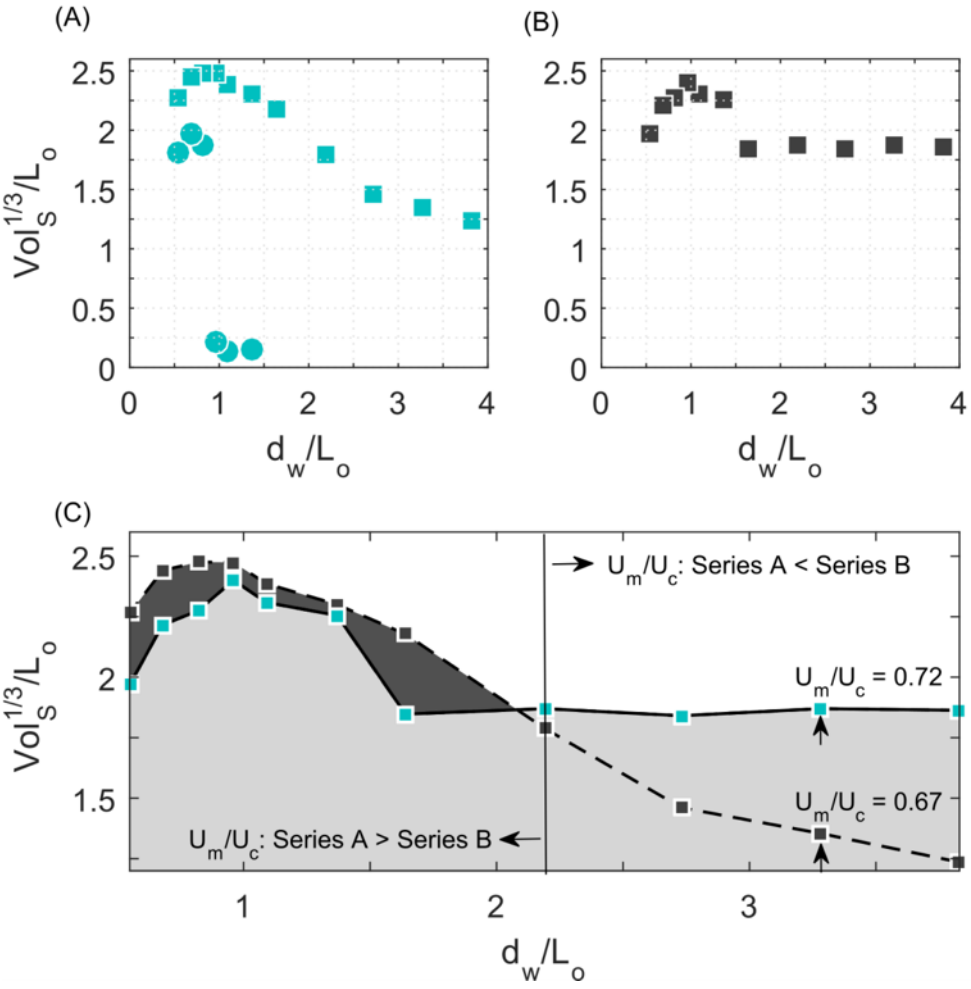


Figure 16. (A) Normalized scour volumes ($Vol_s^{1/3}/L_o$) of runs A1-11 and A17-22. Squares = cuboid obstacle, circles = spherical obstacle. (B) Normalized scour volumes ($Vol_s^{1/3}/L_o$) of runs B34-44. (C) Comparison of (A) and (B) for different d_w/L_o and U_m/U_c. The indications of U_m/U_c = 0.72 and U_m/U_c = 0.67 are valid for the data point marked by the vertical arrows.

The observed threshold condition for maximised $Vol_s^{1/3}/L_o$ at $d_w/L_o \sim 1$ could be validated by series B experiments on the bluff cuboid obstacle ($Sh \geq 0.8$). The actual value of $Vol_s^{1/3}/L_o$ is slightly lower than in the series A experiments because $U_m/U_c = 0.72$ ($U_m/U_c = 0.81$ at $d_w/L_o \sim 1$ in the series A experiments). Moreover, the trend of decreasing $Vol_s^{1/3}/L_o$ compared to the observed maximum is evident for an in- or decrease of d_w/L_o, which is equivalent to the observations of series A experiments (Fig. 16 B). Remarkably, $Vol_s^{1/3}/L_o$ is fairly constant for experimental runs B34 - B38 ($d_w/L_o > 1.6$, $U_m/U_c = 0.72$, $Re_o = 7136$ at $d_w/L_o = 1.64$ to $Re_o = 8050$ at $d_w/L_o = 3.83$). By comparing the $Vol_s^{1/3}/L_o$ at different d_w/L_o for both sets of experiments, it is clear that the assumptions of the parameter framework are correct. Thus, regardless of the shape of the obstacle (Sh), the occurrence of the maximum $Vol_s^{1/3}/L_o$ is solely dependent on the primary control parameter d_w/L_o, while the secondary control parameters U_m/U_c and Re_o influence the actual value of $Vol_s^{1/3}/L_o$ as envelopes to this trend

(Fig. 16 C). Due to limitations of the laboratory equipment, it was not possible to physically model conditions of $d_w/L_o > 3.83$. Therefore, thresholds at which local scour is completely inhibited at the bluff obstruction ($Sh \geq 0.8$) could not be determined.

4.6.2 IMPACT OF OBSTACLE SHAPE ON OBSTACLE MARK FORMATION

For the spherical obstacle ($Sh \leq 0.6$), $Vol_s^{1/3}/L_o$ is maximised for unsubmerged conditions at $d_w/L_o \approx 0.7$ (run A21, cf. Fig. 17 A), while $Vol_s^{1/3}/L_o$ is 20% less than for the angular obstacle. Remarkably, an increase in d_w/L_o towards shallow submergence ($1 < d_w/L_o < 2$) resulted in a different morphology of the obstacle mark. Contrary to the typical obstacle mark morphology, the sedimentary structure then consists of a small frontal scour hole and two lateral depressions in the wake (run A17 - 19, Fig. 17 B). At $d_w/L_o > 1.6$, an "inverse" obstacle mark predominates at the spherical obstacle ($Sh \leq 0.6$), consisting of two lateral depressions in the wake and an adjacent sediment ridge, while a frontal scour hole is absent (Fig. 17 C). For the elliptical obstacle ($Sh \leq 0.4$, runs A23 - 33), the morphology of an inverse obstacle mark prevailed irrespective of d_w/L_o, while the dimensions of the downstream depression (depth, width and length) decreased with increasing d_w/L_o.

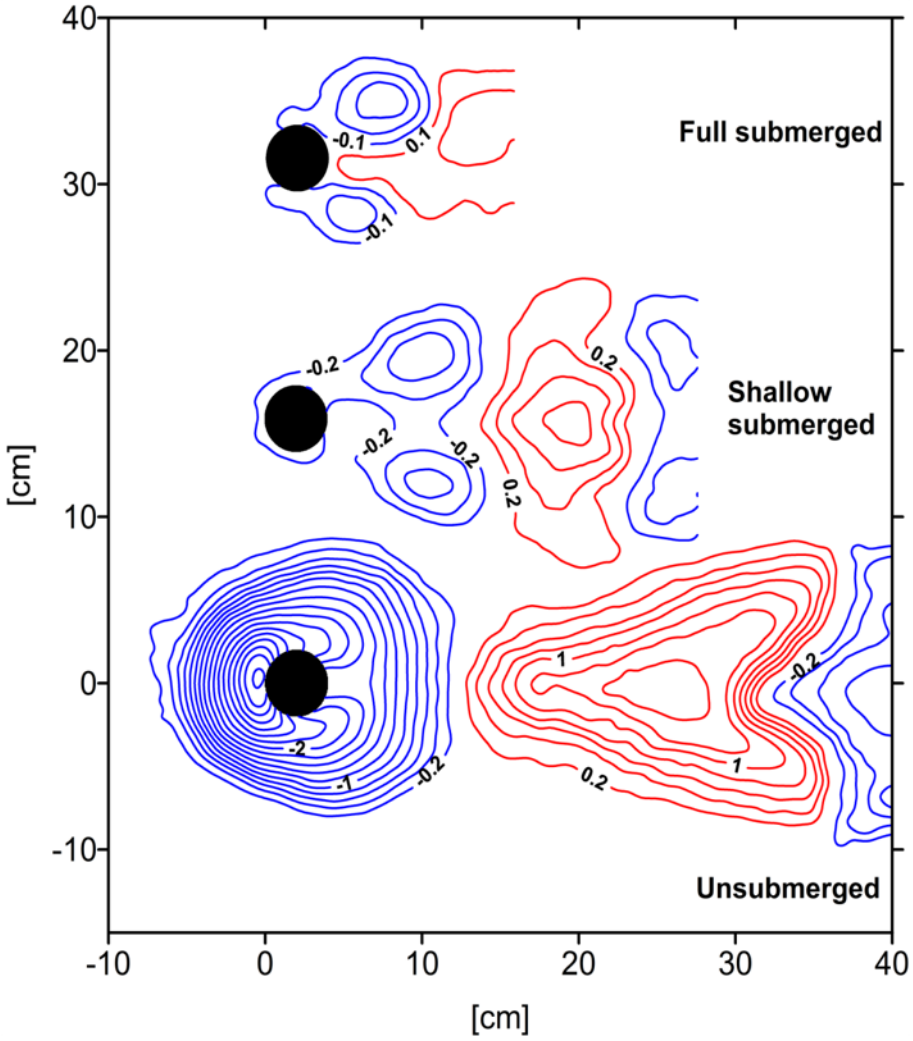


Figure 17. Obstacle mark topography at a spherical obstacle after 24 h runtime for different submergence ratios (d_w/L_o). (A) Inverse obstacle mark, (B) Transitional obstacle mark, (C) Typical obstacle mark. Flow direction from left to right.

Under fully submerged conditions (d_w/L_o = 3.28), the flow field at the spherical and elliptical obstacles showed insignificant downflow due to a weak vertical pressure gradient at the obstacle front. Conversely, the HV at the base is relatively small in size, even smaller than the measurement grid of the ADV measurements (i.e. 0.01 m in horizontal direction and 0.005 m in vertical direction) (cf. Truelsen *et al.*, 2005). In the near wake region, recirculation of the approaching flow was present, which is responsible for the observed wake scouring due to turbulence-induced high shear stresses (Fig. 18).

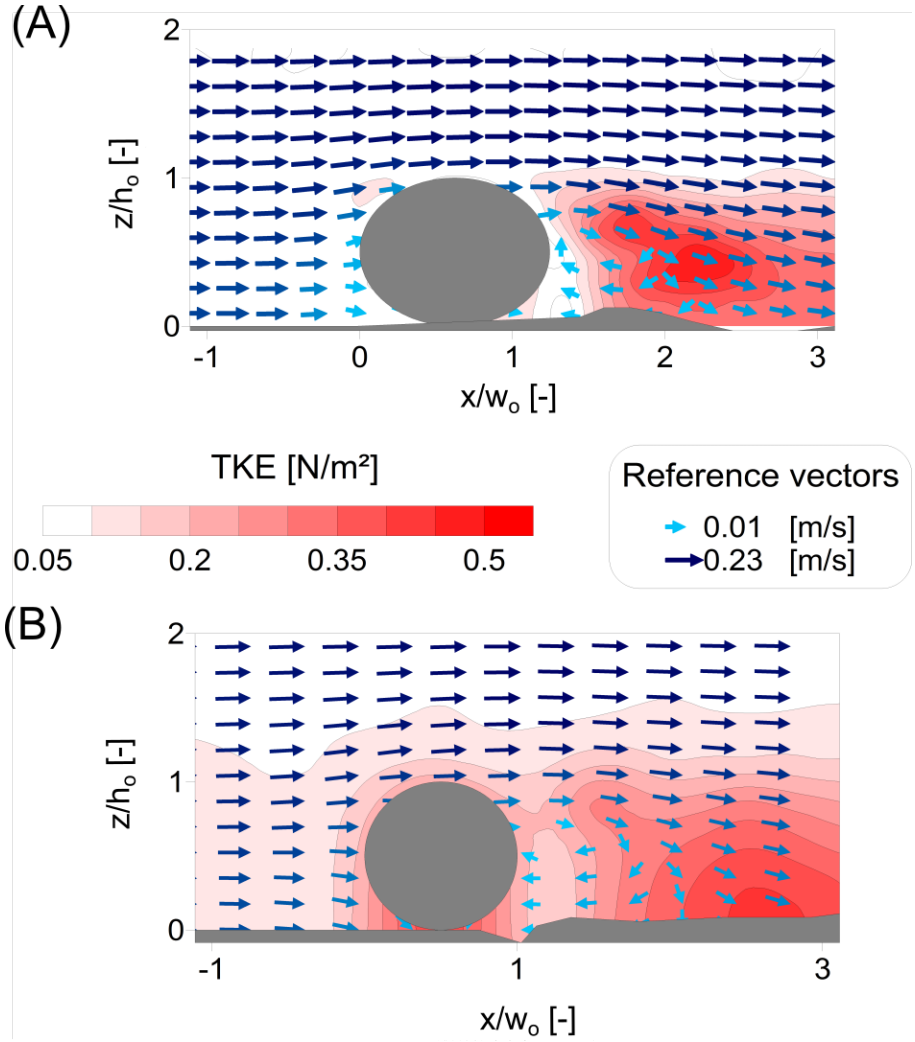


Figure 18. Flow field in the vicinity of (A) elliptical pebble and (B) spherical obstacle for runs A13 an A24. TKE = turbulent kinetic energy (Nm^{-2}). Estimates critical bed shear stress for used sediment is 0.20 N/m^{-2}.

4.7 Conclusions and perspectives

The control of boundary conditions governing the formation of obstacle marks at natural instream obstructions (solitary boulders and vegetation elements) is evaluated through a novel parameter framework that incorporates the extensive body of knowledge derived from hydraulic engineering on local scouring at technical infrastructure (bridge piers, abutments and pipelines). In total, 13 non-dimensional and scale-invariant control parameters are identified that impact morphodynamic processes at natural instream obstructions. The control parameters are integrated into a systematisation that classifies their significance for the size of the morphometric variables of an obstacle mark based on two hierarchical levels. Seven primary control parameters control the geometrical scale of the turbulent horseshoe-vortex system (HV)

at the obstacle and determine the potential maximum size of the structure, while six secondary control parameters impact the dynamics of the HV within the geometrical scale and characterise sensitivities of obstacle mark formation.

The two hierarchical levels are based on empirical thresholds that have been derived from an interdisciplinary review of the phenomenon of local scouring at artificial instream obstructions. The purpose of the framework is to identify the conditions under which the morphometric variables are maximised, the conditions under which the morphometric variables are limited in comparison to the maximum stage, and the conditions under which the formation of obstacle marks is completely inhibited. In order to provide an empirical basis for the proposed classification and to ascertain the threshold conditions of the primary control parameters, namely submergence ratio (d_w/L_o) and obstacle shape (Sh), at which morphometric variables are at their maximum, two series of small-scale flume experiments were conducted. The submergence ratio (d_w/L_o) was modelled by varying the flow depth (d_w) at obstacles of nearly identical size (L_o) but different shape (angular, spherical, elliptical), while also varying the secondary control parameters U_m/U_c and Re_o to a limited extent.

In a near equilibrium condition (after 24 h), the normalized scour hole volume ($Vol_s^{1/3}/L_o$) is maximized at angular (Sh ≥ 0.8) and spherical obstacles (Sh ≤ 0.6). If the ratio of the change in volume to the volume of the obstacle (d_w/L_o) is approximately equal to 0.8–1.0, while the volume of the obstacle ($Vol_s^{1/3}/L_o$) is, on average, 20% larger for Sh values of 0.8 or greater, irrespective of the ratio of change in volume to the volume of the obstacle, then For a pressure gradient of 0.8–1, a high HV prevails at the obstacle base. Conversely, an increase in the distance between the obstacle and the stream (d_w/L_o) limits the spatial extent of the HV. In the case of a spherical obstacle (Sh ≤ 0.6), no typical obstacle mark (frontal scour hole and downstream sediment accumulation) emerged for $d_w/L_o > 1.6$. Conversely, the streamlined shape of the elliptical obstacle (Sh ≤ 0.4) inhibited the formation of an HV capable of inducing local scouring in front of the obstruction, irrespective of d_w/L_o. Moreover, the observed correlation between $Vol_s^{1/3}/L_o$ and d_w/L_o is also valid for a range of secondary control parameters, namely U_m/U_c and Re_o, which influence the dynamics of the HV. These parameters represent envelopes to this trend. The experimental results corroborate the proposed classification of the parameter framework.

It is necessary to test the validity of the defined threshold ranges empirically for more complex scenarios in order to approximate natural conditions at instream

obstructions and their impact on obstacle mark formation. In particular, flume studies are required to mimic unsteady discharge events and the associated variations in d_w/L_o and U_m/U_c over time (t). Physical modelling studies offer the advantage of gradually and systematically varying control parameters to identify cause and effect relationships and quantify sensitivities, assuming scale-independence of processes. In addition to their intrinsic academic value, an increased understanding of the boundary conditions controlling the formation and dynamics of fluvial obstacle marks will lead to a refinement of existing approaches for the hydraulic interpretation of preserved obstacle marks. These can then be used to estimate past flood events (Herget *et al*., 2013).

5. INFLUENCE OF SUBMERGENCE RATIO ON HORSESHOE VORTEX SIZE AT BOULDER OBSTACLES

ABSTRACT

Local scour holes are erosional bed structures that are of significance in the fields of geoscience and hydraulic engineering. While the phenomenon of local scouring around bridge piers and pipelines has been the subject of extensive study, comparatively little attention has been devoted to the subject of local scouring around natural obstacles, such as boulders. The boulders are subjected to varying flow depths, with the potential for them to be partially or fully submerged, contingent on the prevailing flow conditions. The impact of these fluctuating conditions on local scouring and hydraulic processes remains poorly understood. A meta-analysis was conducted on four previously published experimental series on local scouring around boulder-like obstacles with different degrees of submergence. The objective was to assess the influence of flow depth on local scouring. The results indicate that the size of the horseshoe vortex can be determined from the geometry of the local scour hole. Furthermore, it was observed that the diameter of the horseshoe vortex decreases as the submergence of the obstacle increases.

This chapter has been submitted for revision in:
Schlömer, O. and Herget, J. (2025) Influence of submergence ratio on horseshoe vortex size at boulder obstacles. Submitted to *Journal of Hydraulic Research*.

5.1 INTRODUCTION

In rivers and floodplains, various elements such as cobbles, boulders, woody debris and man-made structures such as bridge piers act as obstacles to the approaching flow, causing three-dimensional boundary layer separation and the formation of turbulent eddies around the obstacle. If the obstacle is not submerged (i.e. part of the obstacle is above the water surface), the following processes are common: (i) an increase in flow velocity lateral to the obstacle; (ii) the formation of a jet-like downdraft at the front of the obstacle due to a downward negative pressure gradient; and (iii) the formation of unsteady turbulent necklace-like vortex structures at the base of the obstacle, commonly referred to as a horseshoe vortex system (HV) (Dargahi, 1990; Dey & Raikar, 2007a; Gazi & Afzal, 2020; Zhang *et al.*, 2020).

These processes amplify the bed shear stress relative to the undisturbed upstream flow and induce sediment mobilisation in the vicinity of the obstacle (Radice & Tran, 2012; Chen *et al.*, 2017; Li *et al.*, 2018). As a result, a local scour hole is formed on the luv side of the obstacle, which can be characterised as an inverted truncated cone with an elliptical shape in plan view. Local scouring is a time-dependent process. For non-cohesive alluvial sediments (i.e. sand and gravel), equilibrium conditions are typically reached in an order of magnitude of days (Oliveto & Hager, 2002). However, it is well known that for steady flow, 80% of the local scour hole size at near steady state (t_e) is reached within only 5¬40% of the time to reach this near steady state, mainly depending on flow velocity and grain size (Melville & Chiew, 1999).

The enlargement of the local scour hole is closely related to the HV as the main driver of sediment mobilisation, as the shear stress under the vortex system is estimated to be three times higher than in the undisturbed approaching boundary layer (Baker, 1985; Dargahi, 1989; Graf & Istiarto, 2002; Radice *et al.*, 2009). The HV is actually composed of several interacting and unsteady vortices (Escauriaza and Sotiropoulos 2011). The largest and most stable vortex is referred to as the primary horseshoe vortex (HV1), which sinks into the local scour hole during development (Guan *et al.*, 2019). Within the local scour hole, HV1 exhibits aperiodic bimodal oscillations that cause changes in the position of the vortex core (Paik *et al.*, 2007; Kirkil *et al.*, 2008; Kirkil & Constantinescu, 2010).

For a solidified local scour hole in near steady state, Muzzammil and Gangadhariah (2003) and Muzzammil *et al*., (2004) describe the vortex as elliptical in shape, with horizontal and vertical dimensions determined by the geometry of the

obstacle (i.e. obstacle width) and the thickness of the approaching boundary layer (i.e. flow depth). Kothyari *et al*., (1992) and Dey (1996) described the relationship between the vortex diameter (D_v), the obstacle width (w_o) and the flow depth (d_w) as follows:

$$D_v = 0.28 d_w^{0.15} w_o^{0.85}$$

(Eq. 18)

It should be noted that equation (18) was developed on the basis of experimental data on local scouring at unsubmerged bridge piers. However, natural obstructions such as boulders are affected by flow conditions that may cause the obstruction to be submerged so that it occupies only the lower part of the flow depth; therefore much of the approaching flow diverges without significant flow separation or acceleration at the base of the obstruction. For this condition, other vortical structures in the wake of the obstruction become dominant (Koken & Constantinescu, 2023). In open channel flow studies, the submergence ratio, i.e. the ratio of flow depth to obstacle height, has mostly been used as a dimensionless parameter to describe flow depth-wake structure relationships because of the interest in fish habitat structures (Tsakiris *et al.*, 2014), flow structures around boulders or clasts (Shamloo *et al*., 2001, Sadeque *et al.*, 2008, 2009; Lacey & Rennie, 2012) and sediment transport (Papanicolaou *et al*., 2012).

Lacey and Rennie (2012) showed that for 2.0 ≤ submergence ratio ≤ 3.0, regions of high turbulent kinetic energy move downstream with decreasing depth and the Reynolds shear stress ($-u'w'$) increases by up to 50% near the top of the cube. Hajimirzaie *et al.* (2012) and Hajimirzaie and Buchholz (2013) showed that reducing the submergence ratio significantly increases the strength of the dominant vortex structures and the shedding behaviour. While the obstacles experienced weakly symmetric shedding at a submergence ratio = 3.5, the shedding became highly antisymmetric at a submergence ratio = 1.0. However, neither the effect of submergence on local scouring at boulder-like obstacles nor its effect on the size of the primary horseshoe eddy has been systematically evaluated. Knowledge of the size of the primary horseshoe eddy is not only relevant for estimating the spatial extent of local scour protection countermeasures, but also for refining existing approaches for hydraulic interpretation of preserved obstacle marks, which can be used to estimate past flood events (Herget *et al*., 2013).

To this end, we present a meta-analysis of 74 experimental flume runs on local scouring at boulder-like obstacles previously published in four research papers (Euler & Herget 2011, Euler *et al*., 2017, Schlömer *et al*., 2020, Schlömer *et al*., 2021). The meta-analysis focuses on the research question of how flow depth at submerged boulder-like obstacles affects local scouring and the size of the responsible primary horseshoe vortex at the base of the obstacle. It is further hypothesised that the vortex size is manifested in the local scour hole geometry. Before presenting and discussing the results of the re-evaluation, the experimental boundary conditions of each experimental series and the local scour hole geometry investigated are presented.

5.2 MATERIAL AND METHODS

Experimental data from Euler and Herget (2011), Euler *et al*., (2017), and Schlömer *et al*., (2020) were used in the present analysis. All studies used a flume as a process-focused 1:1 laboratory prototype (Baynes *et al*., 2018) to replicate the processes and resulting morphologies (i.e. local scour holes). The datasets were used because their experimental design is comparable:

(i) Data on characteristic length scales of total local scour holes were provided. These include the local scour hole depth at the obstacle front (d_s), measured from the undisturbed upstream bed; the local scour hole frontal length (l_s) in the plane of symmetry to the incoming flow, measured from the obstacle front to the upstream edge of the scour hole; and the local scour hole frontal width (w_s), measured perpendicular to the incoming flow direction from the lateral edges of the scour hole at the obstacle frontal face (Fig. 4) (Schlömer 2020).

(ii) Different submergence ratios d_w/L_o were created experimentally by varying obstacle size ($L_o = h_o^{2/3}w_o^{1/3}$), where h_o = obstacle height, resulting in d_w/L_o ranging from 0.67 to 12.2. All experimental datasets used L_o as the reference length scale for d_w/L_o to account for not only obstacle height but also obstacle width, as obstacle width has been reported to be important for local scouring processes (Wu & Balachandar 2016).

Euler and Herget (2011) and Euler *et al*., (2017) used brass cylinders as obstacles, while Schlömer *et al*., (2020) and Schlömer *et al*., (2021) used a glass cube. The obstacles were attached to the bottom of the flume to prevent them from tipping into the emerging

scour hole. All experiments were conducted in a 5 m long, 0.32 m wide and 0.27 m deep straight rectangular flume. The bottom gradient of the flume was set to a moderate slope (0.003 m/m). Flow was controlled by a recirculation pump (Lowara FCE Series®, Germany) manually regulated by two cone valves and measured by a magnetic-inductive flowmeter (Schwing MS 1000®, accuracy ± 1% of actual flow). The depth of flow was adjusted with a gate at the downstream end of the flume outlet. The flume bed was completely filled with a 0.055 m thick layer (d_{sed}) of uniform sand ($\sigma_G < 1.3$) with an average grain diameter (D_{50} = 0.75 mm). A more detailed description of the flume used and the instrumentation employed can be found in (Schlömer & Herget, 2023).

The mean flow velocity (U_m) of all experimental runs ranged from 0.162 m/s - 0.262 m/s, and d_w ranged from 0.02 m - 0.14 m. Based on the given D_{50} and d_w values, the estimated critical mean velocity for sediment entrainment (U_c) was estimated using a procedure presented in (Melville & Coleman, 2000), resulting in flow intensities $U_m/U_c < 1$. Thus, all experimental runs were conducted under clear water conditions and steady flow. The flow was subcritical, as indicated by a Froude number (Fr) between 0.2 and 0.57, and fully turbulent, as indicated by a Reynolds number (Re) much greater than 500. Despite the relatively short flume length, vertical flow measurements in the working section of the flume (~2.7 m downstream of the flume inlet) indicated developed boundary profiles for $d_w > 0.02$ m.

Experimental run times (t) ranged from 1200 to 5760 min to achieve a near steady state of local scouring. The dimensions of the geometric length scales were (d_s, l_s and w_s) were measured by a traversing system on top of the flume operating in x/y planes, where x = longitudinal and current direction and y = horizontal, perpendicular to the current direction. Two LED distance meters (Welotec® OWRB series, accuracy ± 0.5 mm) were used to measure l_s and w_s. A laser distance meter (Baumer Electric® ODAM S14C, accuracy ± 1.5 mm) was used to measure d_s (z-plane).

Euler and Herget (2011), Euler *et al*. (2017) and Schlömer *et al*. (2020) measured the geometric length scales of the local scour hole at the end of the experimental runs when the flume was drained; Schlömer *et al*. (2021) measured the time evolution of d_s, l_s and w_s during local scour at t = 30, 60, 120, 240, 480, 1440 and 5760 min, with t = 0 min as the start of the experimental runs.

5.3 RESULTS AND INTERPRETATION

A total of 74 experimental runs were analysed, during which local scour holes emerged from the start of the runs. Regardless of the experimental dataset, observations on the local scouring process were identical. At the beginning of each experimental run, two initial depressions formed at the lateral edges of the obstacle front, which merged to form a conical scour hole in front of the obstacle. The maximum scour depth position migrated from the lateral sides to the obstacle front. The eroded material deposited downstream in the wake of the obstruction as a sediment ridge oriented parallel to the flow direction. During the initial stages of local scouring (i.e. $t/t_e \leq 0.04$, approximately 270 minutes), the scour hole deepened significantly and expanded in length and width (Euler & Herget, 2012). For $t/t_e > 0.04$, the local scour incision significantly decreased, asymptotically approaching a near-steady state. This phenomenon has also been observed in experimental bridge scour research (Melville & Chiew, 1999; Schlömer, 2020). The dimensions of d_s, l_s, and w_s at the end of experimental runs were used to approximate the volume of the local scour hole (Vol_s) using the following equation:

$$Vol_s = d_s \, l_s \, w_s$$

(Eq. 19)

Although this procedure systematically overestimated the actual volume of the scour hole by neglecting its inverted frustum cone shape, it is considered a sufficiently accurate estimate for subsequent analysis. The normalized scour hole volume ($Vol_s^{1/3}/L_o$) was plotted against d_w/L_o, revealing that:

- $Vol_s^{1/3}/L_o$ is maximized for $d_w/L_o = 1$;
- $Vol_s^{1/3}/L_o$ decreases for $d_w/L_o > 2$ and reaches its minimum value for $d_w/L_o = 14$ (Fig. 19).

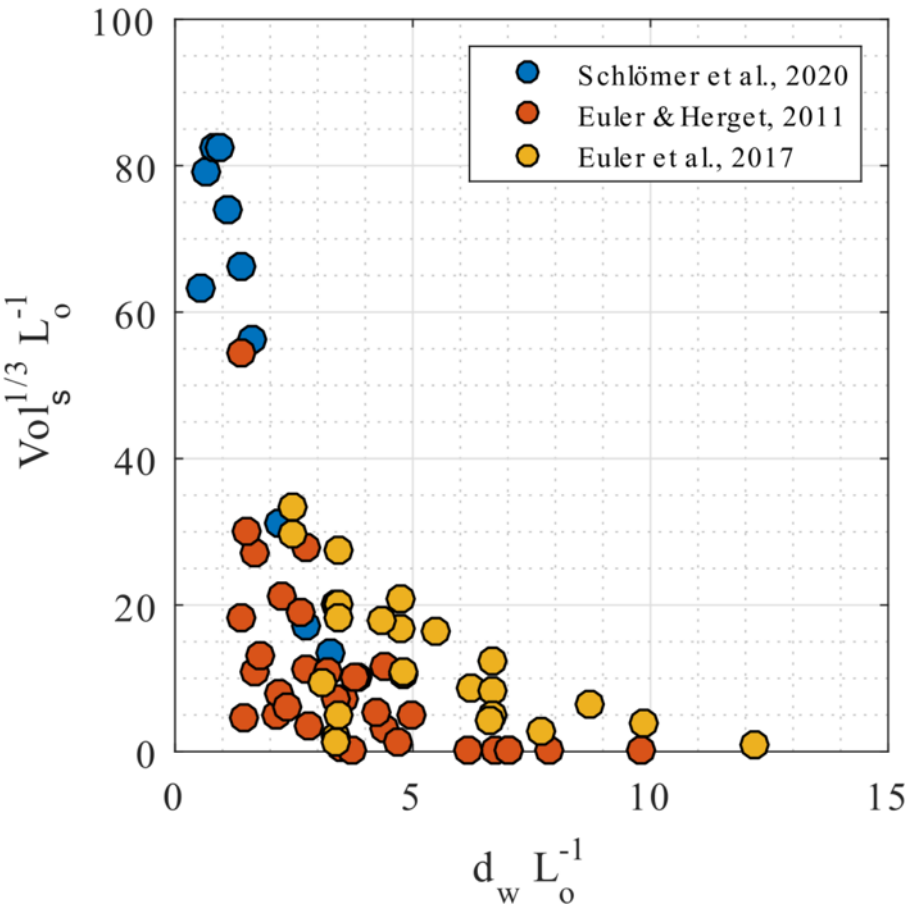


Figure 19. Normalized local scour hole volume over submergence ratio.

Apart from a reasonable scatter due to different flow intensities (U_m/U_c) of individual runs, which is likely for experimental research on local scouring (Unger & Hager 2006), the aforementioned trend is present for all datasets considered. Sarkar (2014) and Bauri and Sarkar (2016) also observed the trend of decreasing ds with increasing d_w/L_o. Their data are not included in the present analysis, as they did not measure all geometric length scales to quantify Vol_s.

The intensification of local scouring processes can be interpreted in terms of the hydraulic processes at the obstacle. For $d_w/L_o \leq 1.5$, there is a high pressure gradient at the obstacle front, which creates an intense downflow and a highly erosive HV system at the base of the obstacle (Schlömer *et al.*, 2020, Schlömer & Herget 2023). The decreasing volume of the local scour hole with increasing submergence ratio can be attributed to the fact that most of the approaching boundary layers flow over the obstacle while the downflow ceases. For these fully submerged conditions ($d_w/L_o > 2$) other vortex systems emerge which are more characteristic. As shown by Dey *et al.*, (2008), Papanicolaou *et al.*, (2012), and Hajimirzaie and Buchholz (2013), flow

separation at the obstacle results in an arched vortex consisting of two lateral vortices at the sides of the obstacle and a vortex at the crest of the obstacle. The arched eddy bends down to the bed immediately downstream of the boulder (i.e. the near-wake region) and creates a recirculation zone where part of the flow is reversed towards the obstacle: In all of the test series used, it was reported that the cross-sectional profiles of the frontal scour holes along their flow axis (i.e. axis l_s to d_s), both during local scouring and for drained conditions at the end of the test runs, show different segments. These segments consist of:

(i) A flat semicircular scour hole bottom (S_b), closely connected to the obstacle base with radius < l_s;

(ii) An inner frontal scour hole (lower slope) characterised by an inclination ≥ critical angle of repose (Φ_{crit});

(iii) An outer frontal scour hole (upper slope) characterised by an inclination ≤ Φ_{crit}. The transition between the two slopes is marked by a sharp edge (or berm) in the cross-sectional profile.

The segmentation of the frontal local scour hole is a consequence of the HV system. During incision, HV1 sinks into the frontal scour hole and extends to S_b, where it promotes sediment mobilisation by saltation and rolling (Dargahi, 1990; Dey & Raikar, 2007a; Chen *et al.*, 2017). Muzzammil and Gangadariah (2003) and Muzzammil *et al.* (2004) used the local scour hole segmentation to derive the mean diameter (D_v) of HV1 as follows:

$$D_v = 2a+2b \quad \text{(Eq. 20)}$$

where a = major longitudinal axis of the vortex (x-plane) and b = vertical axis of the vortex (z-plane), assuming an elliptical vortex shape (Fig. 6).

Using this concept, it was possible to approximate the mean diameter of HV1 of the experimental data set based on the position of the berm relative to the obstacle front. The longitudinal axis of the vortex (a) is equal to the distance from the obstacle front to the onset of the berm in the local scour hole slope, while the vertical axis of the vortex (b) is equal to the height of the berm onset relative to the local scour hole depth (d_s) in S_b. The berm itself is a function of d_s and the critical angle of repose (Φ_{crit}) of the given sediment size (Link *et al.*, 2008). The lower slope is controlled by the rotation of HV1

and the tendency to stabilise at $\Phi > \Phi_{crit}$ during the local scouring process, while the upper slope adjusts to the angle of repose by gravitational movements.

Figure 20 a shows the estimated and normalised vortex diameter (D_v/L_o) over the normalised scoured volume ($Vol_s^{1/3}/L_o$) at the end of the experimental runs at near steady state conditions. The vortex diameter of HV1 is scaled with the size of the local scour hole. This observation is consistent with the experimental data of Muzzammil and Gangadariah (2003) and Guan *et al*., (2019), who show that the mean vortex size at an unsubmerged cylindrical pile correlates with the local scour hole depth, because HV1 sinks into the local scour hole during the local scouring process, where it expands linearly with the size of the local scour hole. The same observation is reported for the time-averaged experimental series of Schlömer *et al*., (2021) on a boulder-like obstacle (Fig. 20 b).

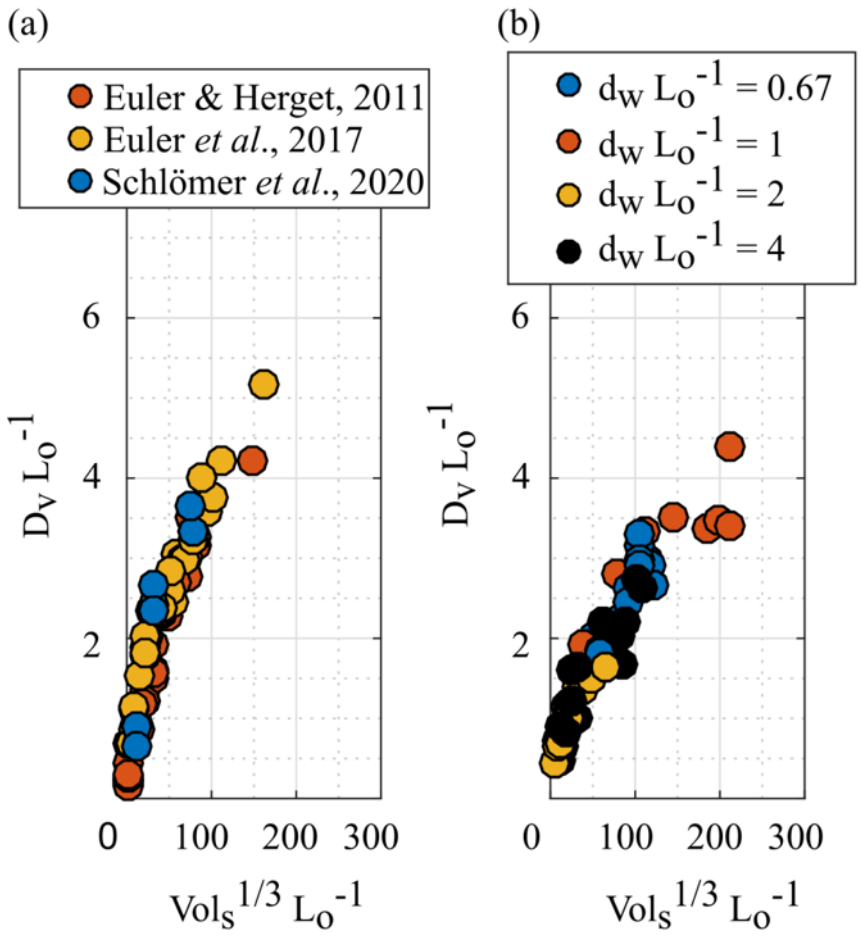


Figure 20. Normalized diameter of HV1 over normalized local scour hole volume. (a) For different experimental series and (b) for different extent of submergence ratio within experimental series.

However, by separating the data set on the basis of submergence, it becomes clear that:

(i) D_v/L_o and $Vol_s^{1/3}/L_o$ scale with submergence ratio and are maximised for d_w/L_o, and
(ii) For a given d_w/L_o, an increase in D_v/L_o with $Vol_s^{1/3}/L_o$ could be observed with increasing test duration.

It should be noted that for $t/t_e > 0.04$ (i.e. > 240 min) the mean size of HV1 remained fairly constant up to t $t_e^1 = 1$ (i.e. 5760 min), indicating that during the initial stages of local scouring (i.e. < 240 min) HV1 sinks into the local scour hole and expands its diameter. For later stages, a near steady state is approached which is characterised by a decreasing expansion of the local scour hole as well as the vortex diameter. The vortex diameter (D_v) is then approximately 66% of d_s.

By plotting D_v versus d_w/L_o for the near steady-state experimental runs, it is clear that the diameter of HV1 is inversely related to the submergence ratio. As the submergence of the obstacle increased, the diameter of the primary vortex became smaller (Fig. 21). This result is interpreted in the context of the hydraulic processes at the obstcale. For fully submerged obstacles ($d_w/L_o > 2$) (Schlömer *et al*., 2020), the size and erosive capacity of HV1 is reduced, while there is insufficient downflow at the face of the obstacle to feed the primary horseshoe vortex. On the other hand, for $d_w/L_o = 1$, the entire boundary layer approaches the obstacle and there is intense downflow, resulting in a larger HV1 at the base of the obstacle and consequently a larger local scour hole size. It is therefore concluded that the submergence ratio, i.e. the approaching flow depth and the size of the obstacle in height and width, have a dominant influence on the size of the horseshoe vortex system responsible for local scouring.

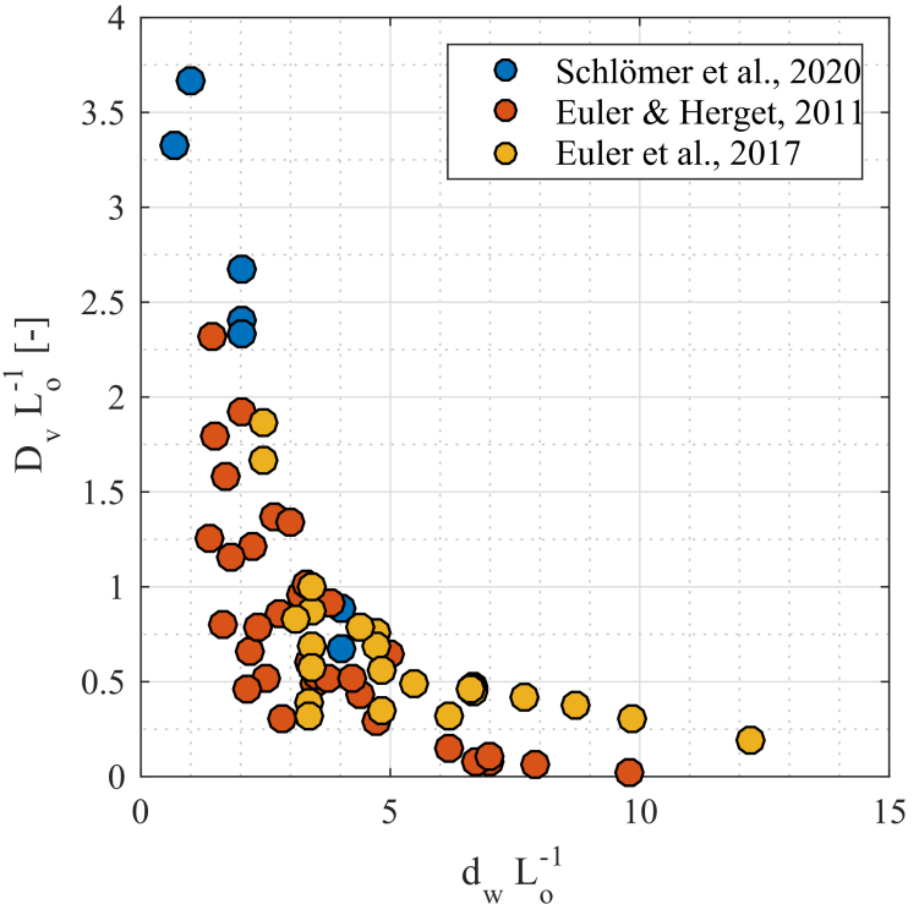


Figure 21. Normalized diameter of HV1 over submergence ratio.

A multiple linear regression was performed on the dimensional data of d_w, L_o, d_s and D_v. For this analysis, only the data sets that reached a near steady state of local scouring were used. The separation of the influencing factors showed a decreasing tendency of D_v with increasing d_w (Fig. 22 a) as well as an increasing tendency of D_v with L_o (Fig. 22 b) and d_s (Fig. 22 c), resulting in:

$$D_v = 0.325d_w + 1.26L_o + 0.92\ d_s$$

(Eq. 21)

The correlation coefficient (R^2) of equation 21 is 0.76, which is indeed low, but may be acceptable in the absence of other alternatives. The 95% confidence intervals for the coefficient estimates are -0.34 to -0.14 for d_w, 0.68 to 1.8 for L_o and 0.45 to 1.4 for d_s. In addition to its purely academic relevance, equation 21 is believed to provide a sufficiently accurate estimate of the extent of flow structures at boulder-like obstacles. In river restoration practice, immobile boulders are often used to initiate natural channel

dynamics due to three-dimensional flow structures in their surroundings (Golpira *et al.*, 2022).

5.4 CONCLUSION

A meta-analysis of three experimental series on local scouring at boulder-like obstacles exposed to different degrees of submergence is presented. The experimental series measured the emerging local scour hole geometry based on characteristic length scales including local scour hole depth (d_s), local scour hole length (l_s) and local scour hole width (w_s) to estimate the scour volume (Vol_s). All experimental series were conducted in the same laboratory flume for subcritical, fully turbulent and steady flow under clear water conditions. The experimental runs were carried out until local scouring reached a near steady state. The experimental series were re-evaluated based on the research question of how flow depth (d_w) at submerged boulder-like obstacles affects local scouring and the size of the responsible primary horseshoe vortex (HV1) at the base of the obstacle. The following conclusions can be drawn from the meta-analysis:

(i) The scoured volume as well as the geometric length scales of the local scour hole are maximised when the flow depth (d_w) was comparable to the size of the obstacle (L_o), i.e. when $d_w/L_o \approx 1 \neg 1.5$. With increasing submergence of the obstacle, i.e. increasing flow depth, the scoured volume and the size of the geometric length scales are reduced.

(ii) The aforementioned is related to the horseshoe vortex system at the base of the obstacle as the main trigger of the local scouring processes. For $d_w/L_o \approx 1 \neg 1.5$, there is an intense downflow at the obstacle front as the entire boundary layer approaches the obstacle. This results in a high pressure gradient at the obstacle front, causing a larger primary horseshoe vortex in terms of its diameter. With increasing submergence of the obstacle, i.e. increasing flow depth, the downflow at the obstacle front ceases and causes a smaller primary horseshoe vortex.

(iii) The actual diameter of the primary horseshoe vortex (D_v) can be estimated from a sharp edge (or berm) in the local scour hole slope. The position of this edge relative to the obstacle allows the longitudinal (along the mean flow

direction) and vertical axes of the vortex to be estimated, which correspond to the major and minor axes of the elliptical primary horseshoe vortex. Although the primary horseshoe vortex sinks into the local scour hole during the local scouring process where it slightly increases its diameter, a correlation between the horseshoe vortex diameter and the submergence ratio (d_w/L_o) was found based on the near steady state geometry of the local scour holes.

(iv) A multiple linear regression showed that the primary horseshoe vortex diameter (D_v) was influenced by flow depth (d_w), obstacle size (L_o) and local scour hole depth. Separation of the influencing factors showed a decreasing tendency of D_v with increasing d_w and an increasing tendency of D_v with L_o and d_s.

6. GEOMETRY OF OBSTACLE MARKS AT INSTREAM BOULDERS – INTEGRATION OF LABORATORY INVESTIGATIONS AND FIELD OBSERVATIONS

ABSTRACT

Obstacle marks are instream bedforms, typically composed of an upstream frontal scour hole and a downstream sediment accumulation in the vicinity of an obstacle. Local scouring at infrastructure (e.g. bridge piers) is a well-studied phenomenon in hydraulic engineering, while less attention is given to the time-dependent evolution of frontal scour holes at instream boulders and their geometrical relations (depth to width, and length ratio). Furthermore, a comparison between laboratory studies and field observations are rare. Therefore, the morphodynamic importance of such scour features to fluvial sediment transport and morphological change is largely unknown. In this study, obstacle marks at boulder-like obstructions were physically modelled in 30 unscaled process-focussed flume experiments (runtime per experiment ≥ 5760 min) at a range of flows (subcritical, clear-water conditions, emergent and submerged water levels) and boundary conditions designed to represent the field setting (i.e. obstacle tilting, and limited thickness of alluvial layer). Additionally, geometries of scour holes at 90 in-situ boulders (diameter ≥ 1m) located in a 50-km segment of the Colorado River in Marble Canyon (AZ) were measured from a 1-m resolution DEM. Flume experiments reveal similar evolution of local scouring, irrespective of hydraulic conditions, controlled by the scour incision, whereas the thickness of the alluvial layer and obstacle tilting into the evolving frontal scour hole limit incision. Three temporal evolution phases ((1) rapid incision, (2) decreasing incision, and (3) scour widening) are identified based on statistical analysis of spatio-temporal bed elevation time-series. A quantitative model is presented that mechanistically predicts enlargement in local scour length and width based on (1) scour depth, (2) the inclination of scour slopes and (3) the planform area of the frontal scour hole bottom. The comparison of field observations and laboratory results demonstrates scale invariance of geometry that implies similitude of processes and form rather than equifinality.

This chapter has been published as: Schlömer, O., Grams, P. E., Buscombe, D. and Herget, J. (2021) Geometry of obstacle marks at instream boulders integration of laboratory investigations and field observations. *Earth Surface Processes and Landforms* 46(3) 659-679. DOI: https://doi.org/10.1002/esp.5055.

6.1 INTRODUCTION

Obstacle marks are bed features related to topographic obstructions exposed to a current (Karcz, 1968; Richardson, 1968; Hargitai, 2014). Typically, obstacle marks are composed of an upstream crescentic frontal scour hole that laterally surrounds the obstacle in the downstream direction, and a dune-like sediment accumulation in the downstream wake of the obstruction, termed sediment ridge (Oliveto & Hager, 2014). Obstacle marks emerge due to due to three-dimensional flow structures and turbulence in the vicinity of an obstacle, even when the threshold velocity for general sediment movement is not exceeded (Euler & Herget, 2012). Obstacles may be large natural bed elements such as solitary boulders or deadwood with a diameter greater than the mean diameter of the surrounding alluvium (Judd & Peterson, 1969; Lisle, 1981; Laronne *et al*., 2001; Thompson, 2008) or instream infrastructure (i.e. bridge piers, spur dikes), (Breusers & Raudkivi, 1991; Hoffmans & Verheij, 1997; Melville & Coleman, 2000). Thus, the flow structures around instream obstacles and the formation of obstacle marks is relevant to various scientific disciplines in Earth-science and hydraulic engineering.

In geomorphology and sedimentology, depositional patterns around isolated small boulders or cobbles in gravel-bed rivers are well documented as particle clusters (Cin, 1968; Carling & Reader, 1982; Storm & Papanicolaou, 2007; Papanicolaou *et al*., 2018). However, in contrast to an obstacle mark, local scouring at the stoss-side of particle clusters is inhibited because individual grains are large relative to the cluster and dissipate energy (Lee & Sturm, 2008). Instead of initiating erosion, particle clusters tend to trap incoming sediment that is transported as bedload sheets or in suspension either on its stoss side or its wake, depending on the submergence ratio (ratio of approaching flow depth to size of the obstacle), (Papanicolaou *et al*., 2011; Papanicolaou *et al*., 2012; Ghilardi *et al*., 2014) and the turbulent flow structure (Lawless & Robert, 2001). Deposits of finer material form frequently in the low-energy wake of large bed obstructions, presumably during waning flows (Carling & Reader, 1982; Thompson, 2008).

Obstacle mark formation at boulder-like obstructions has been described in relatively few empirical laboratory studies (Fisher & Klingman, 1984; Boyer & Roy, 1991; Shamloo *et al*., 2001; Euler *et al*., 2017). Submergence ratio is a particularly important boundary condition, as boulder-like instream obstructions are affected by different water levels. During lower flows, the obstacle might be emergent (some portion of the obstacle protrudes above the water surface) and the flow is affected by

localized flow structures (e.g. hydraulic jumps) as it becomes a function of Froude number. Whereas at higher flow, the obstacle occupies only the lower portion of the flow depth and the obstacle is submerged, while the flow is subcritical (Boyer & Roy, 1991; Shamloo *et al*., 2001; Papanicolaou *et al*., 2010). Moreover, obstacle mark formation at boulder-like instream obstructions in the field is influenced by specific boundary conditions that limit scouring (Schlömer *et al*., 2020). For instance, scour incision at a solitary instream boulder causes the boulder to tilt into the frontal scour hole once a critical depth is crossed, resulting in self-burial of the obstacle (Euler *et al*., 2017). Consequently, this process changes the boulder's exposure to flow and alters scouring processes (Rennie *et al*., 2017). On the other hand, the alluvial layer in which the boulder is embedded might be depth-limited so that only a thin alluvial cover is present over bedrock (Hodge *et al*., 2011), or an armour layer is developed in the scour hole due to non-uniformity of alluvial material. In both cases, ongoing scour incision is restricted due to these morphodynamic feedback mechanisms.

In summary, these specific limiting boundary conditions that control local scour around boulders in the field have been insufficiently investigated via systematic laboratory studies, while integration between laboratory results on obstacle mark geometry with field evidence have been rarely carried out. Improved understanding of the geometry of obstacle marks is needed to (a) refine existing procedures to estimate the magnitude of past flood events (Herget *et al*., 2013), and (b) estimate the spatial extent of countermeasures for local scour protection at technical infrastructure. Consequently, the aims of the present contribution are:

(i) To analyse the processes of enlargement and the resulting geometry of evolving frontal scour holes at boulder-like obstructions under various hydraulic conditions via systematic laboratory flume study;

(ii) To evaluate local scouring at boulder-like obstructions in consideration of limiting boundary conditions of obstacle mobility and in the presence of a depth-limited alluvial layer via systematic laboratory flume study;

(iii) To investigate possible scale invariance and geometrical similitude of frontal scour holes by comparing laboratory results to in-situ obstacle marks at boulders in the Colorado River documented in a digital elevation model (DEM) derived from bathymetric mapping in Marble Canyon (Arizona), (Kaplinski *et al*., 2017a).

6.2 GEOMETRY OF OBSTACLE MARKS

The morphology (i.e. frontal scour hole and downstream sediment ridge) is characterised by certain morphometric variables, including scour hole depth at the obstacle front (d_s) measured from the undisturbed upstream bed; scour hole frontal length (l_s) in the plane of symmetry to the incoming flow, measured from the obstacle frontal face to the upstream edge of the scour hole, and scour hole frontal width (w_s) measured perpendicular to the direction of incoming flow form the lateral edges of the scour hole at the obstacle frontal face (Fig. 4). A corresponding definition can be applied to the sediment ridge, including sediment ridge height (h_r), sediment ridge width (w_r) and sediment ridge length (l_r) measured from the downstream end of the obstruction (Euler & Herget, 2012).

The applied engineering practice focusses on physical modelling to determine predictive equations for equilibrium d_s, defined as maximum depth of the frontal scour hole that is likely after prolonged exposure to steady flow. Equilibrium d_s is used as a design parameter for foundation depth (Simarro *et al*., 2011; Pizarro *et al*., 2020), or as proxy in risk assessment procedures (Tubaldi *et al*., 2017). The evolution of d_s is an asymptotical process in time (Kothyari *et al*., 1992; Oliveto & Hager, 2002, 2005; Lu *et al*., 2011; Mohammadpour *et al*., 2017). From laboratory data at clear-water conditions (flow velocity < threshold velocity for sediment mobilisation), it is well-established that 80% of equilibrium d_s is developed within only 5¬40% of the time to equilibrium that is obtained after several days, mainly depending on flow velocity and grain size (Melville & Chiew, 1999).

Although recent studies have examined the evolution of scour-hole geometry for different types of obstacles and sediment sizes, by utilizing a range of measurement methods (Link *et al*., 2008; Diab *et al*., 2010; Bouratsis *et al*., 2013; Sarkar *et al*., 2015; Bouratsis *et al*., 2017; Poggi & Kudryavtseva, 2019; Rogers *et al*., 2020), these studies have focused on d_s, while ignoring w_s and l_s. Nevertheless, there is general agreement that the geometry of frontal scour holes can be approximated as an inverted frustum cone with an elliptical shape in plan-view ($l_s < w_s$) (Mia & Nago, 2003), whereas the longitudinal shape (i.e. in flow direction) is quite symmetrical (Schalko *et al*., 2019b). However, considering a longitudinal profile from the obstacle frontal face to the upstream edge of the scour hole at equilibrium condition, different segments are distinguishable. These segments consist of: (1) a flat semi-circular scour hole bottom (S_b) that is closely attached to the obstacle base with radius < l_s, (2) an inner frontal

scour hole (lower slope) that is characterised by an inclination ≥ critical angle of repose (Φ_{crit}), and (3) an outer frontal scour hole (upper slope) that is characterised by an inclination ≤ Φ_{crit} (Fig. 6). The transition between both slopes is marked by a knickpoint (berm) in the cross-sectional profile.

6.3 MORPHODYNAMIC PROCESSES AT INSTREAM OBSTACLES

Obstacle marks originate from deformations of the approaching flow in the vicinity of the obstacle that result in the following processes: (1) contraction of streamlines lateral to the obstacle, causing higher flow velocities; (2) a vertical jet-like downflow towards the bed that emerges due to pressure gradient at the obstacle frontal face; (3) formation of a turbulent vortex structure at the obstacle base, resulting from the deflection of the downflow against main flow direction; because the vortex structure laterally wraps past the sides of the obstacle in the downstream direction it is commonly referred as horseshoe-vortex (abbreviated HV); and (4) a decelerated region of flow in the wake of the obstruction including a wake vortex system of detached shear layers with a vertical axis of rotation (Hunt *et al*., 1978; Dargahi, 1990; Shamloo *et al*., 2001; Pattenden *et al*., 2005; Escauriaza & Sotiropoulos, 2011a; Sumner, 2013; Bauri & Sarkar, 2016; Launay *et al*., 2017; Papanicolaou & Tsakiris, 2017; Schlömer *et al*., 2020), (Fig. 5 a).

Processes (1) to (3) amplify the bed shear stress above the critical bed shear for sediment mobilization, inducing local scouring in front and lateral to the obstacle in non-cohesive and cohesive sediment (Allen, 1982; Sonia Devi & Barbhuiya, 2017). The enlargement of the frontal scour hole and its geometry are closely related to the HV as the main driver of sediment mobilization (Dargahi, 1989; Radice *et al*., 2009; Radice & Tran, 2012; Li *et al*., 2018). The HV actually consists of several interacting and unsteady vortices (Kirkil *et al*., 2008; Kirkil & Constantinescu, 2010; Escauriaza & Sotiropoulos, 2011b; Chen *et al*., 2017). The largest and most stable vortex is denoted as the primary horseshoe vortex (HV1) and is located close to the obstacle base. During incision HV1 sinks into the frontal scour hole and extends down to S_b, where it promotes sediment mobilisation by saltation and rolling (Dargahi, 1990; Dey & Raikar, 2007; Chen *et al*., 2019). Upstream of HV1, a smaller and less coherent vortex (HV2) is located within the outer region of the frontal scour hole. HV2 can completely lose coherence, while HV1 exhibits aperiodic bimodal oscillations that cause changes in the position and shape of the vortex core from circular (zero-flow mode) and closely

aligned to the obstacle, to elliptical (back-flow mode), where the core is situated away from the obstacle (Paik *et al*., 2007; Kirkil & Constantinescu, 2015). In back flow mode, the vertical extent of HV1 coincides with the knickpoint in the slopes, differentiating the outer and inner frontal scour hole (Muzzammil & Gangadhariah, 2003; Unger & Hager, 2006). Although the rotation of the HV generally stabilises the lower slope at an angle greater than Φ_{crit} (Hoffmans, 1993), aforementioned temporal oscillations (HV1) and occasional disappearance (HV2) destabilize the slopes and result in collapse characterized by gravitational movements into S_b. In shallow flow (flow depth <<< channel width) and emergent conditions at the obstacle, a surface standing wave at the junction between the upstream frontal face of the obstacle and the free surface is formed (Boyer & Roy, 1991; Shamloo *et al*., 2001). This bow wave can affect HV1 as the vortices have opposite direction of rotation (Gazi & Afzal, 2020). With decreasing flow depth, the bow wave dominates and HV1 is less capable of entraining sediment (Melville & Coleman, 2000). Schlömer *et al*. (2020) have documented that the dimensions of the frontal scour hole are reduced if submergence ratio ≤ 0.55.

6.4 BOUNDARY CONDITIONS OF OBSTACLE MARK FORMATION

The formation of marks at natural obstacles is impacted by different extrinsic and intrinsic environmental boundary conditions that comprise (1) flow conditions, (2) sediment characteristics, (3) properties of the obstacle, and (4) time. Recently, Schlömer *et al*. (2020) have proposed a functional relationship of scale invariant parameters that control local scouring at solitary boulder-like obstructions located in a straight, moderately sloped channel and cohesionless alluvial sediment. The non-dimensional control parameters, derived upon principles of the Buckingham Π theorem (e.g. Barenblatt, 2012) result in an expression for local scour incision d_s/L_o as:

$$d_s/L_o = f\,(d_w/L_o,\ U_m/U_c,\ Re_o,\ L_o/B,\ Sh,\ Mb,\ L_o/D_{50},\ \sigma_G,\ d_{sed}/L_o,\ t/t_e)$$

(Eq. 22)

where d_w/L_o is the submergence ratio (d_w = flow depth [L] and L_o = effective obstacle size $h_o^{2/3}\ w_o^{1/3}$ [L], with h_o = obstacle height [L] and w_o = obstacle width [L], U_m/U_c is flow intensity (U_m = mean approach velocity [LT^{-1}] and U_c = critical mean approach velocity for entrainment of sediment [LT^{-1}]), Re_o is the obstacle Reynolds number (U_mL_o/ν, with ν= kinematic viscosity of water [L^2T^{-1}]), L_o/B is the blockage ratio (with B = channel width [L]), Sh [-] is an indicator for the hydrodynamic shape of the

obstacle, Mb [-] is an indicator for the mobility of boulder-like obstruction due to tilting into the local scour hole, L_o/D_{50} is the relative sediment coarseness (D_{50} = median diameter of the bed sediment [L]), σ_G is the sorting of sediment ($D_{84}/D_{16}^{1/2}$ [-]), d_{sed}/L_o is the relative thickness of the alluvial layer (d_{sed} = thickness of the alluvial layer in which the obstacle is embedded [L]), and t/t_e is the time scale of local scouring.
Each term in equation (22) is measurable or readily simulated with the current state-of-the-art technology for measuring or modelling three-dimensional flows and time-dependent riverbed elevation evolution.

6.5 OBSTACLE MARKS AT DIFFERENT SPATIAL SCALE

Field evidence of obstacle marks has been described for a range of conditions, including overland flow at rock fragments (Poesen *et al*., 1994; Jomaa *et al*., 2012) and around solitary boulders in flash floods in ephemeral streams (Karcz, 1972; Euler *et al*., 2017). Among the largest measured obstacle marks (dimensions up to 10^2 m) are those associated with large boulders and bedrock hills hypothesised to have formed during Quaternary megafloods (Baker & Bunker, 1985; Carling *et al*., 2002b; Herget, 2005). The dominant morphology is thereby consistent over a range of spatial scales. Contrary to the dominant morphology, local scour holes in the wake of boulders located in high-gradient step-pool streams (e.g. Comiti *et al*., 2005) and rock sills (e.g. Pagliara & Palermo, 2008, 2018) are reported. This plunge pool scour occurs as a result of an overtopping jet-stream motion that differs from the HV-induced morphodynamic processes.

Nevertheless, field measurements of frontal scour hole geometry are extremely limited. Although bridge pier scour is frequently monitored in the U.S, only d_s is considered among candidate morphometric variables (USGS National Bridge Scour Database; Mueller & Wagner, 2005). To the authors' knowledge there is only the study by Butch (1991, 1999) that has measured in-situ frontal scour hole geometry (d_s and w_s according to the definition in Fig. 4) at 128 bridge piers. The analysis of field measurements of d_s is complicated, owing to difficulty in connecting scour hole measurements with the formative flow conditions (e.g. Link *et al*., 2019; Pizarro *et al*., 2020), and exacerbated by uncertainty in the maturity of d_s at the time of measurement (Sheppard *et al*., 2014). In general, laboratory estimate of d_s tend to overestimate actual dimensions of d_s in the field (Johnson *et al*., 2015; Pizarro & Tubaldi, 2019).

6.6 MATERIAL AND METHODS

6.6.1 FACILITY FOR LABORATORY STUDIES

Physical modelling was conducted in a 5 m long, 0.32 m wide and 0.27 m deep straight, rectangular flume with fixed slope (0.003 m m^{-1}) entirely filled with a layer of uniform (σ_G < 1.3) sand with median grain diameter (D_{50} = 0.75 mm). Φ_{crit} of the sediment when dry is ~ 33° (Dey, 2014). Discharge (Q) was controlled by a recirculating pump, while flow depth (d_w) was adjusted by a tail-gate at the downstream end of the flume to enable pseudo-uniform flow within the working section of the flume (~ 270 cm downstream of the inlet), (Hager & Hutter, 1984). The water surface profile was measured using an ultrasonic distance meter (Mic +25, Microsonic®, accuracy ± 0.1 mm). The unscaled flume experiments are interpreted as a process-focused physical model (Baynes *et al*., 2018) that attempts to reproduce processes and resulting morphologies, but does not represent a specific natural prototype.

Two obstacles of identical size (L_o = 3 cm), but different shape (cube, Sh ≥ 0.8 and sphere, Sh ≤ 0.6) were used to mimic boulder-like obstructions (i.e. angular and rounded). The obstacles were placed in the working section of the flume in the plane of symmetry to minimize sidewall effects (Nezu & Nakagawa, 2017). Blockage ratio (L_o/B, with B = flume width) and relative sediment coarseness (L_o/D_{50}) were designed to satisfy critical thresholds for the onset of local scouring, i.e. L_o/D_{50} > 8 (Lee & Sturm, 2009), and L_o/B < 0.6 (Chou & Chao, 2000; Williams *et al*., 2019).

The flume was used for a total of 30 individual runs comprised of three different experimental configurations (Fig. 22 a).

In series A, the obstacles were mounted to the flume bottom such that the entire obstacle (L_o=3 cm) was above the initial bed (d_{sed} = 5.5 cm), and were exposed to 10 different hydraulic conditions by variations in d_w/L_o (0.67 to 4) and U_m/U_c (0.49 to 0.81). In series B, the obstacles were mounted to the flume bottom with L_o above the initial bed (d_{sed} = 2 cm) and exposed to hydraulic conditions of series A. In series C, the obstacles were loosely placed on the bed with L_o above the initial bed (d_{sed} = 5.5 cm), but the obstacles were free to move and were exposed to hydraulic conditions of series A and B.

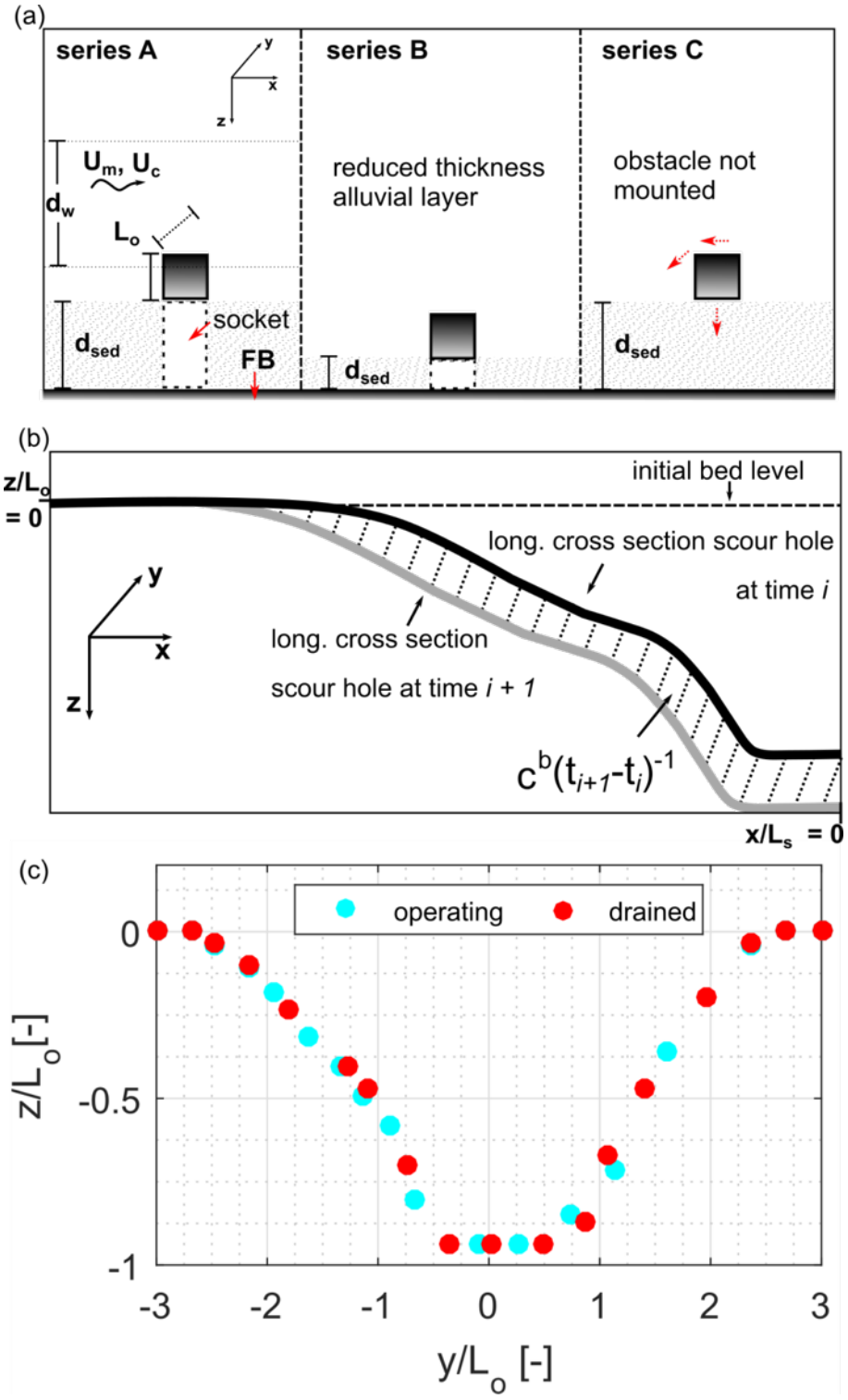


Figure 22. (a) Side view of experimental setups within the working section of the flume; FB = flume bottom. (b) Definition of subsequent cross-sections for the estimation of the sediment transport rate (q^b) exemplified for the upstream cross-section of the frontal scour hole in non-dimensional form. (c) Point measurements of upstream horizontal cross-section in non-dimensional form for run A6 displaying calibrated measurements while flume was operating (cyan) and drained (red).

6.6.2 WORKING HYPOTHESES FOR EXPERIMENTAL SERIES

By neglecting constant boundary conditions of the experiments ($L_o/B = 0.09$, $L_o/D_{50} = 40$, $\sigma_G < 1.3$) scour depth incision can be functionally formulated as:

$$d_s/L_o = f\,(d_w/L_o, U_m/U_c, Re_o, Sh, Mb, t/t_e)$$

(Eq. 23)

By assuming shape similitude of the local scour hole, non-dimensional scour depth (d_s/L_o) in equation 23 can be replaced by non-dimensional scour length (l_s/L_o) or non-dimensional scour width (w_s/L_o).

Furthermore, it is hypothesized that for given sediment size and obstacle size, l_s/L_o and w_s/L_o will scale with d_s/L_o, obstacle shape (Sh) and elapsed time of the experiments (t/t_e), and only indirectly with the actual flow conditions. The same hypothesis is required for the methodology proposed by Chreties *et al*. (2008). Each experiment lasted 5760 minutes, which for given U_m/U_c and L_o/D_{50} is 2 to 5-times larger than the estimated time scale to attain equilibrium d_s proposed by Melville and Chiew (1999). The long duration experiments were chosen, because no empirical values for equilibrium l_s and w_s are reported. Hence, t_e is interpreted as the absolute runtime of individual experiments.

The working hypothesis for series A is:

(A) The dimensions of l_s/L_o and w_s/L_o in time are dependent on d_s/L_o and essentially unaffected by flow conditions.

Therefore, equation (23) reduces to a form more amenable to empirical evaluation:

$$l_s/L_o, w_s/L_o = f\,(d_s/L_o, Sh, t/t_e)$$

(Eq. 24)

In series B experiments, frontal scour hole incision into a depth-limited alluvial layer was evaluated by reducing d_{sed} such that $d_{sed}/L_o < 1$ limits scour incision.

The working hypothesis for series B is:

(B) In the presence of a depth-limited alluvial layer, the time-evolution of d_s/L_o solely depends on d_{sed}/L_o.

Thus, equation (23) reduces to:

$$d_s/L_o = f\,(d_{sed}/L_o, Sh, t/t_e) \quad \text{(Eq. 25)}$$

The working hypothesis for series C is:

(C) Obstacle tilting into the frontal scour hole alters the process dynamics of scour incision in time and impacts the geometrical relations (i.e. d_s/l_s, d_s/w_s). Thus, equation (23) reduces to:

$$d_s/L_o,\ l_s/L_o, w_s/L_o = f\,(Mb,\ Sh,\ t/t_e) \quad \text{(Eq. 26)}$$

6.6.3 HYDRAULIC BOUNDARY CONDITIONS OF EXPERIMENTAL SERIES

Steady and sub-critical flow conditions at clear-water conditions ($U_m/U_c < 1$) were designed, by choosing different values of U_m (16.5, 20 and 24 cm/s) and different flow depths (2, 3, 6, and 12 cm) to mimic emergent ($d_w < L_o$) and full submerged conditions ($d_w >> L_o$) at the obstacles. For given D_{50} and different values of d_w, U_c was computed by a procedure given in Melville and Coleman (2000). The hydraulic boundary conditions of the experimental series are displayed in Table 5.

6.6.4 EXPERIMENTAL PROCEDURE

Dimensions of d_s, l_s, and w_s were measured with two LED-distance meters (Welotec® OWRB-series, accuracy ± 0.5 mm), measuring x- and y-coordinates in a local Cartesian coordinate system, with x = longitudinal, streamwise direction and y = horizontal, perpendicular to streamwise direction; and a laser distance meter (Baumer Electric® ODAM S14C, accuracy ± 1.5 mm) measuring the vertical coordinate (z). The sensors were mounted on a traversing system on top of the flume operating in x/y – plane. The elevation of the initial flat bed in front of the obstacle was used as reference (i.e. x0/y0/z0 = 0/0/0). For individual runs, measurements of d_s, l_s, w_s were sampled at t = 1, 2.5, 5, 7.5, 10, 12.5, 15, 17 and 20 min (with start of the experiment t = 0 min). Irrespective of time, the spatial extent of l_s and w_s was obvious and determined by $z_0 < 0$. For $t \leq 480$ min the measuring interval was relaxed to 10 min. For $t > 480$ min, measurements were randomly sampled, while for $t \geq 1000$ min, morphometric variables were measured only once in 1440 min up to the total runtime of experiments (= 5760 min).

The geometry of the frontal scour hole was measured by 2D cross-sectional profiles in the longitudinal (i.e. streamwise) and horizontal (i.e. perpendicular to streamwise) directions according to the definition in Fig.4 (dashed lines). Profiles were surveyed at t = 30, 60, 120, 240 and 480 min, while for t > 480 min profiles were

randomly sampled once in 1440 min. Measurements of morphometric variables and profiles are interpreted as quasi-dynamic observations, because they were measured while water was flowing (Rogers *et al*., 2020). A systematic error was present for measurements of the z-coordinate due to refraction of the laser beam within the water column. Therefore, a simple calibration (i.e. compensation for the travel time of light in water) was applied to the raw data. The compensation procedure yielded sufficiently accurate results when compared to measurements at drained condition with the same measurement system (Fig. 22 c). The test reproducibility was successfully evaluated for repetitions of runs A6, 9, 10, 16, and 17, producing an average standard error of d_s ~ 3%, l_s ~ 6% and w_s ~ 4%. Considering two consecutive frontal scour profiles the volumetric bed load transport rate (q^b [L^2T^{-1}]) out of the frontal scour in absence of sediment suspension was estimated by calculating the line integral (Fig. 22 b):

$$q^b (l_{sP} \text{ v } w_{sP}, t) \approx c^b / t(i+1) - t(i)$$

(Eq. 27)

with l_{sP} = longitudinal scour hole profile or w_{sP} = horizontal scour hole profile, c^b = depth-integrated frontal scour hole area, and i = 1, …N in which N is the total number of measured profiles in time.

For the subsequent analysis q^b in equation (27) is replaced by the dimensionless bed load q* [-]:

$$q^* = q^b/((\rho_s/\rho\text{-}1)\ gD_{50}^3)^{1/2}$$

(Eq. 28)

with ρ = water density [ML^{-3}] and ρ_s = sediment density [ML^{-3}]. For comparison, frontal scour hole profiles were scaled with the corresponding dimensions of d_s, l_s and w_s, in order to preserve collinearity of distances and angles (i.e. three or more points initially lying on a line still lie on a line after the transformation) (Tregnaghi *et al*., 2007).

Table 5. Non-dimensional hydraulic boundary conditions of all experimental series. C = Cube, S = Sphere. † $U_c = 5.75 \log (5.53\ d_w/D_{50})\ u_c*$, with $u_c* = 0.015+0.0125\ D_{50}^{1.4}$ ($0.1 < D_{50} < 1$mm).

Run	Type	d_w/L_o	U_m/U_c†	Fr
A1	C	0.67	0.67	0.37
A2	C	1	0.62	0.3
A3	C	2	0.55	0.22
A4	C	4	0.49	0.15
A5	C	0.67	0.81	0.45
A6	C	1	0.75	0.37
A7	C	2	0.66	0.26
A8	C	4	0.6	0.18
A9	C	2	0.79	0.31
A10	C	4	0.71	0.22
A11	S	0.67	0.67	0.37
A12	S	1	0.62	0.3
A13	S	2	0.55	0.22
A14	S	4	0.49	0.15
A15	S	0.67	0.81	0.45
A16	S	1	0.75	0.37
A17	S	2	0.66	0.26
A18	S	4	0.6	0.18
A19	S	2	0.79	0.31
A20	S	4	0.71	0.22
B1	C	4	0.6	0.18
B2	C	2	0.66	0.26
B3	C	1	0.75	0.37
B4	S	4	0.6	0.18
B5	S	2	0.66	0.26
B6	S	1	0.75	0.37
C1	C	2	0.66	0.26
C2	C	2	0.79	0.31
C3	S	2	0.66	0.26
C4	S	2	0.79	0.31

6.6.5 FIELD DATA

Field observations of obstacle marks at boulders were derived from a DEM of a 50-km segment of the Colorado River within Grand Canyon National Park (Fig. 23). The DEM is the result of a field survey in May 2009 in which bathymetric (mulitbeam and singlebeam sonar), topographic (ground-based total-station surveys), and grain size data were surveyed in order to monitor the status and trends of sediment storage along the Colorado River (Kaplinski *et al*., 2017a; Grams *et al*., 2019). Surveys were not

conducted in rapids and riffles (Kaplinski *et al*., 2017a), thus all obstacles and associated obstacle marks were submerged ($d_w > L_o$) during the survey. The DEM has a 1 m-resolution and is projected to Arizona Central Zone of the State Plane Coordinate System of 1983, while elevations are ellipsoid heights (i.e. relative to the NAD83 ellipse). Bed-sediment maps were constructed using the methods reported in Buscombe *et al*. (2014a, 2014b, 2017) at 0.25 m-resolution and classify sediment into the Wentworth classes of sand, gravel and undifferentiated cobble/boulder/bedrock. The study area is located in Lower Marble Canyon (Fig. 23) between river mile (RM) 30 and 61, which is the distance downstream from Lees Ferry, Arizona (RM 0) along a digitized channel centerline (Grams *et al*., 2019). The upstream extent of study area is located 75 km downstream from Glen Canyon Dam. The river flows in a bedrock-walled canyon with an average channel width of 100 m at low discharge (~ 225 m^3s^{-1}), except for segments where tributary debris fans constrict flow and create rapids (channel width < 30 m) (Grams *et al*., 2019). Downstream of the debris fans, lateral flow recirculation zones (eddies) form (channel width up to 150 m) (Hazel *et al*., 2006; Grams *et al*., 2013). The river bed is dominated by sand and gravel, and the Paria River (Fig. 23) is the primary source of fine sediments (Buscombe *et al*., 2017). River discharge is controlled by dam releases for hydroelectric power generation, which varies irregularly (monthly and seasonally) and regularly (a daily fluctuation with a constant period). During May 2009, the mean discharge at Lees Ferry was relatively low (~ 270 $m^3\ s^{-1}$) (Grams *et al*., 2013), and flow variability around the time of field measurements was likely minimal while the total sediment load was comparatively small at that time.

The DEM was processed using a GIS to measure dimensions of the obstacle (h_o, w_o) and the dimensions of d_s, l_s, w_s within the resolution of the DEM (i.e. ≥ 1 m). Profiles of the frontal scour hole (cf. Fig. 4) were drawn equivalent to the processing of the laboratory data. The profiles began at the lowest bed elevation at the obstacle frontal face, or at the lowest elevation at the lateral edges of the obstacle (i.e. d_s), and ended where the bed elevation does not longer increase with distance from the obstacle frontal face (Butch, 1999). The elevation of the surrounding bed was therefore considered to be z = 0. The profiles were scaled and post-processed to estimate local minima (i.e. d_s) and maxima (i.e. h_o and w_o).

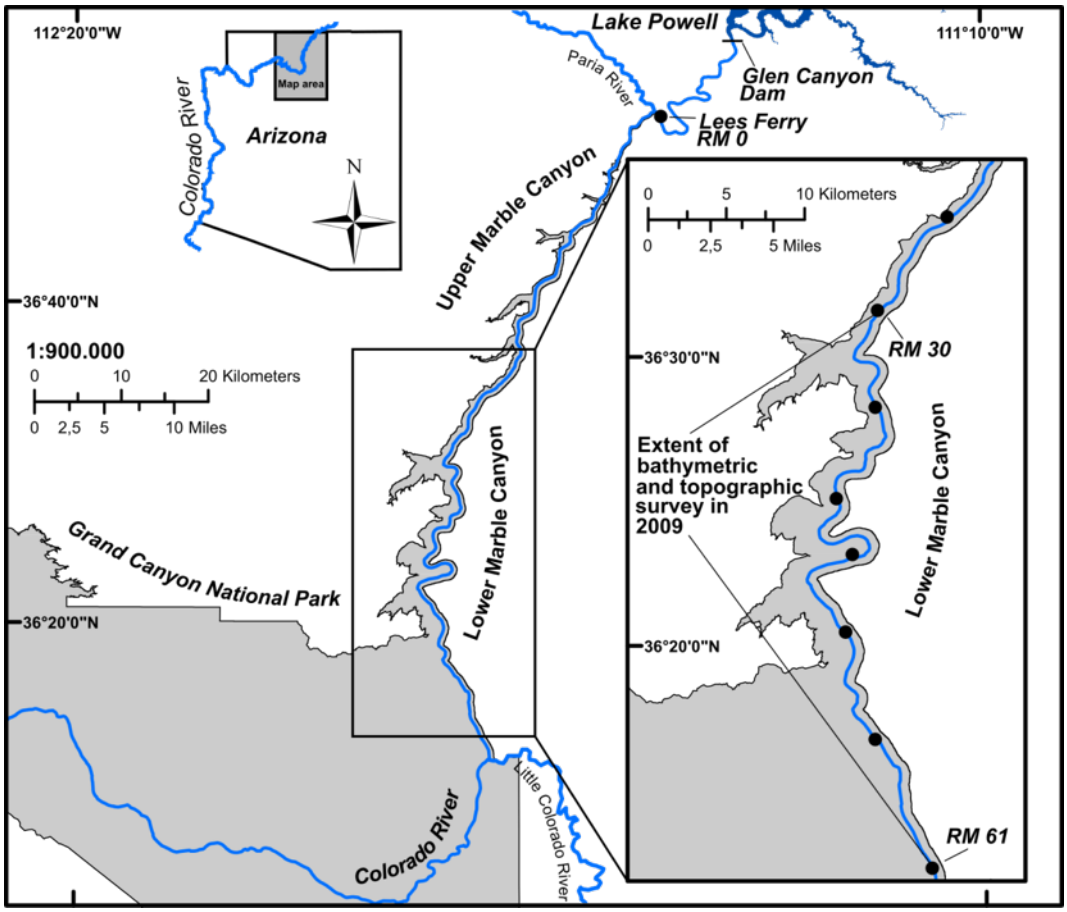


Figure 23. Map of Colorado River in the upstream portion of Grand Canyon National Park (shaded in grey) highlighting extent of bathymetric and topographic survey in lower Marble Canyon in 2009 (Kaplinski *et al*., 2017 a). Distance between black dots in the study segment is 5 river miles. GIS data is provided by the U.S. Geological Survey and the Grand Canyon Monitoring & Research Center (GCMRC), while illustration is inspired by Figure 1 published in Grams *et al*., (2019).

6.7 Results

6.7.1 Scour Hole evolution at laboratory scale

In runs A1 to A10, two small depressions developed immediately at the lateral edges of the obstruction and rapidly merged to form a frontal scour hole ($t/t_e \approx 0.0001 – 0.0004$). The eroded material was deposited downstream in the wake of the obstruction as a sediment ridge with orientation parallel to the flow direction, forming the typical obstacle mark morphology. Subsequently, the frontal scour hole deepened as well as lengthened and widened, while the sediment ridge flattened, widened and elongated in downstream direction. Irrespective of time, the scaled scour depth (d_s/L_o) was larger for shallow flow depth (i.e. $d_w/L_o = 0.76$ to 1) and maximized at $d_w/L_o = 1$ ($U_m/U_c = 0.75$, run A6) (Fig. 24). Compared to fully submerged flow (i.e. $d_w/L_o = 4$ and $U_m/U_c = 0.71$, run A10), d_s was on average 30% larger irrespective of experimental duration. For runs

with a spherical obstacle (A11 – A22), the typical obstacle mark morphology emerged only for run A16. Compared to run A6, d_s/L_o was on average 20% smaller, irrespective of experimental duration. For runs A11 – 14 a wake-scour morphology composed of two lateral scour holes downstream of the obstacle emerged, while a frontal scour hole was absent. For runs A15, 17, 18, 19, 20 the same wake-scour morphology emerged at the beginning of experimental runs. However, with ongoing duration the morphology changed slightly as a minor frontal scour hole emerged (approx. $t/t_e \sim 0.25 – 0.5$), after exceeding a critical threshold of d_s/L_o (~ 0.2).

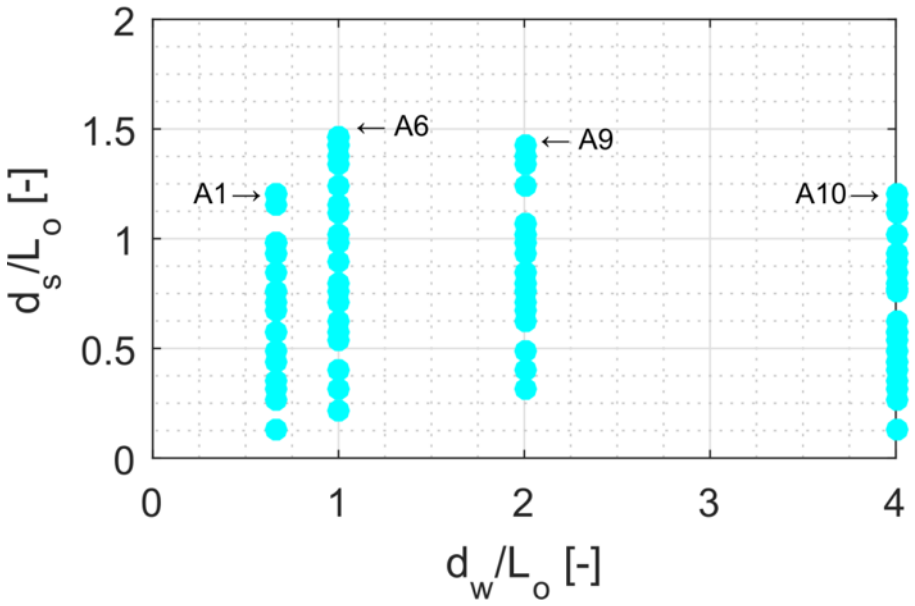


Figure 24. Scaled scour depth (d_s/L_o) against submergence ratio (d_w/L_o) irrespective of time exemplified for runs A1, A6, A9, and A10.

For runs A1-10, and A16, q* showed an asymptotical (limiting) behaviour in time (Fig. 25). Rapid incision and simultaneous enlargement of l_s and w_s occurred at the beginning (i.e. $t/t_e \leq 0.04$) that caused a high q*. However, q* significantly decreased for later stages of the experiments and could be approximated by power law relationships for (i) longitudinal profiles and (ii) horizontal profiles of the frontal scour hole:

(i) $q^*(l_{sP}) = 6.0^* 10^{-6} * t/t_e^{-4.4}$ (coefficient of determination $R^2 = 0.60$)
(Eq. 29)

(ii) $q^*(w_{sP}) = 8.2^* 10^{-7} * t/t_e^{-5.7}$ (coefficient of determination $R^2 = 0.72$) (Eq. 30)

It should be noted that $q^*(w_{sP})$ did not decrease to zero, because slight enlargement in width was detected even for late stages of the experiments (i.e. $t/t_e \geq 0.7$).

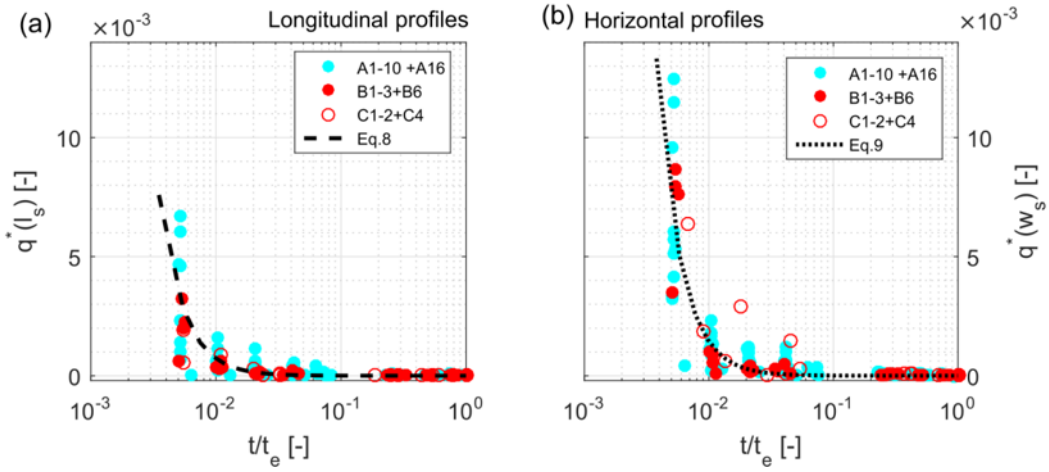


Figure 25. Scaled sediment transport rate over scaled time-scale of all experimental series estimated form (a) upstream longitudinal profiles of the frontal scour hole and (b) upstream horizontal profiles of the frontal scour hole.

6.7.2 INFLUENCE OF DEPTH-LIMITED ALLUVIAL LAYER

For series B, a typical obstacle mark pattern evolved for runs B1-3, and B6, while a wake scour morphology emerged for runs B4. Due to the depth-limited alluvial layer, d_s/L_o, l_s/L_o, and w_s/L were smaller compared to similar runs of series A. Equilibrium conditions of d_s were attained earlier in time (for $U_m//U_c \geq 0.75$ at $t/_{te} \sim 0.0005$ -0.0008, Fig. 26) as d_s reached the channel bottom. However, the enlargement of l_s and w_s continued (Fig.25 and Fig. 26). An ANCOVA test (F-value = 0.67- 0.69, p-value = 0.50 – 0.52) revealed that q* over t/t_e for runs B1-3 and B6 were not significantly different from that predicted by Equations 29 and 30. The dimensions of l_s/L_o and w_s/L_o were on average 30 – 40% larger for the angular obstacle (Sh ≥ 0.8) compared to the spherical obstacle (Sh ≥ 0.6).

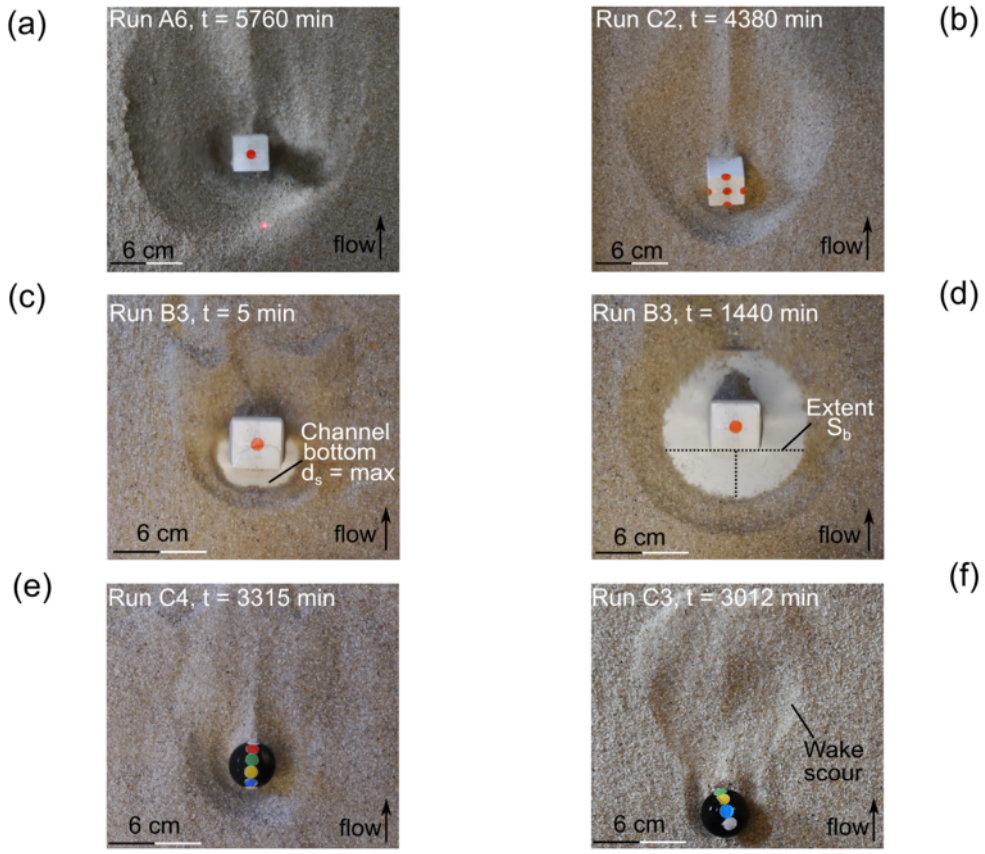


Figure 26. Plan view of frontal scour holes modelled at different stages of evolution and different experimental setups. (a) Frontal scour hole at a mounted cube (b) Frontal scour hole at a moveable cube partially buried in the frontal scour hole and tilted into upstream direction. (c) Frontal scour hole at an alluvial layer of reduced thickness after 5 min runtime indicating that scour incision reached flume bottom and (d) after 1440 min indicating ongoing enlargement of frontal scour hole in length, width as well as in the extent of scour hole bottom. (e) Frontal scour hole at a moveable sphere partially buried in the frontal scour hole and tilted into upstream direction. (f) Wake scour at a moveable sphere.

6.7.3 INFLUENCE OF OBSTACLE MOBILITY

For series C, the typical obstacle mark pattern emerged for runs C1-2 (Fig. 26 b), and C4 (Fig. 26 e), while the wake scour morphology evolved for run C3 (Fig. 26 f). For run C1-2, the scour incision undermined the obstacle and induced movement of the obstacle at $d_s/L_o \sim 0.2$ with respect to the regularly shaped obstacles used within this study. The movement was characterised by (i) upstream tilting of the obstacle relative to its origin position (i.e. x_0) against the direction of flow and (ii) self-burial of the obstacle (i.e. reduction of h_o relative to h_o at $t/t_e = 0$) (Fig. 8 a and b). Both processes show step-wise and asymptotical behaviour in time with rapid activity for $t/t_e < \sim 0.2$ irrespective of Sh (Fig. 27 c). Processes (i) and (ii) altered the obstacle's exposure to flow due to inclination of the obstacle's frontal face into the upstream direction (~ 20°), and by

reducing the height of the obstacle protruding into flow. Both processes significantly decelerated frontal scour hole incision in time and reduced d_s/L_o by 15 – 20% on average compared to series A runs. q* over t/t_e was not significantly different from equations 29 and 10 (Fig. 25) as l_s/L_o and w_s/L_o enlarged further in time.

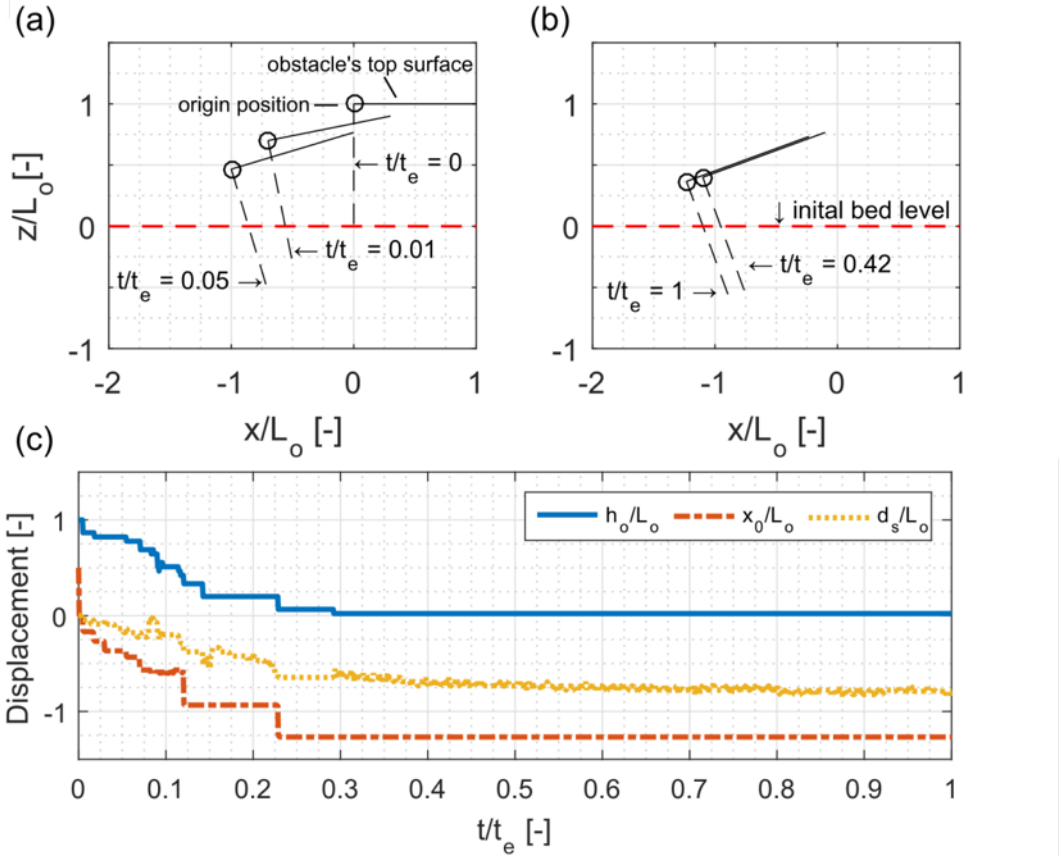


Figure 27. Movement (self-burial and upstream tilting) at a cuboid obstacle (run C1) for (a) initial phase of experiments ($t/te \leq 0.05$) and (b) for final phase of experiments ($t/t_e \geq 0.42$). (c) Trajectory of non-dimensional obstacle movement and scour depth evolution over non-dimensional time observed at run C4 (spherical obstacle).

6.7.4 OBSTACLE MARKS AT FIELD SCALE

In total, 90 obstacle marks were identified along the study at boulders embedded in sand. A total of 83% of the boulders were located close to the channel banks and varied considerably in size relative to the ambient bed elevation (median h_o= 1 m, range h_o = 7 m; median w_o = 5 m, range w_o = 13 m). The boulder shapes ranged from quasi-rectangular to round. It should be noted that no significant inclination of the obstacle's frontal face against upstream direction could be detected, while the comparable low height of the obstacles in relation to the ambient streambed elevation suggests that

obstacles were on the point of self-burial. Of the 90 obstacles, 89 obstacle marks were characterised by a clear definable frontal scour hole (i.e. typical obstacle mark pattern). However, it was challenging to determine the extent of the sediment ridge, mainly due to the presence of dunes in some segments of the study reach. For 92% of the identified frontal scour holes, an armour layer consisting of coarser sediment (i.e. gravel) in relation to the surrounding bed was present in the S_b. The frontal scour holes were shallow compared to their l_s and w_s (Fig. 28, statistical properties provided in Table 6). Compared to absolute values of d_s, l_s, and w_s for runs A1-10, and 16 frontal scour hole dimensions are 50 to 100 times larger. Although frontal scour holes at field scale were not as evenly developed as in the laboratory, shape similitude across spatial scales is obvious (Fig. 26). Remarkably one wake-scour pattern with only a minor frontal scour hole could be detected, similar to laboratory observations at a spherical obstacle (Fig. 29 b and Fig. 26 f). Besides these two morphologies, no different spatial patterns of obstacle marks could be detected in the study section

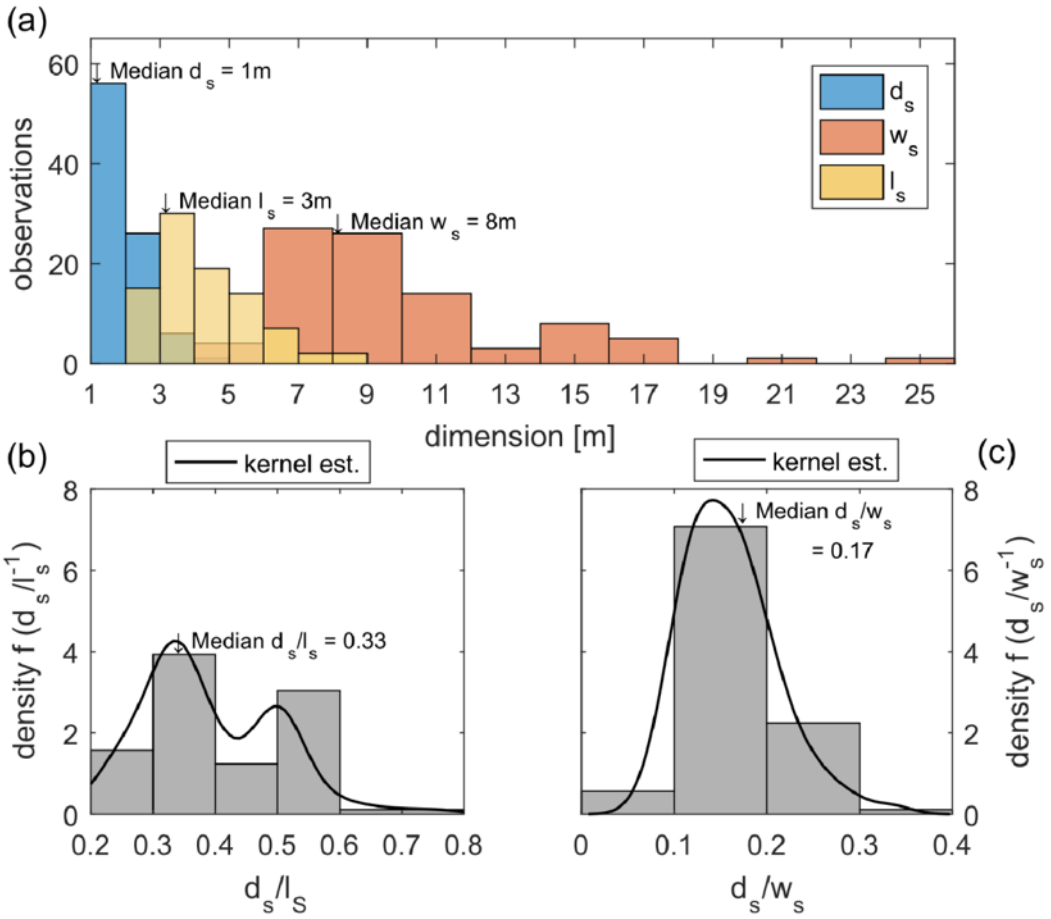


Figure 28. (a) Histogram of absolute scour hole dimensions (d_s, l_s, w_s) at field evidence. (b) Histogram of morphometric relation (d_s/l_s) including kernel density estimation. (c) Histogram of morphometric relation (d_s/w_s) including kernel density estimation.

Table 6. Statistical properties of absolute values of morphometric variables at field evidence (n = 89). IQR = interquartile range, MAD = median absolute deviation.

Parameter	Median	Mean	IQR	MAD
d_s [m]	1	1.47	1	0.59
l_s [m]	3	3.80	2	1.16
w_s [m]	8	9.35	4	2.73

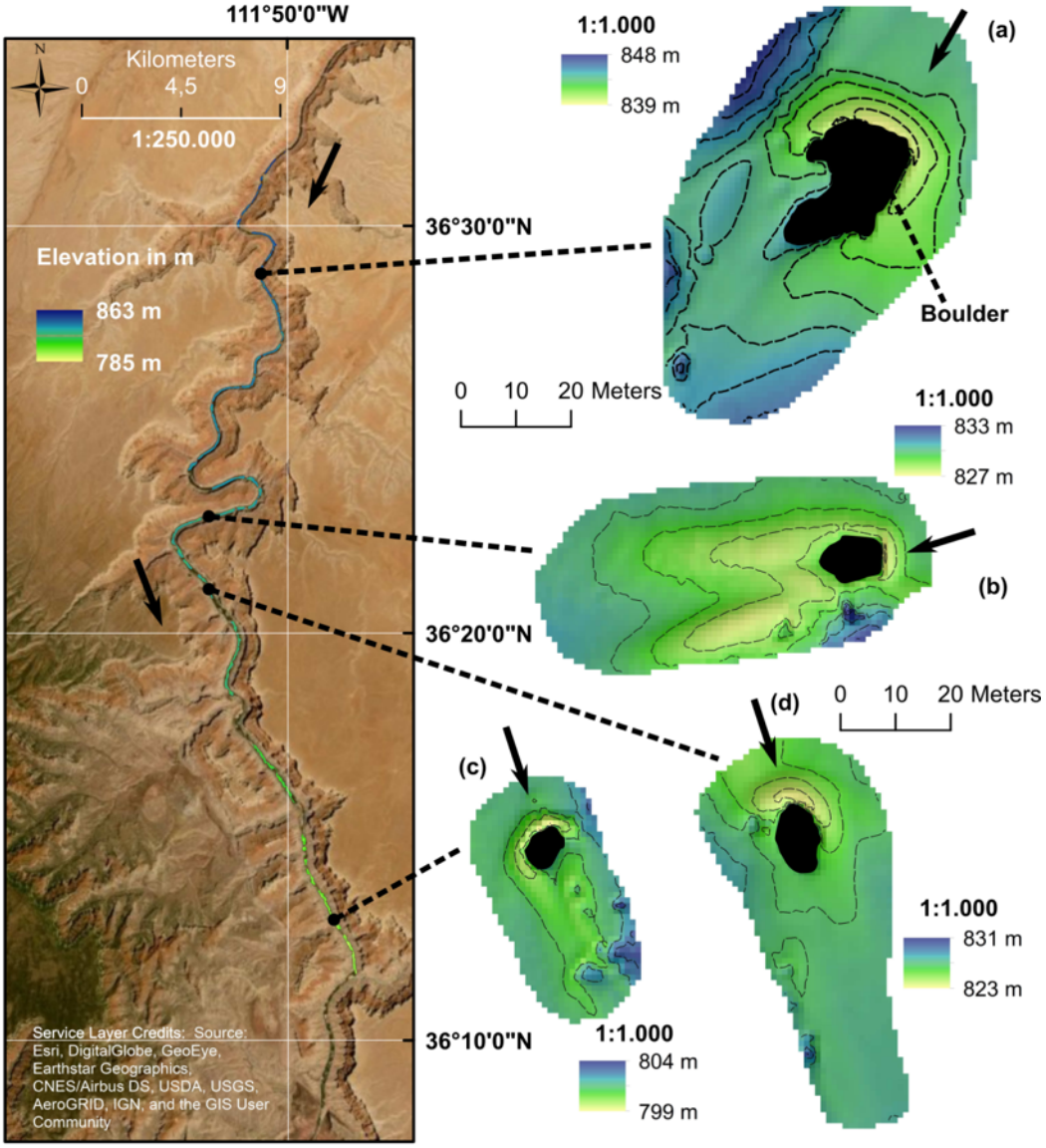


Figure 29. Examples of obstacle mark morphologies at boulders of different size identified within the study area. (a), (c), and (d) represent typical obstacle mark morphologies, while (b) depicts a wake scour pattern. Isoline-interval is 1 m and arrows indicate direction of flow. Boulders are highlighted in black.

6.7.5 Frontal scour hole geometry

Series A showed that the actual size of d_s/L_o in t/t_e depends on d_w/L_o and U_m/U_c. However, neglecting U_m/U_c, d_w/L_o, and t/t_e a monotonic increase and co-variation of l_s/L_o and w_s/L_o with increasing d_s/L_o is obvious (Fig. 30 a and b, Table 7). A co-variation of l_s/L_o and w_s/L_o with increasing d_s/L_o is also evident for the field data, although there is a larger range of boulder sizes (L_o) compared to the experimental series. L_o particularly controls the size of the frontal scour hole which is also present for the field data (Fig. 30 g and h). However, the estimated ß1 of the relationships l_s/L_o and

w_s/L_o on d_s/L_o (Table 7), indicate long and wide frontal scour holes that are relatively shallow. The same applies to series B and series C. For series B, d_s/L_o solely depended on d_{sed}/L_o, while frontal scour holes were wider and longer in relation to their shallow depth and a considerable deviation of l_s/L_o and w_s/L_o on d_s/L_o for $t/t_e = 1$ existed (Fig. 30 c and d). For series C, obstacle tilting and self-burial caused smaller values of d_s, l_s, and w_s compared to series A (Fig. 30 e and f).

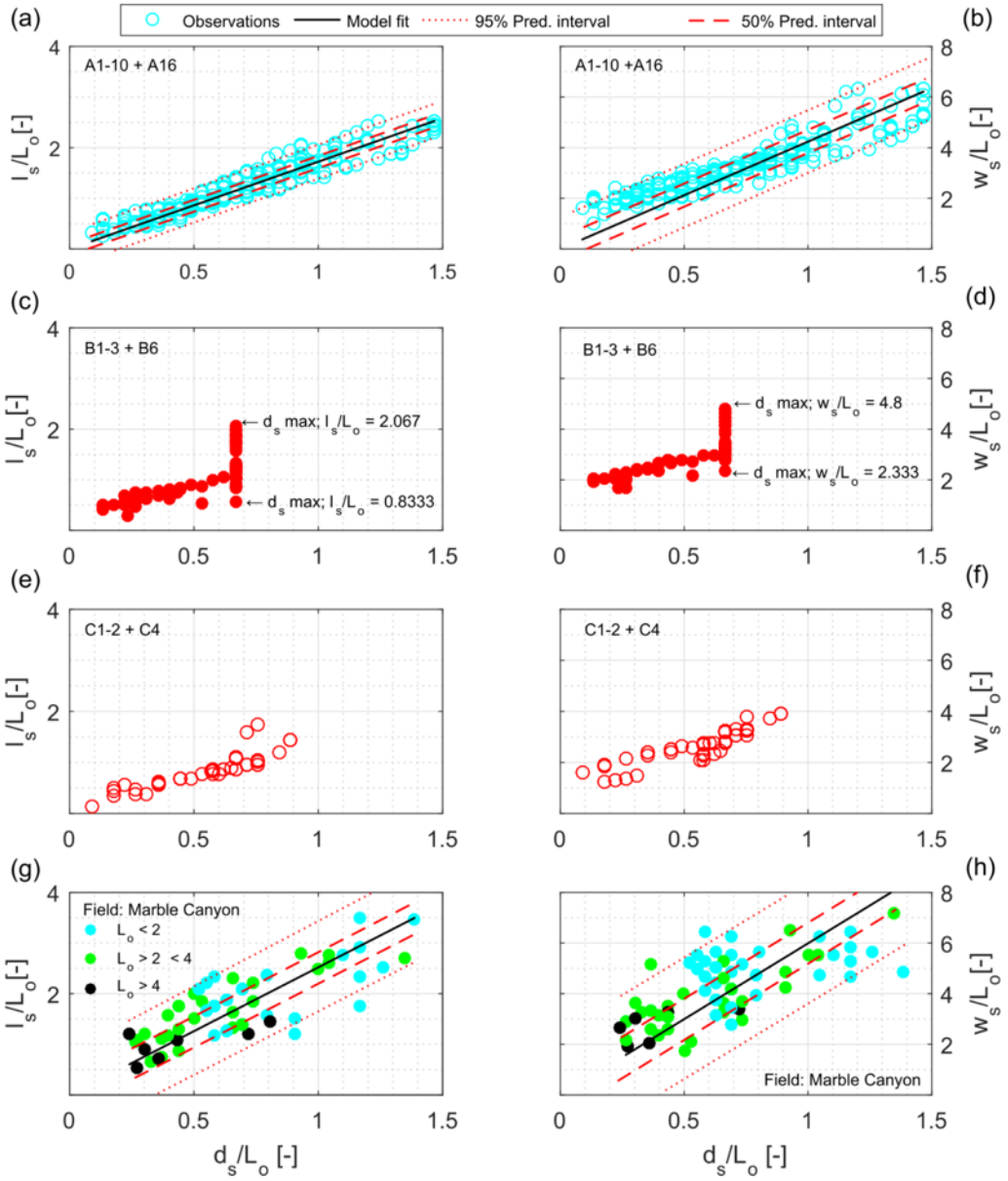


Figure 30. Linear relationships of non- dimensional morphometric variables of the frontal scour hole. (a) l_s/L_o against d_s/L_o for series A, slope (ß1) of the relationship is depicted in Table 7. (b) w_s/L_o against d_s/L_o for series A, slope (ß1) of the relationship is depicted in Table 7. (c) l_s/L_o against d_s/L_o for series B. (d) w_s/L_o against d_s/L_o for series B. (e) l_s/L_o against d_s/L_o for series C. (f) w_s/L_o against d_s/L_o for series C. (g) l_s/L_o against d_s/L_o for field evidence, slope (ß1) of the relationship is depicted in Table 7. (h) w_s/L_o against d_s/L_o for field evidence, slope (ß1) of the relationship is depicted in Table 7.

Table 7. Statistical properties of linear regression (y = ß1 x) for laboratory (n = 231) and field results (n = 89) on non-dimensional morphometric variables. ‡ bootstrapped estimates.

Model fit	R^2	$ß_1$	95% confidence interval for $ß_1$	RMSE of model fit
$l_s/L_o = ß_1 d_s/L_o$ (for Series A)	0.93	1.72‡	1.70, 1.75	0.17
$l_s/L_o = ß_1 d_s/L_o$ (for field evidence)	0.69	2.52‡	2.39, 2.65	0.44
$w_s/L_o = ß_1 d_s/L_o$ (for Series A)	0.85	4.24‡	4.14, 4.34	0.63
$w_s/L_o = ß_1 d_s/L_o$ (for field evidence)	0.63	5.99‡	5.63, 6.35	1.22

6.7.6 SIMILITUDE OF FRONTAL SCOUR HOLE GEOMETRY

For series A, the scaled profiles of the frontal scour collapsed into a narrow band, irrespective of hydraulic conditions and time (Fig.31 a and b). Superimposed profiles were also present for series B and C experiments, irrespective of hydraulic conditions and time (Fig. 31 c-f). However, for series B experiments the scour bottom (S_b) was significantly wider compared to results of series A results, while for series C experiments S_b could not be detected due to the tilting of the obstacles.

For the field evidence, scaled profiles of the frontal scour holes do not properly collapse in a common form (Fig. 31 g and h) as considerable differences in slope inclination were present. However, for the 89 frontal scour holes the median inclination of the longitudinal scour slope was 23°, and 75% of the slopes were less than 28°. The median inclination of the horizontal scour slope was 18°, and 75% of the slopes were less than 24° (Fig. 31 i). Unfortunately, no differentiation between upper and lower slope could be made based on the derived profiles.

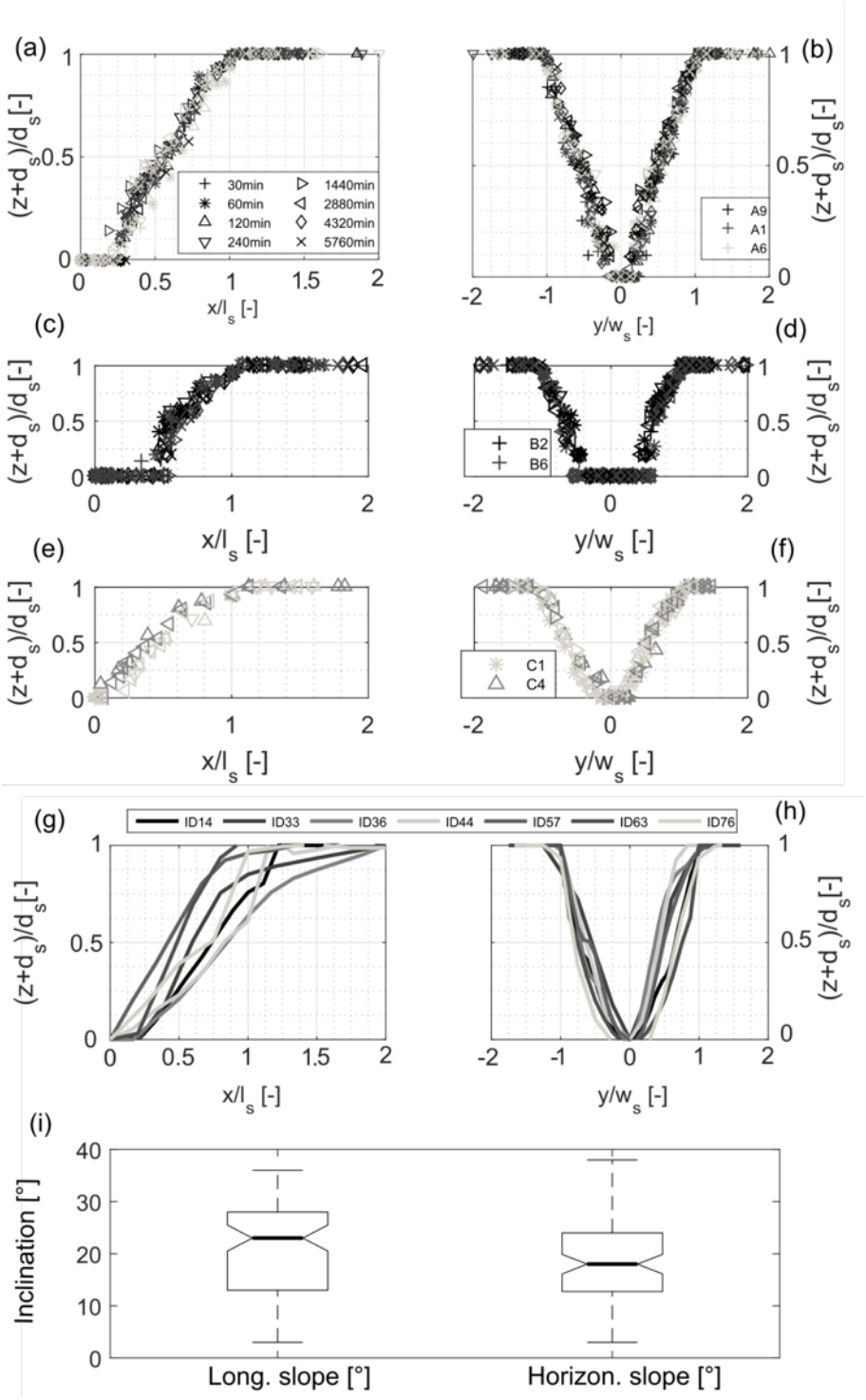


Figure 31. (a) Scaled longitudinal frontal scour hole profiles exemplified for runs A1, A6, and A9 at indicated times (a), runs B2 and B6 (c), and runs C1 and C4 (e). Scaled horizontal frontal scour hole profiles of runs A1, A6, and A9 (b), runs B2 and B6 (d), and runs C1 and C4 (f). (g) Scaled longitudinal frontal scour hole profiles at boulders of different size. (h) Scaled horizontal frontal scour hole profiles at boulders of different size. (i) Inclination of longitudinal and horizontal scour hole slopes for all field evidence (n = 89).

6.7.7 GEOMETRICAL RELATIONS IN TIME AT LABORATORY SCALE

Geometrical relations (i.e. d_s/l_s and d_s/w_s) were not constant over time and show a piecewise linear pattern that is composed of a systematic increase in d_s/l_s and d_s/w_s for $t/t_e < 0.04$, followed by a decreasing tendency for $t/t_e \geq 0.04$ (Fig. 32). For series B experiments, d_s/l_s and d_s/w_s were on average 19-23% smaller compared to runs A1-10, and A16, but showed the same piecewise linear pattern plotted against $\log_{10}(t/t_e)$, while for series C obstacle tilting in the upstream direction caused a relocation of the frontal scour hole, producing relative high values of d_s/l_s for $t/t_e < 0.04$ as the size of l_s was then comparable to d_s.To account for the time-series character of the dataset and in order to achieve stationarity as requirement for statistical modelling, d_s/l_s and d_s/w_s of series A, B, and C was de-trended by subtracting the mean. Upon application of bootstrapped regression (Davison & Hinkley, 2009) on the de-trended data, three different slope coefficients ß1 on d_s/l_s and d_s/w_s over log (t/t_e) were estimated (solid lines in Fig. 32):

(i) $t/t_e \leq 0.002 – 0.003$ rapid incision (ß1 for $d_s/l_s = 0.17$; ß1 for $d_s/w_s = 0.09$);

(ii) $0.003 < t/t_e < 0.04$ decreasing rate of incision (ß1 for $d_s/l_s = 0.01$; ß1 for $d_s/w_s = 0.05$);

(iii) $t/t_e \geq 0.04$ a significant break-point is present, for which the frontal scour hole deepening ceases, while slight widening occurs (ß1 for $d_s/l_s = -0.01$; ß1 for $d_s/w_s = -0.03$).

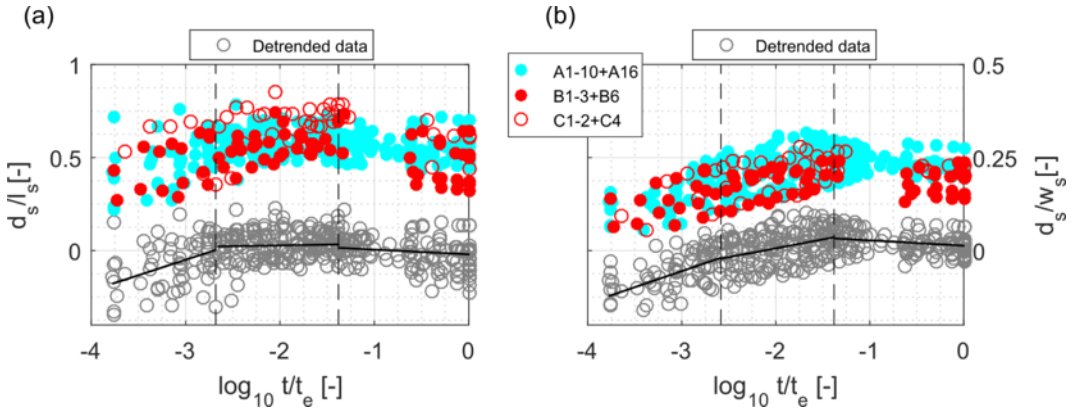


Figure 32. Geometrical relations of the frontal scour hole over non-dimensional time in $\log_{10}$-scale for all experimental series (a) d_s/l_s and (b) d_s/w_s.

6.8 INTERPRETATION OF LABORATORY RESULTS AND FIELD EVIDENCE

6.8.1 PROCESS DYNAMICS OF SCOUR HOLE ENLARGEMENT

The deepening and sediment mobilisation within the inner frontal scour hole caused an expansion of S_b/L_o with t/t_e and d_s/L_o (Fig. 33 a and b). The sediment loss in the inner scour hole destabilised the upper longitudinal frontal scour hole slope and caused intermittent gravitational movements in time. Considering all experimental series, the inclination (Φ) of the upper longitudinal frontal scour hole slope showed a decreasing tendency with $\Phi > \Phi_{crit}$ for $t/t_e < 0.04$ and $\Phi \leq \Phi_{crit}$ for $t/t_e \geq 0.04$ (Fig. 33 c), while Φ of the lower slope was by tendency $> \Phi_{crit}$ irrespective of time and experimental series (Fig. 33 e). Although a decreasing tendency of Φ with time is also present for the upper horizontal frontal scour hole slope (Fig. 33 d). The Φ of the lower slope remained considerable steep over experimental duration (Fig. 33 f).

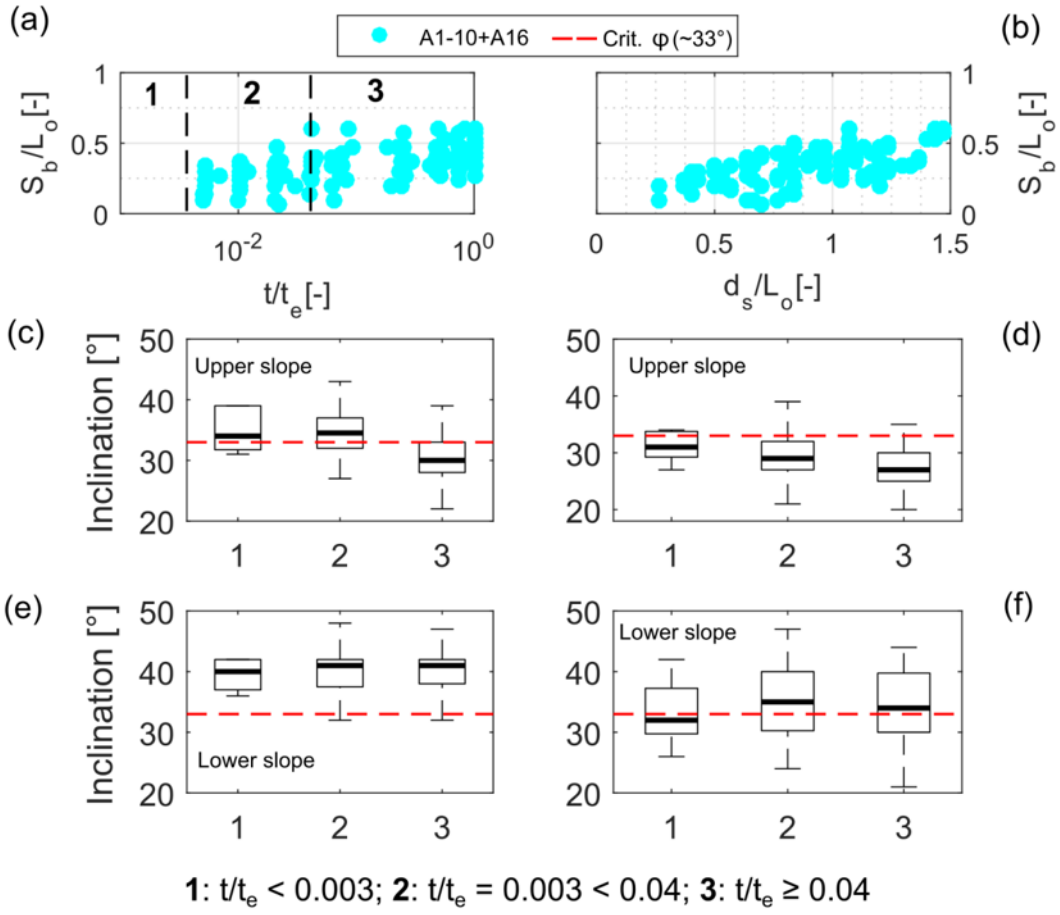


Figure 33. (a) Scaled scour bottom against non-dimensional time (1: $t/t_e < 0.003$; 2: = 0.003 < 0.04; 3: ≥ 0.04. (b) Scaled scour bottom against scaled scour depth. (c) Inclination of upper slope segment (n= 174) of the frontal scour hole estimated from longitudinal profiles grouped by non-dimensional time (1: $t/t_e <$ 0.003; 2: = 0.003 < 0.04; 3: ≥ 0.04). (d) From horizontal scour hole profiles (n=176). (e) Inclination of lower slope segment (n=157) of the frontal scour hole estimated from longitudinal profiles grouped by non-dimensional time. (f) From horizontal profiles (n=109).

6.8.2 QUANTITATIVE MODELS OF ENLARGEMENT

Two mechanistic models are proposed to assess the enlargement of l_s and w_s based on (i) d_s, (ii) cotangent of upper slope inclination ($\tan^{-1}(\Phi)$), and (iii) the span of the scour hole bottom (S_b). The models were constructed upon the log-transformed data of all experimental series and the field evidence using bootstrapped regression for insensitivity to outliers (Fig. 34 a for l_s and Fig. 35 c for w_s and Table 8 for statistical properties). Accordingly, l_s can be estimated by:

$$\log_1(l_s) = 0.88\log_{10}(d_s\cot\Phi + S_b) \quad \text{(Eq. 31)}$$

The analysis of w_s in regard to (i), (ii), and (iii) is complemented by a constant, resulting from the relationship of l_s to w_s, indicating that w_s is approximately 2.4 times l_s (Fig. 35 a and b). However, for a conservative approximation of w_s, the constant 2 is used:

$$\log_{10}(w_s) = 1.32\log_{10}(2d_s\cot \Phi+S_b) \quad \text{(Eq. 32)}$$

Equations 31 and 32 show reasonable agreement in comparison to observations on l_s and w_s for experimental data and field evidence (Fig. 34 b and Fig. 35 d).

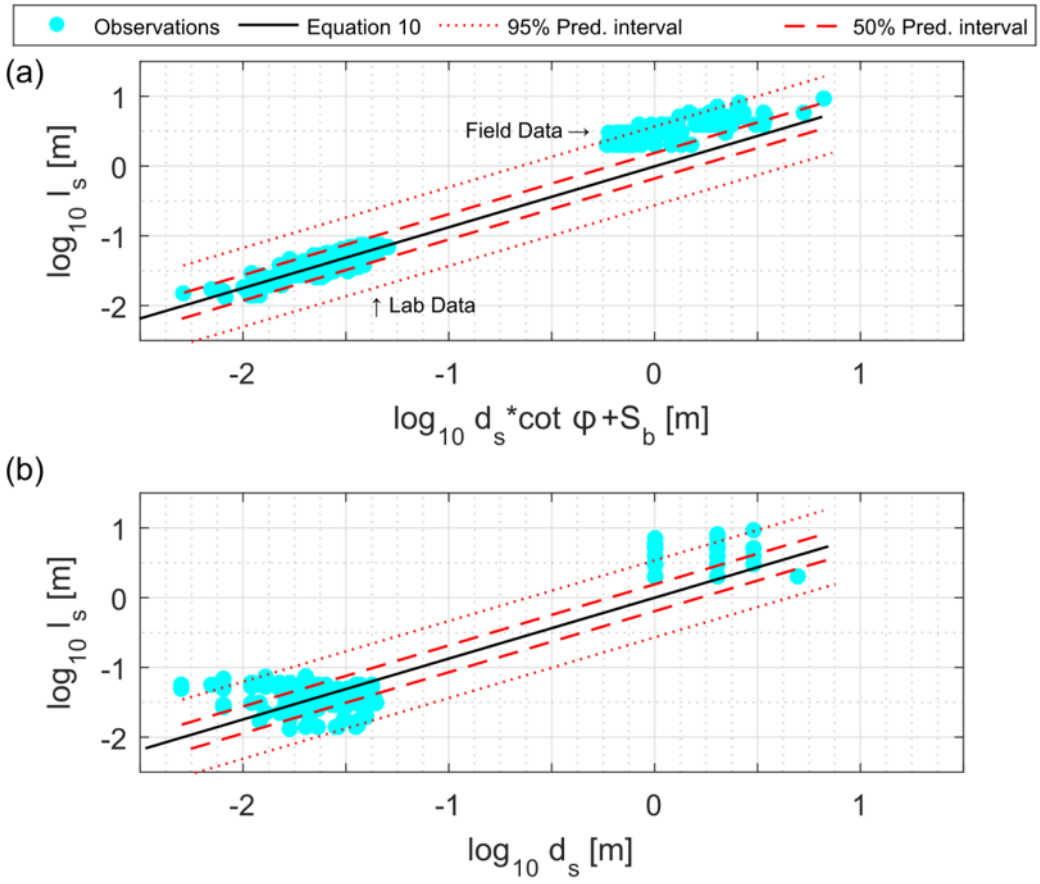


Figure 34. (a) Log-transformed l_s of laboratory data and field evidence against log-transformed model values. (b) Log-transformed l_s against log-transformed d_s for laboratory data and field evidence.

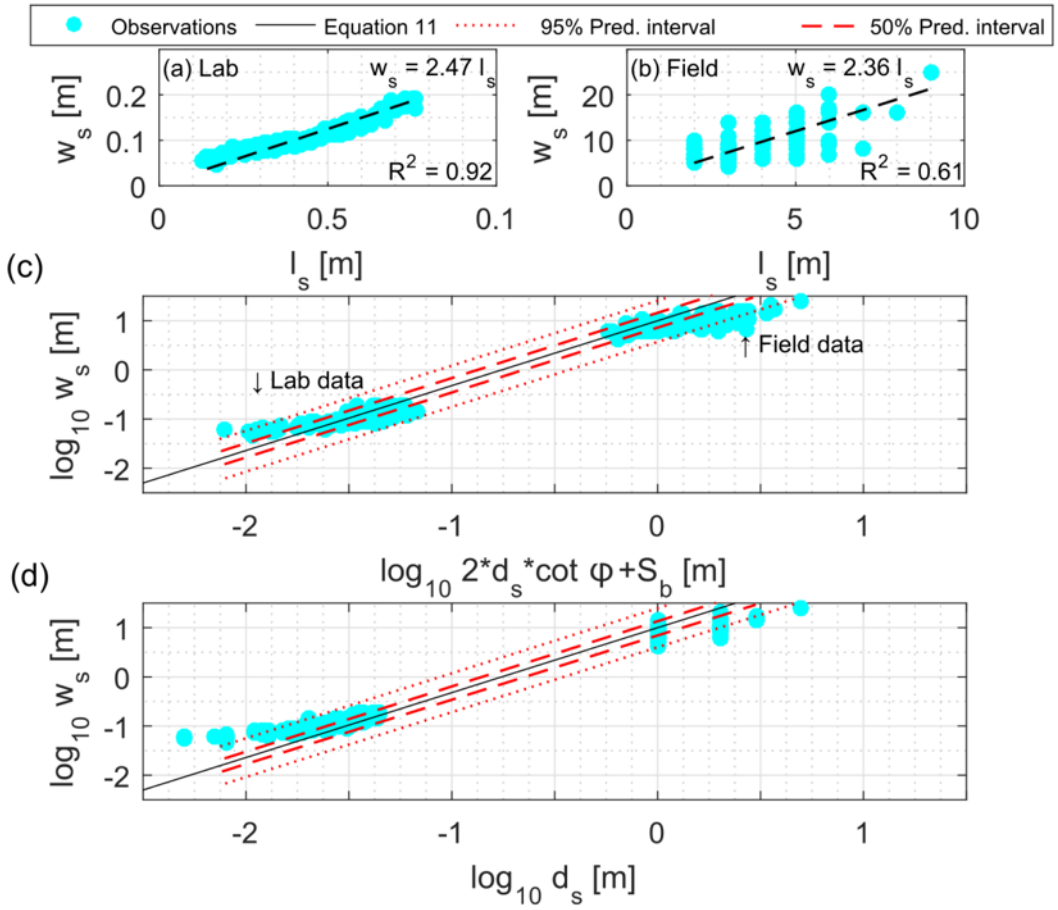


Figure 35. Linear relationships of l_s against w_s for (a) laboratory data and (b) for field evidence. (c) Log-transformed w_s of laboratory data and field evidence against log-transformed model values. (d) Log-transformed w_s against log-transformed d_s for laboratory data and field evidence.

Table 8. Statistical properties of model fits (linear regressions ($y = ß_1 x$)) on-dimensional morphometric variables (n = 320).

Model fit	R^2	ß1	95% confidence interval for ß1	RMSE of model fit
$\log_{10}(l_s)$	0.88	0.88	(0.85, 0.90)	0.284
$\log_{10}(w_s)$	0.95	1.32	(1.30, 1.34)	0.2042

6.9 Discussion of laboratory results and field evidence

Our findings can be interpreted in light of the experimental hydraulic data presented by Schlömer *et al*. (2020), who have attributed the maximisation of d_s/L_o at d_w/L_o = to a high vertical pressure gradient at the obstacle front that creates an intense downflow and efficient HV-system. During scour incision HV1 and HV2 subside into the frontal scour hole where HV1 expands in diameter, indicated by an expansion of S_b/L_o with t/t_e and d_s/L_o. Due to the expansion in diameter, the shear stress beneath the vortex decreases and equilibrium of incision is approached (cf. Kothyari *et al*., 1992).

Thus, hydraulic processes and morphology are connected in time and characterised by feedback-loops that indicate a self-organizing behaviour (Coco & Murray, 2007), while S_b/L_o can be interpreted as proxy for the size of HV1. The enlargement of l_s/L_o and w_s/L_o is directly coupled to d_s/L_o as the scour incision undermines the scour hole slopes and induce gravitational movements. The lower slope is governed by the rotation of HV1 and by tendency stabilized at $\Phi > \Phi_{crit}$, while the upper slope adjusts to the angle of repose by gravitational movements, indicating a positive feedback-loop between scour incision and enlargement in l_s/L_o. Furthermore, the enlargement of w_s can be attributed to the convection of detached shear layers from the legs of the HV1 at the lateral sides of the obstacle that result in strong amplification of shear stress at the bed as shown by Kirkil *et al*. (2008) and Kirkil and Constantinescu (2010). Thus, experimental results support working hypothesis (A), while similar observations are reported by Bateman *et al*. (2006), Chreties *et al*. (2008) and Chreties *et al*. (2013) for the geometry of frontal scour holes at emergent bridge piers.

The observed wake-scouring has to be attributed to recirculation of approaching flow and turbulence-induced high shear stress in the near-wake, while the rounded shape of the obstacle inhibits significant downflow at the obstacle frontal face and causes a small HV. As described by Schlömer *et al*. (2020) the wake scouring occurs at round-shaped obstacles only at high submergence (i.e. $d_w/L_o > 1.6$). Remarkably, the wake scouring pattern was also observed for the field evidence and it is supposed that the same hydraulic processes were responsible. For the field evidence, the wider scatter of of l_s/L_o and w_s/L_o for a given d_s, indicates indicate long and wide frontal scour holes that are relatively shallow, which is in agreement to Butch (1991, 1999) who reported w_s to be 4.7 times d_s based on measurements of frontal scour holes at bridge piers. The sensitivity of d_s was confirmed by series B and C, indicating that scour depth incision (i) depended on the thickness of the alluvial layer, supporting working hypothesis (B), and (ii) was damped by obstacle tilting and self-burial, supporting working hypothesis (C).

The assumption of a depth-limited alluvial layer ($d_{sed}/L_o \leq 1$) for the field data is reasonable based on indication given by Hazel *et al*. (2006), who reported an average sediment thickness in the main channel is ~ 1 m (supported by unpublished 2016 measurements of sand thicknesses using sub-bottom profiling sonar). Hence, the mean value of d_s (i.e. 1 m) can be interpreted as conservative estimate for the thickness of the alluvial layer in Marble Canyon at the time of survey, while $d_{sed}/L_o \leq 1$ suggests being a plausible explanation for the comparable shallow frontal scour holes. However,

fluctuations of the sediment thickness are known, primarily induced by sediment input from tributaries that is subsequently redistributed during controlled floods (Grams *et al*., 2019). Thus, general bedload sediment mobilisation ($U_m/U_c > 1$) occurs at least intermittently if not under most flows, indicated by the presence of near-ubiquitous dunes and the low-stage bedform migration measurements reported by Leary and Buscombe (2020) in a similar downstream reach. Consequently, regular sediment transport into the frontal scour hole results in partial filling and reduction in d_s (Hong *et al*., 2017). Moreover, the armour layer that was detected in 92% of the frontal scour holes prevents further scour incision similar to the physical effects of $d_{sed}/L_o < 1$.

6.9.1 SHORTCOMINGS IN COMPARING FIELD EVIDENCE AND LABORATORY RESULTS

The frontal scour holes observed in the field must be treated as "snapshots" in time that emerged during unsteady hydraulics, while information on these hydraulic boundary conditions and time scale of the scouring is unknown. However, even though laboratory studies were conducted at reduced complexity, the scale-invariance of frontal scour hole geometry documented here, in which morphological details (i.e. S_b) are persistent, lends credence to laboratory-field comparisons. Unfortunately, not every small morphological detail could be identified (i.e. knickpoint in scour slopes) in the field data, due to the 1 m-resolution of the DEM. However, the comparison of field evidence and laboratory results revealed similitude of equifinal form. However, the equilibrium time scale of frontal scouring is reported to be similar in sub-prototype-scale laboratory studies and the prototype field condition (e.g. Sutherland and Soulsby, 2011), which does not imply equifinality of process. Despite the scatter, likely due to the migration of bedforms as discussed above, the co-variation of l_s/L_o and w_s/L_o with increasing d_s/L_o revealed in both laboratory and field results is reasonably strong evidence that the specific scouring processes identifiable from the laboratory results also occur at prototype scale, resulting in similitude of form. The determination of a near-equilibrium condition is therefore attributed to the sediment transport rate out of the frontal scour hole that should average approximately zero over time. The laboratory results have shown that the sediment transport rate approaches near equilibrium conditions, while the relation of d_s/l_s and d_s/w_s enabled the determination of temporal evolution phases. Although the field evidence imply scour-hole persistence for the given boundary conditions, statements on the temporal evolution stage of field evidence are not possible.

6.10 CONCLUSION AND OUTLOOK

Recalling the aims formulated in the Introduction, the following conclusions can be drawn:

(i) The enlargement of frontal scour hole in time is triggered by depth-incision, steepening of slopes, and gravitational movements at the scour slopes, irrespective of hydraulic boundary conditions. Three temporal evolution phases could be determined based on the relations d_s/l_s and d_s/w_s that are supported by the asymptotical sediment transport rate out of the frontal scour hole in time. A quantitative model is formulated that assesses enlargement in local scour length and width based on scour depth, the inclination of frontal scour slopes and the span of the scour hole bottom irrespective of scale that can be applied to estimate the spatial extent of countermeasures for local scour protection.

(ii) The depth of the frontal scour at boulder-like obstructions is impacted by limiting boundary conditions that are supposed to be plausible at field conditions (i.e. boulder tilting and burial, limitations due to the thickness of the alluvial layer, armouring effects as well as infilling of incoming sediments), making d_s a sensitive morphometric parameter.

(iii) Integration of laboratory results and field evidence on obstacle marks demonstrates a scale invariance that implies similitude of processes and form.

However, more complex scenarios have to be addressed in upcoming laboratory research to bridge the gap between simulated obstacle marks and their real-world counterparts. In particular, the impact of unsteady discharge, unsteady upstream sediment supply, and the effects of discharge chronologies and exceedances, to test the consistency of observations on the temporal evolution of geometrical relations (d_s/l_s, d_s/w_s) under these conditions, and the quantitative model presented here for frontal scour hole enlargement. Field evidence revealed that frontal scour holes at large boulders are distinguishable from other sedimentary structures and have preservation potential under complex boundary conditions. However, obstacle marks are ephemeral in the sense that they persist only as long as the obstacle that creates them. Thus, they are a suitable indicator for the evaluation of sediment supply and net change in

thickness of the alluvial layer (Δd_{sed}). An extremely large sediment supply (i.e. $\Delta d_{sed} >> \Delta d_s$) would result in a significant reduction of d_s, burial of the obstacle, and complete disappearance of the obstacle mark.

6. Geometry of obstacle marks at instream boulders integration of laboratory investigations and field observations

7. GEOMETRY OF LOCAL SCOUR HOLES AT BOULDER-LIKE OBSTACLES DURING UNSTEADY FLOW CONDITIONS AND VARYING SUBMERGENCE

ABSTRACT

Local scour holes are erosional bed structures that are related to different scientific disciplines in Earth science and hydraulic engineering. Local scouring at naturally placed boulders is ubiquitous, but many competing factors make it difficult to isolate the effects of a given variable. This is especially true for local scouring at natural instream obstacles that are exposed to unsteady flow conditions in the course of flood hydrograph experiments. Experimental investigations in laboratory flumes offer the advantage that boundary conditions can be systematically varied. We present novel experimental data on the impact of the submergence ratio, hydrograph skewness, and flow intensity on local scouring at boulder-like obstacles during unsteady flow and evaluate the effect of discharge chronologies. In total, 48 flume experiments on subcritical clear-water conditions and channel degradation were performed. The experimental results reveal that local scouring dominantly occurred at the rising limb when flow depth was comparable to the obstacle size, so the obstacle was unsubmerged. The steeper the rising limb, the quicker the local scour hole matured. The experimental results are relevant for the hydraulic interpretation of local scour holes found at boulders in the field. They may be utilized as a proxy for the minimum duration of the beginning stage of a flood.

This chapter has been published as:

Schlömer, O. and Herget, J. (2023) Geometry of local scour holes at boulder-like obstacles during unsteady flow conditions and varying submergence. *Water* 15(5) 958. DOI: https://doi.org/10.3390/w15050958.

7.1 INTRODUCTION

Local scour holes are areas of crescentic deepening in the vicinity of an instream obstacle that result from sediment mobilization due to flow separation, turbulence, and the acceleration of flow in the surroundings of the obstacle (Richardson, 1968; Allen, 1984). Due to the variety of natural and instream artificial obstructions, the phenomenon of local scouring is relevant to different scientific disciplines in Earth science and hydraulic engineering. Local scouring has been extensively investigated at hydraulic structures, such as bridge piers, groynes, spur dikes (Breusers & Raudkivi, 1991; Melville & Coleman, 2000; Ettema *et al*., 2011; Pizarro *et al*., 2020), and submarine pipelines (Chiew, 1990; Sumer & Fredsøe 2005), because of safety problems. At these structures, engineering approaches are interested in the determination of the maximum depth of the local scour hole that likely formed after prolonged exposure to flow. In the case of a flood hydrograph, i.e., the variation in flow velocity and flow depth over time at any fixed point in space (Herget *et al*., 2015, Collischonn *et al*., 2017), it is known that the rising limb and peak flow have the strongest impact on local scouring, while the time to reach the maximum scour depth is usually smaller than the flood duration (Link *et al*., 2017, Link *et al*., 2020).

Natural obstacles, such as solitary boulders in streams, are impacted by significantly different flow conditions in the course of a flood event. During lower flows, the obstacle is unsubmerged (some portion of the obstacle protrudes above the water surface), and the flow is affected by localized flow structures (e.g., hydraulic jumps). However, at higher flows, the obstacle occupies only the lower portion of the flow depth, and the obstacle is submerged; therefore, much of the approaching flow diverges without significant flow separation or acceleration at the obstacle's base (Tsakiris *et al*., 2014). The submergence ratio, i.e., the ratio of the flow depth to the height of the obstruction, has mostly been studied in open channel flows due to interest in fish habitat structures (Tsakiris *et al*., 2014), flow structures around boulders or clasts (Shamloo *et al*., 2001; Lacey & Rennie, 2012; Sadeque *et al*., 2008; Sadeque *et al*., 2009), and sediment transport (Papanicolaou & Kramer, 2006; Papanicolaou *et al*., 2010). The laboratory investigation by Lacey and Rennie (2012) used a cube exposed to submergence ratios = 2.0, 2.5, and 3.0 to provide further insight into flow depth–wake structure relationships. They demonstrated that, for 2.0 ≤ submergence ratios ≤ 3.0, regions of high turbulent kinetic energy move downstream with decreasing depth and that Reynolds shear stress ($-u'w'$) increases up to 50% near the top of the cube.

Hajimirzaie *et al*. (2012) and Hajimirzaie and Buchholz (2013) showed in a fluid mechanics study on low-aspect wall-mounted obstacles that a reduction in the submergence ratio significantly increases the strength of dominant vortical structures and the shedding behavior. A dominant base structure was observed in the streamwise wake at a submergence ratio = 1.0 despite it being barely detectable at submergence ratios ≥ 2.5. The origin and evolution of this base structure downstream remained unanswered. While the obstacles experienced weakly symmetric shedding at an submergence ratio = 3.5, the shedding became highly antisymmetric at a submergence ratio = 1.0.

Considering sediment transport around instream obstacles, a laboratory study by Papanicolaou & Kramer (2006) and Papanicolaou *et al*. (2010) found that submergence-ratio-induced wake dynamics govern the sediment deposition patterns around obstacles. In an array of regularly spaced spherical obstacles in open channel flow, sediment particles (glass spheres) that were transported as a bed-load were found to deposit directly behind the obstacles at a submergence ratio = 3.5, whereas, at a submergence ratio = 0.80, they deposited directly upstream of the obstacles. Opposite to sediment trapping in the wake of an instream obstruction, insights into local scouring at boulder-like obstacles under varying submergence in the course of un-steady discharge are scarce. An improved understanding of these boundary conditions is useful in regard to the hydraulic interpretation of local scour holes. Especially in ephemeral dryland rivers (Reid *et al*., 1998; Powell, 2009) with no baseflow, preserved local scour holes are common features at boulders (Fig. 36 a). The boulders are not transported further downstream and remain part of the river landscape (Calle *et al*., 2017; Shobe *et al*., 2021). For ephemeral dryland rivers, local scouring is triggered by flash floods, i.e., a flow of water that arrives suddenly at a fixed point, changes rapidly in velocity and flow depth, and lasts a short time (Alexander & Cooker, 2016). Herget *et al*. (2013) used the preserved geometry of local scour holes at large boulders located in arid and ungauged basins to estimate the flow velocities of past flood events. Although plausible results could be presented, the spatiotemporal evolution of local scour holes at boulder-like obstacles during a flood hydrograph has not been experimentally investigated yet.

Therefore, the present study experimentally investigates the impact of hydrographs of different amounts of skewness, varying durations, and different flow intensities on the enlargement processes of local scour holes at boulder-like obstacles over time. Within this context, the objectives of this contribution are as follows:

(i) To present experimental data on the enlargement of local scour holes at boulder-like obstacles over time that are exposed to different water levels.

(ii) To analyze the geometry of local scour holes for unsteady discharge over time through a systematic laboratory flume study.

(iii) To evaluate the history dependence of local scouring at a boulder-like obstruction in different hydrograph scenarios because local scouring is not independent from past flood events (Tubaldi *et al*., 2017; Pizarro & Tubaldi, 2019).

Before presenting the experimental boundary conditions and deriving the working hypothesis, a review on the geometry of obstacle marks and the turbulent flow field is presented. This study used a flume as a process-focused laboratory prototype (Baynes *et al*., 2018) to re-produce the processes and resulting morphologies (i.e., local scour holes). Experimental hydrographs were constructed to represent the hydraulic conditions in ephemeral dry-land streams, but they do not represent a specific natural prototype. Hydrographs were operationalized using dimensional parameters, including the dimensionless effective flow work.

The time-series data on local scour hole geometry revealed that local scouring dominantly occurred at the rising limb of the hydrographs when the flow depth was comparable to the obstacle size, so the obstacle was unsubmerged. Up to 80% of the scour hole size at the end of experimental runs was reached in only 10% of the experimental runtime, so the skewness of the hydrograph was an important factor.

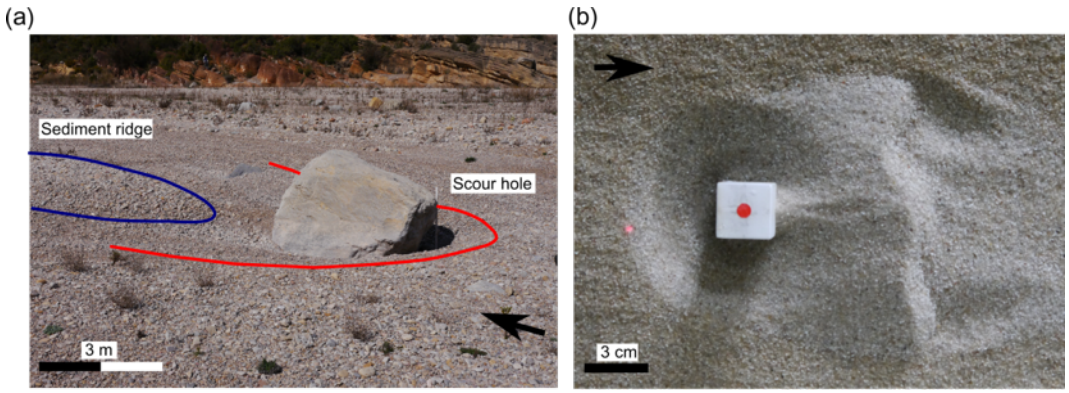


Figure 36. (a) Local scour hole at a boulder in ephemeral Rambla de la Viuda, NE Spain, 2019 . (b) Local scour hole at a cube generated in a flume.

7.2 REVIEW ON LOCAL SCOURING AT BOULDER-LIKE OBSTACLES

7.2.1 GEOMETRY OF THE LOCAL SCOUR HOLES

The morphology of local scour holes at boulder-like obstacles is consistent over a range of spatial scales from a small-scale laboratory (10^{-2} m) to scour holes at boulders (10^{1} m) (Schlömer *et al*., 2021) (Fig. 36). The local scour hole forms at the luv side of the approaching flow upstream of the obstacle. They can be approximated to be an inverted frustum cone with an elliptical shape in plan view (Fig. 4). The geometry of a local scour hole can be characterized by certain geometrical length scales, including the local scour hole depth at the obstacle front (d_s), measured from the undisturbed upstream bed; the local scour hole frontal length (l_s) in the plane of symmetry to the incoming flow, measured from the obstacle frontal face to the upstream edge of the scour hole; and the local scour hole frontal width (w_s), measured perpendicular to the direction of incoming flow from the lateral edges of the scour hole at the obstacle frontal face (Euler & Herget, 2012).

Deviations in the aforementioned spatial pattern are possible, as the size and shape of the boulder are of paramount importance for the local scouring process. In the case of a boulder-like obstacle, its effective size can be described based on its height above the streambed and its width perpendicular to the direction of flow. From experimental observations, it is known that, for a given flow depth and velocity, irrespective of unsubmerged or submerged conditions, the size of a local scour hole at a boulder-like obstacle is proportional to the obstacle size (Euler & Herget, 2011). Additionally, the length of the obstacle in the streamwise direction is important, as it defines the hydrodynamic shape. The hydrodynamic shape can be differentiated in streamlined obstructions with crossflow dimensions smaller than its streamwise dimensions and in bluff obstructions with crossflow dimensions comparable to its streamwise dimensions (Douglas *et al*., 2001). Generally, local scouring at the obstacle front is more intense in bluff obstructions. Moreover, boulders in streams have to be considered mobile in the sense that scouring can undermine the obstacle and induce movement that is characterized by tilting and the self-burial of the obstacle. Consequently, this process changes the boulder's exposure to flow and weakens the scouring processes (Rennie *et al*., 2017).

7.2.2 FLOW FIELD

If a boulder is unsubmerged, which is a condition that is analogous to scouring at bridge piers, the following processes are common: (1) an increased flow velocity lateral to the obstacle; (2) the formation of a jet-like downflow at the obstacle front due to a pressure gradient; and (3) the formation of unsteady turbulent necklace-like vortical structures at the obstacle base, commonly referred to as a horseshoe vortex system (HV) (Escauriaza & Sotiropoulos, 2011; Kirkil & Constantinescu, 2010; Radice & Tran, 2012; Chen *et al*., 2017). These processes amplify bed shear stress relative to the undisturbed upstream flow and induce sediment mobilization in the vicinity of the obstacle (Li *et al*., 2019; Link *et al*., 2012). Downstream of the obstacle, the shedding of von Karman vortices is possible in unsubmerged conditions. It is likely that these shedding vortices contribute to sediment mobilization in the wake of the obstacle and that they cause local scour hole enlargement in the downstream direction (Ettema *et al*., 2004). However, relatively little is understood on how these streamwise vortex structures arise and what the detailed impact on the sediment transport processes is.

Because boulders are relatively squat (height ≲ width), they become submerged during a flood, while additional vortical structures become dominant (Okamoto & Sunabashiri, 1992; Pattenden *et al*., 2005). In submerged conditions, an arch-shaped vortex made of two lateral vortices at the obstacle's sides is present due to flow separation at the obstacle, and a vortex is located at the crest of the obstacle (Dey *et al*., 2011; Hajimirzaie *et a*l., 2014). The arch-shaped vortex bends down to the bed immediately downstream of the boulder (i.e., the near-wake region) and causes a recirculation zone where some part of the flow reverses towards the obstacle (Papanicolaou *et al*., 2012). As shown by (Euler *et al*., 2017; Schlömer, 2020), this recirculation zone can cause local scouring in the obstacle's wake instead of frontal local scouring. If the obstacle is deeply submerged, the mid-wake region (downstream of the reattachment) is characterized by interactions between laterally detached shear layers and the extended horseshoe vortex (Pattenden *et al*., 2005). Other scenarios include the presence of a street of regularly shedding upwelling hairpin vortices originating from the pushed down arch vortex in the recirculation region (Euler & Herget, 2012). In addition to the aforementioned vortices in the wake, base vortices may be formed close to the obstacle that induce an upwash on the symmetry plane of the wake, which may be important for downstream sediment transport (Hajimirzaie, 2023; da Silva *et al*., 2022a; da Silva *et al*., 2022b). At this instance, von Karman type vortex

shedding does not play a significant role in the fully submerged conditions of the obstacle (Fu & Rockwell, 2005; Sumner *et al*., 2004).

In the case of upstream local scouring, the enlargement of the scour hole and its geometry are closely related to the HV as the main driver of sediment mobilization (Dargahi, 1990; Chen *et al*., 2019). Within the local scour hole, the HV actually consists of several interacting and unsteady vortices (Kirkil *et al*., 2008). The largest and most stable vortex is denoted as the primary horseshoe vortex (HV1), which is located close to the obstacle base. Upstream, a smaller and less coherent vortex (HV2) is located within the outer region of the frontal local scour hole (Fig. 5 a).

7.2.3 ENLARGEMENT PROCESSES OF LOCAL SCOUR HOLES

The horseshoe vortex system is responsible for the segmentation of the longitudinal local scour hole slope, originating from the obstacle front and moving to the upstream edge of the local scour hole (Fig. 6). These segments consist of (1) a flat semicircular scour hole bottom (S_b) that is closely attached to the obstacle base with a radius < l_s, (2) an inner frontal scour hole (lower slope) that is characterized by an inclination (Φ) ≥ the critical angle of repose (Φ_{crit}), and (3) an outer frontal scour hole (upper slope) that is characterized by $\Phi \leq \Phi_{crit}$ (Unger & Hager, 2006).

The inner scour hole is shaped by the rotation of the HV1, which generally stabilizes the lower slope at an angle greater than the angle of repose (Muzzammil & Gangadhariah, 2003). A knickpoint in the slopes (i.e., berm) differentiates the inner and outer scour hole. However, as recently demonstrated by, Guan *et al*. (2019) the HV is an unsteady vortex system that randomly oscillates over time, and it, thereby, temporarily weakens due to aperiodic bimodal oscillations (Paik *et al*., 2007, Kirkil & Constantinescu, 2015). During scouring, the HV1 sinks into the frontal scour hole and extends down to S_b. The enlargement of l_s and w_s is directly related to deepening and, occasionally, to the weakening of the HV, which destabilizes the scour slopes and results in gravity mass movements.

7.2.4 BOUNDARY CONDITIONS

Local scouring can be interpreted as the result of a complex two-phase flow involving water and sediment that is controlled by different environmental boundary conditions comprising (1) the flow conditions, (2) the sediment characteristics, (3) the properties of the obstacle, and (4) time (Radice *et al*., 2009; Schlömer *et al*., 2020).

Considering a solitary solid boulder-like obstruction located in a straight, moderately sloped channel (< 0.003 m/m) with subcritical (Fr < 1) flow conditions and cohesionless alluvial sediment (plane-bed type streams), local scouring can be functionally determined by

$$d_s = f(d_w, U_m, \rho, \nu, g, B, h_o, w_o, le_o, Mb, D_{50}, \rho_s, \sigma_G, U_c, d_{sed}, t, t_e)$$

(Eq. 33)

where d_s is the local scour depth (L), d_w is the flow depth (L), U_m is the mean approach flow velocity, ρ is the water density (ML^{-3}), ν is the kinematic viscosity (L^2T^{-1}), g is gravitational acceleration (LT^{-2}), B is the channel cross section (L), h_o is the height of the obstacle (L), wo is the obstacle width (L), le_o is the length of the obstacle (L), Mb is an indicator for the mobility of the boulder-like obstruction due to it tilting into the scoured depression (-), D_{50} is the median grain diameter of the bed sediment (L), ρ_s is the sediment density (ML^{-3}), σ_G is the gradation coefficient of the sediment ($D_{84}/D_{16}^{1/2}$ (-)), U_c is the critical mean approach flow velocity for the entrainment of the bed sediment (LT^{-1}), d_{sed} is the thickness of the bed layer (L), t is time (T), and t_e is the time scale to reach equilibrium (T).

For noncohesive alluvial sediments (i.e., sand and gravel), equilibrium conditions are typically reached in an order of days (Kothyari *et al*., 1992; Oliveto & Hager, 2002; Simarro *et al*., 2011). However, it is well established that, for steady discharge, 80% of the local scour hole size in equilibrium conditions is reached within only 5–40% of the time to equilibrium, mainly depending on the flow velocity and grain size (Melville & Chiew, 1999). In equation (33), 16 independent variables (denoted as n) in 3 basic dimensions (denoted as m) define the problem's inherent degrees of freedom (Sonin, 2004). According to the Π-theorem, equation (33) can be reduced to n− m non-dimensional parameters. To account for squat obstacles in unsubmerged and submerged conditions, the obstacle height (h_o) and width (w_o) are used to define the effective obstacle size ($Lo = h_o^{\alpha} w_o^{\beta} = h_o^{2/3} w_o^{1/3}$), with $\alpha + \beta = 1$. L_o is used as a reference length scale (L), while the exponents were derived from a data analysis presented in Oliveto and Hager (2002) and Euler and Herget (2012). Assuming a constant relative sediment density $(\rho_s - \rho)/\rho)$, i.e., neglecting ρ and ρ_s among other expressions, one obtains:

$$d_s/L_o = f(d_w/L_o, U_m/gL_o^{1/2}, U_m/U_c, U_mL_o/\nu, L_o/B, Sh, Mb, L_o/D_{50}, \sigma_G, d_{sed}/L_o, t/t_e)$$

(Eq. 34)

where d_s/L_o is the non-dimensional scour depth; d_w/L_o is the submergence ratio; U_m/U_c is the flow intensity; $U_m/gL_o^{1/2}$ is the obstacle Froude number (Fro); Um L_o/ν is the obstacle Reynolds number (Re_o); L_o/B is the blockage ratio; Sh (L_o/le_o) describes the shape of a body where, for Sh ≤ 0.5, the obstruction is bluff, while, for Sh ≥ 0.8, the obstacle is more streamlined; L_o/D_{50} is the relative sediment coarseness; and d_{sed}/L_o is the relative thickness of the bed layer, with L_o representing the size above the sediment bed (d_{sed}). For $d_{sed}/L_o < 1$, the sediment layer is too thin, and d_s incision is significantly limited. Meanwhile, the slight enlargement of w_s and l_s can be observed (Schlömer, 2020). If $d_{sed}/L_o = 0$, the formation of obstacle marks into a sedimentary structure is inhibited. t/t_e is the non-dimensional time scale to reach equilibrium, and it is a function of d_w/L_o, U_m/U_c, and L_o/D_{50} (Melville & Chiew, 1999)

While equation (34) applies to steady flow, Pizarro *et al*., (2017) proposed the dimensionless effective flow work (W*) to be the generalization of the flow intensity concept to unsteady flow conditions at unsubmerged cylindrical bridge piers:

$$W^* = \int_0^{t_{end}} \frac{1}{t_{end}} \left(\frac{U_m}{U_c} - 0.5\right)^3 \delta dt$$

(Eq. 35)

where t_{end} is the hydrograph duration and where δ is the Dirac delta function:

$$\delta \begin{cases} 0 & \frac{U_m}{U_c} < 0.5 \\ 1 & \frac{U_m}{U_c} \geq 0.5 \end{cases}$$

(Eq. 36)

7.3 WORKING HYPOTHESIS

It is hypothesized that, in unsteady flow conditions, at a given obstacle size, obstacle shape, and sediment size, the size of the local scour hole over time would be impacted by the degree of submergence of the obstacle. Furthermore, the skewness of the hydrograph and its overall duration are supposed to have an effect on the size of the local scour hole over time.

By neglecting the constant boundary conditions of the experiments ($L_o/B = 0.09$, $L_o/D_{50} = 40$, $\sigma_G < 1.3$, $d_{sed}/L_o = 1.83$, no mobility of the obstacle, single obstacle shape) and by

neglecting the viscous effects at the obstacle (i.e., dropping U_mL_o/ν) (Manes *et al*., 2015) as well as by considering only subcritical flow conditions at the obstacle irrespective of the flow depth (i.e., dropping $U_m/gL_o^{1/2}$), equation (35) is integrated into equation (34), which leads to:

$$d_s/L_o = f\,(d_w/L_o,\ W^*, t/t_e)$$

(Eq. 37)

By assuming the shape similitude of the local scour hole, the non-dimensional scour depth (d_s/L_o) in equation (37) can be replaced with the non-dimensional scour length (l_s/L_o) or the non-dimensional scour width (w_s/L_o) (Schlömer *et al*., 2021). However, the validity of W* has not been tested experimentally for the case of local scouring at squat boulder-like obstacles at different extents of submergence. Link *et al*. (2017) proposed the relationship between the normalized scour hole depth and W* at unsubmerged cylindrical bridge piers to be:

$$d_s/L_o = 0.0075\ (1\text{-}e^{-0.097\ W^{*0.38}})$$

(Eq. 38)

The present experimental results are compared to equation (38), although it was originally determined based on experimental runs on bridge pier models that had different boundary conditions.

7.4 EXPERIMENTAL DESIGN AND PROCEDURES

7.4.1 FLUME SET-UP

Experiments were conducted in a 5 m long, 0.32 m wide, and 0.27 m deep straight rectangular flume that was entirely filled with a 5.5 cm thick layer (d_{sed}) of uniform sand ($\sigma_G < 1.3$) with median grain diameter (D_{50} = 0.75 mm) (Fig. 9). The bottom slope of the flume was not adjustable, as it was fixed to a moderate slope (0.003 m) to ensure water flow in the flume. Within the working section (~ 2.7 m downstream of the inlet), subcritical flow conditions (Froude number ($Fr = U_m/gd_w^{1/2}$) ranging from 0.29 to 0.56) were present at any stage of the hydrograph and at any water depth. The Reynolds number ($Re = U_md_w/\nu$) was >> than 500 for any stage of the hydrograph, indicating turbulent flow. Discharge was controlled with a recirculating pump (Lowara FCE Series®, Langenhagen, Germany) regulated manually by two cone valves and was measured with a magnetic-inductive discharge meter (Schwing MS 1000®, Neukirchen-

Vluyn, Germany, accuracy ± 1% of actual discharge). Flow depth (d_w) was adjusted with a tailgate at the downstream end of the flume outlet. In order to reduce turbulence and to condition flow, a self-made flow straightener made of bundled pipes (approx. 100 pipes, diameter of 3 cm, length of 40 cm) was installed in the flume inlet. A cube (L_o = 3 cm) was used to represent the hydrodynamic shape of a bluff instream obstacle whose crossflow dimensions were comparable to its streamwise dimensions. The authors are aware that the shape of a cubic boulder is unlikely in natural conditions. However, the cube was supposed to represent a maximum angular obstacle for which scouring processes would be intensified. The cube was mounted to the flume bottom to prevent tilting due to scouring, which limited further evolution of local scouring and induced equilibrium conditions more quickly.

7.4.2 LABORATORY HYDROGRAPHS

Hydrographs were constructed to simulate hydrological conditions that are likely in ephemeral dryland streams (i.e., no baseflow and relatively short duration) (Belmonte & Segura Beltrán, 2001). Unsteady discharge was simulated through a quasi-steady approach by applying the principle of stepped hydrographs, i.e., a sequence of constant discharges acting during defined intervals, which is commonly used to imitate varying discharge in flumes (Mao, 2012; López *et al*., 2014; Waters & Curran, 2015).

Four simply shaped single-peaked hydrographs were designed by varying the duration of rising limb (t_r), falling limb (t_f), and peak flow (t_{peak}). Symmetrical (t_r/t_f = 1), pos-itively skewed (t_r/t_f < 1), negatively skewed (t_r/t_f > 1), and flash flood hydrographs (t_r/t_f << 1) were constructed through this procedure. The hydrographs were made of n = 13 intervals of constant discharge: 6 on the rising limb, 1 at peak flow, and 6 on the falling limb (Fig. 37).

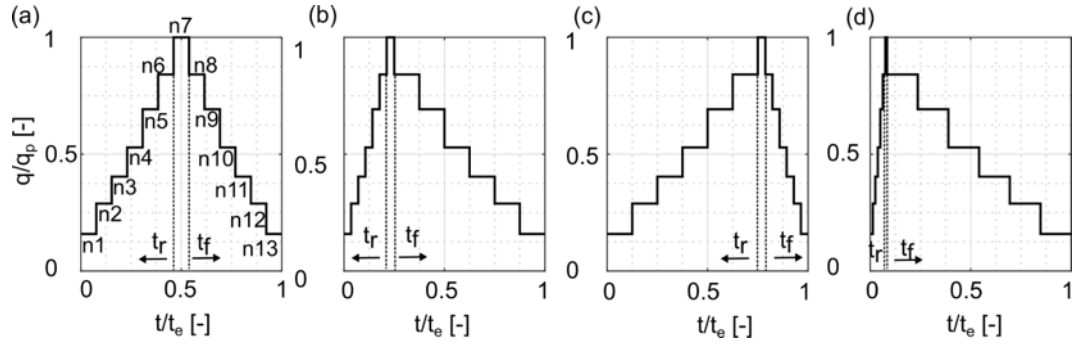


Figure 37. Laboratory hydrographs and indication of discharge intervals (n) and duration of rising limb (tr) and falling limb (tf): (a) symmetrical, (b) positively skewed, (c) negatively skewed, and (d) flash flood.

For each hydrograph shape, three different experimental configurations (Series A, B, and C) were conducted in which the overall hydrograph duration (t_{end}) was different. Through this, the dependence of local scouring on time was evaluated. For Series A, t_{end} equaled 480 min; for Series B, t_{end} was 210 min; and for Series C, t_{end} was 120 min, with $t_{end} = t_r + t_{peak} + t_f$. Therefore, experimental runtime of hydrographs was not designed to define any equilibrium condition for local scouring. The runtime of each discharge interval varied between different hydrograph shapes. An overview on the individual runtime of discharge intervals for each hydrograph shape is provided in Table 10.

For comparison, experimental runs at constant discharge and at peak flow (i.e., d_w = 8, obstacle fully submerged) were performed at different mean flow velocities (i.e., U_m = 0.26 m/s, 0.32 m/s, and 0.37 m/s), and they lasted 480 min. In total, 48 experimental runs were performed. The hydrograph started from a drained flume (i.e., no baseflow). In the rising and falling limbs of the hydrographs, d_w linearly increased from 2 cm to d_w = 8 cm at peak flow. In the falling limb, d_w decreased to 2 cm again, producing different degrees of submergence at the obstacle that were classified based on the deformation of the water surface profile.

In unsubmerged conditions ($0 < d_w/L_o \leq 1$), the obstacle top was above the water surface, and a bow wave at the obstacle front could be detected. Meanwhile, in mid-to-far wake, irregularities of the water surface indicated the presence of trailing vortices due to detached shear layers. Unsubmerged conditions were present at the beginning of the rising limb (i.e., interval n1 and n2) as well as at the end of the falling limb (i.e., n12 and n13) (Fig. 38 a). With shallow submergence, the obstacle top was only slightly below the water sur-face, causing the water level to drop above the obstacle top while a bow wave piled up at the obstacle front (i.e., n3 and n4 of the rising limb and n10 and n11 of the falling limb) (Fig. 38 b). In fully submerged conditions ($d_w/L_o \geq 2$), no disturbance of the water surface profile could be observed, indicating a free flow of the approaching boundary layer above the obstacle top (i.e., n5 and n6 of the rising limb, n8 and n9 of the falling limb, and n7 at peak flow) (Fig. 38 c). However, an arch-shaped vortex might be present at the obstacle's crest and its near-wake region. The water

surface profile in the working section was measured using an ultrasonic distance meter (Mic + 25, Microsonic®, accuracy ± 0.1 mm).

Three different hydraulic scenarios were applied in experimental Series A, B, and C. By increasing U_m at a given d_w, different flow intensities (U_m/U_c) were established. For Scenario 1, clear-water conditions ($U_m/U_c < 1$) prevailed during the hydrographs; for Scenario 2, flow intensity was close to general sediment mobilization ($U_m/U_c \cong 1$); and, for Scenario 3, general sediment mobilization was present during the entire hydrograph ($U_m/U_c > 1$, general sediment movement). The hydraulic boundary conditions of the experimental series are displayed in Table 10.

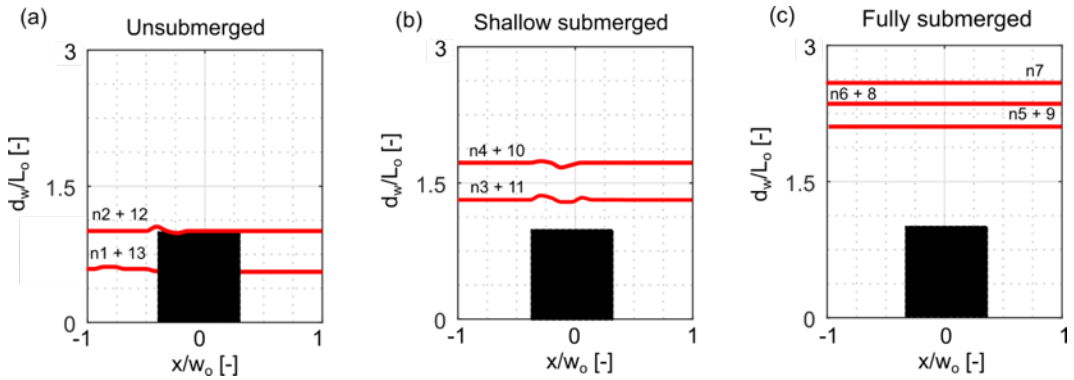


Figure 38. Extent of submergence of the obstacle and indication of discharge interval (n): (a) unsubmerged, (b) shallowly submerged, and (c) fully submerged.

Table 9. Duration of discharge intervals in experimental hydrographs in Series A/B/C.

Interval (n)	Symmetrical ($t_r/t_f = 1$)	Positively skewed ($t_r/t_f = 0{,}28$)	Negatively skewed ($t_r/t_f = 3{,}53$))	Flash flood ($t_r/t_f = 0{,}08$)
1	37 / 18 / 9 min	17 / 4 / 4 min	60 / 30 / 15 min	6 / 1 / 1 min
2	37 / 18 / 9 min	17 / 4 / 4 min	60 / 30 / 15 min	6 / 1 / 1 min
3	37 / 18 / 9 min	17 / 4 / 4 min	60 / 30 / 15 min	6 / 1 / 1 min
4	37 / 18 / 9 min	17 / 4 / 4 min	60 / 30 / 15 min	6 / 1 / 1 min
5	37 / 18 / 9 min	17 / 4 / 4 min	60 / 30 / 15 min	6 / 1 / 1 min
6	37 / 18 / 9 min	17 / 4 / 4 min	60 / 30 / 15 min	6 / 1 / 1 min
7	36 / 18 / 9 min	18 / 4 / 4 min	18 / 4 / 4 min	6 / 1 / 1 min
8	37 / 18 / 9 min	100 / 30 / 15 min	17 / 4 / 4 min	73 / 33 / 18 min
9	37 / 18 / 9 min	100 / 30 / 15 min	17 / 4 / 4 min	73 / 33 / 18 min
10	37 / 18 / 9 min	100 / 30 / 15 min	17 / 4 / 4 min	73 / 33 / 18 min
11	37 / 18 / 9 min	100 / 30 / 15 min	17 / 4 / 4 min	73 / 33 / 18 min
12	37 / 18 / 9 min	100 / 30 / 15 min	17 / 4 / 4 min	73 / 33 / 18 min
13	37 / 18 / 9 min	100 / 30 / 15 min	17 / 4 / 4 min	73 / 33 / 18 min

Table 10. Hydraulic boundary conditions of flow intervals used to design hydrographs.

a: Series A/B/C 1, 4, 7, and 10. b: Series A/B/C 2, 5, 8, and 11. c: Series A/B/C 3, 6, 9, and 12.

Interval (n)	d_w	U_c	Scenario 1 [a] U_m	Scenario 1 [a] q	Scenario 2 [b] U_m	Scenario 2 [b] q	Scenario 3 [c] U_m	Scenario 3 [c] q
	(m)	(m/s)	(m/s)	(m²/s)	(m/s)	(m²/s)	(m/s)	(m²/s)
1 + 13	0.02	0.248	0.165	3.35×10^{-5}	0.20	4.06×10^{-5}	0.25	5.07×10^{-5}
2 + 12	0.03	0.268	0.20	6.09×10^{-5}	0.22	6.70×10^{-5}	0.27	8.22×10^{-5}
3 + 11	0.04	0.282	0.21	8.53×10^{-5}	0.24	9.75×10^{-5}	0.29	1.17×10^{-4}
4 + 10	0.05	0.293	0.22	1.11×10^{-4}	0.26	1.32×10^{-4}	0.31	1.57×10^{-4}
5 + 9	0.06	0.302	0.24	1.46×10^{-4}	0.28	1.70×10^{-4}	0.33	2.01×10^{-4}
6 + 8	0.07	0.316	0.25	1.77×10^{-4}	0.30	2.13×10^{-4}	0.35	2.48×10^{-4}
7	0.08	0.327	0.26	2.11×10^{-4}	0.32	2.60×10^{-4}	0.37	3.00×10^{-4}

7.4.3 EXPERIMENTAL PROCEDURE

Each experiment started by adjusting the discharge per unit width (q) and d_w to the first interval of the hydrograph (n1). Afterwards, the obstacle was placed in the working section in the plane of symmetry to minimize sidewall effect (Nezu & Nagagawa, 2017). The sediment surface in the entire flume was leveled to a flat-bed surface. Experimental runtime started at t = 0 min after the cube was installed. Between the intervals, in the rising limb, the tailgate was raised 1 to 2 cm to interrupt local scouring while q was adjusted via the cone valves of the pump to the next interval. In the falling limb, first, q was decreased while the tailgate was lowered to the

corresponding d_w. Adjustments of q and d_w took approximately 3 to 5 min and were done manually. The time of adjustment was not considered to be part of experimental runtime, as local scouring was interrupted.

Although the cone valves were operated manually, the standard error of the actual discharge was less than 9.0 10^{-6} m^2s^{-1}, i.e., less than 3% of the desired discharge. Thus, it was argued that desired hydrographs depicted in Fig. 37 were representative of actual laboratory conditions. During experimental runs, the sizes of d_s, l_s, and w_s were measured with two LED distance meters (Welotec® OWRB Series , Laer, Germany, accuracy ± 0.5 mm), measuring x- and y-coordinates in a local Cartesian coordinate system, with x = longitudinal as well as streamwise direction and y = horizontal, perpendicular to streamwise direction. A laser distance meter (Baumer Electric® ODAM S14C, Fraunfeld, Switzerland, accuracy ± 1.5 mm) was used to measure the vertical coordinate (z). All sensors were mounted on a traversing system on top of the flume operating in x-/y-planes. The elevation of the initial flat bed in front of the obstacle at t = 0 min was used as reference (i.e., x0/y0/z0 = 0/0/0).

For Series A, d_s, l_s, and w_s were measured every third minute for each hydrograph interval. Irrespective of time, the spatial extent of ls and ws was determined by $z0 < 0$. For Series B and C, the measurement frequency was relaxed to one and two minutes in order to generate sufficient data on each hydrograph step. Measurements of the geometrical length scales were interpreted as quasi-dynamic observations because they were measured while water was flowing (Rodgers *et al*., 2020). Thus, measurements of the z-coordinate (d_s) were biased due to refraction of the laser beam within the water column. In absence of suspension of sediment, a simple calibration method (i.e., compensation for the travel time of light in water) was applied that yielded sufficiently accurate results when compared to measurements in drained conditions with the same measurement system. The error was less than two times D_{50}. Additionally, the geometry of the local scour hole was measured using 2D longitudinal cross sections, i.e., streamwise direction (x-/z-coordinates) and perpendicular to streamwise direction (y-/z-coordinates). The longitudinal cross sections were used to estimate the volumetric bedload transport rate. Cross sections were surveyed every 20 min of experimental runtime up to t_{end}.

7.5 Results and discussion

7.5.1 Local scour evolution

Irrespective of the hydraulic scenario or hydrograph shape, local scouring immediately started at interval n1 of the hydrographs after placing the obstacle in the working section. Two initial depressions formed at the lateral edges of the cube front that merged to a conical scour hole in front of the obstacle ($t \leq 1$ min). The position of the maximum scour depth then migrated from the lateral sides to the obstacle front. The eroded material was deposited downstream in the wake of the obstruction as a sediment ridge with an orientation parallel to the flow direction. During this time, the obstacle was unsubmerged, and the observed processes were analogous to the processes reported in the experimental research on bridge pier scouring (Bouratsis *et al.*, 2017). With increasing experimental runtimes, the incision of d_s slowed down and asymptotically approached its maximum value at t_{end} irrespective of the hydrograph shape or hydraulic scenario (Fig. 39).

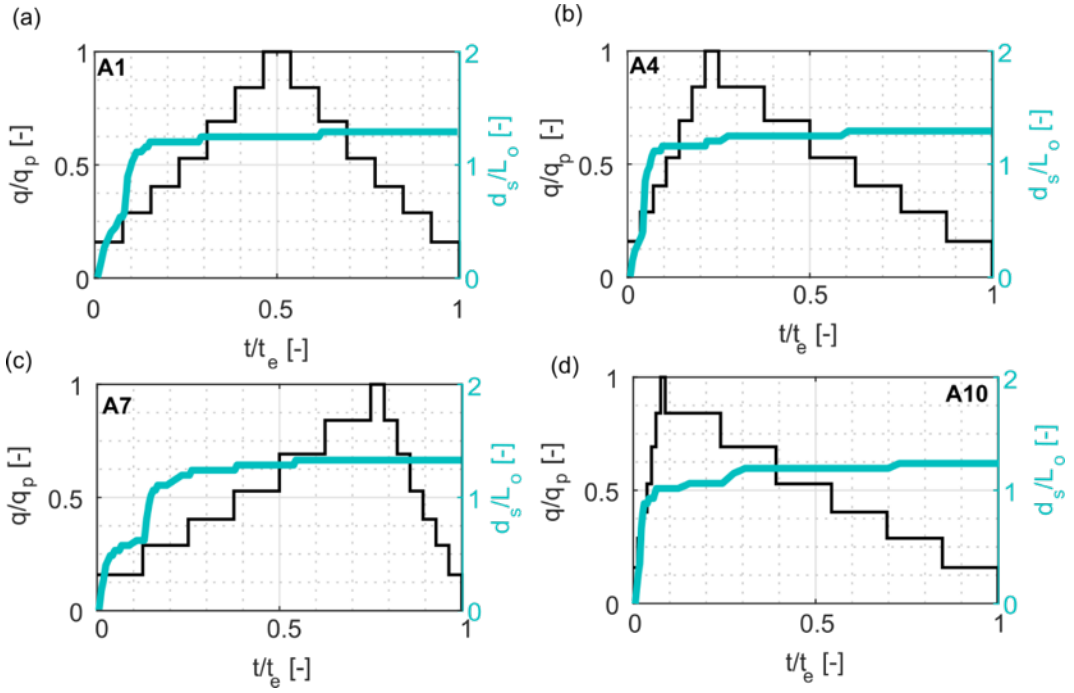


Figure 39. Evolution of normalized scour depth (d_s/L_o) over non-dimensional time (t/t_e) for different hydrograph shapes in Series A experiments: (a) symmetrical, (b) left-skewed, (c) right-skewed, (d) flash flood.

7.5.2 IMPACT OF SUBMERGENCE

At hydrograph interval n2, d_w was equal to L_o, which intensified local scouring. The scour hole significantly deepened as well as lengthened and widened, while the sediment ridge flattened, widened, and elongated in the downstream direction. The intensification of the local scouring processes at $d_w/L_o = 1$ was attributed to a high pressure gradient at the obstacle front creating an intense downflow and an erosive HV system at the obstacle base. Despite the relatively short flume length, it is argued that a characteristic boundary layer profile was present for all the intervals of the hydrographs.

With increasing submergence in the rising limb of each hydrograph (i.e., intervals n3 and n4), local scouring was reduced. At hydrograph intervals n6 and n7 (peak flow), the obstacle was fully submerged ($d_w/L_o \geq 2$), and local scouring was considerably reduced compared to $d_w/L_o = 1$. This was attributed to the fact that (i) the majority of the approaching boundary layers flow over the obstacle and that the downflow ceases and to the fact that (ii) the size and strength of the HV system is reduced in submerged conditions as outlined by (Dey *et al*., 2008; Sarkar, 2014; Du & Liang, 2019). The presence of base vortices in the wake of the obstacle in fully submerged conditions could not be verified with the present experimental setup. However, the HV system could be observed at the obstacle base due to the saltating movement of the sediment grains within the local scour hole bottom (S_b). The peak flow did not significantly contribute to the local scour hole size, as the obstacle was fully submerged during peak flow. Therefore, the present experimental results differ from observations reported on local scouring at bridge piers during hydrograph experiments (Lu *et al*., 2018; Gjunsburg *et al*., 2018; Tabarestani & Zarrati, 2017). Here, the obstacle was unsubmerged during peak flow, while the flow depth and velocity were considerably high. Thus, the approaching flow generated an intense downflow at the bridge pier's frontal face and an effective HV system at the obstacle base that favored scouring and vice versa.

Considering the dimensionless flow work (W*), W* varied between the individual runs depending on the hydrograph shape and hydraulic scenario. For Series A experiments, W* ranged from 1308 (clear-water) to 28.382 (live-bed) (Fig. 40).

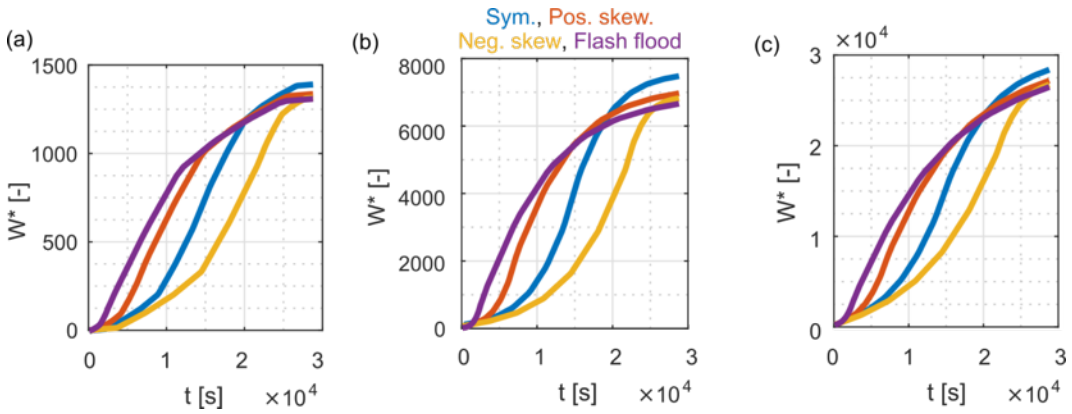


Figure 40. Dimensionless flow work (W*) of Series A experiments: (a) scenario 1 (clear water), (b) scenario 2 (transitional), and (c) scenario 3 (channel degradation).

The dimensionless scour hole depth (d_s/L_o) was proportional to W* as exemplified by the experimental runs on symmetrical hydrographs (A1, C1, and A1 constant) in clear-water conditions (Fig. 41). However, the experimental results do not fit equation (38) perfectly. This was attributed to the fact that a bluff angular obstacle was exposed to flow depths that were comparable to the obstacle size, which caused deeper scour holes at the beginning stages of the hydrographs prior to peak flow at W* ≈ 750. Moreover, the asymptotical trend of the enlargement of the scour depth at peak flow and during the first stages in the falling limb was attributed to the impact of the fully submerged conditions on the obstacle.

The size of d_s/L_o at t_{end} was comparable between A1 and the constant A1 run, which highlights the importance of time in local scouring. This became obvious in hydrograph C1, as the overall duration was reduced to 25% compared to Series A, which resulted in a 12% smaller dimensionless local scour hole depth irrespective of the hydrograph shape (Fig. 41, orange dots).

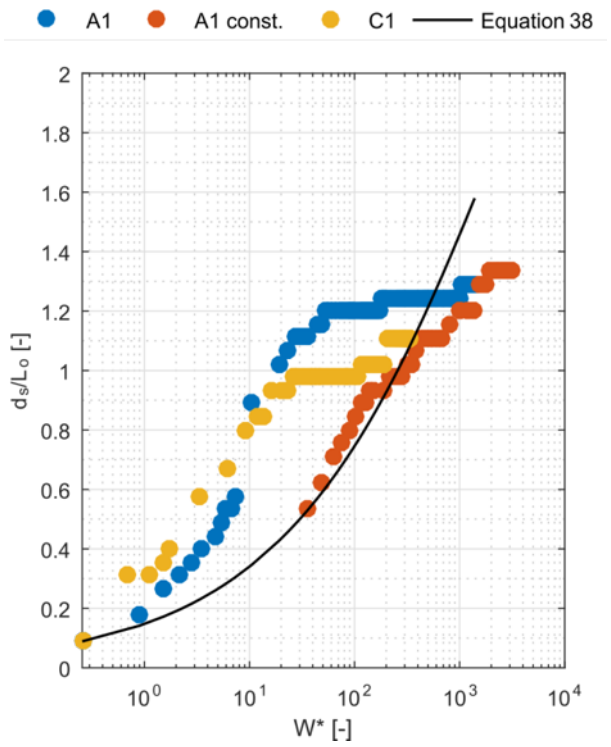


Figure 41. Dimensionless scour hole depth (d_s/L_o) versus dimensionless flow work (W*) observed in symmetrical hydrographs of different durations in clear-water conditions.

7.5.3 IMPACT OF HYDROGRAPH SHAPE

Local scouring for different hydrograph shapes in clear-water conditions showed an asymptotic evolution over time. The enlargement of the local scour depth occurred in the rising limb (t_r) prior to peak flow (q_p) irrespective of the hydrograph shape, while substantial enlargement in the falling limb (t_f) was negligible (Fig. 42, blue dots).

For the Series A experiments (t_{end} = 480 min), irrespective of the hydrograph shape, d_s/L_o already reached 76% of its size by tend at t/t_{end} = 0.1. However, the skewness of the hydrograph (t_r/t_f) affected local scouring over time. For the negatively skewed hydrograph (t_r/t_f = 3.53) of the Series A experiments, 99% of d_s/L_o at t_{end} was reached during t_r and prior to q_p (Fig. 42 d), while, for the flash flood hydrograph (t_r/t_f = 0.08), 82% of d_s/L_o at t_{end} was reached during t_r, which corresponded to 7.5% of the duration of t_e. This observation is supported by the two extremums of the investigation (Series B, t_{end} = 210 min). For t_r/t_f = 0.05, 69% of d_s/L_o at t_{end} was reached during t_r, while, for t_r/t_f = 7.06, 99% of d_s/L_o at t_{end} was reached during t_r and prior to reaching q_p. Thus, it can be stated that, the steeper t_r (i.e., positively skewed), the quicker ds achieves a size comparable to its final size for a given hydraulic condition and experimental runtime, which coincides with the experimental results on the time evolution of ds at

bridge piers during hydrograph experiments (Chang *et al*., 2004; Salamatian & Tabarestani, 2014).

The superimposition of d_s/L_o, i.e., the memorization of the previous scour depth is present for all the hydrograph shapes. This has been also documented by Hong *et al*. (2017) for experiments on scouring at bridge piers during unsteady flow. The size of d_s/L_o at tend was similar irrespective of the hydrograph shape or experimental series as indicated by a relative standard deviation of 0.0282, which is consistent with the observations reported by Link *et al*. (2017) on bridge pier scouring.

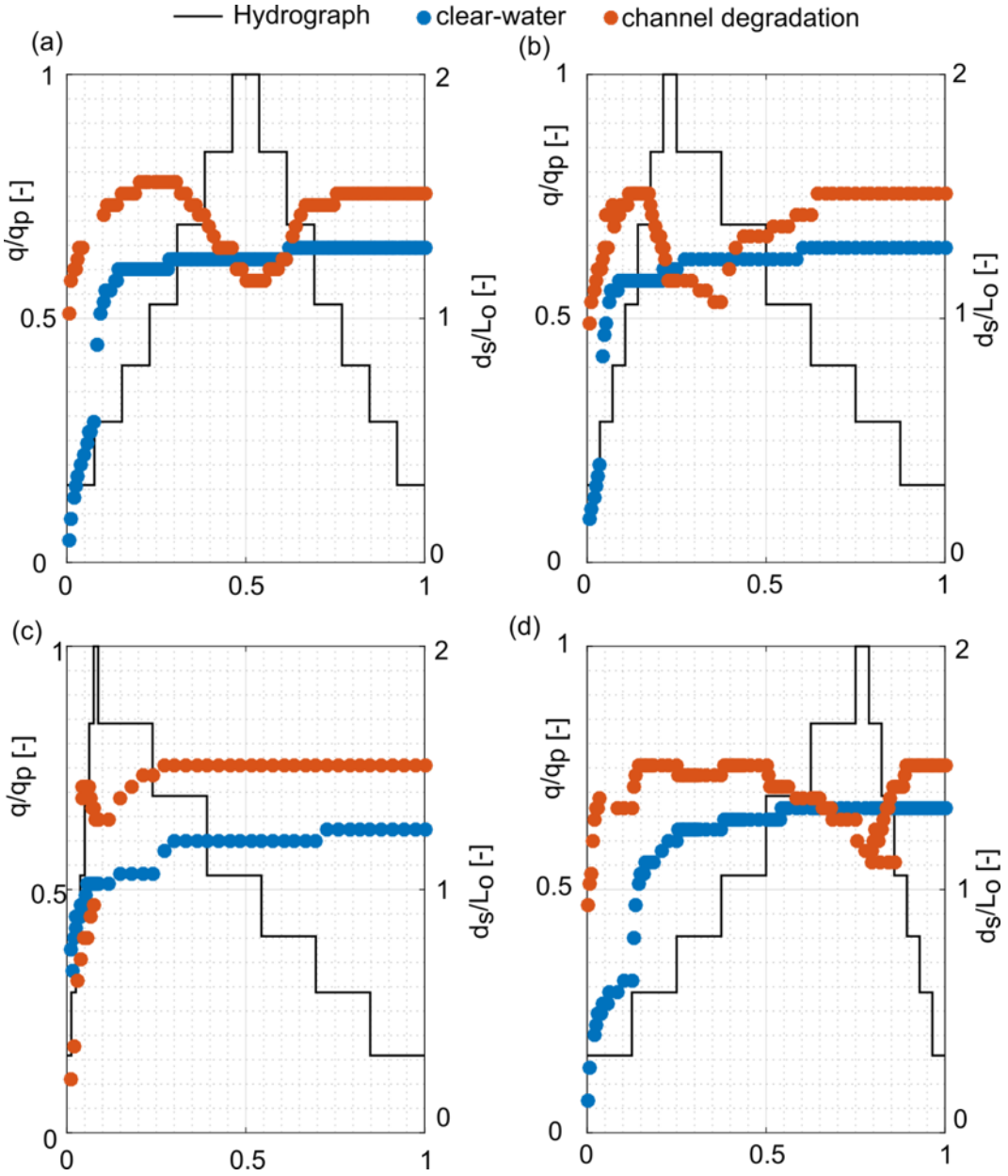


Figure 42. Trajectory of dimensionless scour hole depth (d_s/L_o) versus dimensionless time (t/t_e) for general sediment transport and clear-water conditions in Series A experiments and for different hydrograph shapes: (a) symmetrical, (b) positively skewed, (c) flash flood, and (d) negatively skewed.

7.5.4 IMPACT OF FLOW INTENSITY

Local scour evolution was different for general sediment transport ($U_m/U_c > 1$) in a degrading channel (Fig. 42, orange dots). In the rising limb of the hydrographs, the local scour holes were larger when compared to clear-water conditions, which can be attributed to two facts:

(i) Due to higher flow velocities at flow depths $d_w/L_o \leq 1.5$, the HV system could more effectively mobilize the sediment particles at the local scour hole bottom;

(ii) The sediment output out of the local scour hole was greater than the sediment input from upstream.

The second fact especially is in accordance with previous findings reported for bridge pier scouring (Sheppard & Miller, 2006). In this regard, it is necessary to indicate that no sediment feeding at the upstream part of the flume was conducted. Thus, the experimental setup has to be considered a degrading channel. At peak flow, the sediment input from upstream reached its maximum, and the downstream migrating bedload sheets approached the local scour hole and partially re-filled and buried it, which was indicated by a reduction in all the geometrical length scales (i.e., d_s/L_o, l_s/L_o, and w_s/L_o). At the same time, the sediment output of the scour hole was reduced due to the weak erosive capacity in fully submerged conditions.

The skewness of the hydrographs controlled the amount of the refilling of the scour hole. For t_r/t_f = 0.08 at q_p, d_s/L_o was reduced by 9% compared to its prior maximum value. For t_r/t_f = 3.53 at q_p, d_s/L_o was reduced by 26% compared to its prior maximum value due to a larger timespan of sediment input into the local scour hole. The amount of bedload (q_b) that was transported out of the frontal local scour hole along its longitudinal axis (l_s-d_s, Fig. 4) was also estimated based on two consecutive frontal scour cross sections over time by calculating the line integral (Fig. 43).

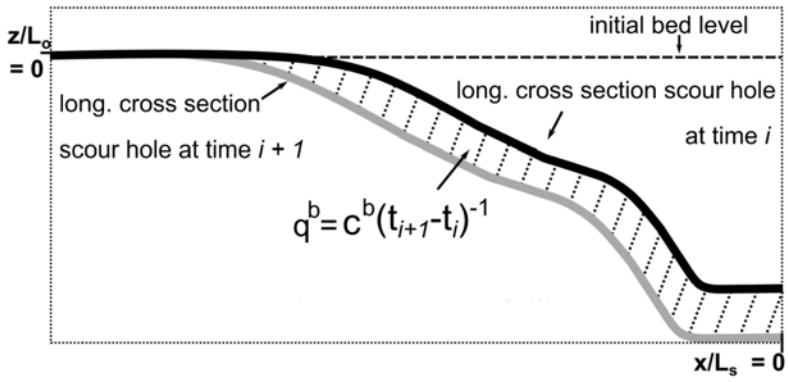


Figure 43. Estimation of bedload transported out of the local scour hole along its longitudinal axis.

Calculations were made considering l_{sP} = longitudinal scour hole profile, c^b = depth-integrated frontal scour hole area, and i = 1,… N in which N is the total number of

measured cross sections over time. In the absence of suspension, the sediment flux of the scour hole in terms of bedload could be estimated with an accuracy of +/- $2D_{50}$. For further analysis, q_b was replaced with the dimensionless bedload flux (q*):

$$q^* = qb/((\rho s/\rho - 1)\, gD_{50}^3)^{1/2} \quad \text{(Eq. 39)}$$

In general, q* showed a nonlinear evolution over time irrespective of the hydrograph shape and flow intensity. The relationship of q* over the non-dimensional time scale could be approximated through a power law relationship and an ordinary least squares estimation with a mean coefficient of determination (R^2) equaling 0.83 (Fig. 44).

In clear-water conditions (Fig. 44 a), q* was high in the rising limb (t_r) of the hydrographs due to intense scouring and the enlargement of the geometrical length scales at $d_w/L_o \leq 1.5$. Afterwards, q* significantly decreased proceeding peak flow (vertical grey lines) and reached an almost null value in the falling limb. For general sediment transport, q* turned negative at peak flow for each hydrograph shape, as approaching the bedload sheets refilled the scour hole. Afterwards, q* turned positive again, recovering to a bedload comparable to q* prior to peak flow, so the scour hole reconstituted to a size comparable to the prepeak flow conditions as the sediment supply into the local scour hole was mitigated (Fig. 44 b). An analysis of covariance (F-value = 1.32–1.59, p-value = 0.02) on the log-transformed values of q* and t/t_{end} revealed that the relationship did not statistically differ amongst the hydrograph shapes at a 95% confidence interval in clear-water conditions and for general sediment transport.

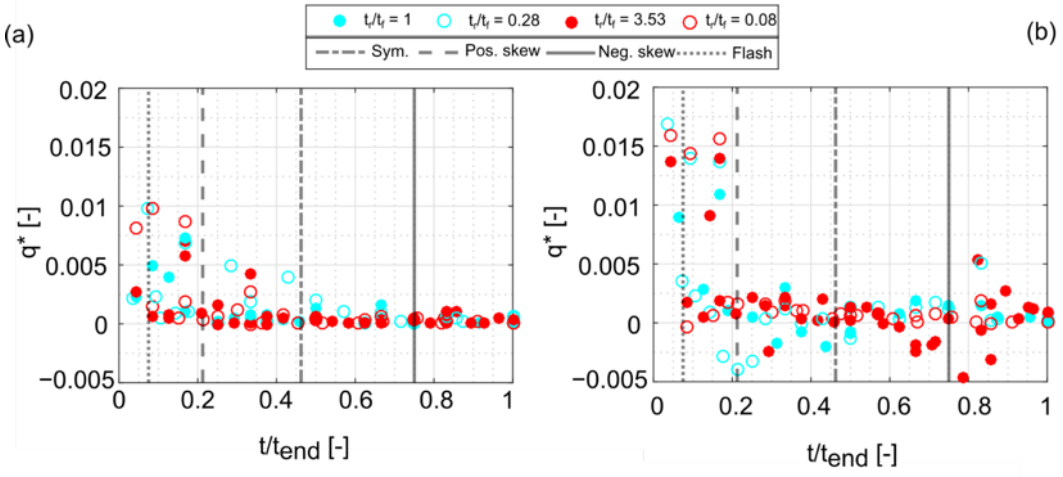


Figure 44. Dimensionless bedload (q*) versus dimensionless time scale of experiments (t/t_{end}): (a) clear water and (b) general sediment transport.

Because the bedload transported out of the frontal local scour hole varied with different unit discharges in different hydraulic scenarios, hysteresis was present in the experimental results. In clear-water conditions, a clockwise hysteresis pattern was present (Fig. 13 a), while, for general sediment transport, a "Figure-8" hysteresis-loop was present (Williams, 1989), (Fig. 45 b). The observed hysteresis loops coincided with the field observations on local scouring at logs embedded in sand and affected by different extents of submergence during flood events reported by Borg *et al*. (2007).

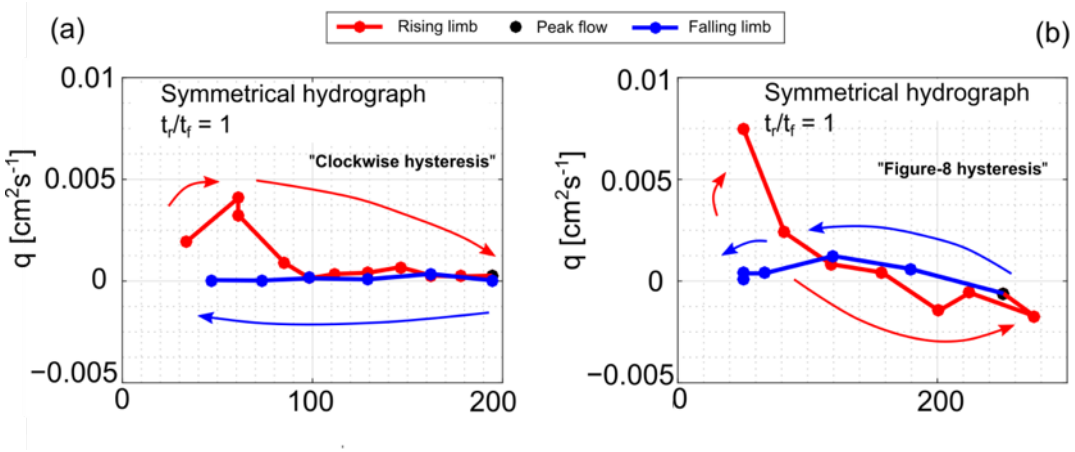


Figure 45. Hysteresis pattern: (a) clear water and (b) channel degradation.

7.5.5 LOCAL SCOUR GEOMETRY

The enlargement of l_s and w_s was triggered by the deepening of d_s in the inner scour hole, which undermined the scour slopes and induced intermittent gravitational movements at the flanks. In the developing scour holes, segmentation (Fig. 6) was visible during the experiments. The inclination of the upper scour slope (Φ) showed a decreasing tendency over time. For $t/t_{end} \leq 0.25$, Φ ranged from 32° to 40°, and the frequent sliding of the sediment could be observed. Meanwhile, for $0.5 > t/t_{end} \leq 1$, Φ was 23° to 32, and the gravitational movements at the slope eased. Over the same time, the span of the scour hole bottom (S_b) expanded from $S_b/L_o \approx 0.3$ to $S_b/L_o \approx 0.6$. The enlargement of S_b was attributed to the expansion of the HV during scouring, which has been documented in an experimental study on bridge pier scouring reported by Schlömer (2020). The expansion of the HV decreased the shear stress beneath the vortex for sediment mobilization and contributed to the asymptotical approach of an equilibrium condition of the scour depth (Dargahi, 1990; Unger & Hager, 2006).

By neglecting different hydrograph shapes and durations, a monotonic increase and covariation of l_s/L_o and w_s/L_o with d_s/L_o was present in clear-water conditions and for general sediment transport in all the experimental series that could be estimated by:

$$l_s/L_o = 1.79\ d_s/L_o$$

(Eq. 40)

$$w_s/L_o = 3.89\ d_s/L_o$$

(Eq. 41)

with a coefficient of determination (R_2) = 0.88 (Fig. 46 a) and 0.82 (Fig. 46 b), respectively.

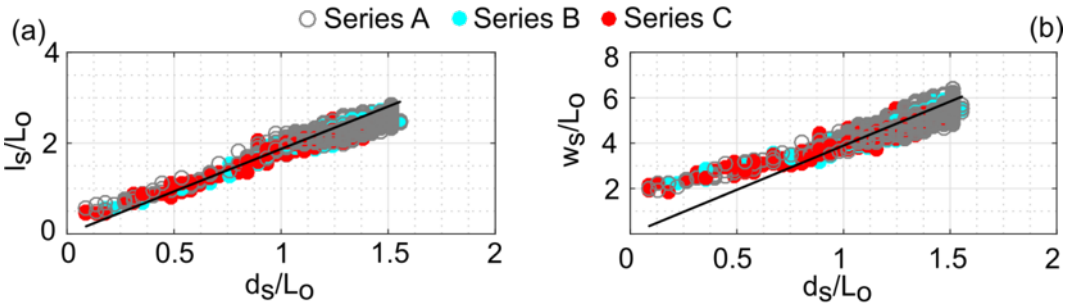


Figure 46. Dependence of non-dimensional geometrical length scales on non-dimensional scour hole depth in different experimental series: (a) scour hole length and (b) scour hole width.

The longitudinal and horizontal cross sections of the scour hole were scaled with the corresponding dimensions of ds and ls in order to preserve the collinearity of the distances and angles (i.e., three or more points initially lying on a line still lie on a line after transformation), (Tregnaghi *et al*., 2007). The scaled cross sections of the scour hole superimposed and col-lapsed into a narrow band irrespective of time, which is consistent with the experimental observations reported by Tregnaghi *et al*. (2009). Thus, it is stated that the conical shape of the local scour hole remained constant during local scour evolution. Based on its shape, the evolution of longitudinal and horizontal cross sections over time could be modeled by Gaussian functions Schalko *et al*. (2019):

$$(z + d_s)/d_s = 1.037\ e^{(-((l_s/x-1.7138)/0.7463)2) + 0.6074\ e(-((l_s/x-0.8417)/0.4782)2)}$$

(Eq. 42)

$$(z + d_s)/d_s = 1.0112\ e^{(-((w_s/y-1.0899/0.64412) + 1.0086\ e(-((w_s/y-1.1140)/0.5726)2)}$$

(Eq. 43)

with a coefficient of determination (R^2) = 0.99 (Fig. 47 a) and 0.97, respectively (Fig. 47 b).

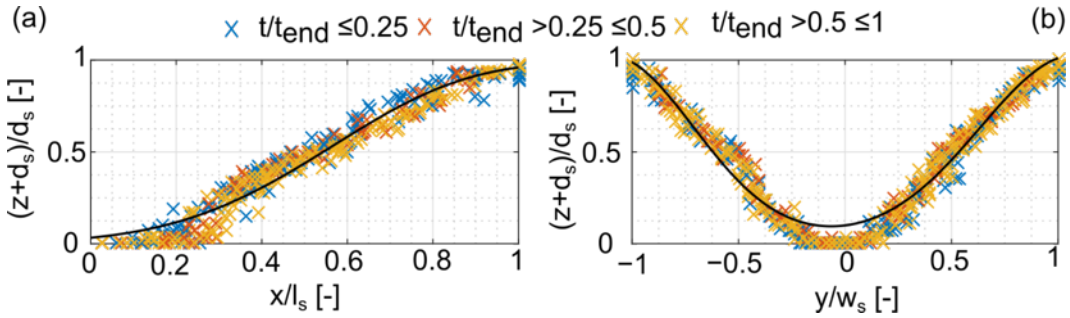


Figure 47. Scaled scour hole cross sections at different time intervals: (a) longitudinal (l_s to d_s) and (b) horizontal (w_s to d_s).

By assuming the shape of an inverted frustum cone, the volume of the local scour hole (Vol_s) could be estimated by:

$$Vol_s = (d_s\ \pi/3)\ (l_s^2 + S_b l_s + S_b^2)$$

(Eq. 44)

In clear-water conditions, irrespective of the hydrograph shape, the normalized local scour hole volume ($Vol_s/B^{1/3}$) showed reasonable agreement to a mechanistic model proposed by Schloemer *et al*. (2021) that assesses local scour hole enlargement over time based on:

(i) d_s;

(ii) the cotangent of slope inclination ($\tan^{-1}\Phi$);

(iii) S_b.

The coefficient of determination (R^2) was 0.91 (Fig. 48).

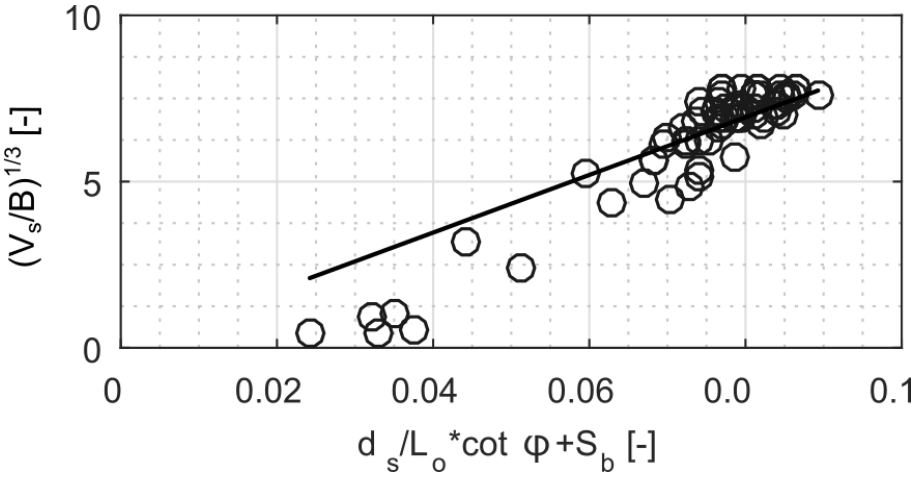


Figure 48. Normalized local scour hole volume of present experimental results versus model of local scour hole enlargement by Schlömer *et al*. (2021).

7.5.6 GEOMETRICAL RELATIONSHIPS OVER TIME

The geometrical relationships of the local scour hole (d_s/l_s and d_s/w_s) were not constant over the experimental runtime. In clear-water conditions, irrespective of the hydrograph shape, a piecewise linear pattern was present that was composed of (Fig. 49):

(i) The considerable enlargement of d_s/l_s and d_s/w_s at the beginning of the experiments as d_s increased quicker than l_s and w_s, approaching the maximum value of d_s/l_s and d_s/w_s;

(ii) The easing of the enlargement and the decreasing of the tendency of d_s/l_s and d_s/w_s afterwards as d_s matured to its finale size, while a slight increase in w_s occurred (Fig. 50).

Quantitatively, the stages were separated by change points that marked instabilities in the slope coefficients (ß1) during the regression of d_s/l_s and d_s/w_s over t/t_{end}. Between the change points, the slope coefficients were significantly different irrespective of the hydrograph shape. Before the change point, over time, ß1 was >> 1, which corresponded to the conditions described in (i). After the change point, ß1 reached near zero or became negative, which corresponded to the processes formulated in (ii). Analyses to derive ß1 were performed on the detrended data.

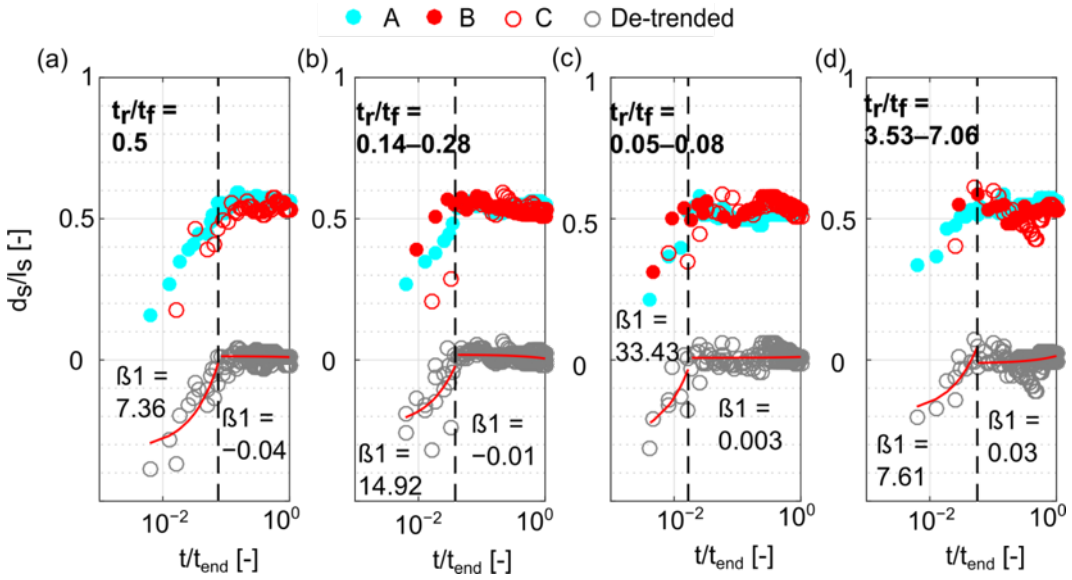


Figure 49. Geometrical relationship of d_s/l_s vs. non-dimensional time in clear-water conditions and for different hydrograph shapes: (a) symmetrical, (b) positively skewed, (c) flash flood, and (d) negatively skewed.

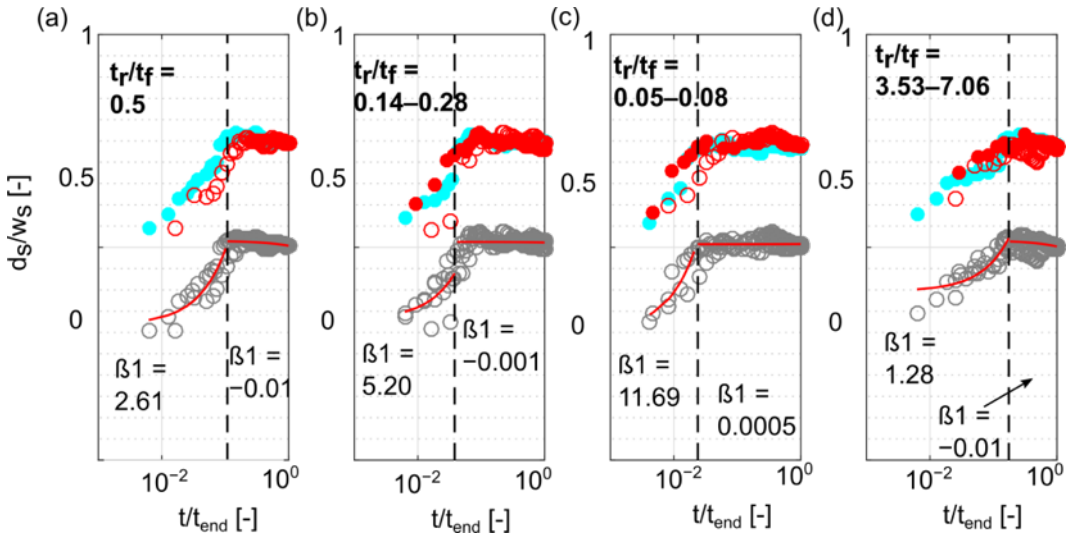


Figure 50. Geometrical relationship of d_s/w_s vs. non-dimensional time in clear-water conditions and for different hydrograph shapes: (a) symmetrical, (b) positively skewed, (c) flash flood, and (d) negatively skewed.

For different hydrograph shapes, in clear-water conditions, the occurrence of change points in d_s/l_s over t/t_{end} slightly varied, ranging from t/t_{end} = 0.0167 at t_r/t_f = 0.05–0.08 to t/t_{end} = 0.0563 at t_r/t_f = 3.53–7.06. For d_s/w_s over t/t_{end}, the change points occurred at t/t_{end} = 0.0238 to 0.175. Thus, it is proposed that two temporal stages can be described based on the geometrical relationships of the local scour hole.

The first stage is characterized by the considerable deepening of the local scour hole. The second stage is characterized by reduced deepening, while the local scour hole then widens. The presence of the two stages can be explained by the expansion of the HV during scouring, which reduced the erosive energy of the vortex and the potential of the HV to further deepen the local scour hole and vice versa (Manes & Brocchini, 2015). The further enlargement of w_s was attributed to the convection of the detached shear layers from the legs of the HV1 at the lateral sides of the obstacle, which resulted in the strong amplification of shear stress at the bed as shown by (Kirkil *et al*., 2008; Kirkil & Constantinescu, 2015). The present observation of the different stages of local scouring corresponds to results reported in Schlömer (2020) and Schlömer *et al*. (2021) and for local scouring at boulder-like obstacles exposed to long-lasting (t_{end} = 5760 min) constant discharge where substantial depth incision occurred for $t/t_{end} \leq 0.04$.

7.5.7 IMPACT OF HYDROGRAPH CHRONOLOGIES

In addition to the individual runs, the positive, negative, and flash flood hydrographs in Series C (t = 120 min) and scenario 1 were repeated three times in row (t_{end} = 480 min) to evaluate the impact of the hydrograph chronologies (i.e., the sequences of hydrographs with a certain shape) on local scouring. After each experimental run, the pump was stopped, and the flume was carefully drained. Afterwards, the flume was filled again to d_w = 2 cm before the pump was started at the q of the first hydrograph step. The procedure did not cause distortions in the local scour hole (i.e., the collapsing of the local scour hole flanks). The digital elevation models (DEMs) of the local scour hole after each hydrograph in drained conditions were derived by applying structure-from-motion multiview stereo photogrammetry (SfM-MVS), which can resolve a 3D structure from overlapped images taken from varying perspectives (i.e., camera positions), (Westoby *et al*., 2012; Smith *et al*., 2016; Morgan *et al*., 2017).

The images were acquired using a Panasonic Lumix DMC-G5 (DSLM) camera with a 4/3” (17.3 × 13.0 mm) 16 megapixel image sensor and a Lumix G-Vario 14–42 mm zoom lens set at a 21 mm focal length for minimal image distortion (35 mm full frame equivalent) (Javernick *et al*., 2014; James *et al*., 2019), capturing images at a 4608 × 3072 pixel size and at a 52° field of view. The camera was mounted on a cart ~60 cm above the flume, which corresponds to a ground sampling distance of 0.1 mm/pixel. By moving the cart along the longitudinal and horizontal axis of the flume,

nadir images (i.e., pointing below a particular direction) were captured at ≥80% side and forward overlap over the area of interest (~30 × 50 cm). Additionally, images at an oblique angle (~45° off-nadir imagery) were taken to enhance capturing the steep features of the morphology (i.e., the local scour hole). After each hydrograph, a complete data set consisted of ≥95 images captured in ≤10 min. Prior to taking images, eight ground control points (GCPs) were distributed throughout the area of interest, which consisted of coded circles with a 4 cm diameter. Target centroids were measured with the measurement technique described above to obtain the x-/y-/z-coordinates. For processing, PhotoScan software (version 1.2.6) was utilized. The SfM-MVS workflow is an iterative process that comprises of the following: (i) It includes photo alignment using a point-matching algorithm that detects key points in overlapping images and solves for the camera position and camera lens parameters; the alignment accuracy was set to "high", and pair selection was disabled (key point limit of 40,000 and tie point limit of 1000), identifying >1500 key points in each photoset. (ii) It includes georeferencing based on 2/3 of the GCPs (the remaining GCPs were used for the accuracy assessment) that optimizes the alignment and refines the camera locations by minimizing the error between the modeled locations and measured locations; according to (Lane *et al*., 2000; James *et al*., 2019), the mean error (ME) is used to estimate the accuracy, the mean absolute error (MAE) is used to estimate the nondirectional height differences, and the standard deviations (SD) are used to estimate the precision. This yielded ME = −0.003 m (x-axis), −0.001 m (y-axis), and 0.001 m (z-axis); MAE = 0.005 m (x-axis), 0.003 m (y-axis), and 0.0007 m (z-axis); and SD = 0.009 m (x-axis), 0.004 m (y-axis), and −0.001 m (z-axis). (iii) It includes the modeling of dense point clouds based on the camera locations and multiview stereo reconstruction, generating dense clouds with >8 × 106 points for each dataset; (iv) DEM generation based on dense point clouds at a 0.2 mm/pixel (subgrain size) resolution was used in each dataset to enable comparison.

Geomorphic changes caused by subsequent flood events were afterwards quantified with DEMs of difference (DoDs). DoDs were generated using Geomorphic Change Detection software (version 7) (Wheaton *et al*., 2010). Thresholds of change detection (i.e., levels of detection (LoD)) used to evaluate uncertainty were evaluated using standard Gaussian error propagation:

$$LoD = ((\delta(z)_{DEM\ t1})^2 + (\delta(z)_{DEM\ t2})^2)^{1/2} \quad \text{(Eq. 45)}$$

where $\delta(z)_{DEM\ t1}$ is the vertical error at time step 1 and where $\delta(z)_{DEM\ t2}$ is the vertical error at time step 2, respectively. Areas below LoD were considered to be noise, and areas above LoD were interpreted as topographic changes. DoDs could be constructed for a LoD = 0.1 cm. The experiments of repeated discharge revealed that the local scour hole was persistent over time, while the considerable erosion of the entire area of the local scour hole was present in DoD 1 (Fig. 51 e). The amount of erosion was decreasing in DoD 2 (Fig. 51 f). In DoD 3, deposition was dominant due to the sediment reworking at the sediment ridge, which extended in the downstream direction.

The increments of d_s and l_s were largest in the rising limb of the first hydrograph for which 80–90% of the dimensions at tend were reached. The substantial enlargement of ds and ls did not occur in the second flood event (i.e., hydrograph II). The geometrical length scales then asymptotically approached their final values at tend = 480 min irrespective of the hydrograph shape.However, a slight increase in w_s was present past hydrograph II for all the considered hydrograph shapes. The size of the geometrical length scales after hydrograph IV (i.e., 480 min) was equal to the size of the d_s, l_s, and w_s of the Series A experiments with equal experimental durations. Although d_s, ls, and w_s were cumulating, it became obvious that local scouring is a history-dependent phenomenon. Thus, a relative change in the geometrical length scales during a subsequent hydrograph event would depend on the d_s, l_s, and w_s which were reached before the occurrence of the event itself. This attribute was previously described by Tubladi *et al*. (2017) and Pizarro and Tubaldi (2019) as the so-called “memory effect” of local scouring.

7. Geometry of local scour holes at boulder-like obstacles during unsteady flow conditions and varying submergence

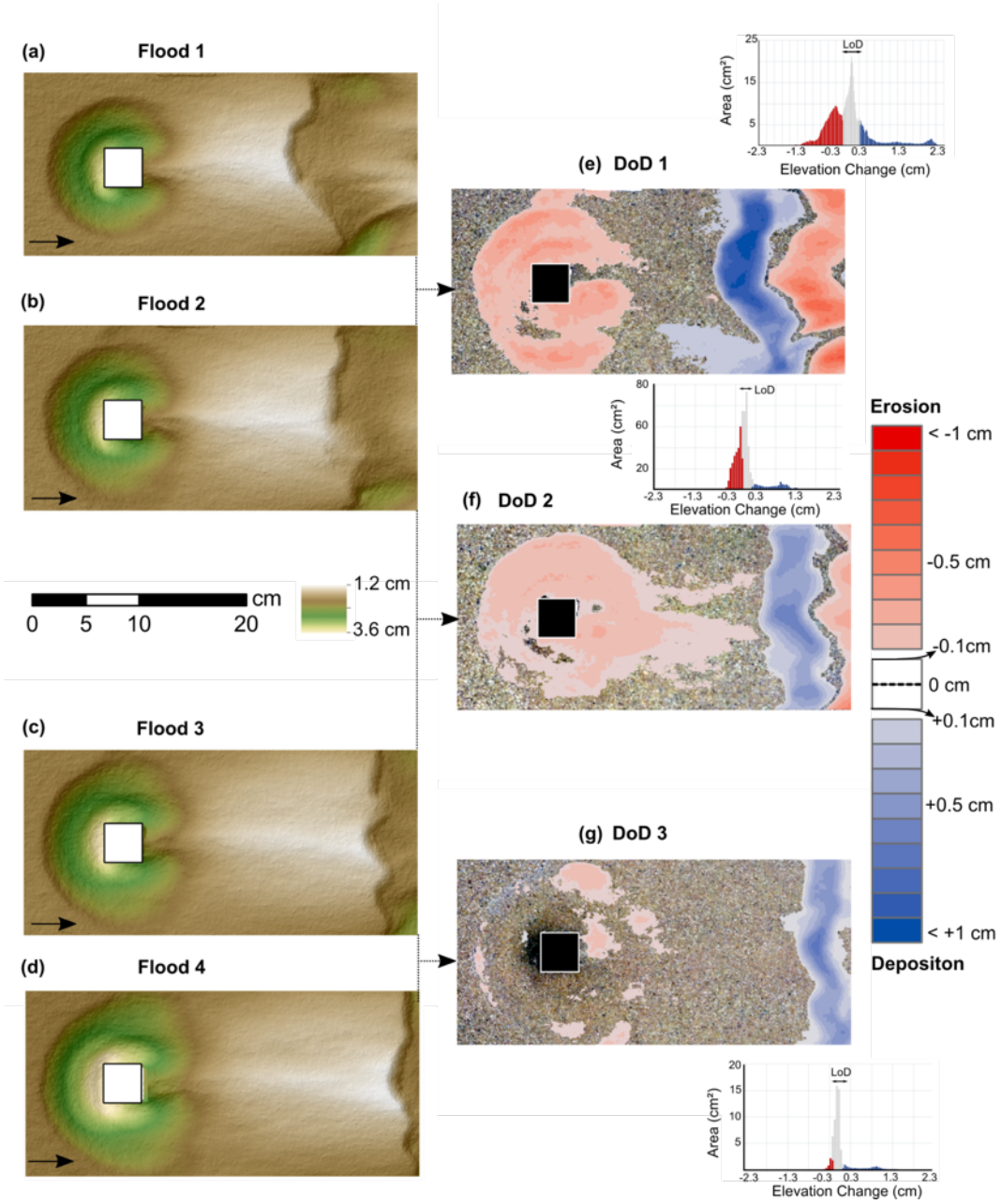


Figure 51. Modeled DEMs (a–d) and associated DoDs (e–g) for flash flood hydrographs in clear-water conditions: (a) Flood 1, (b) Flood 2, (c) Flood 3, (d) Flood 4, (e) DoD 1, (f) DoD 2, and (g) DoD 3. Arrows indicate direction of flow.

7.6 CONCLUSIONS

Local scouring at an angular obstacle was experimentally investigated for unsteady discharge and variable submergence in obstacle conditions, in clear-water conditions, and for general sediment transport. Opposite to prior studies on sediment trapping in the wake of instream obstacles, this study focused on the local scouring phenomenon. The experiments were designed to mimic local scouring at boulders in ephemeral streams affected by the occurrence of flash floods. Although only simply shaped single-peaked hydrographs were constructed, which are in contrast to the possibly infinite range of the different hydrograph shapes in natural conditions, the following conclusions considering local scouring at boulders in ephemeral streams were drawn:

(i) Considerable local scouring was attributed to the rising limb of the hydrographs when the flow depth (d_w) was comparable to the size of the obstacle (L_o), i.e., when $d_w/L_o \approx 1$. The obstacle then was unsubmerged, which had paramount impact on the size of the emerging local scour hole in depth (d_s), length (l_s), and width (w_s) because an intense downflow at the obstacle front was present due to a high pressure gradient that, in addition to a strong horseshoe vortex system (HV) at the obstacle base, favored the scouring processes. Similar conditions are described for scouring at bridge piers. The size of the local scour hole was proportional to the dimensional flow work of the hydrograph (W*) as proposed by Pizarro *et al*. (2017). With increasing submergence, in the course of the hydrograph ($d_w/L_o > 1$), local scouring eased the downflow while the HV also weakened. Therefore, it is supposed that, with dependence on the flow depth, the peak flow of a flood might only marginally impact the size of the local scour hole if the obstacle is fully submerged, which is in contrast to bridge pier scouring.

(ii) Up to 80% of the local scour hole size at the end of the experimental runs was reached in only 10% of the experimental runtime, and the shape of a hydrograph in terms of its skewness played an important factor. The steeper the rising limb, the quicker the size of d_s, l_s, and w_s matured. The enlargement of l_s and w_s was therefore attributed to the deepening of the local scour hole, which undermined the local scour hole slopes and induced gravitational movements. A simple mechanistic model was presented that assessed local scour hole volume over time

based on the scour depth, the inclination of the local scour hole slopes, and the span of the local scour hole bottom.

(iii) Two temporal evolution stages of the local scour hole were identified based on its geometrical relationships (d_s/w_s and d_s/l_s). It is speculated that the geometrical relationship of preserved local scour holes at boulder obstacles located in ephemeral streams may be used as a length scale to plausibly estimate the minimum duration of the rising limb of a flood hydrograph.

(iv) The experimental runs on the impact of the discharge chronologies in clear-water conditions revealed that local scour holes are transient bed features in the sense that they persist as long as the obstacles that create them are present. However, boulders are mobile, and scouring can cause tilting and the self-burial of the obstacle. Additionally, general sediment transport during floods and the passage of bedforms might cause the disappearance of the entire structure.

(v) Local scouring is history-dependent on subsequent hydrograph events, and memory effects are present that describe the dependence on the antecedent sizes of d_s, l_s, and w_s. The greatest impact on the size of the local scour hole was attributed to the rising limb of the initial hydrograph event for which 80–90% of the dimension at the end of the experiments was attained.

However, the validity of the experimental results is restricted to the case of local scouring at a solitary boulder-like obstacle. If an array of boulders is present, the boulder spacing is supposed to be a key variable that has an effect on the flow field and sediment transport processes and vice versa. Therefore, future research should focus on the impact of boulder spacing on local scouring processes and the bed shear stress distribution within the array under variable boulder spacing. Insights into the latter would allow for the physically based correction of the bed shear stress used.

8. ON THE USAGE OF LOCAL SCOUR HOLES AT BOULDERS FOR FLOW RECONSTRUCTION IN EPHEMERAL STREAMS

ABSTRACT

Local scour holes are sedimentary bedforms that form in front of an obstacle, such as a boulder, and are exposed to a current. Consequently, they are pertinent to a number of scientific disciplines within the fields of Earth science and hydraulic engineering. They are frequently documented in the context of ephemeral streams subjected to flash floods, yet there is a paucity of knowledge regarding their utility as hydraulic indicators of historical flood events. This study presents a novel framework for reconstructing the most likely flow conditions in terms of flow depth, velocity, and duration during formation based on preserved local scour hole geometries at boulders. This framework is based on an empirical approach combining laboratory and field data. The approach is based on the identification of a knickpoint in the local scour hole slope, initially discerned in laboratory studies, which can be corroborated at obstacle marks in the field. The knickpoint represents a measure of the diameter of the primary horseshoe vortex at the obstacle base, which serves as the primary driving force behind local scouring. The diameter of the knickpoint correlates with the depth of the approaching flow, the depth of the local scour hole, and the size of the obstacle. The framework was applied to ten local scour holes at boulders in the ephemeral Rambla de la Viuda. The estimated flow depths derived from the local scour hole geometry ranged from 0.6 to 1.9 metres during the rising limb hydrograph. The reliability and scale-invariance of these reconstructions have been corroborated by analogous results of velocity estimations obtained through alternative approaches at the same location. It is proposed that the present approach is also applicable in ungauged basins for estimating flow depth from local scour hole geometry.

This chapter has been submitted for revision in:
Schlömer, O., Herget, J., and Benito, G. (2025) On the usage of local scour holes at boulders for flow reconstruction in ephemeral streams. Submitted to *River*.

8.1 INTRODUCTION

Local scour holes are conical depressions upstream of instream boulders, often found in semiarid environments (Carling & Leclair, 2019; Karcz, 1968, 1972). In interaction with the adjacent depositional region in the wake of the obstacle, known as the sedimentary ridge, they are referred to as obstacle marks (Richardson, 1968). The obstacle itself is considered an integral part of the structure and consists of a large bed obstruction (i.e. boulder), typically with a diameter greater than the grain size of the surrounding non–cohesive alluvium (Allen, 1984), (Fig. 52). Local scour holes are formed at the boulders due to flow separation and acceleration leading to sediment mobilisation. This process results in the emergence of three-dimensional vortical structures. The phenomenon of local scouring has been extensively researched at man-made infrastructure in streams, including bridge piers and groynes, due to safety concerns (Melville & Coleman, 2000; Pizarro *et al*., 2020). Thus, it is established that the rising limb and peak flow have the greatest impact on local scouring, whereas the time to reach a near-steady state of local scouring is usually smaller than the flood duration.

In semiarid ephemeral streams local scouring at boulders is triggered by flash floods, i.e., a flow of water that arrives suddenly at a fixed point, changes rapidly in velocity and flow depth, and lasts a short time (Alexander & Cooker, 2016). These conditions are commonplace in Ramblas, Mediterranean gravel-bed streams in Spain, as documented by Benito *et al*. (2020) and Machado *et al*. (2017). These Ramblas, are modest in size and have a short length of less than 100 km. They drain small catchments of several hundred km^2 and rely on intense rainfalls to generate streamflow (Camarasa Belmonte & Segura Beltrán, 2001). Preserved obstacle marks at boulders have been described from Rambla de la Viuda, one of the largest ephemeral rivers in the Valencia region, eastern Spain (Euler *et al*., 2017).

Obstacle marks have been identified as remnants even of large-scale floods (Herget, 2005; Wells *et al*., 2022). While sedimentary bedforms, such as dunes (Bradley & Venditti, 2017; Carling, 1996) and antidunes (Froude *et al*., 2017; Shaw & Kellerhals, 1977), have been used to reconstruct flow patterns, obstacle marks were not commonly used to reconstruct flow conditions during their formation. A first quantitative framework for reconstructing the mean velocity of approach flow from preserved local scour holes at solid solitary boulders was presented by Herget *et al*. (2013). Besides considerable progress, this framework is linked to uncertainty regarding

the depth of mean flow during formation, which is a crucial hydraulic boundary condition for the local scouring process at boulders during flash floods. This is because the boulder may undergo unsubmerged (where some portion of the obstacle protrudes above the water surface) or submerged conditions during the event.

Small-scale laboratory experiments investigating mark formation on obstacles during simulated flash floods demonstrate that the size of vortical structures within the local scour hole is affected by the depth of the approach flow (Schlömer & Herget, 2023, 2025). Moreover, Dey and Raikar (2007a) and Muzzammil and Gangadhariah (2003) have shown that the size of vortical structures is evident in the morphological characteristics of the local scour hole. By comparing small-scale local scour holes at boulder-like obstacles with *in situ* local scour holes at boulders at field scale, Schlömer *et al*. (2021) demonstrated the scale-invariant nature of the geometry. Thus, the starting hypothesis is that preserved obstacle marks are suitable indicators for the estimation of flow depth during their formation. The case study for testing this hypothesis are persistent obstacle marks at boulders in Rambla de la Viuda. The specific aims of the study are:

(i) To estimate flow depths from given local scour hole geometry based on an empirical approach merging laboratory and field-scale data.

(ii) To refine an existing framework for the quantitative hydraulic interpretation of obstacle marks.

(iii) To discuss limitations of the presented approach.

Prior to presenting estimations of the most probable flow depths during local scour hole formation, which are based on field evidence from boulders in Rambla de la Viuda, a review on the geometry of local scour holes and sediment ridges as well as the turbulent flow field in their surroundings is provided. Additionally, the mean approach flow velocity is calculated based on obstacle mark geometry and is verified for plausibility through comparison with alternative flow reconstruction methods, specifically Manning's equation. Finally, this paper considers the limitations of the improved framework for reconstructing flow properties based on preserved obstacle marks at boulders.



Figure 52. Obstacle mark at a boulder in the Rambla de la Viuda (OM5). Arrow indicates direction of flow. The width of the boulder perpendicular to the flow is 2.7 m

8.2 REVIEW ON OBSTACLE MARKS AT BOULDERS

8.2.1 GEOMETRY

The morphology of local scour holes from laboratory experiments as well as *in situ* local scour holes in the field can be characterised by certain morphometric variables, including scour hole depth at the obstacle front (d_s), measured from the undisturbed upstream bed; scour hole frontal length (l_s) in the plane of symmetry to the incoming flow, measured from the obstacle front to the upstream edge of the scour hole; and scour hole frontal width (w_s), measured perpendicular to the incoming flow from the lateral edges of the scour hole at the obstacle front (Fig. 4). A corresponding definition can be applied to the sediment ridge, including sediment ridge height (h_r), sediment ridge width (w_r) and sediment ridge length (l_r), measured from the downstream end of the obstacle (Euler & Herget, 2012).

Considering a cross–sectional profile from the obstacle front to the upstream edge of the local scour hole (i.e. l_s) a segmentation to the local scour hole slopes is obvious (Fig. 6). These segments consist of: (1) a flat semi–circular scour hole bottom (S_b) that is closely attached to the obstacle base with radius < l_s; (2) an inner frontal scour hole (lower slope) that is characterized by an inclination ≥ critical angle of repose (Φ_{crit}); and (3) an outer frontal scour hole (upper slope) that is characterized by an inclination ≤ Φ_{crit}. The transition between both slopes is marked by a knickpoint (or berm) in the cross–sectional profile.

The segmentation is the consequence of the so–called horseshoe vortex system (HV), an unsteady turbulent necklace–like vortical structure at the obstacle base (Hajimirzaie *et al*., 2014; Shamloo *et al*., 2001). The HV consists of two interacting and

unsteady vortices (Chen *et a*l., 2019; Kirkil & Constantinescu, 2010). The largest and most stable vortex is denoted as the primary horseshoe vortex (HV1), which is located close to the obstacle base. Upstream, a smaller and less coherent vortex (HV2) is located within the outer region of the local scour hole.

Muzzammil *et al*. (2004) used the segmentation of the local scour hole to derive the mean diameter of HV1 (D_v) by:

$$D_v = 2a\ 2b \quad \text{(Eq. 46)}$$

with a = major horizontal axis of the vortex (x–plane), and b = vertical axis of the vortex (z–plane) assuming an elliptical shape of the vortex. Thereby, the longitudinal axis of the vortex (a) equals the distance from the obstacle frontal face to the onset of the berm in the local scour hole slope, while the vertical axis of the vortex (b) is equal to the height of the berm's onset relatively to local scour hole depth (d_s) in S_b. Based on a laboratory investigation in a solidified local scour hole they found that the horizontal and vertical dimensions of HV1 are governed by the obstacle geometry (i.e. obstacle width) and the thickness of the approaching boundary layer (i.e. flow depth).

8.2.2 FORMATION DURING FLASH FLOODS

Assuming no baseflow, the initial requirements for obstacle mark formation at boulders exposed to flash floods are:

(A) the impulsive and drag forces exerted by the approaching flood front do not move the boulder (Greenbaum *et al*., 2020; Huber *et al*., 2020), but the relation of mean approaching flow velocity (U_m) to critical mean approach velocity for entrainment of bed sediment (U_c) is greater than 0.3–0.5 (Chiew, 1995; Simarro *et al*., 2007).

(B) The size of the boulder in relation to the size of sediment (typically D_{50}, measured in m) in which the obstacle is embedded in is greater than 8 (Lee & Sturm, 2009; Schlömer *et al*., 2020).

If the relative coarseness (L_o/D_{50}) < 8 local alluvial sediment particles are too coarse compared to the obstacle size and inhibit local scouring completely, because of the dissipating effects of large sediment particles on the responsible hydrodynamic processes. The size of the boulder in this context is operationalized by the characteristic length scale of the obstacle front ($L_o = h_o^{\alpha}\ w_o^{\beta} = h_o^{2/3}\ w_o^{1/3}$),

with $\alpha + \beta = 1$ (Oliveto & Hager, 2002), because boulders are exposed to unsubmerged and submerged conditions. Submergence is therefore defined as ratio of approaching flow depth (d_w) to size of the boulder (L_o).

For the beginning stages of the rising hydrograph limb, when the boulder is unsubmerged, the following hydrodynamic processes are common:

(i) Contraction of streamlines lateral to the boulder that causes higher flow velocities at the lateral edges of the obstacle;

(ii) Formation of a vertical jet–like downflow towards the bed that emerges due to the pressure gradient at the obstacle frontal face;

(iii) Formation of a horseshoe vortex system (HV) at the obstacle base (Dargahi, 1990).

Processes (i) to (iii) enhance the bed shear stress above the critical bed shear stress for sediment mobilization, inducing local scouring in front and laterally to the obstacle, even though there is no general sediment movement in the surroundings. The HV1 is the main driver of sediment mobilization in the vicinity of the obstacle (Dargahi, 1989; Li *et al*., 2018). During incision, the HV sinks into the emerging local scour hole, where it promotes sediment mobilization by saltation and rolling (Guan *et al*., 2019). At boulders embedded in non–cohesive sediments this undermines the obstacle which then induce movement (Rennie *et al*., 2017). This movement is characterized by (i) upstream tilting of the obstacle relative to its origin position against the direction of flow and (ii) self–burial of the obstacle, i.e. a reduction of h_o relative to h_o prior to the onset of local scouring. Processes (i) and (ii) alter the boulder's exposure to flow due to inclination of the obstacle's frontal face into the upstream direction, and by reducing the height of the obstacle protruding into the flow. Both processes significantly decelerated frontal scour hole incision in time (Schlömer *et al*., 2021).

The enlargement of l_s and w_s is directly related to deepening and, occasionally, to the weakening of the HV, which destabilizes the scour slopes and results in gravity mass movements. From a laboratory study by Schlömer and Herget (2023) on local scouring at boulder like obstacles during unsteady flow it is known that considerable enlargement of the local scour hole occurs only at the rising limp, when the flow depth (d_w) was comparable to the size of the obstacle (L_o), i.e., when $d_w/L_o \approx 1$. As the obstacle becomes fully submerged (i.e. when $d_w/L_o > 2$), local scouring processes weaken, irrespective of approaching flow velocity. The approaching current then predominantly flows over the obstacle, which reduces downflow and the erosive capacity of the HV at

the obstacle front (Du & Liang, 2019). Additional vertical structures become dominant. The flow separation at the obstacle's top causes an arch–shaped vortex consisting of two lateral vortices at the obstacle's sides, along with a vortex situated at the crest of the obstacle (Dey *et al*., 2011; Pattenden *et al*., 2005). Generally, local scour exhibits a non–linear evolution over time, ultimately reaching a steady state in which geometric length scales do not increase further. From laboratory studies it is known that up to 80% of the local scour hole size at the end of the experimental runs are reached in only 10% of the experimental runtime (Melville & Chiew, 1999).

8.3 STUDY AREA

8.3.1 RAMBLA DE LA VIUDA

Field evidence on obstacle marks was investigated in the Rambla de la Viuda, a 36 kilometer long ephemeral gravel bed river located in eastern Spain that drains a catchment area of 1523 km^2. Rambla de la Viuda is composed of two main tributaries: Montlleó River and Rambla Carbonera. Both their headwaters are located at the Iberian Range Mountains at 1250–1720 m above sea level, while Rambla de la Viuda flows into the Mediterranean Sea. The study sites were situated upstream of the Maria Cristina reservoir which is located approximately 12 kilometres upstream of the river mouth. In this section Rambla de la Viuda has a meandering river planform. The study reaches (Reach I and Reach II, 70–100 m in width) were separated by a meander arc while their floodway was straight (Fig. 53). Like many streams in the Mediterranean region, Rambla de la Viuda has been affected by intense gravel mining in the second half of the 20th century which has produced a flat valley bottom (Calle *et al*., 2015). Boulders with a diameter greater than 1 meter at their widest are remnants from the extraction processes and are responsible for the formation of obstacle marks (Euler *et al*., 2017). Rambla de la Viuda is susceptible to flash floods, whilst stream flow occurs for an average of 20 days annually. Individual flash floods (duration of a few hours to days) occur as consequence of intensive rains, exceeding a run-off threshold of 65 mm (Segura-Beltrán & Sanchis-Ibor, 2013). The run-off threshold can fluctuate between seasons based on soil moisture levels and the frequency of rainfall (Lotsari *et al*., 2018). The mean annual precipitation in the watershed ranges between 450 and 600 mm with a main rainy season in autumn and spring. The heaviest floods on record occurred in October 1962, October 2000, December 1989, and October 1969, with mean daily

discharges of > 640, 385, 286, and 238 m^3/s, respectively (Calle *et al.*, 2017; Calle *et al.*, 2020)

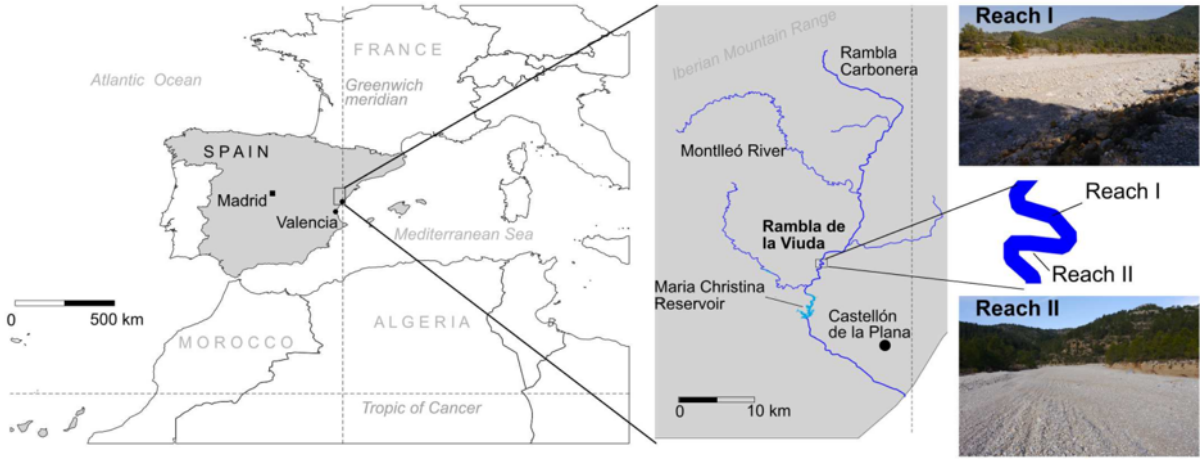


Figure 53. Map of the study area at Rambla de la Viuda (Spain) View in the study reaches is downstream.

The first field campaign took place in March 2018, during which obstacle marks were identified and their morphology was measured using tape measures and laser distance meters. For the 2013-2018 period, only flood events with discharges ≤ 100 m^3/s have been registered at the Maria Christina gauging station (Fig. 54). The most considerable discharge event occurred at the beginning of April 2015 were a peak discharge of 99.46 m^3/s was obtained on March 23th as consequence of intense rainfall. The hydrograph of this event (Fig. 54 b) is typical for a flash flood, as it nearly instantaneously peaked. The stream flow lasted for 14 days after the peak on the falling limb of the hydrograph. In autumn of the same year an additional flood with a peak discharge of 77.13 m^3/s occurred in November starting from no baseflow (Fig. 54 c). Past the 2015 events several smaller events were registered after the with peak discharges < 40 m^3/s.

It is therefore assumed that the events of 2015 and subsequent years have affected the obstacle mark under study. In March 2019 the obstacle marks where again surveyed with a geodetic total station. In between March 2018 and March 2019 no significant modifications to the obstacle marks could be visually detected.

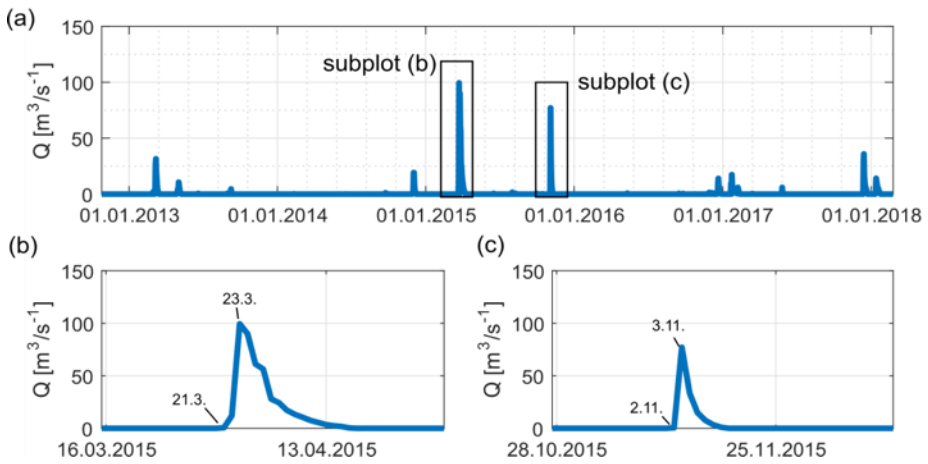


Figure 54. The registered daily mean discharge at the Maria Christina Reservoir from 2013 to 2018. The data was sampled by the Júcar River Basin Authority (Confederación Hidrográfica del Júcar).

8.4 Methods and Data

8.4.1 Framework for flow reconstruction

Obstacle mark geometries at boulders are operationalized to estimate (i) flow depth, and (ii) mean flow velocity as hydraulic boundary conditions during their formation.

Based on a multiple linear regression of laboratory data on obstacle mark formation, Schlömer and Herget (2025) found that D_v could be estimated by:

$$D_v = -0.325\ d_w + 1.26\ L_o + 0.92\ d_s$$

(Eq. 47)

To reconstruct (i) the dataset was re–evaluated to derive a relation using D_v, L_o and d_s as independent variables and d_w as the dependent variable. This procedure was chosen, because a rearrangement of equation (47) would introduce a significant bias (Williams, 1983). Besides laboratory data we have included field data on obstacle marks at boulders in the Colorado River (L_o = 2-6 m; d_s = 2-5 m; D_v = 2-8 m; d_w = 4-8 m), (Schlömer *et al*., 2021). The re-evaluation yielded the following relation that is further used in analysis:

$$d_w = e^{\ln(0.47\ D_v)} + e^{\ln(2L_o)} - e^{\ln(2.8d_s)}$$

(Eq. 48)

with *e* as Euler's number and ln as natural logarithm. The correlation coefficient (R^2) of equation 48 is 0.9, which is acceptable in the absence of other alternatives.

Equation (48) applies in situations where a fully established HV system is present, which becomes evident in the local scour hole geometry. This is usually achieved within the first four to five hours of local scouring, regardless of steady or unsteady flow conditions (Schlömer & Herget, 2023). To reconstruct (ii) during obstacle mark formation a procedure by Euler and Herget (2012) and Herget *et al*. (2013) was applied that proposed:

$$U_m = d_s^2 \, \sigma_G \, (d_w \, g)^{1/2} \, (10(L_o \, 0.4)^2)^{-1}$$

(Eq. 49)

with U_m as mean approach flow velocity, σ_G as gradation coefficient of sediment $(D_{84}/D_{16})^{1/2}$, and g as gravitational acceleration. For the current study, we utilised d_w in equation (49) as assessed by the estimates derived from equation (48). To ensure the plausibility of our results, we estimated U_m during peak flow by applying the Manning equation (Chow, 1988) and utilizing high–water marks on the channel banks (Baker, 1987), instead of relying on obstacle mark characteristics:

$$U_m = R^{2/3} \, S^{1/2} \, n^{-1}$$

(Eq. 50)

with R as hydraulic radius (A/P), where A is the cross–sectional area of flow and P is the wetted perimeter, S as slope of the energy line, and n as empirical hydraulic roughness coefficient. Estimates by equation (48) to (50) where than used for discharge estimations (Q) based upon the continuity equation $Q = U_m A$

8.4.2 FIELD METHODS

Obstacle marks within the study reaches were analyzed with respect to geometry and size of the local scour hole, size and shape of the obstacle, as well as grain size in, on and around the obstacle mark. A Zeiss Elta C30 total station that worked in a local coordinate system was used to: (i) measure the geometrical length scales of the local scour hole, (ii) measure maximum height and width of the boulder's exposed front, (iii) measure longitudinal profiles of the local scour hole from the upstream edge of the depression to the obstacle's frontal face, and (iv) measure cross–sectional profiles of the reaches.

The cross sectional profiles originated at ubiquitous jetsam deposits of woody debris those were present in shrubs and trees at the both banks of the channel. For three

well preserved obstacle marks the entire morphology was captured by aerial photos to derive digital elevation models (DEM) by applying structure–from–motion multiview stereo photogrammetry (SfM–MVS) from overlapped images taken from varying camera positions (Eltner & Sofia, 2020; Morgan *et al*., 2017; Smith *et al*., 2016; Westoby *et al*., 2012). For this, a DJI Phantom III© drone equipped with a 1/2.3" (6.17 x 4.56mm) CMOS image sensor was used. The focal length is 3.6mm, giving a 94° field of view. The camera produces images of 4000 x 3000 pixels. The altitude of the drone was between 8 and 10 m above the ground, resulting in a ground sampling distance of 0.34 to 0.64 cm/pixel. First, a set of nadir images (i.e., pointing below a specific direction) were acquired with ≥80% lateral and forward overlap over the area of interest (James *et al*., 2019; Javernick *et al*., 2014). In addition, images were taken at an oblique angle (~45° off-nadir images) to better capture the steep features of the morphology (i.e. the local scour hole). In total, 40 to 70 photographs were taken for each obstacle mark. Prior to image acquisition, 10 to 14 ground control points (GCPs), consisting of 30 cm diameter coded circles, were distributed throughout the area of interest. The centroids of the targets were measured with a total station to obtain x/y-/z-coordinates in a local coordinate system. The current streambed elevation was therefore taken as height reference (i.e. z = 0 m).

Processing was carried out using PhotoScan software (version 1.2.6), which uses a point matching algorithm that detects key points in overlapping images and solves for the camera position and lens parameters to produce point clouds. The point clouds were georeferenced using 2/3 of the GCPs. The remaining GCPs were used for accuracy assessment (Lane *et al*., 2000). For processing, PhotoScan software (version 1.2.6) was utilized. The SfM-MVS workflow is an iterative process that comprises of the following: (i) It includes photo alignment using a point-matching algorithm that detects key points in overlapping images and solves for the camera position and camera lens parameters; the alignment accuracy was set to “high”, and pair selection was disabled (key point limit of 40,000 and tie point limit of 1000), identifying >1500 key points in each photoset. (ii) It includes georeferencing based on 2/3 of the GCPs (the remaining GCPs were used for the accuracy assessment) that optimizes the alignment and refines the camera locations by minimizing the error between the modelled locations and measured locations.The mean error (ME) is used to estimate the accuracy, the mean absolute error (MAE) is used to estimate the nondirectional height differences, and the standard deviations (SD) are used to estimate the precision. This yielded ME = −0.04 m

(x-axis), −0.04 m (y-axis), and 0.05 m (z-axis); MAE = 0.05 m (x-axis), 0.06 m (y-axis), and 0.04 m (z-axis); and SD = 0.07 m (x-axis), 0.06 m (y-axis), and 0.04 m (z-axis).

DEMs with a resolution of 4 to 6 mm/pixel (sub-grain size) could be derived from dense point clouds. The grain size distribution of the surface layer within the local scour hole and around the obstacle mark were estimated based on image data. The images were captured using a Panasonic Lumix DMC–G5 (DSLM) camera with a 4/3" (17.3 × 13.0 mm) 16 megapixel image sensor and a Lumix G–Vario 14–42 mm zoom lens set at a 21 mm focal length. In each image a clearly visible scale bar was placed that was used as calibration. Gravelometric analysis was later performed by the automatic object detection software BASEGRAIN (Detert & Weitbrecht, 2012, 2020). Grain size estimation based on images was preferred over the volumetric sampling methods in order to reduce the effort and time involved in collecting data by hand.

8.5 RESULTS AND DISCUSSION

8.5.1 OBSTACLE MARKS AT RAMBLA DE LA VIUDA

In total 14 obstacle marks at boulders could be detected at the study reaches (five in Reach I, nine in Reach II). The boulders were randomly distributed across the entire width of the channel (70 to 100 m wide). Only obstacle marks that did not obstruct each other were investigated. An overview of the obstacle marks that were surveyed is included in Table 11.

Although obstacle marks in the field were not as well–defined as those in the laboratory, the spatial extent of the local scour hole in front of and alongside the boulders was clearly discernible. Contrarily, it proved difficult to discern the exact reach of the sediment ridge in the trail of the boulder due to its assimilation with the downstream gravel bars and lobes. Thus, the present analysis focuses on the geometry of the local scour holes. All the local scour holes were in a state where they had already surrounded the boulders in front and expanded in downstream direction as depicted in Fig. 55 that shows two DEMs derived from drone flights and SfM-MVS analysis. The morphology of the local scour hole could be taken as an indication that suitable hydraulic boundary conditions for local scouring (i.e. $d_w/L_o \approx 1$, $U_m/U_c > 0.3 – 0.5$, $D_{50}/L_o > 8$) may have prevailed for a sufficiently long time. According to laboratory observations, local scour starts at the lateral edges of the obstacle to the incoming flow with two small depressions, which then merge into a single frontal scour hole within the first two hours of local scouring (Link *et al*., 2008). The HV is then fully developed within the local scour hole. Substantial local scour hole enlargement is observable within the first 4 to 5 hours.

Table 11. Surveyed obstacle marks in Rambla de la Viuda. † Coordinates in WGS 84.

ID	h_o (m)	w_o (m)	L_o (m)	d_s (m)	w_s (m)	l_s (m)	Lat.†	Lon.†	Reach
OM1	0.55	2.45	0.9	0.4	1.2	4.6	40.111131	–0.141434	II
OM2	1.04	1.09	1.06	0.5	1	2.5	40.110893	–0.141541	II
OM3	0.88	2.04	1.16	0.3	0.8	3	40.110917	–0.140333	II
OM4	0.77	1.35	0.93	0.4	1	4	40.110811	–0.138559	II
OM5	0.95	2.67	1.34	0.8	1.5	3.4	40.111000	–0.140361	II
OM6	0.85	1.8	1.09	0.5	1.4	3.6	40.115250	–0.142556	I
OM7	0.68	1.53	0.89	0.4	1.3	3	40.114060	–0.140168	I
OM8	0.44	2.55	0.79	0.4	1	2.2	40.113445	–0.138730	I
OM9	0.56	2.5	0.92	0.4	1.2	4.7	40.110909	–0.137539	II
OM10	1.10	1.30	1.16	0.4	0.9	2.2	40.110967	–0.138365	II
OM11	0.92	1.80	1.66	0.5	3.6	1.4	40.113722	–0.140417	I
OM12	0.47	0.80	0.82	0.2	1.4	0.4	40.113806	–0.140389	I
OM13	1.0	1.53	1.50	0.4	1.3	3	40.110833	–0.138556	II
OM14	0.85	2.45	1.45	0.4	1.2	4.6	40.110917	–0.140000	II

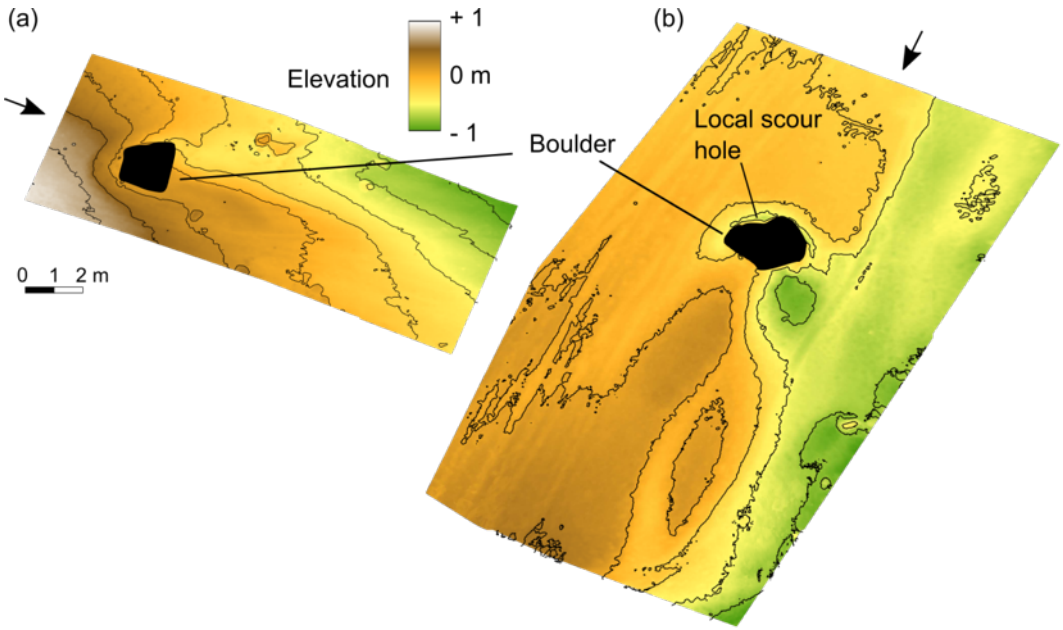


Figure 55. DEM of OM2 (a) and OM8 (b). The distance between isolines is 0.25 m. Arrow indicates direction of flow.

Local scour holes were found at boulders with widths ranging from 0.8 to 2.7 metres perpendicular to the incoming flow. The shape of the obstacle's front varied from almost rectangular to round. Boulders were relatively squat as their height only ranged from 0.6 to 1.1 metres above the current streambed. The effective obstacle size (L_o) therefore ranged between 0.8 to 1.5 metres. The relatively low exposed height of the obstacles indicates their self-burial due to local scouring. Consequently, there could have been a decrease of ho in comparison to its initial value before the commencement of local scouring. This hypothesis is substantiated by the findings on nearly rectangular obstacles, where the frontal face was inclined upstream.

Nevertheless, the depth of the local scour holes (d_s) was comparatively shallow, ranging from 0.3 to 0.8 metres, when compared to local scour hole width (w_s) (2.2 to 4.6 metres) and local scour hole length (l_s) (0.5 to 1.5 metres). Long and wide frontal scour holes that are relatively shallow are also documented for local scour holes at boulders in the Colorado River (Schlömer *et al*., 2021) and around bridge piers in New York streams (Butch, 1991). Butch (1999) reported w_s to be 4.7 times ds.

Shallow scour holes may result from general sediment transport that occurs in conjunction with local scouring at the rising limb and during peak flow. This is a more plausible boundary condition than a limited thickness of the alluvial layer in Rambla de la Viuda. Calle *et al*. (2017) discovered that despite gravel mining and channel degradation, the large magnitude flood in 2000 led to an increase in alluvial deposition in Rambla de la Vidua. This is likely to have resulted in a thickness of over one meter, measured from the current streambed elevation to the underlying bedrock.

Sediment transport in the local scour hole leads to filling and a decrease in d_s, if the hydraulic variables under specific boundary conditions are insufficient to move the sediment any further (Hong *et al*., 2017). For six obstacle marks coarser sediment (D_{50} > 100 mm) than in upstream of the structure was found in the scour hole bottom (S_b). It is hypothesised that this coarser sediment was transported into the emerging local scour hole in course of the 2015 flood events while subsequent floods in 2017 and the beginning of 2018 could not mobilize the sediment any further. Calle *et al*. (2015) quantified that 12-41 mm sized gravel (D_{50}) in Rambla de la Viuda are already transported for discharges of 13- 23 m^3/s. The flood that occurred at the beginning of 2018 had a peak discharge of 36 m^3/s at the Maria Christina Reservoir. As a result, the armour layer (Dey & Raikar, 2007b) sediment could not be mobilised any further, and ongoing local scouring was inhibited under given hydraulic boundary conditions.

However, it remains an open question whether the coarse sediment was transported during local scour hole formation on the rising limb, or during the declining flood hydrograph. Nevertheless, there is a linear relationship of l_s and w_s to d_s for the field evidence, where w_s and l_s scale with ds which is common to local scouring at steady und unsteady flow conditions (Schlömer & Herget, 2023) (Fig. 56).

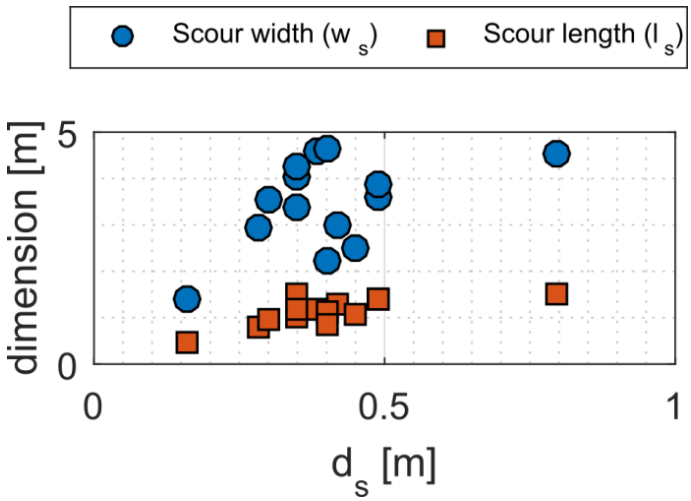


Figure 56. Morphometric relationship of the geometrical length scales of the local scour holes at boulders in Rambla de la Viuda.

In both reaches the grain size downstream of the boulders was finer compared to the upstream part. In Reach I the average D_{50} was 22 mm upstream of the boulder and 16 mm downstream. In Reach II the average D_{50} was 21 mm upstream and 19 mm downstream of the boulder. The deposition of finer material downstream of the boulder is associated to a recirculating, low-energetic flow pattern in the wake of the obstruction that favours deposition there (Papanicolaou *et al*., 2012; Thompson, 2008).
However, the sediment distribution in both reaches must be considered as non–uniform. For Reach I, the median gradation coefficient (σ_G) was 3.2 while it was 3.7 in Reach II.

8.5.2 Estimation of horseshoe vortex size

Ten out of 14 obstacle marks showed the internal differentiation into inner and outer local scour hole, which is known from laboratory experiments. The differentiation is based on the local scour hole slopes, which distinguish a flat region close to the obstacle base (S_b) and two slope segments of different inclination separated by a knickpoint or berm that was clearly visible and persistent even in drained conditions (Fig. 57). The position of the berm in vertical and horizontal position could be

determined from a cross–sectional profile form the outer edge of the local scour hole to the obstacle front in the plane of symmetry to the approaching flow. The 2D cross–sectional profile was measured with the total station in a local coordinate system, with the obstacle front marking the origin. The profile was measured at the beginning of each local scour hole measurement. The profiles displayed varying inclinations across slope segments.

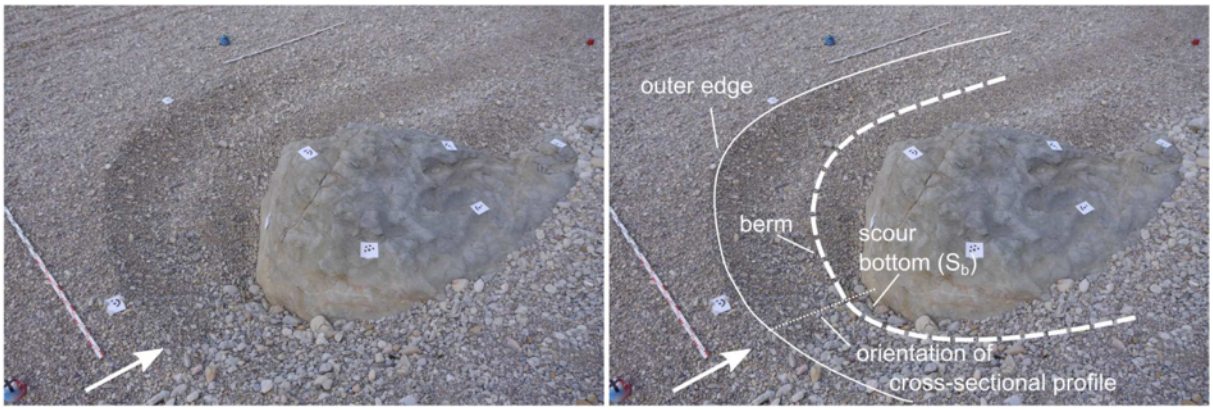


Figure 57. Persistent segmentation of local scour hole slope at a boulder in Rambla de la Viuda (OM13). Arrow indicates direction of flow. Scale bar is 2 metres.

The segment spanning from the outer edge to the beginning of the berm demonstrated a moderate inclination (12 to 23° from the horizontal). Meanwhile, from the berm towards the obstacle front, the inclination intensified, reaching values of 30 to 35° (Fig. 58). As known from Link *et al*. (2008) the knickpoint itself is a function of d_s and the critical angle of repose (Φ_{crit}) of the given sediment size. During scouring the lower slope is governed by the rotation of HV1 and by tendency stabilized at $\Phi > \Phi_{crit}$, while the upper slope adjusts to the angle of repose by gravitational movements. The mean diameter of HV1 (D_v) was estimated using equation (47), with the position of the berm as the reference point. The horizontal axis of the vortex was determined by measuring the distance from the obstacle's frontal face to the onset of the berm. The vertical axis was estimated based on the height of the berm's onset relative to d_s. The estimated D_v ranged from 0.18 to 0.40 m. As briefly mentioned in the beginning, the mean diameter of HV1 is dependent on obstacle geometry and flow depth. Therefore, the range of observed D_v estimates seems probable given the varying size of the boulders.

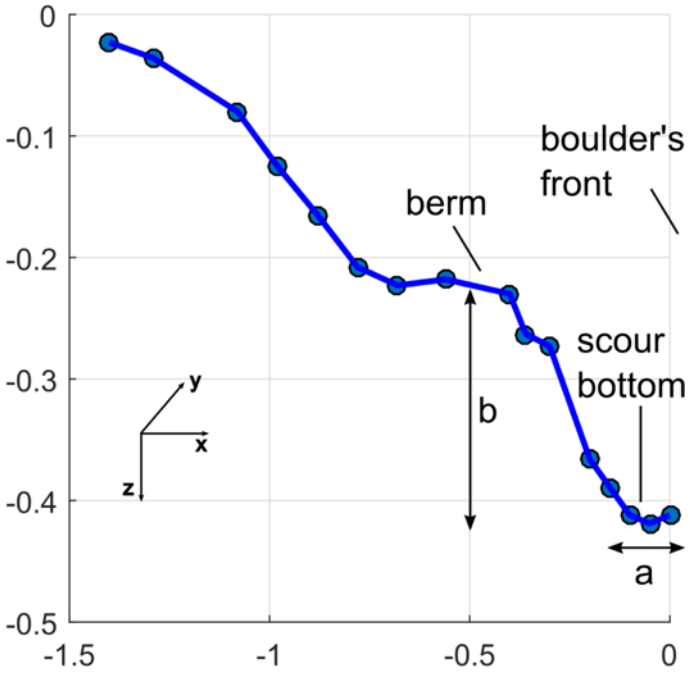


Figure 58. Longitudinal cross-section of the local scour hole (OM7) indicating position for axis estimation of D_v (a and b). Flow is from left to right. Scale is in metres. Points are measurements that are connected through interpolated line.

8.6 ESTIMATION OF HYDRAULIC BOUNDARY CONDITIONS

8.6.1 ESTIMATION OF FLOW DEPTH

The estimated mean diameters (D_v) at the boulder were used to estimate the flow depth (d_w) responsible for given vortex and local scour hole size upon using equation (48). The input parameters D_v, d_s, and L_o were given in metres. As the local scour holes were relatively shallow, they have been affected by sediment infill, resulting in a reduction of the input parameter ds. Consequently, the original value of d_s, which corresponds to the mean size of HV1, has been obscured. Therefore, an empirical correction by Herget *et al*. (2013) is applied that deducts d_s at steady state condition based on w_s ($d_s = 0.009 + 0.1\ w_s$). This procedure is valid as the geometrical length scales have a substantial linear connection with each other (Fig. 56).

As a result, a range of flow depths was likely responsible for shaping the local scour hole rather than a single value, with depths ranging from 0.6 to 1.9 metres. The median value is 1 meter (Table 12). In interaction with the characteristic boulder size (L_o) the estimated flow depths show that the boulders likely were unsubmerged ($0 < d_w/L_o \leq 1$) to shallow submerged ($d_w/L_o \leq 1.6$) during substantial local scouring processes. This conclusion is based on empirical data gathered from examining local scouring during flash flood hydrographs (Schlömer & Herget, 2023). For $d_w/L_o \approx 1$, a

high–pressure gradient at the obstacle front causes an intense downflow and strong HV1 at the obstacle base, resulting in intense local scouring. Given the current geometry of the local scour hole, the reconstructed values of d_w are deemed as the minimum flow depths during the rising limb of the flash flood. The estimated values of d_w/L_o are therefore also conservative estimates as the height of the obstacle may have slightly changed due to local scouring.

For plausibility check the flow depth during peak flow of the 2015 flash floods (Fig. 54) was estimated. The estimation was based on the woody jetsam deposits found on the channel banks, which were assumed to have been transported as debris during the largest floods between 2013 and 2018.

Channel cross–sectional profiles were measured for this purpose (Fig. 59). The maximum flow depth during peak discharge was between 1.9 and 2.2 metres in both reaches, as indicated by the jetsam deposits. Thus, depending on the size of the obstacles, they ranged from shallow ($1> d_w/L_o < 2$) to fully submerged ($d_w/L_o \geq 2$) conditions during peak flow. Since the flow depth projections obtained from the geometry of the local scour hole are below or equal to the specified limits, the suggested estimates for the flow depth during the rising limb appear to be plausible.

Table 12. Measured geometrical length scales of obstacle marks and estimated flow depth during formation.† estimated by equation (47) ‡ estimated by equation (48).

ID	h_o [m]	w_o [m]	L_o [m]	d_s [m]	l_s [m]	w_s [m]	D_v† [m]	d_w‡ [m]
OM1	0.55	2.45	0.9	0.4	1.2	4.6	0.27	0.7–0.9
OM2	1.04	1.09	1.06	0.5	1	2.5	0.26	1–1.5
OM3	0.88	2.04	1.16	0.3	0.8	3	0.22	1.6–1.9
OM4	0.77	1.35	0.93	0.4	1	4	0.25	0.8–1
OM5	0.95	2.67	1.34	0.8	1.5	3.4	0.4	0.6–1.3
OM6	0.85	1.8	1.09	0.5	1.4	3.6	0.33	1–1.3
OM7	0.68	1.53	0.89	0.4	1.3	3	0.28	0.6–1.0
OM8	0.44	2.55	0.79	0.4	1	2.2	0.37	0.6–1.1
OM9	0.56	2.5	0.92	0.4	1.2	4.7	0.18	0.6–0.9
OM10	1.10	1.30	1.16	0.4	0.9	2.2	0.36	1.3–1.9

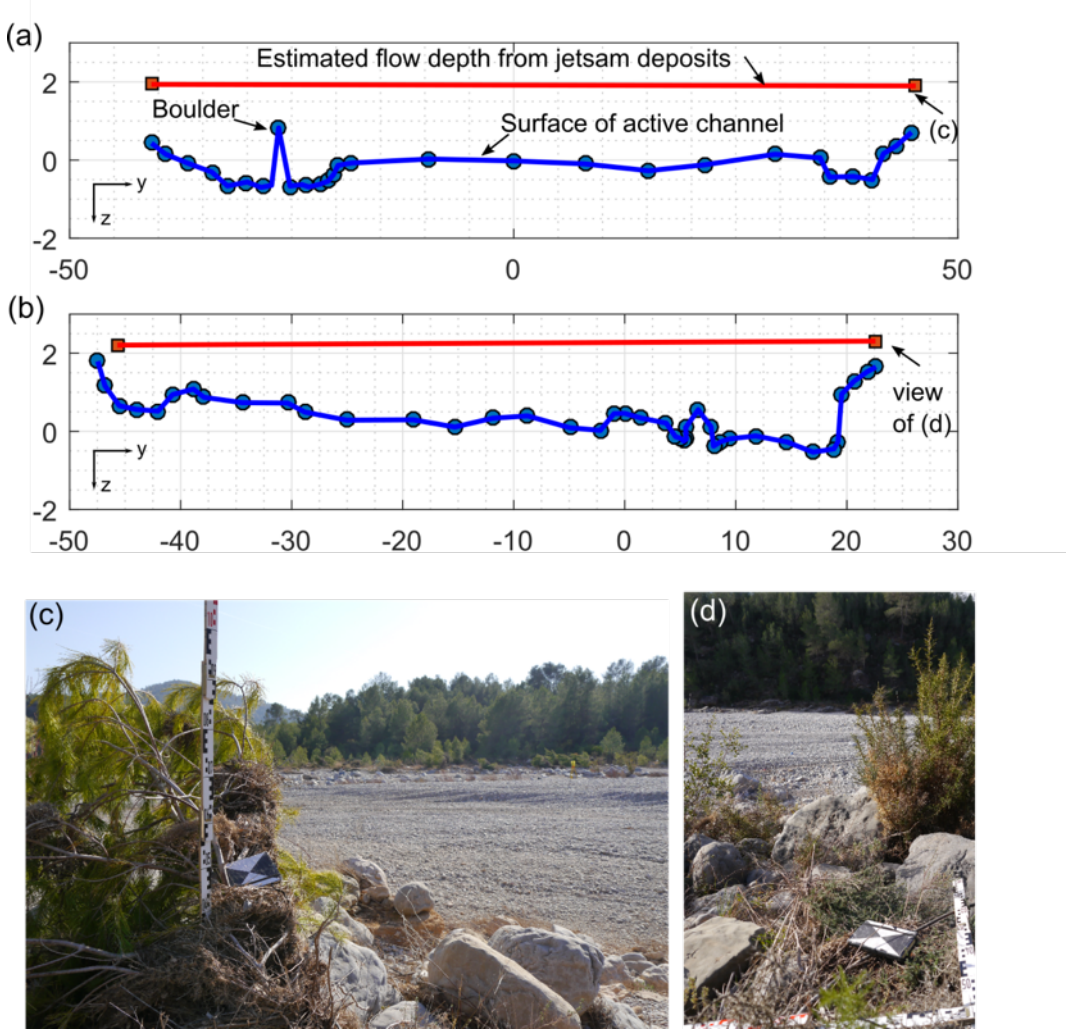


Figure 59. Channel cross-sectional profiles in Rambla de la Viuda with estimated flow depth from jetsam deposits. (a) Reach I. (b) Reach. (c), (d) woody jetsam deposits as indicators for maximum flow depth during peak flow.

8.6.2 Estimation of Peak Discharge

Based on the estimated flow depths (d_w) form local scour hole geometry, the mean approach flow velocity (U_m) during formation was estimated by equation (49). For the gradation coefficient (σ_G) median values of both reaches were used (σ_G = 3.2 in Reach I, σ_G = 3.7 in Reach II). Accordingly, U_m of the rising limb of the hydrograph ranged between 0.8 to 2.0 m/s. Reconstructed flow velocity from obstacle marks in Reach I have a median value of 1.2 m/s while for Reach II the median value was 1.5 m/s. For plausibility check, U_m during the peak flow was also estimated using equation (50). It is important to note that the peak flow in this context is associated with the large floods in 2015. Channel slope values in both reaches (0.004 in Reach I, 0.003 in Reach II) were interpreted as equivalent to the slope of the energy line (Herget *et al.*, 2014). The

empirical roughness coefficients (n) for the active channel in the reaches (Fig. 59 a and b) were 0.03 / 0.04 / 0.05 (Chow, 1988, Calle *et al*., 2015). Applying Manning's equation (equation 50) to the transects of Reach I produces average flow velocities ranging from 0.8 to 1.3 m/s. For Reach II, they range between 0.7 to 1.4 m/s. For both reaches, the upper edge of the estimated U_m during peak flow using Manning's equation, closely approximates the median values determined by the suggested protocol of using the local scour hole geometry as an indicator for (a) the flow depth most likely to occur during formation and (b) the mean flow velocity most likely to occur during formation. Using reconstructed U_m estimates in the continuity equation ($Q = U_m A$) gives a peak discharge of between 57 to 96 m^3/s in both reaches. The April and November 2015 flash floods (peak discharges of 99.46 and 77.13 m^3/s, respectively) are likely to have influenced the local scour processes at the studied boulders, as they were the largest prior to the field campaign. However, a direct link between the given geometric local scour hole characteristics and these events is crucial.

Nevertheless, the measured discharges of the April 2015 and November 2015 flash floods at the Maria Christina gauge are underestimated by the present procedure, which is worthwhile in the context of flow reconstruction purposes and indicates the plausibility of the presented methodology. Applying the median value of flow depth during the obstacle formation on the rising limb (i.e. d_w = 1 m), gives a discharge ranging from 15 to 25 m^3/s.

8.7 SHORTCOMINGS

The present approach assumes that significant local scouring of boulders occurs during flash floods on the rising limb of the hydrograph and estimates flow depths likely to be caused by local scour hole geometry. However, in course of multiple flash flood events within a reach, the local scour holes might get modified due to sediment infill of subsequent floods (Euler *et al*., 2017). Therefore, there is a significant source of uncertainty in associating a given local scour hole geometry with a single flood event due to the unknown flood history and exposure time of the boulder in the stream bed.

From laboratory studies it is known that local scouring at obstacle exposed to subsequent flood events exhibited a so-called memory effect (Pizarro *et al.*, 2017; Pizarro & Tubaldi, 2019). A relative change in the geometric length scales during a subsequent flood event would depend on the d_s, l_s and w_s achieved prior to the event itself and the sediment supply during that event. A significant sediment supply would

result in the burial of the boulder and the complete disappearance of the local scour hole. The persistence of local scour holes and the geometric characteristics of the local scour holes in the Rambla de la Viuda rule out a large sediment supply from recent floods, while a direct connection of local scour hole modification due to a single flood event is only possible by a detailed monitoring program in the field.

When looked at in more detail, this tends not to detract from the validity of the present estimates. It is highly likely that flow depths of between 0.6 and 1.9 metres were reached during the rising limb of flood events with peak discharge ≤ 100 m^3/s in Rambla de la Viuda, which then shape the local scour and mainfests in their geometry due to the position of the berm. During the period of 2013-2018, numerous events of significant magnitude were recorded at Rambla de la Viuda, which may have affected the local scour hole geometry. Therefore, the estimates provided by the proposed method should be considered as the minimum flow depths during the rising limbs of individual flood hydrographs.

8.8 CONCLUSIONS

Field evidence from Rambla de la Viuda shows that local scour holes on large boulders are distinct from other sedimentary structures and have preservation potential in ephemeral gravel bed streams affected by the occurrence of flash flood events. A knickpoint in the local scour hole slope, first identified in laboratory studies, was validated at *in situ* obstacle marks in the field. The knickpoint is a measure of the diameter of the primary horseshoe vortex that correlates with the approaching flow depth, and an empirical relationship was evaluated to reconstruct the most likely flow depth during the formation of the local scour hole and the knickpoint. To the authors knowledge this is the first time that geometric characteristics of preserved local scour holes at boulders have been used as a quantitative indicator of flow depth during their formation. The reliability of these reconstructions is confirmed by plausibility checks of other reconstruction approaches at the same location. It is therefore argued that the present approach is also applicable in ungauged basins for estimating flow depth from local scour hole geometry. Recalling the specific aims of the present study, the following conclusions can be drawn:

(i) The estimated mean flow depth during the formation of local scour holes at boulders in the Rambla de la Viuda was 1 meter, which is less than the flow depths estimated from debris deposits of recent floods (1.9 to 2.2 metres). It is

therefore concluded that the reconstructed flow depths that form local scour holes express the minimum flow depths during the rising limb of the hydrograph that formed local scour holes.

(ii) An existing approach to estimate the minimum flow velocity during local scour hole formation from preserved local scour holes could be refined based on the estimation of minimum flow depth. The plausibility of the estimated velocities and discharges from local scour hole geometry could be checked by recently gauged floods in Rambla de la Viuda.

(iii) In addition to progress in the hydraulic interpretation of local scour holes, it remains crucial to link the geometric characteristics of local scour holes to specific flood events due to the historically dependent nature of local scour. This would require a detailed monitoring programme.

9. VEGETATION-INDUCED SEDIMENTARY STRUCTURES: POROSITY OF RIPARIAN SHRUBS AS CONTROL PARAMETER OF SEDIMENTARY PROCESSES DURING FLOODS

ABSTRACT

Vegetation-induced sedimentary structures (VISS) are bed features resulting from flow-vegetation feedback and turbulence induced by vegetation at riparian sites. Generally, these sedimentary structures commence at the individual plant level, but sediment accumulation over time may lead to the formation of fluvial islands. Additionally, riparian vegetation exposed to current may provoke local scouring. However, little research has been done on how the permeability of plants affects flow fields and sedimentary processes. Therefore, the main aim of the current study is to experimentally investigate patterns of local scour and deposition around artificial obstacles with six different levels of porosity, using a systematically designed flume experiment. Two experimental setups were implemented, with sediment transport occurring either as bed load or in suspension. Porosity, as a measure of the volume of porous space to bulk volume, was determined using optical porosity which was estimated from digital photographs. Furthermore, the VISS of individual *P. nigra* L. shrubs were investigated at different seasonal stages (leafless and full foliage) at the Loire River, France, for comparison. Results show that increasing porosity caused a reduction in sediment deposition from suspension and locally scoured bed load sediment. A threshold value for optical porosity was determined, at which point a prolonged area of flow calm develops behind the barrier, promoting the accumulation of suspended sediment and suppressing local scour caused by bed load transport. An empirical model is presented, which assesses sediment erosion and deposition volumes at porous obstructions, considering (a) the flow-exposed surface area, (b) the obstruction's optical porosity, and (c) the intensity of the incoming flow. On the field scale, local scour holes were identified at *P. nigra* L. shrubs where flood-caused debris obstructions were stuck at their front, lowering the obstruction’s porosity and encouraging local scour processes.

This chapter has been published as:
Schlömer, O., Luneau, S., Rodrigues, S. and Herget, J. (2024) Vegetation-induced sedimentary structures: Porosity of riparian shrubs as control parameter of sedimentary processes during floods. *International Journal of Sediment Research* 39(4) 497-513. DOI: https://doi.org/10.1016/j.ijsrc.2024.05.006.

9.1 INTRODUCTION

Vegetation is a ubiquitous feature of fluvial environments, whether in the channel, along the banks, or on the floodplain (Camporeale *et al*., 2013; Gregory *et al*., 1991; Huai *et al*., 2021; Marjoribanks *et al*., 2014). In the riparian zone, vegetation is a key geomorphological agent at the boundary between the terrestrial and aquatic zones, influencing water, sediment, and nutrient fluxes (Gurnell, 2014; Hupp & Osterkamp, 1996; Murray *et al*., 2008; O'Briain *et al*., 2022). Knowledge of the interactions between vegetation, flow, and sediment dynamics is critical for sustainable river management at multiple spatial scales, including the (i) individual plant scale, (ii) reach scale, and (iii) planform scale (Curran & Hession, 2013). From temperate riparian zones, pioneer species such as European black poplar (*Populus nigra* L., i.e., *P. nigra* L.) are known to be able to alter hydraulic and geomorphic processes to their advantage due to their rapid above and below ground growth rates, thereby "engineering" resource availability for other organisms (Corenblit *et al*., 2014, 2016). Field observations of the ability of riparian species to trap incoming sediment and woody debris led to a model of fluvial island development (Gurnell *et al*., 2001, 2012). These accumulations create microhabitats that provide ecological services and support biodiversity. The morphological and ecological evolution of fluvial pioneer islands has been linked to timescales ranging from single floods to decades (Gurnell *et al*., 2019; Schlömer & Reimann, 2021). On even longer timescales, the presence of such pioneer islands may even modify the channel planform due to channel bifurcation (Henriques *et al*., 2022; Merritt, 2022; Tooth & Nanson, 2000).

The origin of these morphodynamic processes is linked to the individual plant or shrub scale (Schnauder & Moggridge, 2009). In this context, vegetation can be classified as either solitary elements or clump-like vegetation patches. Vegetation patches are defined as areas that are distinct from their surroundings in that they are occupied by vegetation at a relatively high density and with relatively sharp edges (Caroppi et al., 2022). The flow pattern around and through individual vegetation elements or patches has been investigated in laboratory studies (Nepf, 1999; Tinoco & Coco, 2014; Yagci *et al*., 2010) and for field experiments (Sukhodolov & Sukhodolova, 2012; Sukhodolova & Sukhodolov, 2012). From this it is known that similarities can be drawn to the typical flow-body interaction, where coherent vortices are formed in the vicinity of the obstacle. This increases the shear stress around the plant and triggers the phenomenon of local scour, which mobilizes bed material as bed load (Chen *et al*.,

2012; Yagci *et al*., 2016). However, a shrub exposed to a flow must be considered permeable in the sense that the approaching flow is able to pass through the object. The porosity of a vegetal element can be estimated based on the void space relative to the space occupied by stems, branches, twigs, and leaves.

It is known from experimental studies that the porosity of an obstacle can significantly alter the flow structure in its vicinity, as it determines (i) the reduction of the approaching flow velocity downstream of the obstacle and (ii) the turbulence distribution in the vicinity of the vegetation element (Kitsikoudis *et al*., 2016; Zhao & Fan, 2017; Zong & Nepf, 2012).

Estimating the true physical porosity of a shrub is rather difficult due to its irregular size and shape, as well as the variable distribution of voids. Porosity varies with vegetation species, leaf thickness and leaf area index (Loeffler *et al*. 1992). Furthermore, in temperate riparian zones, porosity is not constant throughout the year due to different phenological stages, making it a complex and variable boundary condition in time. Field studies show that under flood conditions, shrubs and tree trunks induce sediment deposition in their downstream wake as sediment ridges (also called sediment tails or sediment shadows), which in part consist of finer sediment than those of the surrounding bed (Euler *et al*., 2014; Nakayama *et al*., 2002; Rodrigues *et al*., 2007). In some observations, local scour holes in the downstream wake of the approaching current were also present as erosional bed features (Fig. 60). Such bed features at vegetation elements have been characterized as “vegetation-induced sedimentary structures (VISS)” by Rygel *et al*. (2004). However, Tinoco *et al*. (2020) point out that it is not yet fully understood whether vegetation enhances turbulence and promotes local scout or dissipates sufficient energy to enhance sediment deposition. In this regard, the porosity of riparian vegetation is thought to be important either for the initiation of local scour processes due to bedload transport, or for the deposition of suspended sediment in the wake of the vegetal element (Follett & Nepf, 2012; Yagci & Strom, 2022).

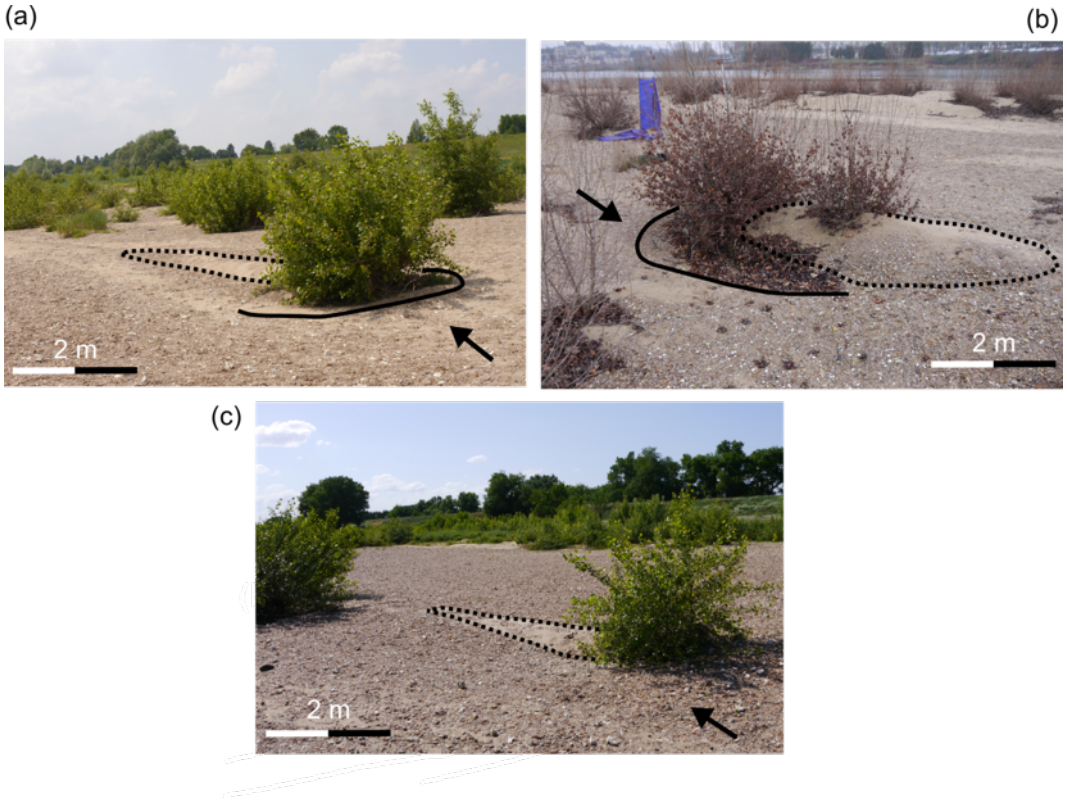


Figure 60. Vegetation-induced sedimentary structures on *P. nigra* L. shrubs in the Loire River. Local scour hole (solid line) and sediment ridge (dashed line) on a shrub at two different seasonal stages (a) full foliage, (b) leafless. (c) Sediment ridge in the wake of a shrub without a local scour hole. Arrows indicate flow direction.

9.1.1 OBJECTIVES OF THE STUDY

The main objective of the current study is to evaluate the effect of porosity on flow patterns, turbulence, and sediment transport at permeable barriers from a single plant perspective. To this end, flume studies offer the advantage of isolating and replicating complex processes under systematically varied boundary conditions. In this small-scale flume study, the porosity of the plant body is the target variable of the investigation, mimicked by artificial obstacles. Porosity as a measure of pore space was operationalized based on an adapted procedure for estimating optical porosity from digital photographs.

Two different experimental setups were used, with sediment transport either as bed load or in suspension. For both sets of experiments, the hydraulic and sedimentary boundary conditions were kept constant, while the porosity of the obstacles was systematically varied. In addition to the small-scale experimental test series, VISS has been investigated on *in situ P. nigra* L. stands in the middle reaches of the Loire River, France. The field campaign aimed to verify whether the geometry of sedimentary

structures generated at artificial obstacles is comparable to natural VISS at the field scale. Additionally, the campaign aimed to identify a range of optical porosity values at the field scale that are likely for *P. nigra* L. individuals at different seasonal stages, i.e., leafless and full-foliage. It is generally argued that a comprehensive understanding of the small-scale processes involved is necessary to understand the role of vegetation in the morphological development of fluvial pioneer islands at the field scale.

9.1.2 WORKING HYPOTHESIS

The foregoing considerations lead to the main working hypothesis of this paper:

(i) The porosity of an obstacle/individual plant can be adequately described by the optical porosity, which can be assessed for laboratory and field conditions based on digital photographs.

(ii) Under certain hydraulic and sedimentary boundary conditions, the porosity of an obstacle affects (a) the amount of sediment deposited when a sediment-laden flow encounters the obstacle, and (b) the triggering of local scour around the obstacle.

(iii) Vegetation-induced sedimentary structures (VISS) are scale-invariant features, so that small-scale laboratory results are comparable to large-scale field results.

9.1.3 FLOW FIELD AT POROUS OBSTACLES

From research on solid obstacles (i.e., boulders or bridge piers) exposed to a flow but not submerged, it is known that deformations of the approaching flow in the vicinity of the obstacle lead to the following processes (1) a contraction of the streamlines lateral to the obstacle, resulting in higher flow velocities; (2) a vertical jet-like downflow towards the bed, resulting from the pressure gradient at the front of the obstacle; (3) the formation of a turbulent vortex structure at the base of the obstacle, resulting from the deflection of the downflow against the main flow direction; because the vortex structure laterally wraps around the sides of the obstruction in the downstream direction, it is commonly referred to as a horseshoe vortex (abbreviated as HV); and (4) a deceleration region of flow in the wake of the obstruction, including a wake vortex system of detached shear layers with a vertical axis of rotation (Dargahi, 1990; Melville & Coleman, 2000; Papanicolaou & Tsakiris, 2017; Shamloo et al. , 2001).

Processes (1) to (3) increase the bed shear stress above the critical bed shear for sediment mobilization and induce local scour in front of and lateral to the obstacle in non-cohesive and cohesive sediment (Allen, 1982). These processes occur even under clear water conditions, i.e., no general sediment mobilization in the approaching current. The HV is located in the inner part of the local scour hole, close to the base of the obstacle. It must be considered as the main driver of local scour as sediment is picked up under the legs of the HV by the transport modes of saltation and rolling (Maity & Mazumder, 2014). The mobilized sediment particles are transported downstream under the expanding legs of the HV as bed load. In the mid to far wake region, the sediment particles are deposited as dune-like sediment ridges due to decreasing bed shear stress (Oliveto & Hager, 2014). Sediment transport on the sediment ridge is composed of rolling and sliding (Euler *et al*., 2017).

The initiation of local scour at instream obstacles is triggered by the crossing of thresholds in certain control parameters that describe the governing boundary conditions (Schlömer *et al*., 2020). For example, local scour is inhibited when the flow intensity, i.e., the ratio of the mean approach velocity (U_m) to the critical mean approach velocity for sediment entrainment (U_c), is $< 0.3 – 0.5$ (Chiew, 1995; Simarro *et al*., 2007). However, riparian vegetation exposed to a flow must be considered as permeable. Thus, a fraction of the approaching flow is forced to pass through the voids, with consequences for the flow field in the wake of the obstacle. Zong and Nepf (2012) demonstrated in laboratory experiments that at the patch scale, flow around emergent vegetation induces bleed flow through the vegetation patch. This creates a stable wake region downstream of the obstacle, where flow velocity and turbulence are reduced relative to the approaching free flow and sediment deposition is favored. The bleed flow also delays vortex shedding downstream of the vegetation patch (Marjoribanks *et al*., 2019). Typically, vortex shedding in the wake of emergent obstacles is characterized as a von Kármán vortex street (Chen *et al*., 2012). In the presence of bleed flow, the von Kármán vortex street forms downstream of the stationary wake region (Zong & Nepf, 2012). In the case of a submerged vegetation patch, where the flow depth is greater than the canopy height, a von Kármán vortex street is absent, as shown by Liu *et al*. (2018). Closely related to bleed flow are stem generated turbulence on branches and twigs, which play an important role in deposition within a vegetation patch. As shown by Liu and Nepf (2016), deposition within the patch is only enhanced compared to a bare channel control in the absence of stem generated turbulence.

Within the steady wake region, the reduced velocity and turbulence favors net deposition of incoming sediment, either transported as bedload (Yager & Schmeeckle, 2013) or in suspension (Box *et al*., 2019), resulting in the formation of a sediment ridge in the middle to far wake of the obstruction (Fig. 5 b). On the other hand, bleed flow weakens the pressure gradient at the front of the obstacle and conversely reduces downflow. As a result, only a weak HV is present at the base of the obstacle, limiting local scour in front of the obstacle. It is, therefore hypothesized that if the porosity exceeds a threshold, no HV will form at the obstacle and local scour will be inhibited. To the authors' knowledge, no such threshold has been determined.

9.1.4 GEOMETRY OF THE VISS

Rygel *et al*. (2004) identified five types of VISS resulting from hydrodynamic forcing. For the current study, the pertinent ones are (i) centroclinal cross-strata, which are local scour holes upstream of the obstacle, and/or (ii) upturned beds, which are sediment ridges in the downstream wake of the obstruction. Sedimentary structures around solid obstacles, referred to as "obstacle marks" (Karcz, 1968), display similarities. Local scour holes are crescent-shaped depressions in front and lateral to an obstacle. They can be approximated as an inverted frustum cone with an elliptical shape in plan view. The adjacent sediment ridge originates on the lee side of the approaching flow and expands downstream. At varying flow velocities, a laboratory study by Euler *et al*. (2014) identified two morphological patterns of local scour holes around submerged porous obstacles. At flow velocities close to the general mobilization of sediment, a frontal scour hole was observed. At lower flow velocities (i.e., just above the threshold of local scour incipience), only minor local scour holes were formed at the obstacle front.

The VISS geometry is distinguishable by various length scales. Local scour holes formed in front and beside the obstacle can be identified by: The depth of the local scour hole at the front of the obstacle (d_s), measured from the undisturbed bed upstream. The length of the scour hole front (l_s), measured in the plane of symmetry to the incoming flow, from the obstacle's front face to the upstream edge of the scour hole. The width of the scour hole front (w_s), measured from the lateral edges of the scour hole at the obstacle's front face, perpendicular to the incoming flow (Fig. 4). A flat semicircular scour hole bottom (S_b) with a radius of less than ls is situated close to the base of the obstacle. A definition can be applied to the sediment ridge formed in the

wake of an obstacle. This includes measuring the sediment ridge height (h_r), width (w_r), and length (l_r) from the downstream end of the obstruction (Euler & Herget, 2012). The aforementioned geometrical length scales serve as the target variables in experimental investigations and analyses of field evidence.

9.2 STUDY AND FIELD EVIDENCE

Field evidence of VISS was investigated at riparian pioneer vegetation located in the middle reaches of the 1012 km long Loire River in France. The channel pattern within this region consists of an incised main channel that is bordered by narrow banks and floodplain areas, alongside several secondary channels that only become inundated during flood events, as noted by Wintenberger *et al*. (2015). The research sites were situated at Amboise and Luynes, upstream and downstream of Tours (760 km downstream of the origin), (Fig. 61). The river flows through sedimentary rocks of Cretaceous and Tertiary ages with a bedload primarily consisting of siliceous sand and gravel (Cordier *et al*., 2018). *P. nigra* L. sprouts and shrubs at various stages of maturity have colonized the banks and floodplain areas. Here, the focus was on VISS found near shrubby *P. nigra* L. specimens situated on either bare or partially vegetated sediment surfaces along the channel banks and close to the river (i.e., less than 100 metres into the floodplain). These shrubs are characterized by one or more main trunks, along with branches and twigs that reach the sediment surface that are generally less than 6-10 years old (Corenblit *et al*., 2016).

The Loire River's hydrology experiences high-magnitude floods during winter and spring. The river's average discharge measures at 374 m^3/s and approximately 1500 m^3/s during the 1-in-2-year flood, as reported by Rodrigues *et al*. (2007). In January 2018, four months prior to the first field campaign in May, a flood with a peak discharge of 2190 m^3/s occurred. The peak discharge was measured at the Langais gaging station located 65 km downstream from our study sites. Regrettably, there was a lack of available data regarding the hydraulic boundary conditions, specifically the flow velocity, at the floodplain, which further hindered the analysis. In January 2019, a subsequent survey was done out to approximate the optical porosity of the same *P. nigra* L. individuals under leafless conditions.

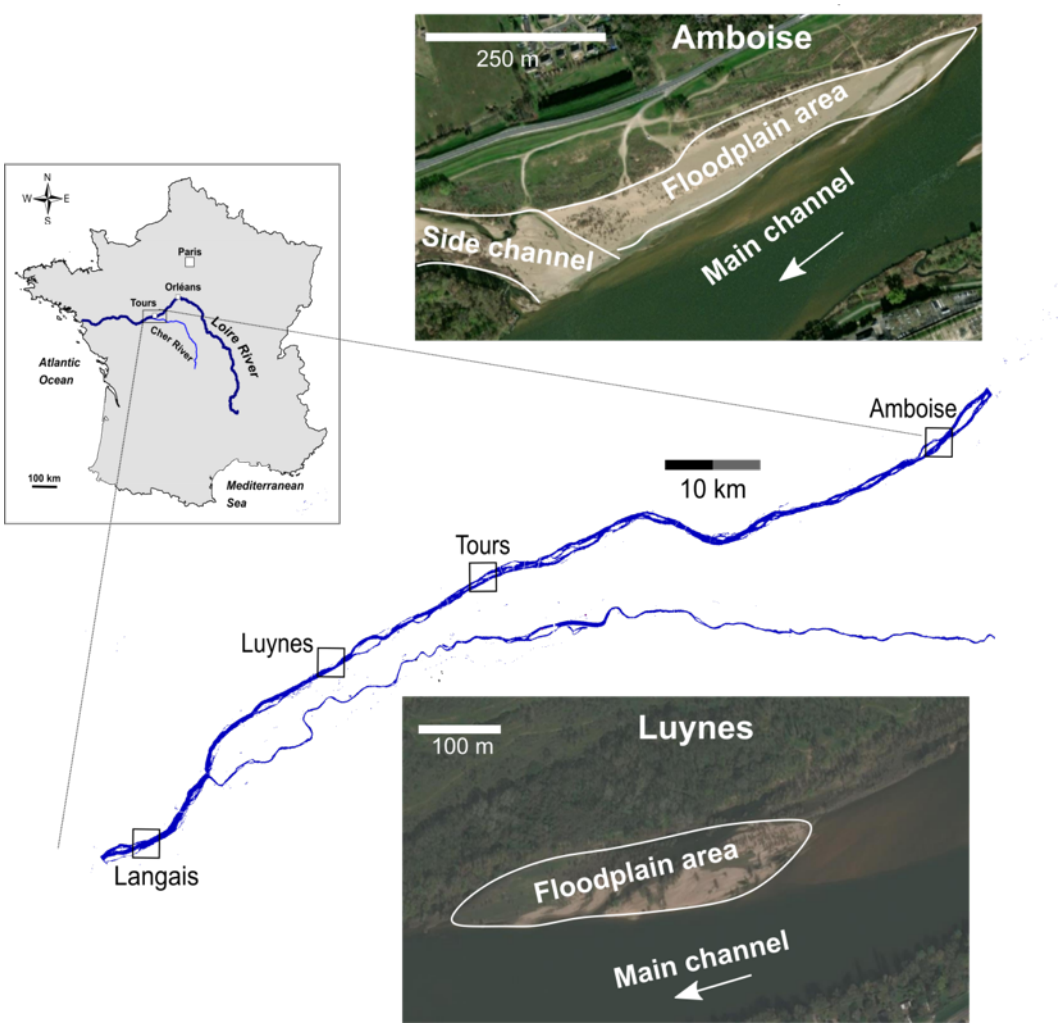


Figure 61. Schematic map and photographs of the study area at the Loire River.

9.3 METHODS AND ANALYSIS

9.3.1 ESTIMATION OF POROSITY AT FIELD AND LABORATORY SCALE

Porosity was estimated using the "optical porosity" index, which was introduced by Grant and Nickling (1998) and Kenney (1987). Although this index underestimates the ratio of porous space volume to bulk volume since it does not consider the three-dimensional nature of void spaces, it is sufficiently accurate to apply in laboratory settings (Hao *et al*., 2020; Montakhab *et al*., 2013) as well as in field conditions (Bekkers *et al*., 2022). The photographs were taken in front of a monochrome purple screen with high contrast, made of a shower curtain, which maximizes contrast between vegetation and the background screen according to Straatsma *et al*. (2008). Images were captured using a Panasonic Lumix DMC-G5 digital single-lens mirrorless (DSLM) camera, equipped with a 16-megapixel image sensor with a 4/3" size (17.3 x 13.0 mm) and a Lumix G-Vario 14-42 mm zoom lens set at 21mm focal length to minimize image

distortion. The images have a resolution of 4608 x 3072 pixels with a 52° field of view. Photos were taken perpendicular to the *P. nigra* L.shrubs, about 0.3 m above the ground. This height was selected due to driftwood jams that were tangled in the shrubs ($h_{o\ debris}$). The driftwood jams indicate the average depth of the flow during the peak flood. Photos were taken using the given camera setup in close proximity to the object to guarantee visibility of all pores and branches. The fractional coverage of the screen was approximately 50%, and the photos were taken to obtain the shrubs' frontal total height (h_o) and the maximum width of the foliage exposed to flow (w_o). These methods were taken from studies conducted by Grant and Nickling (1988), Kenney (1987), and Vigiak *et al*. (2003). However, the distance to the *P. nigra* L. shrubs was consistently over 2 m. Straatsma *et al*. (2008) have determined that optical porosity estimation accuracy reduces as screen distance decreases. Additional physical characteristics of the shrubs were examined, consisting of the number of trunks emerging from the surface and their diameter. To determine the maximum surface exposed to peak flood flow (SOF) (m^2), the product of $h_{o\ debris}$ and w_o was calculated. (Fig. 62)

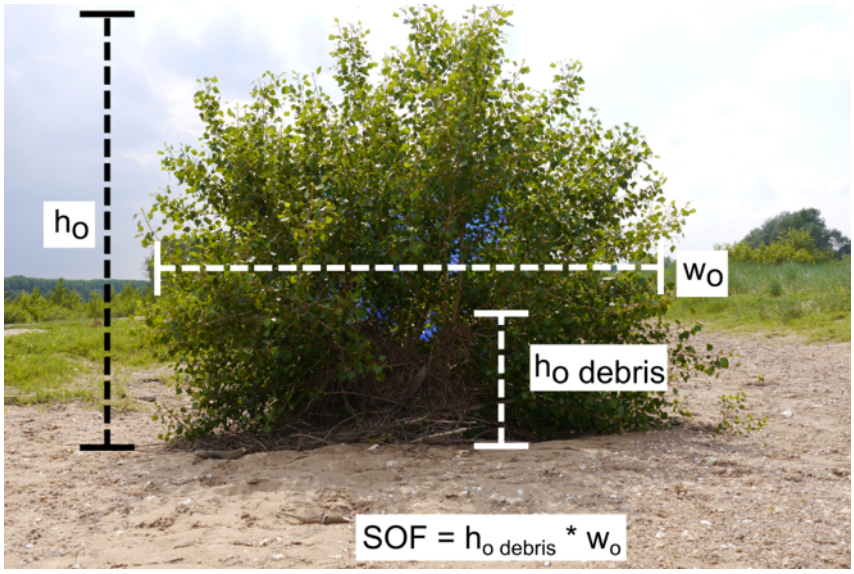


Figure 62. Definition of representative length scales of field evidence) (Rodrigues *et al*., 2007).

A simplified geometry was used to characterize a single shrub under laboratory conditions. Cylindrical dish scrubbers (i.e., brushes), with a diameter of 0.03 m and a height of 0.08 m served as obstacles. The brushes comprised a central metallic trunk with plastic bristles spanning the entire height and were not flexible or inclined in the downstream direction when subjected to the current. The porosity of the brush's optics

was altered by either decreasing the density of its plastic bristles to heighten porosity or by wrapping steel wool around the brush to lower porosity levels. To provide a comparison, a solid brass cylinder was used with an optical porosity level of zero and dimensions corresponding to the height and width of the brush. The photos of the brushes were taken following the field evidence methodology.

All photographs were subsequently converted from the RGB (red, green, blue) color scheme to the HSV (hue, saturation, value) color scheme. Subsequently, the hue value of the screen visible through the empty spaces, was used to adjust the photographs (270 degrees, ranging from hyacinth to violet). After applying the thresholding, a binary image was created with white pixels (w_p) representing the hue threshold value and black pixels (b_p) corresponding to those below or above the hue threshold value. (Fig. 63). To calculate the optical porosity (V_p), the number of white pixels was divided by the total number of pixels (t_p) in the photographs. The resulting value was then multiplied by 100 to obtain the optical porosity:

$$V_p = (w_p/t_p)\,100$$

(Eq. 51)

The photos were not trimmed to avoid altering the total pixel count. The analysis mentioned earlier was done using a MATLAB script. Six brushes with varying optical porosity were tested in the experimental series (V_p = 4, 5, 6, 8, 9, and 14). The brushes' volumetric porosity (Vol_p) was approximated using the water-replacement method, whereby they were submerged in a graduated beaker halfway filled with water. Vol_p was derived by calculating the difference in water volume before and after immersion. Upon comparison of the V_p and Vol_p values for the utilized brushes, it is apparent that there is a correlation whereby an increase in V_p results in an increase in Vol_p. This conclusion further illustrates the viability of estimating porosity through digital photographs (Grant & Nicking, 1998), (Fig. 64).

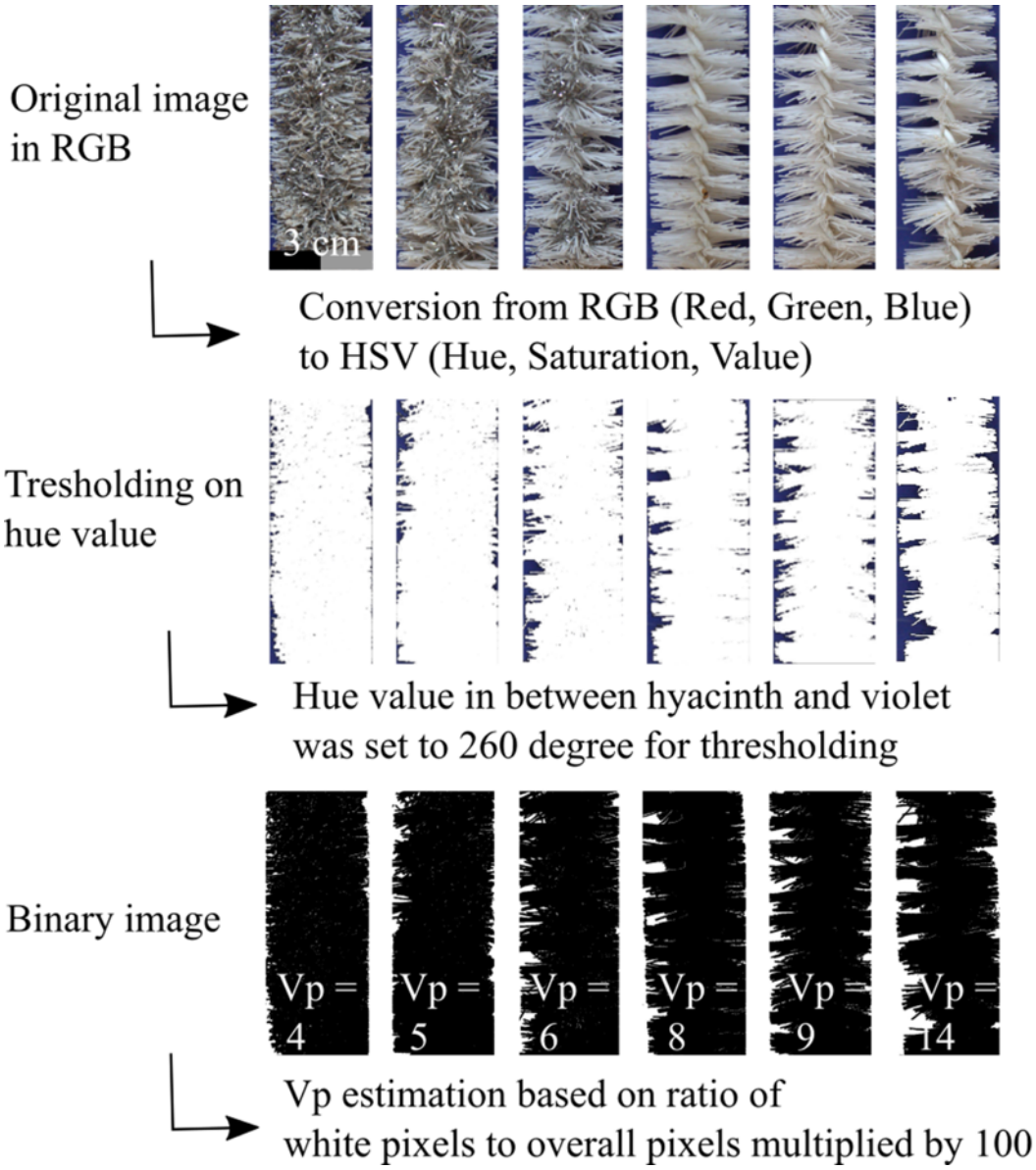


Figure 63. Workflow of optical porosity estimation exemplified for artificial obstacles.

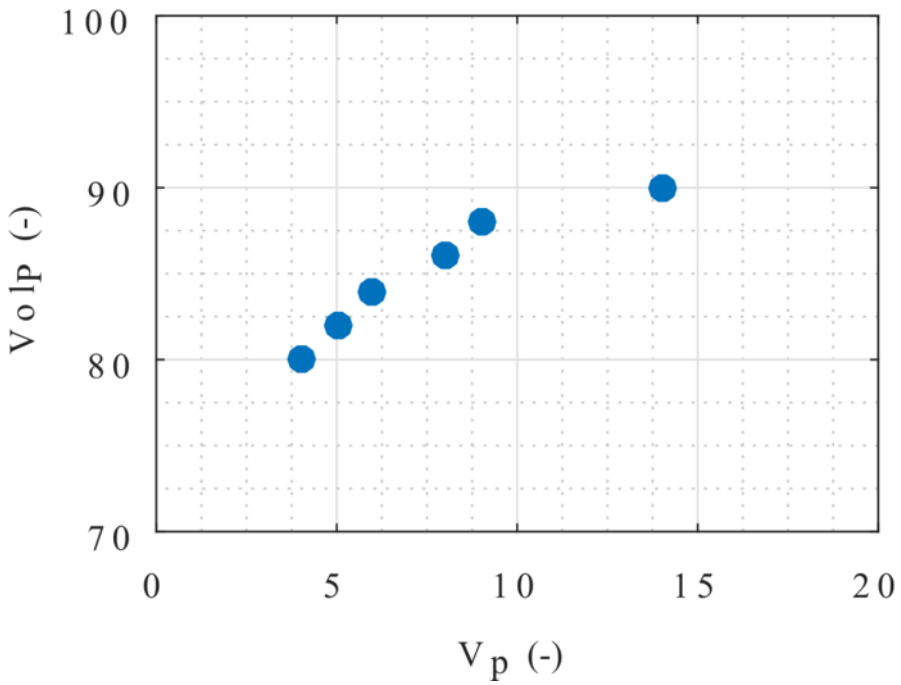


Figure 64. Relation between optical porosity (V_p) and volumetric porosity (Vol_p) for artificial obstacles used in the laboratory study.

9.3.2 EXPERIMENTAL CONDITIONS

Experiments were done in a straight rectangular flume measuring 5 metres in length, 0.32 metres in width, and 0.27 metres in depth. The flume had a fixed slope of 0.003 m m^{-1} (Fig. 9). Water was supplied by two reservoirs placed downstream, while the discharge was manually managed by a recirculating pump (Lowara FCE-Series®) using two cone valves. The discharge was measured using a magnetic-inductive discharge meter (Schwing MS 1000®, accuracy ± 1% of actual discharge). To reduce turbulence and ensure an even flow, a flow straightener created from bundled pipes (around 100 pipes, with a 0.03 m diameter and 0.4 m length) was installed in the flume inlet. A downstream tailgate was used to regulate the depth of the flow (d_w). An ultrasonic distance meter (Mic +25, Microsonic®, with an accuracy of ± 0.1 mm) was used to assess water surface measurements along the working section, located roughly 2.7 metres downstream of the inlet. The brush assembly was positioned on the symmetry plane of the flume's working section to reduce side-wall effects (Nezu & Nakagawa, 2017).

Two experimental series were devised to accommodate distinct sediment transport modes. The said series were done with a constant d_w of 0.08 metres to ensure brush emergence in the experimental runs. For series A, sediment was transported in

suspension while assessing the impact of varied V_p on sediment deposition in the wake of the obstruction. The unit discharge (q) was 0.028 m/s, and the mean flow velocity (U_m) was 0.35 m/s. The experiment utilized natural fine-grained quartz sand possessing a uniform particle size distribution (Wentworth, 1922). The sediment median diameter (d_{50}) was 0.2 mm, with d_{16} and d_{84} measuring 0.15 mm and 0.35 mm, respectively (Fig. 65 a). The sediment's gradation coefficient ($\sigma_G = d_{84}/d_{16})^{½}$ was 1.5, indicating the sediment uniformity (Lee & Sturm, 2009).

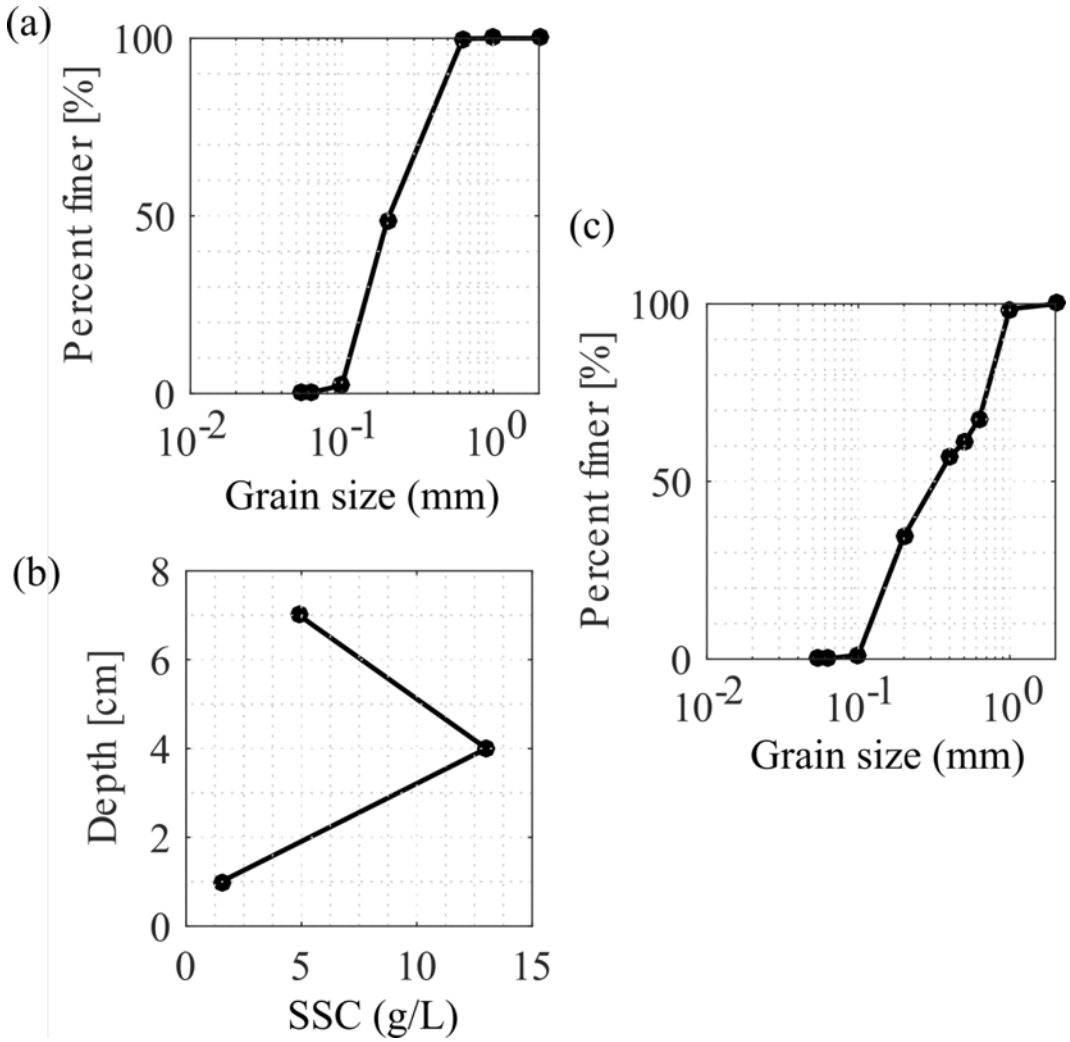


Figure 65. (a) Results of sieving analysis for sediment used in series A experiments where d_x is the diameter for which x percent of the sediment is finer); (b) suspended sediment concentration (SSC) approaching the obstacle for Series A experiments; and (c) results of sieving analysis for sediments used in Series B experiments).

Sediment was fed by a self-constructed system approximately 1 metre upstream of the working section. The system comprised a conical feeding hopper, placed about 0.1

m above the water surface. The flume lacked any sediment bed as the floor was entirely constructed with polystyrene insulating board and was 0.05 metre thick. The sediment hopper was loaded with 4 kg of sediment, which was then released at a constant feeding rate of 2.7 g/s into the water column to initiate suspension transport, similar to the experimental procedure presented by Box *et al*. (2019). Sediment feeding was done out in the plane of symmetry. The experiments continued until the sediment hopper was depleted and sediment that had reached the flume reservoir was not re-circulated. Consequently, the experimental duration was approximately 25 minutes. The settling velocity of the sediment fractions (w_{set}) was estimated using the procedure proposed by Ferguson and Church (2004). The settling velocities (w_{set}) were calculated as 0.065 m/s for D_{50}, 0.056 m/s for D_{16}, and 0.084 m/s for D_{84}.

The estimated critical mean approach velocity for entrainment (U_c) was 0.247 m/s for D_{50}, 0.246 m/s for D_{16}, and 0.256 m/s for D_{84} (Melville & Coleman, 2000). As a result, live bed conditions ($U_m/U_c > 1$) prevailed for each sediment fraction. Since the sediment was introduced from the water surface, the vertical profile of the suspended sediment concentration (SSC) was still in progress as it approached the brush. The SSC was measured manually using a self-made sampler located 0.1 metre upstream from the obstacle in the symmetry plane. Samples were taken at 0.02, 0.04, and 0.06 metre above the bottom of the flume, with the highest SSC measurement recorded at 0.04 metre (Fig. 65 b). The results show a deviation from conventional concentration profiles that usually show a decrease in concentration towards the water depth's top (Shugar *et al*., 2010). Thereby, the highest sediment concentration occurs near the bed as a result of the maximum shear stress and turbulent momentum, which give rise to lift force and mixing dynamics leading to sediment entering the flow (Li *et al*., 2020). However, the experimental conditions are deemed adequate for portraying sediment deposition in the wake of the brush where suspended transport dominates under flow conditions. The repetition of the experiments for different V_p was done out three times in order to test the reproducibility and to eliminate random results. Series A encompassed a total of 21 experiments.

Local scour at brushes with varying velocities was studied for bed load transport conditions in series B. A sediment recess with a length of 1 m and a depth of 0.05 metre has been installed in the working section of the flume. It contained 37 kilogram of fine sand, with a slightly coarser grain size distribution compared to Series A (Fig. 65 c). The sediment median diameter (D_{50}) was 0.31 mm, while D_{16} and D_{84} were 0.17 and

0.75 mm, respectively. With a gradation coefficient of 2.1, the sediment is classified as non-uniform.

Two hydraulic scenarios were tested for Series B, aiming to represent different flow conditions at the brushes. Scenarios 1 and 4 were implemented to depict flow conditions slightly above the threshold required for local scour (i.e., $U_m/U_c \leq .0.62$). In scenarios 2 and 3, the flow intensity was close to the general mobilization of sediment (i.e., U_m/U_c = 0.81-0.82). For scenarios 2 and 4, the flow depth was the same as the height of the obstacle, whilst for scenarios 1 and 3, the ratio between flow depth and obstacle height was 0.5. It is important to note that the experiments done in series B were done out under clear-water conditions, resulting in no general sediment transport throughout the experimental runs. Furthermore, the flow was subcritical for all scenarios, which was indicated by a Froude number (Fr) smaller than 1. All experiments were performed under turbulent flow conditions, as indicated by a Reynolds number (Re) higher than 500. All hydraulic conditions are listed in Table 13. Based on previous experiments investigating local scour at in-stream obstacles (Schlömer, 2020; Schlömer *et al*., 2021), a total experimental run time (t_e) of 480 minutes was allocated for Series B experiments to adequately capture any local scour phenomena occurring over time. A total of 24 experimental runs were done for Series B. It is noteworthy that the flume experiments were unscaled, and consequently, they serve as a process-focused physical model that strives to replicate the processes and resulting morphologies (Baynes *et al*., 2018).

Table 13. Hydraulic conditions of Series B experiments.

Scenario	d_w (m)	U_m (m/s)	U_m/U_c (-)	Fr (-)	Re (-)
1	0.04	0.14	0.62	0.22	5600
2	0.08	0.2	0.81	0.23	16.000
3	0.04	0.18	0.82	0.29	7200
4	0.08	0.15	0.61	0.17	12.000

9.3.3 EXPERIMENTAL PROCEDURE

Experimental trials started at time t = 0 minutes after the brushes were positioned in the working area and the pump was activated. For both experimental series, the frontal face of the brush was defined as the origin of a local Cartesian coordinate system, where x denotes the longitudinal, streamwise direction, y denotes the horizontal direction perpendicular to the streamwise direction, and z denotes the vertical direction. The origin coordinates (x0/y0/z0) were set to 0/0/0, with the coordinates upstream of the origin being negative and coordinates in the streamwise direction being positive. Two distance meters (Welotec® OWRB-Series), which use LED technology to measure x- and y-coordinates, along with a laser distance meter (Baumer Electric® ODAM S14C) to measure the vertical coordinate (z), were utilized to measure the geometrical length scales of the emerging sedimentary structures. The accuracy of the LED-distance meters was ± 0.5 mm, while that of the laser distance meter was ± 1.5 mm. All sensors were installed on a traversing system that operated in the x/y-plane atop the flume.

For Series A, an Acoustic Doppler Velocimeter (ADV) was used to measure the instantaneous velocity components with an accuracy of ±1% and a sampling frequency of 25 Hz. The ADV utilized was a Vectrino model from Nortek AS® and was positioned downwards. It measured the flow in three directions, namely the streamwise (u), lateral to streamwise (v), and vertical (w) directions near the obstruction. The results were used to establish the averaged quantities of the velocity components ($\bar{u}$, $\bar{v}$, and $\bar{w}$) and their deviations ($\bar{u}'$, $\bar{v}'$, and $\bar{w}'$). The turbulence intensities (TI) in the streamwise and vertical directions were calculated using the root mean square of the fluctuating components ($\bar{u}'_{rms}$ and $\bar{w}'_{rms}$) as measured by Guan *et al*. (2019) and Kim *et al*. (2000):

$$TI = ((\bar{u}'_{rms})^2 + (\bar{w}'_{rms})^2)^{½}/U_m \quad \text{(Eq. 52)}$$

Data were collected at three heights above the flume bed along the centerline of the obstacle, namely at dw = 0.006, 0.015, and 0.03 m. Measurements were obtained upstream and downstream of the obstacle for x = -2.5 to x = 5, at streamwise intervals of 0.005 m. Each measurement lasted 120 s and the raw data were processed using WinADV (Version 2.031) (Wahl, 2000), where a spike removing filter and a correlation filter (>70%) (Goring & Nikora, 2002) were applied. The sediment trapped near the obstacle was evaluated by measuring the geometric length scales of the sediment structure at the end of the experimental runs and by weighing the dried sediment. For

Series B, the shape of the local scour hole was assessed through two-dimensional (2D) cross-sectional profiles taken in the longitudinal (parallel to the water flow) and transverse (perpendicular to the water flow) directions, according to the description in Fig. 4 (dashed lines). The profiles were examined at t = 120, 240, 300, and 480 minutes for scenarios 1 and 2.

9.4 Results and discussion

9.4.1 VISS at the Loire River

During the first field survey in May 2018, 34 VISS were identified on individual *P. nigra* L. sprouts at the Amboise and Luynes floodplains. 80% of them were present in the Amboise floodplain. Due to their different maturity, the *P. nigra* L. varied considerably in size, ranging from 1 to 3 metres in height (h_o) and 0.5 to 4.1 metres in width (w_o). The median diameter of the main trunk was 0.06 meter and the diameter of the branches was 0.03 meter. Local scour holes in front of the shrubs were present at 21 *P. nigra* L. individuals in the Amboise floodplain. In all these VISS, inflexible woody debris was present due to flooding. The height of the driftwood ($h_{o\ debris}$) ranged between 0.2 and 0.5 m above the actual surface and is interpreted as a proxy for the water level during the causitive flood. No driftwood or debris was found in the *P. nigra* L. individuals at higher elevations, so that the $h_{o\ debris}$ is interpreted as the water level during at the peak flow of the flood. It is highly likely that the debris jams were caused by the January 2018 flood event. Manning's equation was applied by assuming $h_{odebris}$ as a proxy for water level and incorporating representative roughness values (i.e., n values = 0.0035 to 0.060) as well as the local channel slope (0.0003 m/m), Rodrigues *et al*. (2006). A mean flow velocity of < 0.6 to 0.8 m/s was approximated for the Amboise floodplain.

As h_o debris approached the water level, the height of the obstacle (h_o), and, therefore, the area exposed to flow was significantly reduced, while the porosity in this area was reduced due to the accumulation of debris. In May 2018, all individuals of *P. nigra* L. were analyzed for foliage (Fig. 66 a, c, and e). Upon examination, the optical porosity median (V_p) of all 34 individuals of *P. nigra* L. was determined to be $V_p = 8$, with the greatest observed value of $V_p = 27$. In the case of driftwood jams, the optical porosity was observed to decrease to $V_p = 1$ to 4. Therefore, it is hypothesized that the driftwood jams play a vital role in creating local scour holes near porous shrubs. This is because they minimize the bleed flow by obstructing the path and enhance the

downflow and HV-formation at the frontal face of the shrubs. Previous experimental studies by Stolle *et al*. (2018) and Schalko *et al*. (2019a) have established that debris damming causes this compaction effect.

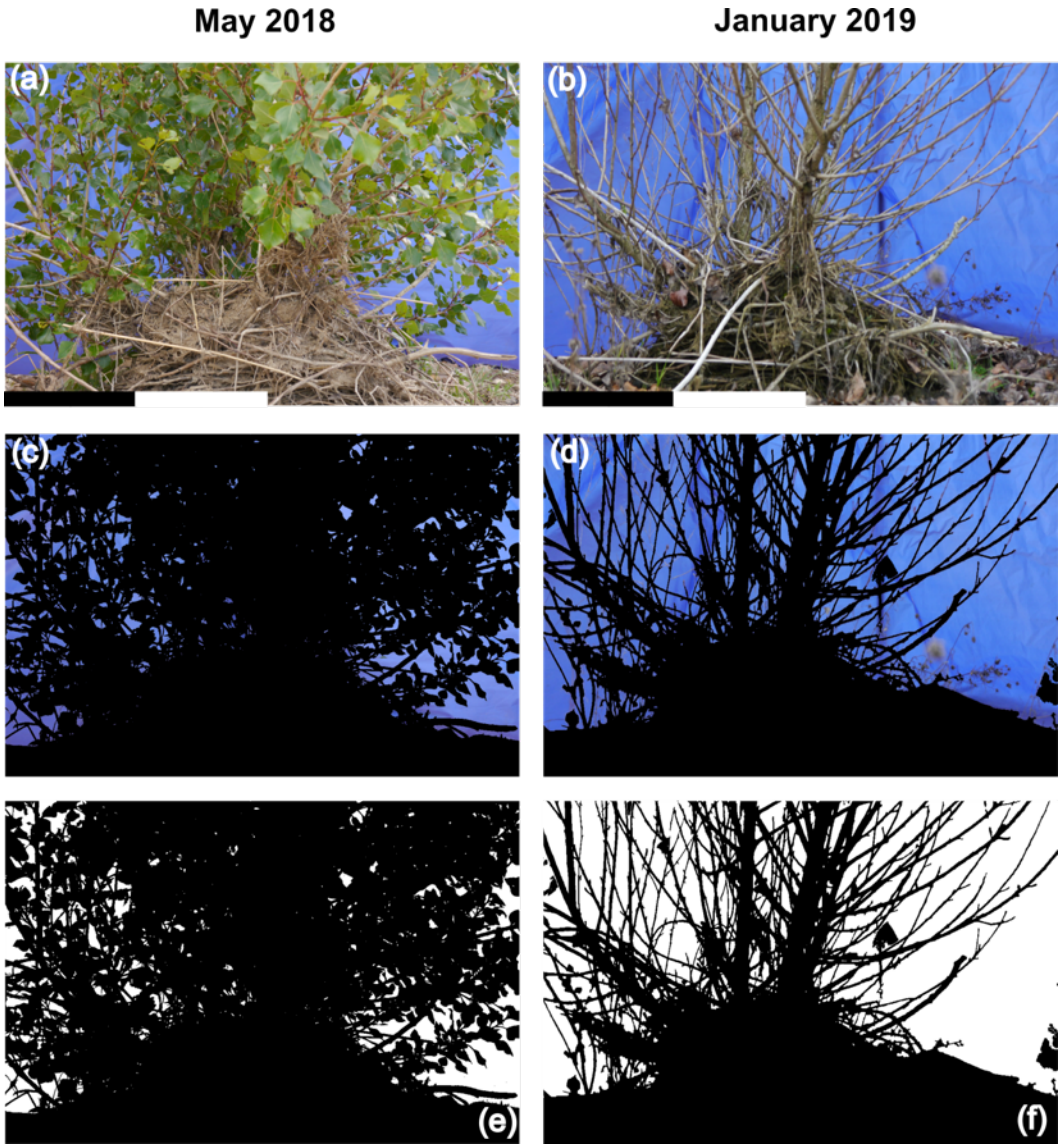


Figure 66. Workflow for estimating optical porosity in field conditions. (a), (c), and (e) display measurements taken during full foliage in May 2018, while (b), (d), and (f) exhibit measurements taken during leafless conditions in January 2019. The scale bar is 0.2 m.

During the leafless conditions observed in January 2019 (Fig. 66 b, d, and f), the median value of V_p for the same individuals increased to 33. However, the optical porosity (V_p) of the debris jam sections in front of the shrubs remained < 5 (compare Fig. 66 e and f). The geometric length scales of the sedimentary structures were measured using a Zeiss® Elta C30 tachymeter. Bulk sediment samples were collected upstream of the bush, within a local scour hole (if present) and from the sediment ridge in the wake.Determination of the spatial extent of local scour holes and especially sediment ridges in the field proved to be more difficult than in the flume. While the local scour hole in front of the *P. nigra* L. individuals was clearly identifiable as a conical depression, the sediment ridges in the field had a wedge-like shape that extended in the downstream direction. Its maximum extent in length and width was, therefore, determined by the presence of finer grained sediment and the surrounding materials.

In the case of local scour holes, the median local scour hole depth (d_s) and length (l_s) in front of the shrubs had a median value of 0.1 metre. The median local scour hole width (w_s) had a value of 0.6 metre. Based on the ratio of d_s to w_s (i.e., $d_s/w_s = 0.17$), it is concluded that local scour holes have reached a near steady state (Schlömer 2020; Schlömer *et al*., 2021). Compared to the relatively shallow local scour holes, the adjacent sediment ridges in the wake of the shrubs were considerably larger in terms of width (w_r) (median: 1 metre) and length (l_r) (median: 3.8 m). Due to this imbalance in the amount of scoured zone compared to the amount of sediment deposited in the wake, it is suggested that the sediment ridges result from (i) the deposition of scoured sediment and (ii) the sediment trapping of suspended sediment that approached the shrub during the flood wave. This hypothesis is supported by the sediment sample's grain size distribution. The sediment ridges were composed of relatively fine sand that was more uniform and partially finer compared to the coarse sand and fine gravel particles from upstream (Fig. 67 a). This observation was also valid for the VISS of *P. nigra* L. individuals that did not have a local scour hole in their upstream part due to missing driftwood jams (Fig. 67 b). The average grain size of sediment ridges was found to be 70–90% finer downstream of the shrubs as compared to its upstream. Corresponding findings have been documented by Tanaka and Yagisawa (2010) for sediment accumulations behind Salix shrubs in the Arakawa River, Japan. This condition supports the establishment of herb and grass species, which contribute to

sediment stabilization once deposited (Gurnell & Bertoldi, 2022; Hortobágyi *et al*., 2018).

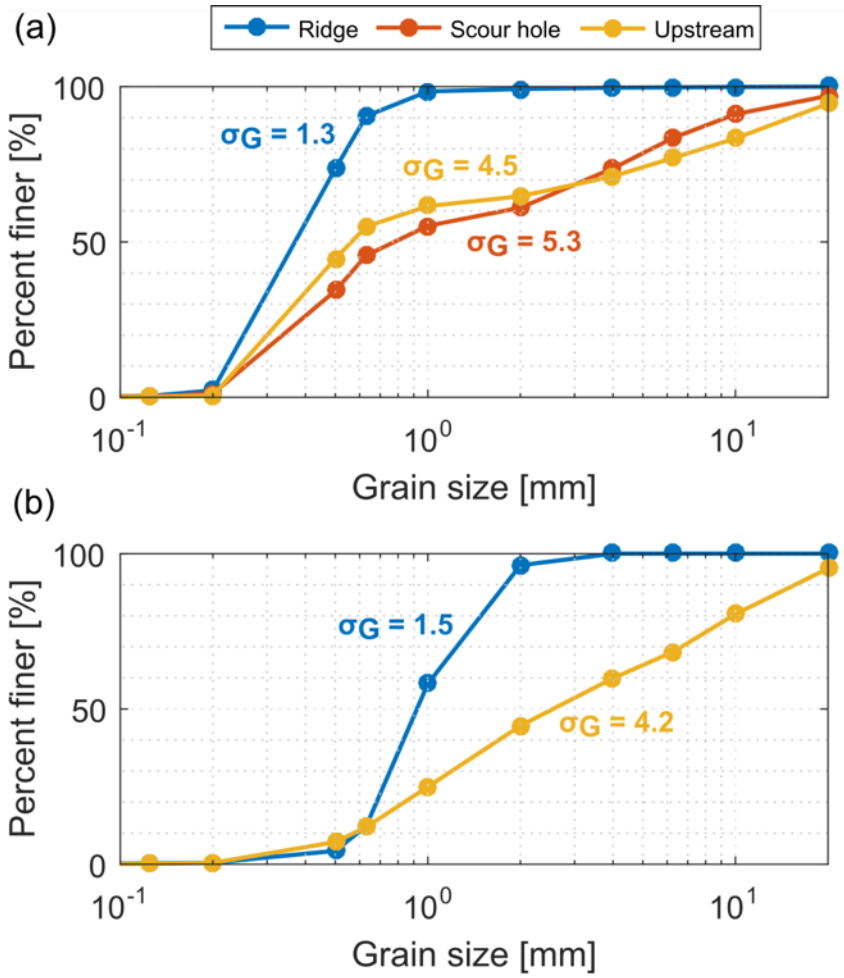


Figure 67. Results of sieving analysis of field evidence. (a) VISS composed of local scour hole and adjacent sediment ridge, and (b) VISS from sediment alone in the wake.

The largest sediment ridge (h_r = 0.3 metre, w_r = 3.1 metre, l_r = 8.4 metre) at the Amboise floodplain, exposed intricate cross-stratification consisting of fine to medium sand. The sediment ridge also contained intervening layers of organic material, gravel, and mussel shell (Fig. 68 a and b). Additionally, thin layers of muddy sediment also could be observed (Fig. 68 c). These muddy layers have been described by Rodrigues *et al*. (2007) and Euler *et al*. (2014) in detail for VISS at the Loire River. It is suggested that the sedimentation of the mud is connected to the retreating flood flows. As such, it is necessary to acknowledge at least four flood events as having contributed to the formation of the sediment ridge (Fig. 68 d). Grass colonized the center of the ridge, and its root network extended to the deeper parts of the sediment deposit, helping to stabilize it (Yu *et al*., 2020, black arrow in Fig. 68 b and d). The sediment grain size

inside the local scour hole was coarser and had less uniformity (σ_G > 1.3–1.5, Raudkivi & Ettema, 1985) compared to the sediment samples taken from the upstream area.

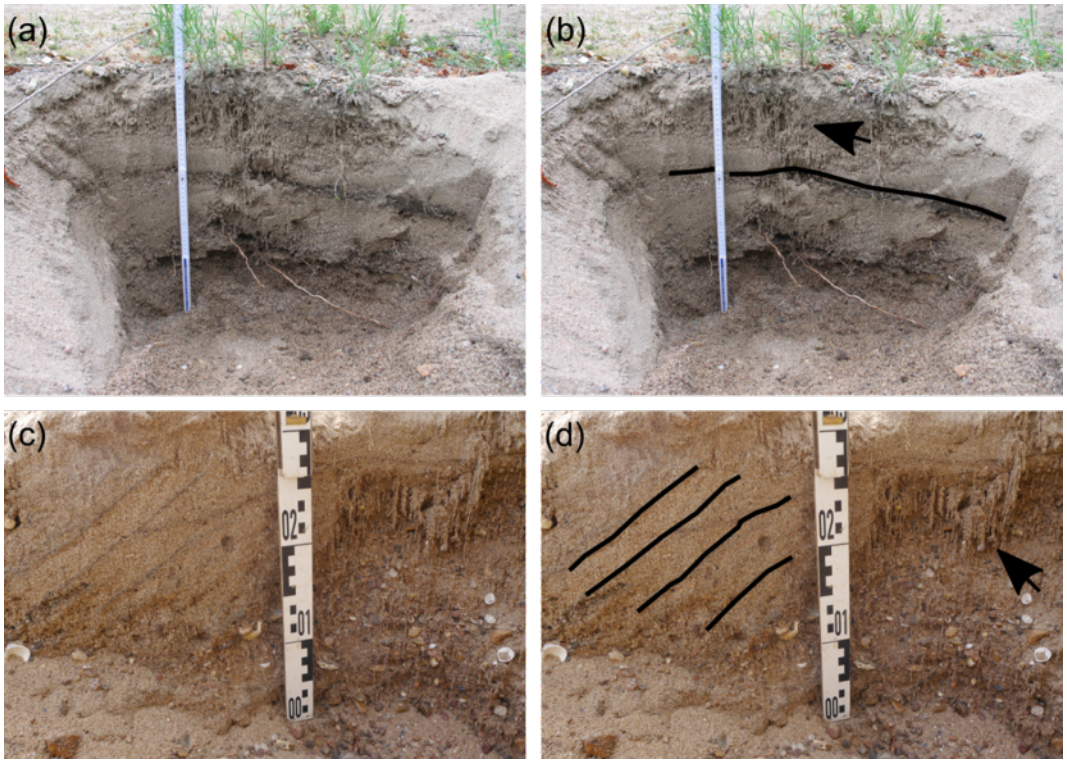


Figure 68. Sediment ridge outcrop reveals herbaceous vegetation root network as depicted in images (a) and (b). Muddy layers are visible in the uniform medium sand deposition shown in images (c) and (d).

90% of the observed local scour holes were found to be covered by a small gravel armor layer on top of the coarse sand. Research has shown that the presence of an armour layer can effectively halt local scour processes around solid bridge piers, particularly when the current hydraulic conditions are inadequate to mobilize the sediment present in the armor layer (Dey & Raikar, 2007; Sui *et al*., 2010). The observed VISS exhibit a positive correlation between their geometric length scales and the maximum area exposed to the peak flow (SOF). This correlation is evident for both the geometric length scales of the local scour hole (Fig. 69 a, b, and c) and the geometric length scales of the sediment ridge (Fig. 69 d, e, f). It can be concluded that the more surface area exposed to the flow, the larger the dimensions of the emerging VISS around the bushes.

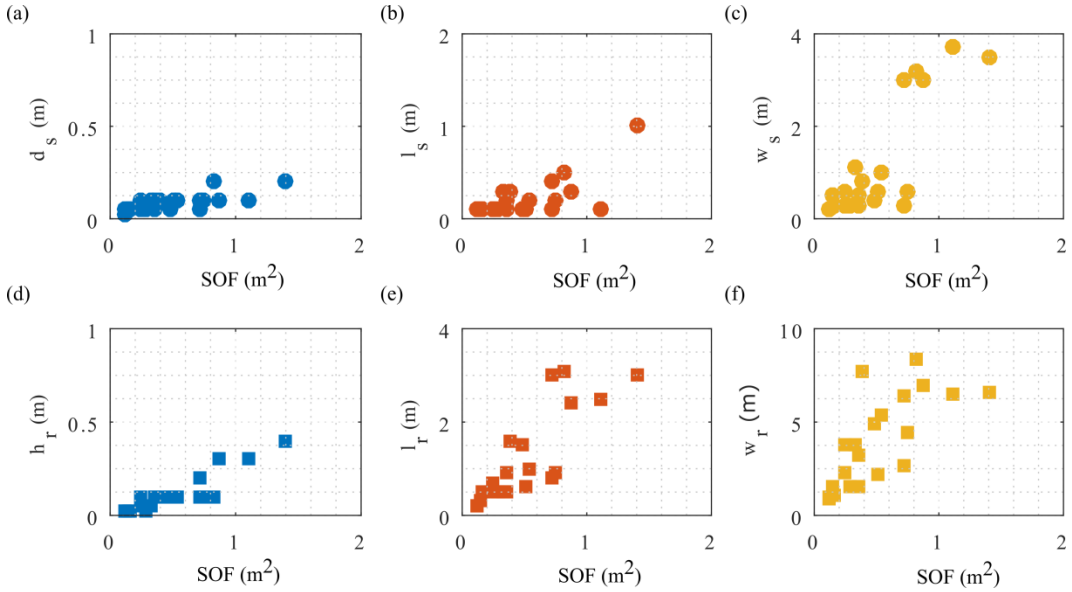


Figure 69. Dependence local scour hole (a–c) and sediment ridge (d–f) geometrical length scales on the surface exposed to flow.

9.4.2 SEDIMENT TRAPPING OF SUSPENDED LOAD AT PERMEABLE OBSTACLES ON LABORATORY SCALE

For Series A, sediment ridges formed parallel to the flow direction due to sediment deposition in the wake of the obstacle for all experimental runs. For different V_p, sediment deposition started immediately centrally in the wake of the brushes after the suspended sediment approached the obstacle. Regardless of V_p, the sediment ridges were wedge-shaped. The sediment ridges originated directly in the wake of the porous obstacle in its plane of symmetry. The ridges widened in the downstream direction, while their width and height increased with increasing distance downstream. The maximum ridge height (h_r) and width (w_r) of the sediment ridges occurred in the far wake downstream of the brush at $x/w_o \geq 4.5$.

For the repeated experimental runs, the shape and geometric length scales at the end of the experimental runs could be reproduced. When comparing individual runs, the standard deviation (σ_G) for the size of w_r and h_r was less than 0.26, excluding randomness in the experimental setup. The amount of trapped sediment was quantified by $Vol_r = h_r * w_r * l_r$. Although this quantification does not take into account the shape of the sediment ridge, and, thus, systematically overestimates the actual sediment ridge volume, the estimated dimensionless volume ($Vol_r^{1/3}/w_o$) is in reasonable agreement with the dimensionless weighted volume ($Vol_w^{1/3}/w_o$) of the sediment ridges sampled after the experiments (Fig. 70 a). The samples were weighed after drying. Taking into

account the optical porosity (V_p), the estimated amount of sediment trapped in the wake of the obstacles varied considerably (Fig. 70 b). A piecewise linear pattern was observed for the regression of $Vol_r^{1/3}/w_o$ /w_o over V_p, indicating a threshold condition for V_p of 4 to 6 in the current set of experiments. At this threshold condition, the volume of sediment ridges increases slightly as V_p increases, while the slope coefficient of the linear regression (ß1) is positive (1.3). For $V_p > 6$, $Vol_r^{1/3}/w_o$ decreases with increasing V_p, and the slope coefficient is negative (-0.23). For the solid and impermeable cylinder ($V_p = 0$), $Vol_r^{1/3}/w_o$ is the lowest for the entire series of experiments. Here, sediment deposition did not occur for $x/w_o \leq 2.5$.

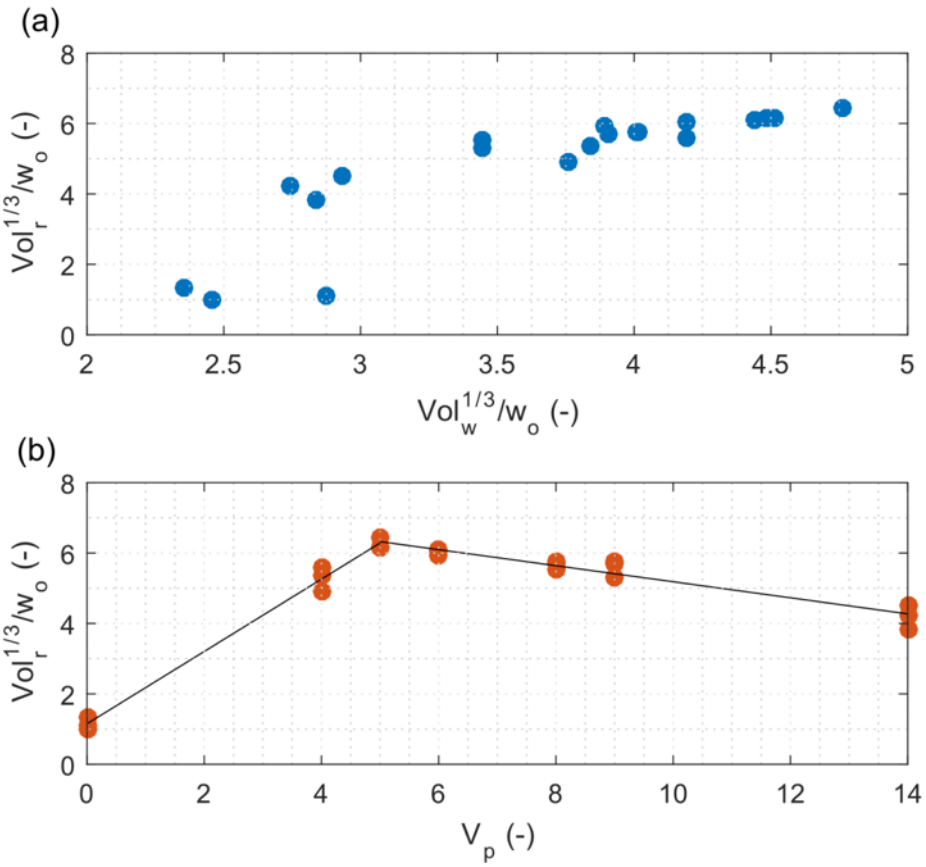


Figure 70. (a) Estimated normalized sediment ridge volume ($Vol_r^{1/3}/w_o$) as a function of normalized sediment ridge volume from weighed sediment samples ($Vol_w^{1/3}/w_o$). (b) Dependence of estimated normalized sediment ridge volume ($Vol_r^{1/3}/w_o$) on optical porosity (V_p). Error bars represent standard errors and means.

The deposition pattern observed in the vicinity of permeable barriers can be partly explained by the flow field in the wake of the barriers. A solid, impermeable obstacle exhibits a zone of reverse flow immediately behind the cylinder in the downstream

direction, a phenomenon known as recirculation (Pattenden *et al*., 2005). The recirculation zone consists of two components: (i) a backflow component with slightly negative values of u and (ii) a strong upward flow component with positive values of w, independent of d_w (i.e., 0.006, 0.015, and 0.003 m), (Fig. 71 a – c and g – i, blue line). The strength of the upward component is directly proportional to the distance from the flume bed. The recirculation and upward flow in the wake are caused by a velocity and pressure gradient that arises when the approaching flow encounters the non-permeable front of the cylinder. The shedding of von Karman vortices was observed downstream of the obstacle, which is typical for unsubmerged flow-obstacle interactions (Li *et al*., 2018, Link *et al*., 2012). The turbulence intensity (TI) in the wake of the solid cylinder was significantly high, probably due to the recirculating and upward flow (Fig. 71 d – f). Therefore, it is hypothesized that the high TI prevented sediment deposition at the solid non-permeable cylinder for $x/_{wo} \leq 2.5$.

For the porous obstacles ($V_p = 5$ and $V_p = 14$), an upward flow component was observed for $x/w_o \leq 5$; however, the values of w were lower compared to the results for $V_p = 0$. The weakening of the velocity and pressure gradient at the faces of the obstacle is due to the bleed-flow through the obstacle. The reduction of the upward component was proportional to the bleed flow and the increasing porosity of the barrier (Fig. 71 g – i, yellow and orange lines). As a result, turbulence levels behind the permeable obstacles were lower than those of the non-permeable cylindrical structures for $x/w_o \leq 5$, regardless of water depth. Consequently, the bleed flow passing through the permeable barriers effectively dissipates energy from the flow through turbulent diffusion (Sharpe & James, 2007), facilitating sediment deposition in the wake of the barrier zone. This is because TI < settling velocity of sediment (w_{set}) for sediment fractions D_{16} to D_{84}, at $x/w_o \leq 5$. This hypothesis also is supported by other experimental setups: Tinoco and Coco (2014, 2018) identified turbulence as the primary driver of sediment resuspension in flow-vegetation interactions, rather than bed shear stress caused by mean flow velocity.

Based on this assessment, it would be expected that there would be a direct correlation between the increasing porosity of an obstacle and the volume of the sediment ridge, as turbulence intensity decreases as the porosity of the obstacle increases. However, this is not evident in the current series of experiments. Therefore, it is speculated that the amount of bleed flow is a key factor in sediment deposition in the wake of porous obstacles. If the bleed flow exceeds a critical value, it will reduce

sediment deposition on the lee side. For this series of experiments, the critical value was observed to be $V_p = 5$. Further research is needed to understand the function of this flow structure in sediment transport processes.

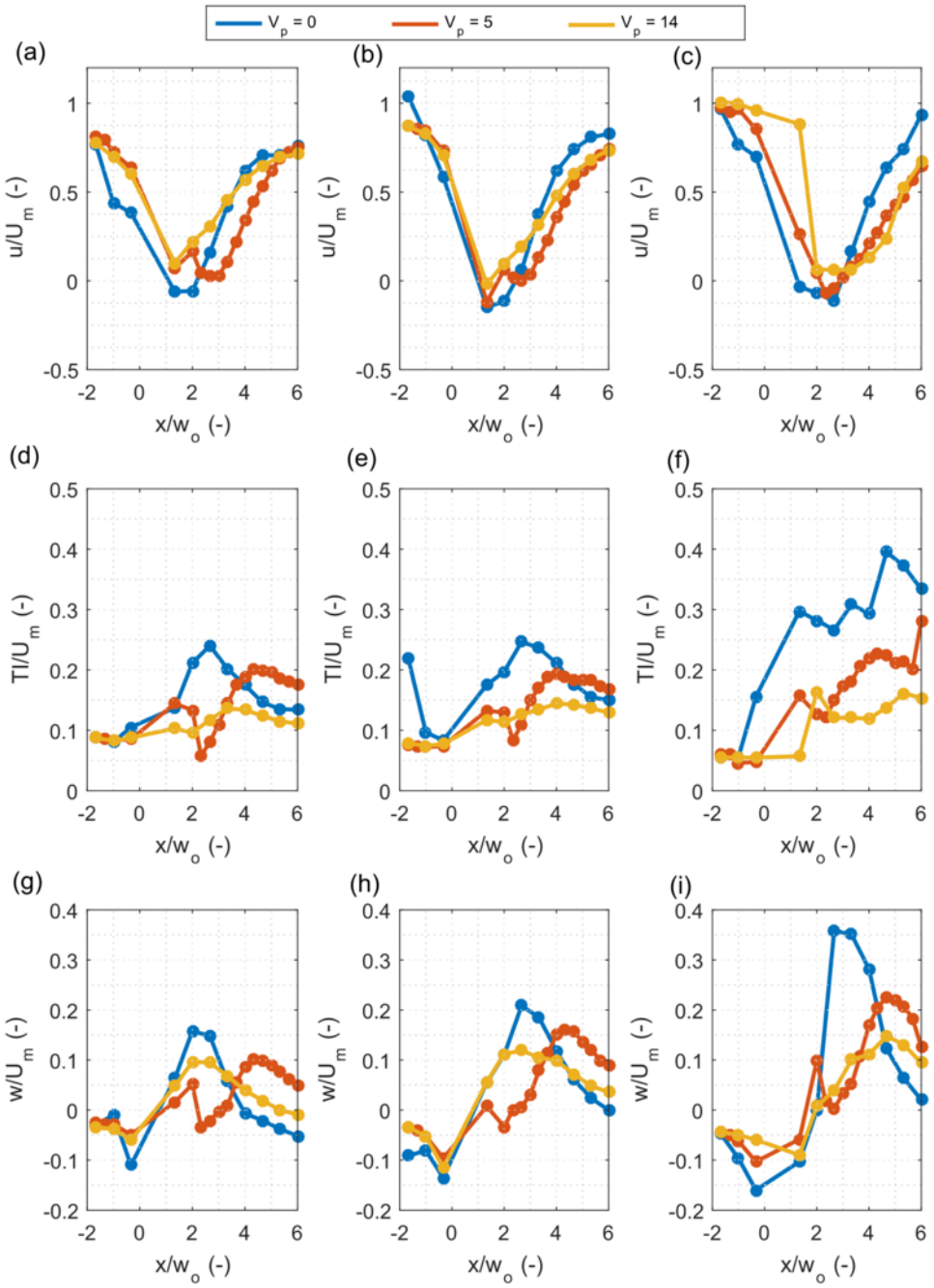


Figure 71. Flow field quantification near porous obstruction for d_w = 0.006 m, 0.015 m, and 0.03 m: (a-c); streamwise flow component normalization (d-f) of turbulence intensity (TI); and (g-i) vertical flow component.

9.4.3 LOCAL SCOURING AT PERMEABLE OBSTACLES ON THE LABORATORY SCALE

For Series B, local scour holes occurred in 54% of all test runs. Local scour started at the lateral edges of the obstacles by the formation of two initial depressions which rapidly merged into a conical local scour hole in front of the obstacle during t < 5 min. The position of the maximum scour depth then migrated from the lateral sides to the front of the obstacle. The eroded material was deposited downstream in the wake of the obstacle as a sediment ridge with an orientation parallel to the flow direction. Subsequently, the frontal scour hole deepened, lengthened, and widened, while the sediment ridge flattened, widened, and lengthened downstream as the sediment was reworked in the wake of the obstacle.

For scenarios 1 and 2, the normalized bed load (q*) from the local scour hole was estimated in the streamwise (l_s) and perpendicular to the streamwise (w_s) directions. Two temporally consecutive local scour profiles (i.e., after 120, 240, 300, and 480 min) were used to estimate the volumetric bed load transport rate (q_b (L_2/T)) out of the frontal scour by calculating the line integral:

$$qb\ (l_{sP}, w_{sP}, t) \approx c^b/t(i+1) - t(i)$$

(Eq. 53)

with l_{sP} = longitudinal scour hole profile, w_{sP} = horizontal scour hole profile, c^b = depth-integrated frontal scour hole area, and i = 1, …N where n is the total number of profiles measured in time.

In the absence of suspension the sediment flux of the scour hole in terms of bed load could be estimated with an accuracy of +/- 2 D_{50}. For further analysis qb was normalized to be q* (-):

$$q^* = q_b/((\rho_s/\rho\text{-}1)\ gD_{50}{}^3)^{1/2}$$

(Eq. 54)

with ρ_s = sediment density, ρ = water density, and g = gravitational acceleration.

The results showed an asymptotic (limiting) behavior in time (Fig. 72). In the beginning (i.e., $t/t_e \leq 0.25$), there was rapid incision and simultaneous enlargement of l_s and w_s, resulting in a high q*. However, q* decreased significantly in the later stages of the experiments, almost to q* = 0 for $t/t_e \leq 0.75$. The value of q* exhibited an inverse relation with V_p. For the most impermeable obstacle (V_p = 0.04) the highest estimates of q* were estimated at the start of the experimental trials. As porosity increased, q*

consistently decreased over time. Alongside V_p, the hydraulic conditions, specifically the approaching flow depth (d_w), also influenced the transport of q* from the local scour hole. Although the flow intensity (U_m/U_c) was almost identical for both scenarios, a greater amount of q* was estimated to have been transported out of the local scour hole when the flow depth (d_w) equalled the obstacle height (h_o). For $d_w/h_o = 1$, a stronger downflow at the frontal face of the obstacle persisted, triggering an efficient hydraulic vortex at the obstacle's base and facilitating sediment mobilization. Therefore, at the end of the experimental runs (t_e), it was observed that the geometrical length scales of the local scour hole were greater for scenarios 2 and 4. Kim *et al*. (2015) and Gu *et al*. (2018) presented comparable findings in their experimental series on local scour at vegetation patches with varying degrees of submergence ratio under clear water conditions. However, as the vegetation patch in their studies was aligned at the flume sidewall, the morphology of the local scour hole differed from that reported in the current study. However, both studies found that the greatest scour depth occurred when the flow depth was equal to the height of the vegetation patch above the sediment surface. Additionally, a negative scaling relation between d_s, l_s, and w_s with respect to optical porosity (V_p) was apparent.

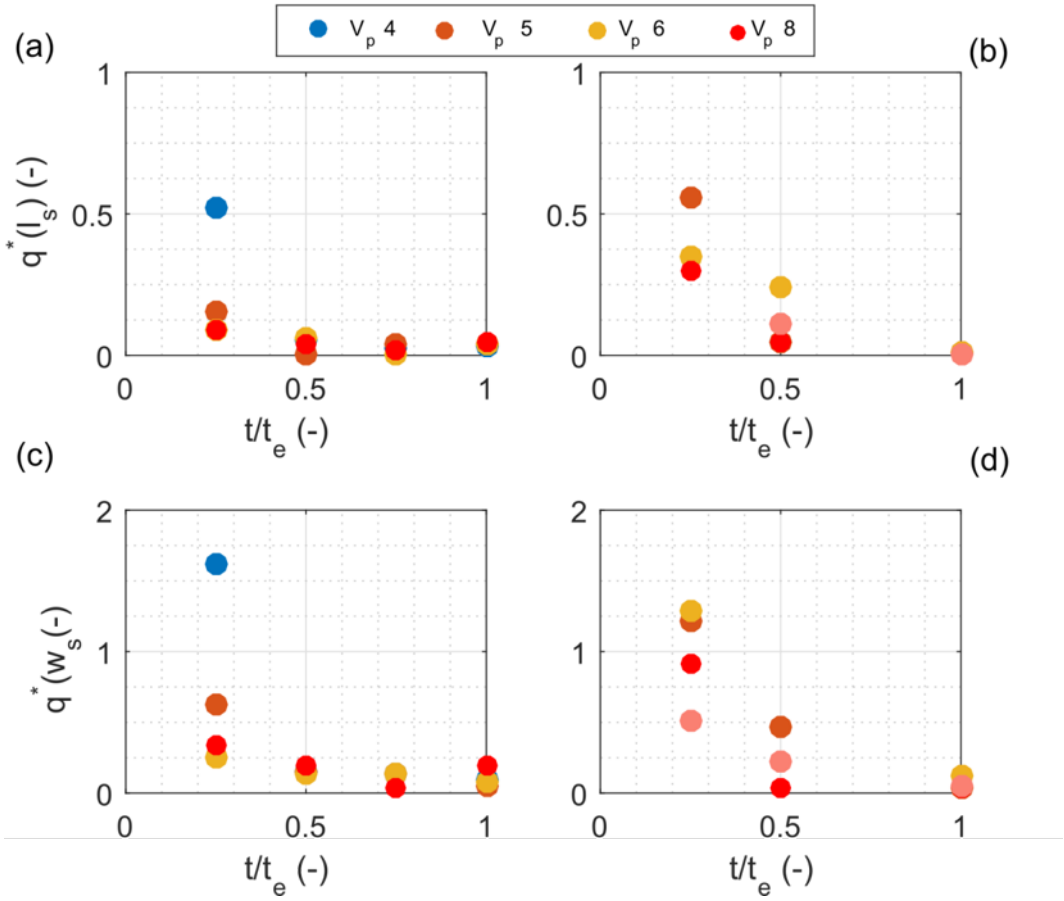


Figure. 72. Estimated normalized bed load (q*) exiting the local scour hole during the normalized experimental duration for longitudinal cross-sections (a, b) and horizontal cross-sections (c, d). This is for hydraulic scenario 3 (a, c) and hydraulic scenario 2 (b, d).

For the obstacle with the least porosity (i.e., small value of V_p), the largest local scour hole was present in terms of d_s, l_s, and w_s, (Fig. 73 a-c). Nevertheless, local scour did not occur in all experimental runs of Series B, and a threshold value in optical porosity was identified, inhibiting local scour. Irrespective of the hydraulic scenario, no local scour hole was formed at the obstacle's frontal face for $V_p \geq 0.14$. The obstacle is then excessively porous, which weakens the downflow at the frontal face, thus, hindering the formation of a high-velocity flow responsible for the creation of a frontal local scour hole. This finding concurs with the investigations of by Yagci *et al.* (2016) and Kitsikoudis *et al.* (2016).

The geometric length scales of the sediment ridge also showed an inverse scaling on V_p, as seen in Fig. 73 d, e, and f. The relation between the eroded and deposited sediment volumes was nearly equal, which is conceivable under clear-water conditions (Euler *et al.*, 2014). The volume of the local scour hole was estimated by assuming an inverted frustum cone shape. This was due to a flat semicircular scour hole bottom (S_b)

which is closely attached to the obstacle base. It has a radius smaller than the extent of the local scour hole at the surface (l_s), (Schlömer & Herget, 2023). Therefore, the volume of an inverted frustum cone was estimated by (Ehsbach, 1975):

$$Vol_s = 1/3\ d_s\ \pi\ (l_s^2 + l_s * S_b + S_b^2)$$

(Eq. 54)

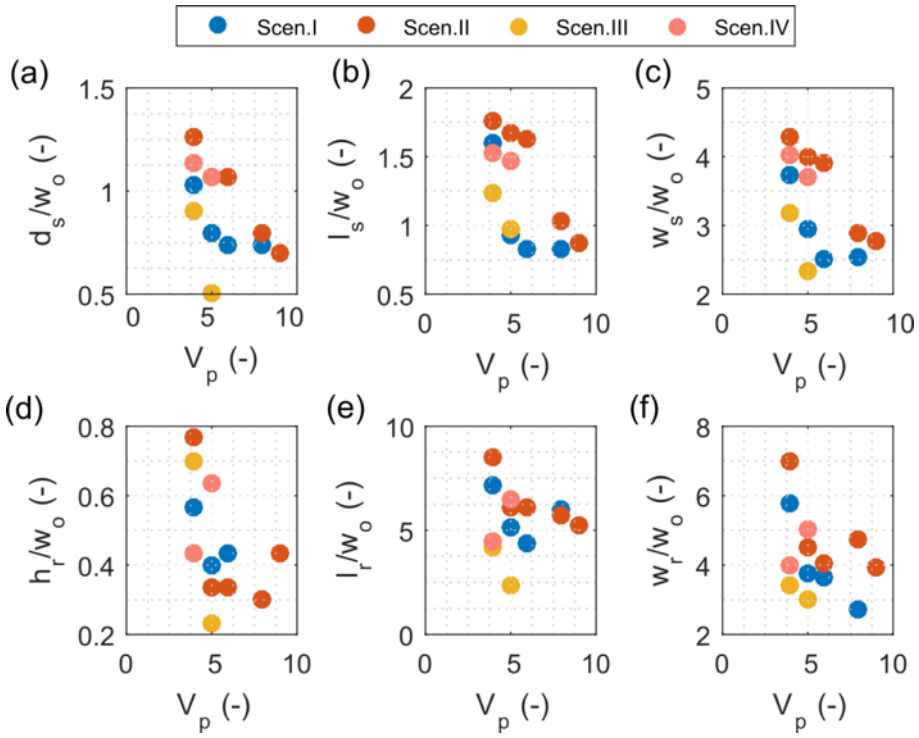


Figure 73. Dependence of geometric length scales on optical porosity (V_p). (a-c) Local scour hole. (d-f). Sediment ridge.

9.4.4 DATA INTEGRATION ON LOCAL SCOUR

Based on the experimental results of Series B, an empirical model is presented for the estimation of local scour hole and sediment ridge volumes at porous obstacles. It is based on (i) the surface area exposed to flow (SOF), where SOF is equal to the flow depth of the approaching flow (d_w) multiplied by the width of the obstruction (w_o); (ii) the optical porosity of the obstruction (V_p), where $V_p < 14$; and the approaching flow intensity (U_m/U_c). The model shows acceptable agreement with experimental observations when the model values are plotted against the estimated volumes of local scour holes and adjacent sediment ridges. The proposed model has a coefficient of determination (R^2) of 0.74 for the scoured volume (Fig. 74 a), while the deposited volume (Fig. 74 b) has an R^2 of 0.66. The empirical model's validity could not be

verified by comparing it to other studies due to the lack of reported input parameters, particularly optical porosity, in previous research on local scour at vegetation elements. Additionally, insufficient information on the hydraulic conditions during VISS formation of *P. nigra* L individuals prevented the integration of field data. Therefore, to practically apply the model, it is necessary to collect a larger amount of field data to accurately calculate correlations.

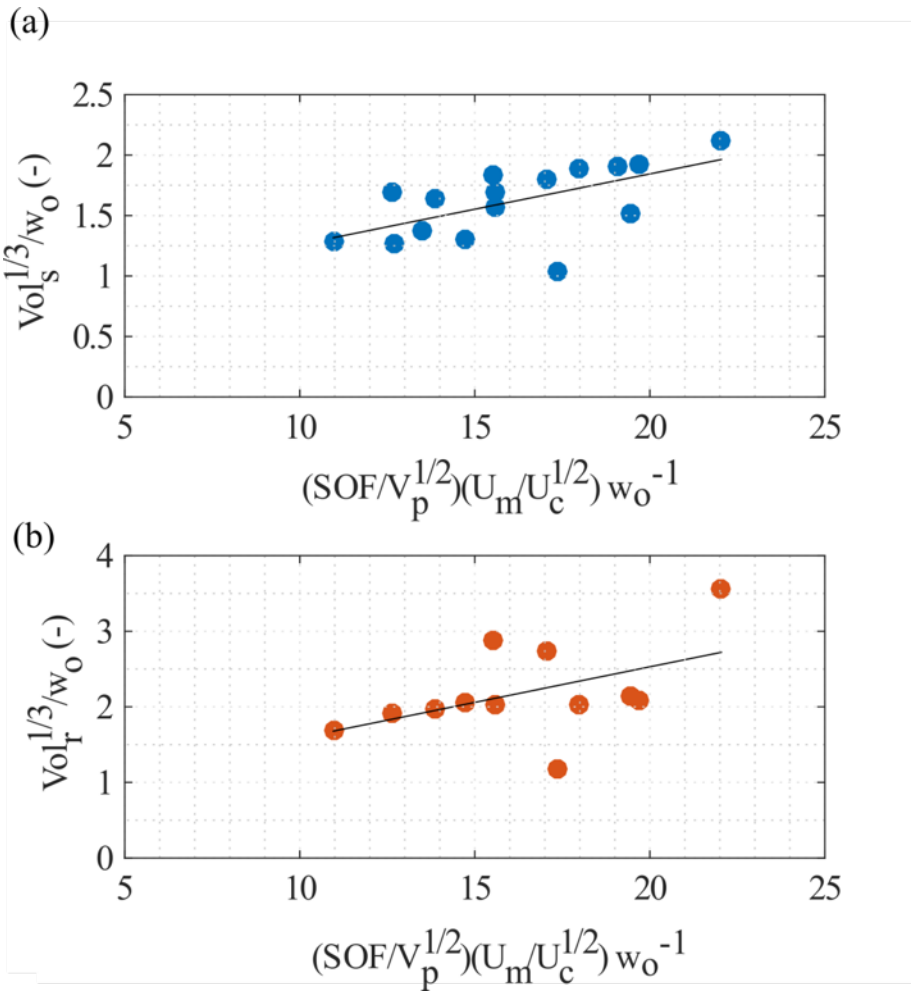


Figure 74. Dependence scoured volume ($Vol_s^{1/3}$) (a) and normalized deposited volume ($Vol_r^{1/3}$) (b) on proposed empirical model.

9.5 REVISITING THE WORKING HYPOTHESIS AND SHORTCOMINGS

(i) The porosity of an obstacle and individual plant can be adequately described by the optical porosity which can be assessed for laboratory and field conditions based on digital photographs.

The porosity of artificial obstacles and *P. nigra* L. specimens was assessed using the optical porosity (V_p), which is a two-dimensional measurement that overlooks the three-dimensional aspect of void spaces (Grant & Nickling, 1998). As demonstrated by Montakhab *et al*. (2013), the actual volumetric porosity (Vol_p) is slightly higher. However, measuring the volumetric porosity of a plant under field conditions usually is complicated, whereas the method presented in the current study allows for a rapid assessment of optical porosity (V_p) for both laboratory and field conditions. However, it should be noted that, as highlighted by Loeffler *et al*. (1992) and Yagci *et al*. (2016), each vegetation species has unique morphometric, biomechanical, and seasonal characteristics, making porosity a challenging parameter to compare under natural conditions. In considering natural shrubs exposed to a current, it is necessary to acknowledge their flexibility. This entails their tendency to bend in the streamwise direction as a result of flood exposure (Yagci *et al*., 2010; Zhu & Tsubaki, 2022). Consequently, branches and leaves become compressed and porosity is reduced. As the experiments of the current study did not consider this boundary condition, it is uncertain how obstacle bending affects the formation of VISS. However, Euler *et al*. (2014) demonstrated that the horseshoe vortex (HV) system, which causes frontal local scour, ceases to exist below inclinations of 25-30 degrees in the streamwise direction.

(ii) Under certain hydraulic and sedimentary boundary conditions, the porosity of an obstacle affects (a) the amount of sediment deposited when a sediment-laden flowencounters the obstacle, and (b) the triggering of local scouring around the obstacle.

Analyzing the shrub's porous structure identifies consequences on hydraulic processes and sedimentary features. The results highlight the substantial impact of obstacle porosity on the surrounding flow field and sediment transport near obstructions. The impact is attributed to the flow that passes through the porous obstacle, known as the bleed flow, which is dependent on the porosity level. The bleed flow consequently

influences (a) the flow velocity in the obstacle's wake and (b) the intensity of the downflow at its front. The study findings demonstrate that the downflow increases with the decrease in porosity, whereas the flow in the wake is smoother with lower porosity levels. However, the study of six porosity levels in the current study clearly showed that there is a threshold of porosity above or below which there is a decrease in the volume of sediment deposited. Therefore, for maximum sediment accumulation behind an obstacle, there must be an ideal relation between downflow, bleed flow, and the recirculation zone. A critical value of optical porosity (V_p) between 4 and 6 was identified. At this porosity, a long-lasting flow calming zone was observed behind the obstacle, which promotes the deposition of suspended sediment and leads to the highest accumulation volume compared to other porosity levels. For $V_p \geq 14$ a threshold was found in the experimental data where local scour processes are completely inhibited. The obstacle is then too porous and no significant downflow occurs at the front of the obstacle. Consequently, there is no erosive horseshoe vortex system at the base of the obstacle. An empirical model could be formulated to estimate the local scour hole and sediment ridge volumes at porous obstacles based on the area exposed to flow, optical porosity, and the flow intensity of the approaching current.

(iii) Vegetation-induced sedimentary structures (VISS) are scale-invariant features, so that small scale laboratory results are comparable to large-scale field results.

The geometry of VISS at *P. nigra* L. shrubs in two floodplain areas of the Loire River was found to be similar to that observed during flume experiments. At the field scale, the VISS consisted of either sediment ridges in the downstream wake of the obstacle without frontal local scour holes, or local scour holes in front of the obstacle and adjacent sediment ridges. Both geometries also were observed in the current experimental study. The geometry is assumed to be scale invariant, implying similarity of process and shape rather than equifinality (Schlömer *et al.*, 2021). During full-foliage, the observed median value of optical porosity at *P. nigra* L. individuals was comparable to the optical porosity values used in the experimental campaign. However, for leafless conditions, the mean optical porosity was larger than that investigated in the laboratory flume. However, local scour holes were only observed in association with driftwood jams entangled in the shrubs, which reduced the porosity of the obstacle. This

field-scale observation is consistent with experimental results, where the size of local scour holes decreased with decreasing porosity. Similar observations on the effect of debris accumulation at flow obstacles and the intensification of local scour processes were also reported by Al-Zawaidah *et al*. (2021) and Ravazzolo *et al*. (2022). The deposition of finer sediment in the wake, induced by the porosity of the shrubs, led to the formation of microhabitats that were already colonized by herbaceous species. This stabilized the sediment ridges to some extent. The establishment of such a stabilizing vegetation cover requires periods without flood stress (Gurnell *et al*., 2012; Euler *et al*., 2014). It is difficult to associate a particular VISS with a specific flood event without careful monitoring. Therefore, laboratory studies are essential to understand the interactions between vegetation, flow, and sediment transport. To increase the applicability of such simulated studies to nature, further analysis of more complex hydraulic conditions is necessary. Additionally, experiments under natural flow conditions should be done. The method of manipulative experiments may offer a solution, whereby controlled parameters are subjected to natural forcing conditions in the field.

10. SYNTHESIS

10.1 RECALLING THE RESEARCH QUESTIONS

Summarising the previous chapters, the main research questions posed in the introduction can now be answered as follows:

> **Q1**: *What are the boundary conditions that enhance or limit the formative processes of fluvial obstacle mark evolution at natural instream obstructions, and how can they be operationalised as physical control parameters*?

A framework is established that describes a spectrum of extrinsic and intrinsic boundary conditions that control the hydraulic and sedimentary processes of obstacle mark formation at natural obstructions such as boulders or vegetation elements. The framework is composed of dimensionless control parameters separated by a hierarchical order of importance for obstacle mark formation. The "typical" obstacle mark morphology resulting from the erosive action of the horseshoe vortex system and local scour incision serves as the target for the parameter framework. The framework identifies three conditions: the conditions under which the characteristic geometric length scales of obstacle marks are maximised, the conditions under which the length scales are limited compared to the maximum state, and the conditions under which obstacle mark formation is completely inhibited. The hierarchical order distinguishes primary and secondary control parameters. Primary control parameters determine the geometric scale of the flow field at the obstacle and thus control the potential maximum size of the obstacle mark. Secondary control parameters affect the dynamics of the flow field within the geometric scale and limit the potential maximum size of the emerging obstacle mark when certain thresholds are exceeded. Seven primary control parameters control the geometric scale of the horseshoe vortex system at the obstacle and determine the potential maximum size of the structure:

(i) Submergence ratio:
The approaching flow depth relative to the size of the obstacle controls the geometric scale of the primary horseshoe vortex (HV1).

(ii) Relative sediment coarseness:
The size of the horseshoe vortex system is influenced by the ratio of obstacle size to median grain size if the sediment is too coarse relative to the obstacle due to dissipative effects.

(iii) Blockage ratio:
For a very wide obstacle, there is no continuous horseshoe-vortex system at the front of the obstacle. Instead, the horseshoe vortex system branches into several smaller vortices at the lateral edges of the obstacle.

(iv) The shape of the obstacle:
For streamlined obstacles, a weak pressure gradient at the obstacle front prevents the formation of an interconnected horseshoe-vortex system.

(v) Porosity of vegetation elements:
If the obstacle is too porous, the void spaces not occupied by branches and leaves will be drained, preventing the formation of a horseshoe-vortex system in front of the obstacle.

(vi) Deflection height of flexible parts:
The branches and leaves of shrubs bend and flex in the direction of the flow as it passes over or through them, reducing the height of the obstruction compared to the condition when no flow is approaching the object. This reduces the drag in front of the vegetation element, thereby inhibiting the formation of a horseshoe vortex.

(vii) Stem inclination:
If the stem of mature riparian vegetation elements is inclined in the flow direction compared to its orientation perpendicular to the river bed (i.e. 90°), this also reduces the pressure gradient in front of the obstacle and conversely the geometric size of the horseshoe-vortex system.

Six secondary control parameters affect the dynamics of the horseshoe-vortex system within its geometric scale and characterise the sensitivities of obstacle mark formation:

(viii) Flow intensity:

The erosive capacity of the horseshoe-vortex system scales with increasing mean flow velocity. If the approaching flow velocity exceeds the critical flow velocity for sediment entrainment, the local scour hole may be buried by sediment input and passage of bedload sheets.

(ix) Grading coefficient:

Coarser sediment particles can form an armour layer within the local scour hole for non-uniform alluvial sediment. This can prevent further local scour as the horseshoe vortex may not be able to erode the sediment particles for the given flow conditions.

(x) Mobility:

Local scour at natural solid obstacles, such as boulders, can undermine the obstacle and result in tilting into the local scour hole, limiting further incision.

(xi) Thickness of the alluvial layer:

The depth of a local scour hole will be significantly limited, regardless of flow conditions, if an obstacle is located in a thin layer of alluvial sediment above bedrock.

(xii) Viscosity/obstacle Reynolds number:

The formation of a horseshoe vortex system and the emergence of an obstacle mark are inhibited when viscous stresses dominate at the obstacle, regardless of flow conditions and obstacle size, due to a high amount of debris in the approaching flow.

(xiii) Time:

The formation of an obstacle patch is an asymptotic process that approaches an equilibrium or steady state condition where the size of the obstacle patch is maximised. The time scale for reaching a steady state condition depends on the approaching flow velocity and grain size. The majority of the obstacle mark size in equilibrium conditions is reached within the first few hours of local scour and sediment aggradation in the wake.

Q2: *Can control parameter thresholds be identified that modify hydraulic and sedimentary processes and regulate transitions in the spatial pattern and geometric relationship of fluvial obstacle marks*?

Obstacle marks are complex geomorphic systems that exhibit feedback loops between hydraulic and sedimentary processes, resulting in non-linear evolution over time. This behaviour is commonly referred to as self-organisation, which is controlled by the presence and crossing of thresholds. Within these contribution thresholds, primary and secondary control parameters are identified that either (i) must be crossed to initiate obstacle mark formation, or (ii) mark conditions for which the geometric length scales of an obstacle mark are maximised. Between these threshold conditions, the size of the obstacle mark is reduced from its potential maximum. Table 3 provides a comprehensive overview of the identified thresholds in the primary and secondary control parameters. This paper also presents new experimental work that reveals previously undescribed thresholds in submergence ratio, shape and vegetation porosity. The geometric length scales of an obstacle mark on a boulder-like obstacle are maximised when the depth of the approaching flow is similar to the size of the obstacle. The dimensions of the obstacle mark are 20% larger for steep, angular obstacles compared to rounded obstacle shapes for this condition. An intense pressure gradient forms at the front of the obstacle when the vertical extent of the approaching flow depth approximates the size of the obstacle for the steep, angular obstacle. A highly erosive horseshoe vortex system is then present at the base of the obstacle.

Changing the flow depth or submergence ratio beyond this threshold will reduce the size of the obstacle mark. If the flow depth is less than the size of the obstruction, a non-submerged condition occurs. This condition causes a bow wave to form at the front of the obstruction, particularly in the case of a boulder-like obstruction. At shallow depths, the bow wave disrupts the horseshoe vortex, reducing the formation of local scour and sediment aggradation. As the depth of flow and the submergence ratio of the obstacles increase, the geometric length scales of the near-steady-state obstacle mark become smaller. This occurs because much of the approaching current flows over the top of the obstacle, which does not contribute to the formation of the horseshoe vortex at the base of the obstacle.

For rounded obstacles, no typical obstacle mark with a frontal local scour hole and sediment ridge in the wake was formed for conditions where the flow depth was 1.6

times the size of the obstacle. The absence of frontal local scour therefore indicates the absence of the horseshoe vortex. Instead, an “inverted” obstacle mark pattern prevailed, consisting of two lateral depressions in the wake of the rounded obstacle and an adjacent sediment ridge. The rounded shape of the obstacle favours a recirculation zone in the wake of the obstacle, where part of the flow reverses towards the obstacle, increasing turbulence and inducing local scouring. The inverse obstruction pattern was also found in a field dataset from the Colorado River, Arizona, suggesting similarity of process and shape rather than equifinality. With respect to the field evidence from the Colorado River, a plausible explanation for the observation of shallow local scour holes that were still relatively wide and long could be reduced sediment layer thickness. Laboratory experiments with a reduced thickness sediment layer gave similar results, provided that the sediment layer was thinner than the size of the obstacle.

An optical porosity threshold has been experimentally determined for vegetation porosity, which inhibits the formation of an obstacle mark under clear water conditions. Optical porosity is defined as a dimensionless measure of the ratio of voids to space occupied by twigs, branches and leaves. The assessment is based on digital photographs. If the porosity of the obstacle is equal to or greater than 14, no obstacle mark is formed, regardless of the thresholds crossed in the hydraulic boundary conditions. This is because the obstacle is excessively porous, which weakens the frontal flow and prevents the formation of a horseshoe vortex system, which is responsible for the formation of a local scour hole. Within the optical porosity range of 4 to 6, the geometric length scales of the local scour hole were largest for the experimental campaign. As the optical porosity increased, the geometric length scales of the local scour hole decreased. This inverse scaling was also observed for the geometric length scales of the sediment ridge.

Under live-bed conditions and general sediment transport, where sand is transported in suspension over a rigid bed, sediment trapping occurs in the wake of the permeable barrier, forming a sediment ridge in the absence of a local scour hole. The amount of trapped sediment is maximised at an optical porosity of 5, with increasing or decreasing optical porosity reducing the amount of trapped sediment in the wake. The decrease in trapped sediment at optical porosities less than 5 can be attributed to the shedding of trailing vortices in the wake of the obstacle, which further mobilise the suspended sediment. Hydraulic measurements indicate that the amount of bleed flow is a critical factor in sediment deposition as optical porosity increases. When the bleed

flow exceeds a critical value (i.e. 5), it reduces sediment deposition on the lee side of the obstacle due to increased turbulence. An empirical model based on laboratory results is presented to estimate sediment erosion and deposition volumes at porous barriers. The model takes into account the flow exposed surface area, the optical porosity of the barrier and the intensity of the incoming flow.

Structures similar to those observed in the laboratory were also observed in individual *Populus nigra* L trees under field conditions. The median optical porosity ranged from 8 (full foliage) to 33 (leafless). However, a localised scour hole was only present in shrubs where debris had accumulated on the frontal surface. This reduced porosity and consequently favoured downflow, leading to the formation of a horseshoe vortex at the base of the obstacle. These observations are consistent with the experimental results and demonstrate the scale invariance of the processes and the shape.

Q3: *What is the effect of changing time-dependent boundary conditions on the evolution of fluvial obstacle geometry*?

Previous laboratory research within the engineering community has shown that the evolution of local scour depth towards a maximum value is an asymptotic process over time. The present experiments have shown that the increase in local scour hole geometry over time is triggered by this depth cut. This oversteeps the local scour hole slopes and causes gravitational motions that lead to the enlargement of the conical local scour hole in width and length.

The relationship between the depth and width/length of the hole over time can be used to infer different phases in the temporal evolution of local scour holes. The temporal evolution of local scour holes can be divided into three phases: (i) rapid local scour hole incision at the beginning, resulting in deep local scour holes; (ii) decreasing local scour hole incision; and (iii) decreasing local scour hole deepening, with slight widening. The transition between (ii) and (iii) marks a statistically significant breakpoint in time, which can be narrowed down to the first four hours of local scour. The origin of this asymptotic evolution of the local scour hole in time is related to the primary horseshoe vortex, which sinks into the developing local scour hole during stages (i) and (ii) and expands in size for stage (iii), reducing its erosive capacity and thus mitigating the local scour process.

Experimental observations support the importance of the temporal evolution phases on the asymptotic bedload transport rate out of the local scour hole. Local scour undermines freely moving obstacles placed on the sediment bed and induces their movement. This is a typical boundary condition for the formation of obstacle marks at natural boulder-like obstacles. The movement is characterised by (a) upstream tilting of the obstacle relative to its original position against the flow direction and (b) self-burial of the obstacle, i.e. a reduction of the obstacle height relative to the obstacle height prior to local scouring processes. Both processes show a stepwise and asymptotic behaviour in time, with rapid activity for the initial stages of local scouring, corresponding to the determined temporal phase of (i). Processes (a) and (b) alter the exposure of the obstacle to the flow by tilting the front of the obstacle towards the upstream direction (~20°) and by reducing the height of the obstacle projecting into the flow. Both processes significantly slowed down local scour hole incision in time and reduced the normalised (i.e. relative to the size of the obstacle) local scour hole depth by an average of 15-20% compared to local scour at a fixed obstacle of the same size and subject to the same hydraulic boundary conditions. A quantitative model is formulated to assess the temporal increase in local scour length and width based on scour depth, frontal scour slope slope and scour hole bottom span independent of scale, which can be applied to estimate the spatial extent of local scour protection countermeasures.

During flood events with unsteady flow conditions, where flow depths and velocities vary with time and can be characterised as a flood hydrograph, up to 80% of the local scour hole size was observed at the end of the experimental runs in only 10% of the experimental time. The above temporal evolution phases (i)¬(iii) were also valid for local scouring under unsteady flow conditions. Significant local scouring was attributed to the rising limb of the hydrographs when the flow depth was comparable to the size of the obstacle. At the obstacle there was an intense downflow which, together with a strong horseshoe vortex system at the base of the obstacle, facilitated scouring processes. With increasing submergence, as the hydrograph progressed, localised scouring attenuated the downflow, while the horseshoe vortex also weakened. It is therefore suggested that the peak flow of a flood may have little effect on the size of the local scour hole as a function of flow depth when the obstacle is fully submerged, in contrast to bridge pier scour. The slope of a hydrograph is an important factor in determining the shape and size of local scour holes. A steeper rising limb will result in faster maturation of the depth, length and width of the local scour hole.

Q4: *Can the geometry of fluvial obstacle marks be used as hydraulic indicators to improve procedures for estimating the magnitude of past flood events*?

Field evidence from the Rambla de la Viuda shows that obstacle marks on large boulders are distinct from other sedimentary structures and have preservation potential in ephemeral gravel-bed streams affected by flash floods. Although the obstacle marks in the field were not as well defined as those generated in the laboratory flume, the spatial extent of the local scour hole in front of and alongside the boulders was clearly discernible. In contrast, the exact extent of the sediment ridge in the boulder track proved difficult to discern due to its assimilation with the downstream gravel bars and lobes. However, a knickpoint in the local scour hole slope, first identified in laboratory experiments, was validated by in-situ obstacle marks in the field. The kink in the local scour hole slope results from the erosive action of the primary horseshoe vortex (HV1) and is the main driver of sediment mobilisation at the base of the obstacle. Laboratory experiments have shown that the actual diameter of the primary horseshoe vortex can be estimated from the position of the kink point relative to the face of the obstacle. From this it is possible to estimate the longitudinal (along the mean flow direction) and vertical (perpendicular to the mean flow direction towards the sediment bed) axes of the eddy, which correspond to the major and minor axes of the elliptical primary horseshoe eddy. Although the primary horseshoe vortex sinks into the local scour hole during the local scour process, where it slightly increases its diameter, a correlation between the horseshoe vortex diameter and flow depth, obstacle size as well as local scour hole depth was found. The analysis was performed on the near steady state geometry of the local scour holes from the present experimental series as well as external data sets. A multiple linear regression showed that the vortex diameter tended to decrease with increasing flow depth and increased with increasing obstacle size and local scour hole depth. For the purpose of the application, the data sets were re-evaluated with flow depth as the dependent variable. The derived empirical relationship applies to situations where a fully established HV system is present, as evidenced by the local scour hole geometry. This is usually achieved within the first four to five hours of local scour, regardless of steady or unsteady flow conditions. In addition to laboratory data, field data from in-situ obstacle marks on boulders in the Colorado River have been integrated. The derived empirical relationship is suitable for solving the most likely flow depth during local scour hole formation and the kink in the local scour hole slope.

Based on experimental observations, it is further argued that the estimated flow depth corresponds to conditions during the rising limb of the hydrograph when significant local scour hole enlargement occurs. To the authors' knowledge, this is the first time that the geometric characteristics of preserved local scour holes on boulders have been used as a quantitative indicator of flow depth during their formation. The approach for estimating the minimum flow velocity during local scour hole formation from preserved local scour holes (Herget *et al*., 2013) could be improved based on the newly obtained estimate of the most likely flow depth during local scour hole formation. Previously, the approach relied on water level indicators from external sources (i.e. debris deposits) rather than the geometry of the obstacle mark itself. However, these deposits are related to the peak discharge. As the unsteady flow experiments show, much of the obstacle mark geometry is formed during the rising part of the flood hydrograph. If the obstacle was deeply submerged during the peak flow, the peak flow may not even have a significant effect on the geometry of the obstacle mark. The mean flow depth during the formation of ten local scour holes in the Rambla de la Viuda, which indicate a sufficient time scale of local scour based on their depth and width/length ratios, could be estimated. The estimated mean flow depth during the formation of local scour holes on boulders in the Rambla de la Viuda was 1 m, which is less than the flow depths estimated from debris deposits of recent floods (1.9 to 2.2 m), which belong to the peak discharge. The minimum flow velocity during the rising part of the hydrograph could be further assessed from the estimated flow depths. The minimum flow velocity during formation ranged from 0.7 to 1.4 m/s, corresponding to an average discharge of 77 m^3/s. The plausibility of the estimated velocities and discharges from the local scour hole geometry could be validated by recent floods measured in Rambla de la Viuda. However, during multiple flash flood events in a given reach, local scour holes may be altered by sediment infill from subsequent floods. As a result, it is difficult to associate a specific flood event with a specific local scour hole due to the unknown flood history and exposure time of the boulder in the stream bed. It is therefore essential to link the geometric characteristics of local scour holes to specific flood events, in addition to making progress in the hydraulic interpretation of these holes. This would require a detailed monitoring programme. Limitations and other outstanding issues relating to the research questions are briefly discussed in the following chapter.

10.2 OPEN QUESTIONS IN RELATION TO THE RESEARCH QUESTIONS

Like many PhD projects, this one was limited by time and budget. As a result, some of the open questions that arose during the project could not be definitively answered. However, these open questions could serve as a starting point for future research projects. The following questions are included:

The boundary condition framework may not include certain boundary conditions. (**Q1**)

The proposed framework describes a spectrum of extrinsic and intrinsic boundary conditions that control the hydraulic and sedimentary processes of obstacle mark formation at natural obstacles such as boulders or vegetation elements. In its current form, the framework should resemble the most dominant environmental boundary conditions for obstacle mark formation at natural obstacles. However, as a PhD project has time and resource limitations, it is important to note that the present framework can be extended to include additional boundary conditions and dimensionless control parameters that may not be included in the present form. Additional boundary conditions of interest for particular experimental studies can be easily added and classified according to their hierarchical order, which is a significant advantage.

One boundary condition that is already included in the present framework, but has not been systematically investigated, is the flexibility of plant parts such as twigs and branches when exposed to a flow. This is of particular interest from a biogeomorphological perspective. In particular, submerged aquatic vegetation is highly flexible when exposed to a current, passively following the flow downstream to prevent uprooting (Calvani & Solari, 2019). This behaviour could completely prevent local scouring, while it could initiate net deposition in the wake of the vegetation element if fine sediment is transported in suspension. Unfortunately, quantifying the bending stiffness of vegetation is challenging and could not be performed within the scope of the Ph.D. project. However, this finding suggests a possible direction for further research, including additional laboratory and field studies.

Are the identified thresholds applicable at different spatial scales? (**Q2**)

The thresholds described indicate the conditions that must be met to initiate the formation of obstacle patches, or the conditions under which the dimensions of obstacle patches are maximised. The thresholds for the primary and secondary control parameters are formulated in terms of dimensionless quantities which, at least in theory, prevent the property of being scale invariant. Thus, they should accurately describe the underlying processes of obstacle mark formation from small scale laboratory environments to natural field scale counterparts. However, the problem of inadvertently introducing laboratory-scale effects is inherent in small-scale parameter studies due to the scaling down of flow and sediment properties. In the worst case, this can lead to spurious correlations in the interpretation of experimental data. As the sediment properties in this paper were constant and no finer than the sand fraction, any laboratory scale effects that may have been introduced were likely due to the reduction in flow depth for the submergence ratio experimental series and the effects of unsteady flow. However, it has been argued that the effects of submergence ratio and flow intensity on the dimensions of the obstacle mark cannot be attributed to laboratory scale effects and spurious correlation. The threshold condition for maximising obstacle mark dimensions for a boulder-like obstacle with flow depth occurs when the approaching flow depth is comparable to the size of the obstacle. There is a plausible physical explanation for this phenomenon. As the flow depth approaches the size of the obstacle, a strong pressure gradient is created, leading to the formation of a highly erosive horseshoe vortex system at the base of the obstacle. This system causes extensive local scouring. This ensures reproducibility even in installations where the flow depth exceeds the centimetre to decimetre range and extends into the metre range. It is therefore essential to validate the observed and described threshold conditions for primary and secondary control parameters at different spatial scales, including larger laboratory flumes and controlled field experiments.

Based on the laboratory results, could a steady state of fluvial obstacle mark formation be observed over time? (**Q3**)

Obstruction formation is a time-dependent process that asymptotically approaches a maximum value of geometric length scales. Beyond this point, no further enlargement is observed and this condition is considered to be the steady state or equilibrium condition of obstacle mark formation. The steady state is therefore defined as the "gold standard" for physical experiments in laboratory flumes. However, the experimental time to reach steady state is often arbitrarily chosen, ranging from 24 to 72 hours. Traditionally, the engineering community introduced the motivation to observe a steady state condition of local scour for laboratory experiments to quantify the maximum local scour hole depth likely to occur during the operating hours of a bridge pier or other engineering infrastructure. However, the definition of a steady state is purely academic as various environmental boundary conditions and interdependent processes at the field scale can disrupt this timescale. The experimental studies show that when an obstacle mark forms on a solid boulder obstacle, it tilts and self-buries due to local scouring in front of the obstacle. This attenuates the forming processes and induces a near steady state already in the initial phase of obstacle mark formation. The experimental series also showed that the majority of obstacle mark formation occurs within the first few hours of the phenomenon, irrespective of steady or unsteady flow conditions in the laboratory flumes. It is argued that considering the temporal evolution phases defined in this paper based on the geometry of the local scour hole is more meaningful than searching for an equilibrium condition under given hydraulic and sedimentary boundary conditions, which may never be reached under natural field conditions. A problem with determining a steady state of obstacle mark formation through laboratory studies is the asymptotic evolution with time. This is particularly problematic for experiments lasting longer than five days, as it can lead to measurement uncertainty due to technical limitations and detection limits of the measurement equipment. Thus, if the run time exceeds 48 hours, a detected marginal change in the geometric length scales may be due to a true magnification or to measurement uncertainty, i.e. measurement error. In order to minimise the uncertainty, several experiments were repeated for each series of experiments. The replicate runs were performed using the same measurement system. Therefore, it was still crucial to determine an equilibrium condition of the obstacle mark formation for long term experimental runs under steady flow conditions, as a slight widening of the local scour hole could be observed even after five days of experimental

run. Determining the steady-state condition was even more challenging for the widening of the sediment ridge in the wake, as its expansion did not stop at steady flow. Although much of this dynamics was decoupled from the formation processes of the HV system, as the subaqueous sediment ridge itself perturbs the flow, movement is triggered by flow acceleration at its crest, inducing sediment movement. Therefore, the determination of a steady state based on experimental runs in both steady and unsteady flow conditions can be ambiguous. It is argued that the first few hours of the phenomenon are particularly relevant for the hydraulic interpretation of obstacle marks, and that feasible temporal evolution phases could be determined based on this time span.

Does the procedure of using fluvial obstacle marks as hydraulic indicators yield meaningful results? (**Q4**)

In addition to their importance for basic research, the systematic channel studies were also designed to evaluate whether the geometry of obstacle marks on boulders at the field scale can be used as a hydraulic indicator to assess hydraulic boundary conditions, in particular flow depth during formation. Experimental results show that the diameter of the horseshoe vortex system at a boulder-like obstacle depends on flow depth, obstacle size and local scour hole depth. The horizontal and vertical extent of the primary horseshoe vortex can therefore be estimated from a bend in the local scour hole slope, which was found to be preserved at the field scale. For a given obstacle size, the mean diameter of the horseshoe vortex and the local scour hole depth will be greatest at a flow depth whose vertical extent approximates the size of the boulder. An empirical model has been formulated to estimate the most likely flow depth during formation. When applied to the kink points in the local scour hole slopes observed in the Rambla de la Viuda field evidence, the estimated mean flow depth during formation of the local scour holes on the boulders was 1 metre, whereas jetseam deposits from recent floods indicate a mean flow depth during peak flow that is more than double (1.9 to 2.2 metres). The reconstruction results therefore raise the question of the triviality of the proposed method: One would expect a mean flow depth of 1 metre to occur during a typical flood in an ephemeral stream, even if the jetseam deposits indicate a flow depth more than double that. However, the lack of “spectacular” results in terms of flow depth does not necessarily mean that the results are trivial, as most of the local scour dynamics due to the primary horseshoe eddy are associated with the rising limb of the

flood hydrograph at a flow depth comparable to the size of the boulder obstacle. It is therefore hypothesised that preserved local scour holes on boulder-like obstacles, which are predominantly found on ephemeral streams, are reasonable hydraulic indicators of the initial stages, i.e. the rising limb of a flood hydrograph, whereas their indicative function for the flow depth during peak flow is limited, as they may become completely submerged, which has been shown to have no influence on the local scouring dynamics. In addition, the presence of a well preserved obstacle mark, i.e. a local scour hole, also gives an impression of the shape of a flood hydrograph and the conditions for sediment transport. As already pointed out by Herget (2005), the complete disappearance of the obstacle mark is possible if the discharge on the falling limb decreases rapidly, resulting in the refilling of the local scour hole by sediment transported as bedload. Substantial sediment deposition at this stage would result in the complete burial of the obstacle, eliminating any evidence of its presence. Therefore, in order to preserve obstruction marks on ephemeral streams, it is necessary that the falling limb does not drop too steeply to avoid this.

Consequently, analogous conclusions can be drawn regarding the local scour in Chagan Uzun (Fig. 7). The preliminary results obtained from the application of equations 47 and 48 and the potential maximum local scour hole depth of 35 metres (Herget *et al*., 2013) indicate that the minimum water depth, which is a critical factor influencing the observed local scour structure, must have been approximately 70 to 75 meters. A comparison with the dimensions of the obstacle indicates that the bedrock hill was only partially submerged. However, the circumstances that gave rise to the scour in Chagan Uzun were somewhat distinct from those that led to the deposition of the boulders under investigation. The bedrock hill was situated at the base of a glacial lake, which began to drain following the rupture of a natural glacial dam. Consequently, the rising limb of the flood hydrograph appears to have been less influential than the falling limb, which ensured that the water level of the lake had declined sufficiently to induce scouring processes at the obstacle. Concurrently, and at comparable (or even reduced water depths), the fluvial dunes (Carling, 1996) in the proximate vicinity of the local scour hole likely also developed, which resulted in sediment input into the local scour hole and a reduction in the local scour depth. It should be noted in this context that these are preliminary results that fall outside the central questions addressed in this dissertation.

REFERENCES

Alexander J., Cooker M.J. (2016) Moving boulders in flash floods and estimating flow conditions using boulders in ancient deposits. *Sedimentology* 63(6), 1582–1595.

Allen, J.R.L. (1965) Scour Marks in snow. SEPM Journal of Sedimentary Research, Vol. 35, 331–338.

Allen, J.R.L. (1984) *Sedimentary structures: Their character and physical basis*. Elsevier: Amsterdam, The Netherlands.

Al-Zawaidah, H., Ravazzolo, D., & Friedrich, H. (2021) Local geomorphic effects in the presence of accumulations of different densities. *Geomorphology* 389, 107838.

Baker, C.J. (1985) The position of points of maximum and minimum shear stress upstream of cylinders mounted normal to flat plates. *Journal of Wind Engineering and Industrial Aerodynamics* 18(3), 263–274.

Baker, V.R. (2009) Channeled Scabland morphology. In: Burr, D.M., Carling, P.A. & Baker, V.R. (eds.) *Megaflooding on Earth and Mars*. Cambridge University Press: Cambridge, UK, 65–77.

Baker, V.R. & Bunker, R.C. (1985) Cataclysmic Late pleistocene flooding from glacial Lake Missoula: A review. *Quaternary Science Reviews* 4(1), 1–41.

Baker V.R. (1978) Large-scale erosional and depositional features of the Channeld Scabland. In: Baker VR, Nummedal D (eds.) *The Channeld Scabland: A Guide to the Geomorphology of the Columbia Basin.* National Aeronautics and Space Administration: Washington, D.C., 81–115.

Barenblatt, G.I. (2012) *Scaling*. Cambridge University Press: Cambridge, UK.

Bateman, A., Fernández, M. & Parker, G. (2006) Morphodynamic model to predict temporal evolution of local scour in bridge piers. In: Parker, G. & García, M.H. (eds.) *River, Coastal and Estuarine Morphodynamics: RCEM 2005. Proceedings of the 4th IAHR Symposium on River, Coastal and Estuarine Morphodynamics*, 4–7 October 2005, Urbana, IL, USA. London: Taylor & Francis, 911–920.

Bauri, K.P. & Sarkar, A. (2016) Flow and scour around vertical submerged structures. *Sādhanā* 41(9), 1039–1053.

Baynes, E.R.C., van de Lageweg, W.I., McLelland, S.J., Parsons, D.R., Aberle, J. & Dijkstra, J. *et al*. (2018) Beyond equilibrium: Re-evaluating physical modelling of fluvial systems to represent climate changes. *Earth-Science Reviews* 181, 82–97.

Beebee, R.A. (2022) Recent history of glacial lake outburst floods, analysis of channel changes, and development of a two-dimensional flow and sediment transport model of the Snow River near Seward, Alaska. U.S. Geological Survey Scientific Investigations Report 2022–5099.

Bekkers, C. C. A., Angelou, N., & Dellwik, E. (2022) Drag coefficient and frontal area of a solitary mature tree. *Journal of Wind Engineering and Industrial Aerodynamics*, 220, 104854.

Belmonte, A.M.C., Segura Beltrán, F. (2001) Flood events in Mediterranean ephemeral streams (ramblas) in Valencia region, Spain. *CATENA* 45, 229–249.

Benito, G., Sanchez-Moya, Y., Medialdea, A., Barriendos, M., Calle, M. & Rico, M. *et al*. (2020) Extreme Floods in Small Mediterranean Catchments: Long-Term Response to Climate Variability and Change. *Water* 12(4), 1008.

Bennett, S.J., Ashmore, P. & Neuman, C.M. (2015) Transformative geomorphic research using laboratory experimentation. *Geomorphology* 244, 1–8.

Biron P.M., Robson C., Lapointe M.F., Gaskin S.J. (2004) Comparing different methods of bed shear stress estimates in simple and complex flow fields. *Earth Surface Processes and Landforms* 29(11), 1403–1415.

Bishop, M.A. (2011) Aeolian scours as putative signatures of wind erosion and sediment transport direction on Mars. *Geomorphology* 125(4), 569–574.

Borg, D., Rutherfurd, I., Stewardson, M. (2007) The geomorphic and ecological effectiveness of habitat rehabilitation works: Continuous measurement of scour and fill around large logs in sand-bed streams. *Geomorphology* 89, 205–216.

Bombar, G. (2020) Scour evolution around bridge piers under hydrographs with high unsteadiness. *Iranian Journal of Science and Technology, Transactions of Civil Engineering* 44, 325–337.

Bouratsis, P., Diplas, P., Dancey, C.L. & Apsilidis, N. (2017) Quantitative spatio-temporal characterization of scour at the base of a cylinder. *Water* 9(3), 227.

Bouratsis, P., Diplas, P., Dancey, C.L. & Apsilidis, N. (2013) High-resolution 3-D monitoring of evolving sediment beds. *Water Resources Research* 49(2), 977–992.

Box, W., Västilä, K., & Järvelä, J. (2019) The interplay between flow field, suspended sediment Concentration, and net deposition in a channel with flexible bank vegetation. *Water* 11(11), 2250.

Boyer, C. & Roy, A.G. (1991) Morphologie du lit autour d'un obstacle soumis à un écoulement en couche mince. *Géographie physique et Quaternaire* 45(1), 91–99 (in French).

Bradley, R.W. & Venditti, J.G. (2017) Reevaluating dune scaling relations. *Earth-Science Reviews* 165, 356–376.

Branco, P., Boavida, I., Santos, J.M., Pinheiro, A. & Ferreira, M.T. (2013) Boulders as building blocks: improving habitat and river connectivity for stream fish. *Ecohydrology* 6(4), 627–634.

Brandimarte, L., Montanari, A., Briaud, J.-L. & D'Odorico, P. (2006) Stochastic flow analysis for predicting river scour of cohesive soils. *Journal of Hydraulic Engineering* 132(5), 493–500.

Bressan, L., Guerrero, M., Antonini, A., Petruzzelli, V., Archetti R., Lamberti A. *et al*. (2018) A laboratory experiment on the incipient motion of boulders by high-energy coastal flows. *Earth Surface Processes and Landforms* 43(14): 2935–2947.

Breusers, H.N.C. & Raudkivi, A.J. (1991) *Scouring*. Balkema: Rotterdam, The Netherlands.

Briaud, J.-L., Ting, F.C.K., Chen, H.C., Gudavalli, R., Perugu, S. & Wei, G. (1999) SRICOS: Prediction of scour rate in cohesive soils at bridge piers. *Journal of Geotechnical and Geoenvironmental Engineering* 125(4), 237–246.

Buffington, J.M., Lisle, T.E., Woodsmith, R.D. & Hilton, S. (2002) Controls on the size and occurrence of pools in coarse-grained forest rivers. *River Research and Applications* 18(6), 507–531.

Burkow, M. & Griebel, M. (2016) A full three dimensional numerical simulation of the sediment transport and the scouring at a rectangular obstacle. *Computers & Fluids* 125, 1–10.

Buscombe, D., Grams, P.E. & Kaplinski, M.A. (2014a) Characterizing river-bed sediment using high-frequency acoustics: 1. Spectral properties of scattering. *Journal of Geophysical Research- Earth Surface* 119(12), 2674–2691.

Buscombe, D., Grams, P.E. & Kaplinski, M.A. (2014b) Characterizing river-bed sediment using high-frequency acoustics: 2. Scattering signatures of Colorado River bed sediment in marble and grand canyons. *Journal of Geophysical Research - Earth Surface* 119(12), 2692–2710.

Buscombe, D., Grams, P.E. & Kaplinski, M.A. (2017) Compositional signatures in acoustic backscatter over vegetated and unvegetated mixed sand–gravel riverbeds. *Journal of Geophysical Research -Earth Surface* 122(10), 1771–1793.

Butch, G.K. (1991) Measurement of bridge scour at selected sites in New York, excluding Long Island: Water Resources Investigations Report 91-4083. Albany, NY: USGS/New York State Department of Transportation.

Butch, G.K. (1999) Scour-hole dimensions at selected bridge piers inNew York. In: Richardson, E.V. & Lagasse, P.F. (eds.) *Stream Stability and Scour at Highway Bridges*. Reston, VA: ASCE, 557–566.

Calle, M., Calle, J., Alho, P. & Benito, G. (2020) Inferring sediment transfers and functional connectivity of rivers from repeat topographic surveys. *Earth Surface Processes and Landforms* 45(3), 681–693.

Calle, M., Lotsari, E., Kukko, A., Alho, P., Kaartinen, H. & Rodriguez-Lloveras, X. *et al*. (2015) Morphodynamics of an ephemeral gravel-bed stream combining Mobile Laser

Scanner, hydraulic simulations and geomorphological indicators. *Zeitschrift für Geomorphologie, Supplementary Issues* 59(3), 33–57.
Calle, M., Alho, P., Benito, G. (2017) Channel dynamics and geomorphic resilience in an ephemeral Mediterranean river affected by gravel mining. *Geomorphology* 285, 333–346.
Camarasa Belmonte, A.M. & Segura Beltrán, F. (2001) Flood events in Mediterranean ephemeral streams (ramblas) in Valencia region, Spain. *CATENA* 45(3), 229–249.
Camporeale, C., Perucca, E., Ridolfi, L., & Gurnell, A. M. (2013) Modeling the interactions between river morphodynamic and riparian vegetation. *Reviews of Geophysics* 51(3), 379e414.
Carling, P.A. & Leclair, S.F. (2019) Alluvial stratification styles in a large, flash-flood influenced dryland river: The Luni River, Thar Desert, north-west India. *Sedimentology* 66(1), 102–128.
Carling P.A., Hoffmann M., Blatter A.S. (2002a) Initial motion of bouldersin bedrock channels. In: House P.K. (ed.) *Ancient Floods, Modern Hazards: Principles and Applications of Paleoflood* Hydrology, American Geophysical Union: Washington, D.C., 147–160.
Carling, P.A., Kirkbride, A.D., Parnachov, S., Borodavko, P.S. & Berger, G.W. (2002b) Late Quaternary catastrophic flooding in the Altai Mountains of south–central Siberia: A synoptic overview and an Introduction to flood deposit sedimentology. In: Garzón, G., Martini, I.P. & Baker, V.R. (eds.) *Flood and megaflood processes and deposits: Recent and ancient examples*. Blackwell Science: Oxford, Malden, MA, 17–35.
Carling, P.A. (1996) Morphology, sedimentology and palaeohydraulic significance of large gravel dunes, Altai Mountains, Siberia. *Sedimentology* 43(4), 647–664.
Carling, P.A. & Reader, N.A. (1982) Structure, composition and bulk properties of upland stream gravels. *Earth Surface Processes and Landforms* 7(4), 349–365.
Caroppi, G., Västilä, K., Järvelä, J., Lee, C., Ji, U., Kim, H. S., & Kim, S. (2022) Flow and wake characteristics associated with riparian vegetation patches: Results from field-scale experiments. *Hydrological Processes* 36(2), e/4506.
Chang, W.-Y., Lai, J.-S. & Yen, C.-L. (2004) Evolution of Scour Depth at Circular Bridge Piers. *Journal of Hydraulic Engineering* 130(9), 905–913.
Chanson H., Trevethan M., Shin-ichi, A. (2008) Acoustic Doppler velocimetry (ADV) in small estuary: field experience and signal post-processing. *Flow Measurement and Instrumentation* 19(5), 307–313.
Chen, Q., Qi, M., Zhong, Q. & Li, D. (2017) Experimental study on the multimodal dynamics of the turbulent horseshoe vortex system around a circular cylinder. *Physics of Fluids* 29(1), 15106.
Chen, Q., Yang, Z. & Wu, H. (2019) Evolution of Turbulent Horseshoe Vortex System in Front of a Vertical Circular Cylinder in Open Channel. *Water*, 11(10), 2079.
Chen S.C., Chan H.C., Li Y.H. (2012) Observations on flow and local scour around submerged flexible vegetation. *Advances in Water Resources* 43, 28–37.
Chen, Z., Ortiz, A., Zong, L. & Nepf, H. (2012) The wake structure behind a porous obstruction and its implications for deposition near a finite patch of emergent vegetation. *Water Resources Research* 48(9), W09517.
Chiew Y.M. (1995) Mechanics of riprap failure at bridge piers. *Journal of Hydraulic Engineering* 121(9), 635–643.
Chiew, Y.M. (1990) Mechanics of Local Scour Around Submarine Pipelines. *Journal of Hydraulic Engineering* 116(4), 515–529.
Chojnacki, M., Banks, M.E., Fenton, L.K. & Urso, A.C. (2019) Boundary condition controls on the high-sand-flux regions of Mars. *Geology* 47(5), 427–430.
Chou J.H., Chao S.Y. (2000) Branching of a horseshoe vortex around surface-mounted rectangular cylinders. *Experiments in Fluids* 28(5), 394–402.
Chow, V.T. (1988) *Open-channel hydraulics*. McGraw-Hill: Boston, Mass.
Chreties C., Simarro G., Teixeira L. (2008) New experimental method to find equilibrium scour at bridge piers. *Journal of Hydraulic Engineering* 134(10), 1491–1495.

Chreties, C., Teixeira, L. & Simarro, G. (2013) Influence of flow conditions on scour hole shape for pier groups. *Proceedings of the Institution of Civil Engineers*: *Water Management* 166(3), 111–119.

Church M, Haschenburger JK. 2017. What is the "active layer"? *Water Resources Research* 53(1): 5–10.

Cin, R.D. (1968) "Pebble clusters": Their origin and utilization in the study of palaeocurrents. *Sedimentary Geology* 2(4), 233–241.

Coco, G. & Murray, A.B. (2007) Patterns in the sand: From forcing templates to self-organization. *Geomorphology* 91(3-4), 271–290.

Comiti, F., Andreoli, A. & Lenzi, M.A. (2005) Morphological effects of local scouring in step–pool streams. *Earth Surface Processes and Landforms* 30(12), 1567–1581.

Collischonn, W., Fleischmann, A., Paiva, R.C.D., Mejia, A. (2017) Hydraulic Causes for Basin Hydrograph Skewness. *Water Resources Research* 53, 10603–10618.

Cordier, F., Tassi, P., Claude, N., Crosato, A., Rodrigues, S., & van Bang, D. P. (2018) Influence of hydrology, sediment supply and sediment gradation on river bar morphodynamics: Application to the Loire River at Bréhémont (France). *E3S Web of Conferences* 40, 02023

Corenblit, D., Steiger, J., González, E., Gurnell, A. M., Charrier, G., *et al*. (2014) The biogeomorphological life cycle of poplars during the fluvial biogeomorphological succession: A special focus on Populus nigra L. *Earth Surface Processes and Landforms* 39(4), 546–563.

Corenblit, D., Steiger, J., Charrier, G., Darrozes, J., Garófano-Gómez, V. & Garreau, A. *et al*. (2016) Populus nigra L. establishment and fluvial landform construction: biogeomorphic dynamics within a channelized river. *Earth Surface Processes and Landforms* 41(9), 1276–1292.

Curran, J. C., & Hession, W. C. (2013) Vegetative impacts on hydraulics and sediment processes across the fluvial system. *Journal of Hydrology* 505, 364–376.

da Silva, B.L., Sumner, D., Bergstrom, D.J. (2022) Mean and dynamic aspects of the wakes of a surface-mounted cube and block. *Journal Fluids Engineering* 144, 011302.

da Silva, B.L., Hahn, D.G.H., Sumner, D., Bergstrom, D.J. (2022) Mean wake and aerodynamic forces for surface-mounted finite-height square prisms of very small aspect ratio. *Physics of Fluids* 34, 115118.

Dargahi, B. (1989) The turbulent flow field around a circular cylinder. *Experiments in Fluids* 8, 1–12.

Dargahi, B. (1990) Controlling Mechanism of Local Scouring. *Journal of Hydraulic Engineering* 116 (10), 1197–1214.

Davison, A.C. & Hinkley, D.V. (2009) *Bootstrap Methods and their Application*. Cambridge University Press: Cambridge, UK.

Debnath, K. & Chaudhuri, S. (2010) Laboratory experiments on local scour around cylinder for clay and clay–sand mixed beds. Engineering Geology 111(1-4), 51–61.

Detert, M. & Weitbrecht, V. (2012) Automatic object detection to analyze the geometry of gravel grains – a free stand-alone tool. In: Murillo Munoz, R. (Ed.) *River flow 2012: Proceedings of the international conference on fluvial hydraulics, San José, Costa Rica, 5-7 September 2012.* CRC Press: Boca Raton, 595–600.

Detert, M. & Weitbrecht, V. (2020) Determining image–based grain size distribution with suboptimal conditioned photos. In: Uijttewaal, W.S.J. (Ed.) *River flow 2020: Proceedings of the 10th conference on fluvial hydraulics, Delft, The Netherlands, 7-10 July 2020.* CRC Press/Balkema: Leiden, The Netherlands, 1045–1052.

Dey, S. (1996) Sediment pick-up for evolving scour near circular cylinders. *Applied Mathematical Modelling* 20(7), 534–539.

Dey, S. (1999) Time-variation of scour in the vicinity of circular piers. *Proceedings of the Institution of Civil Engineers - Water, Maritime and Energy* 136(2), 67–75.

Dey, S. (2014) *Fluvial Hydrodynamics: Hydrodynamic and Sediment Transport Phenomena*. Springer: Berlin, Germany.

Dey, S., Bose, S.K. & Sastry, G.L.N. (1995) Clear Water Scour at Circular Piers: a Model. *Journal of Hydraulic Engineering* 121(12), 869–876.
Dey, S. & Raikar, R.V. (2007a) Characteristics of horseshoe vortex in developing scour holes at piers. *Journal of Hydraulic Engineering* 133(4), 399–413.
Dey, S. & Raikar, R.V. (2007b) Clear-water scour at piers in sand beds with an armor layer of gravels. *Journal of Hydraulic Engineering* 133(6), 703–711.
Dey, S., Raikar, R.V. & Roy, A. (2008) Scour at Submerged Cylindrical Obstacles under Steady Flow. *Journal of Hydraulic Engineering* 134(1), 105–109.
Dey, S., Sarkar, S., Bose, S.K., Tait, S. & Castro-Orgaz, O. (2011) Wall-wake flows downstream of a sphere placed on a plane rough wall. *Journal of Hydraulic Engineering* 137(10), 1173–1189.
Diab, R., Link, O. & Zanke, U. (2010) Geometry of developing and equilibrium scour holes at bridge piers in gravel. *Canadian Journal of Civil Engineering* 37(4), 544–552.
Douglas J.F., Gasiorek J.M., Swaffield J.A. 2001. Fluid Mechanics. Prentice Hall: Harlow, UK.
Drumond, G.P., Pasqualino, I.P., Pinheiro, B.C. & Estefen, S.F. (2018) Pipelines, risers and umbilical failures: A literature review. *Ocean Engineering* 148, 412–425.
Du, S., Liang, B. (2019) Comparisons of local scouring for submerged square and circular cross-section piles in steady currents. *Water* 11, 1820.
Dżułyński, S. (1965) *Sedimentary features of flysch and greywackes*. Elsevier Pub. Co: Amsterdam, The Netherlands.
Ehsbach, O. W. (1975) *Handbook of engineering fundamentals*. John Wiley & Sons: New York, USA.
Eltner, A. & Sofia, G. (2020) Structure from motion photogrammetric technique. In: Tarolli, P., Mudd, S.M. (eds.) *Remote Sensing of Geomorphology*. Elsevier: Amsterdam, The Netherlands, 1–24.
Endreny, T., Lautz, L. & Siegel, D.I. (2011) Hyporheic flow path response to hydraulic jumps at river steps: Flume and hydrodynamic models. *Water Resources Research* 47(2), W02517.
Escauriaza, C. & Sotiropoulos, F. (2011a) Initial stages of erosion and bedform development in a turbulent flow around a cylindrical pier. *Journal of Geophysical Research* 116(F3), 671.
Escauriaza, C. & Sotiropoulos, F. (2011b) Reynolds number effects on the coherent dynamics of the turbulent horseshoe vortex system. *Flow, Turbulence and Combustion* 86(2), 231–262.
Ettema, R., Constantinescu, G. & Melville, B. (2011) *Evaluation of bridge scour research: Pier scour processes and predictions*. Transportation Research Board: Washington, D.C.
Ettema, R., Kirkil, G. & Muste, M. (2006) Similitude of large-scale turbulence in experiments on local scour at cylinders. *Journal of Hydraulic Engineering* 132(1), 33–40.
Ettema, R., Yoon, B., Nakato, T., Muste, M. (2004) A review of scour conditions and scour-estimation difficulties for bridge abutments. *KSCE Journal of Civil Engineering* 8(6), 643–650.
Ettema, R., Melville, B.W. & Barkdoll, B. (1998) Scale Effect in Pier-Scour Experiments. *Journal of Hydraulic Engineering* 124(6), 639–642.
Euler, T., Herget, J., Schlömer, O. & Benito, G. (2017) Hydromorphological processes at submerged solitary boulder obstacles in streams. *CATENA* 157, 250–267.
Euler, T., Zemke, J., Rodrigues, S. & Herget, J. (2014) Influence of inclination and permeability of solitary woody riparian plants on local hydraulic and sedimentary processes. *Hydrological Processes* 28(3), 1358–1371.
Euler, T. & Herget, J. (2012) Controls on local scour and deposition induced by obstacles in fluvial environments. *CATENA* 91, 35–46.
Euler, T. & Herget, J. (2011) Obstacle-Reynolds-number based analysis of local scour at submerged cylinders. *Journal of Hydraulic Research* 49(2), 267–271.
Ewing, R.C. & Kocurek, G. (2010) Aeolian dune-field pattern boundary conditions. *Geomorphology* 114(3), 175–187.

Ferguson, R. I., & Church, M. (2004) A simple universal equation for grain settling velocity. *SEPM Journal of Sedimentary Research* 74(6), 933–937.

Filhol, S. & Sturm, M. (2015) Snow bedforms: A review, new data, and a formation model. *Journal of Geophysical Research: Earth Surface* 120(9), 1645–1669.

Follett, E. M., & Nepf, H. M. (2012) Sediment patterns near a model patch of reedy emergent vegetation. *Geomorphology* 179, 141e151.

Firat M., Gungor M. (2009) Generalized regression neural networks and feed forward neural networks for prediction of scour depth around bridge piers. *Advances in Engineering Software* 40(8), 731–737.

Fisher, A.C. & Klingman, P.C. (1984) Local Scour at Fish Rocks. In: Schreiber, D.L. (ed.) *Water forResource Development: Proceedings of the conference of the American society of civil engineers*, Coeur d'Alene, ID, 14–17 August. ASCE: New York, 286–290.

Friedrich C.T., Rennie S.E., Brandt A. (2016) Self-burial of objects on sandy bed by scour: a synthesis of observations. In Harris J., Whitehouse R., Moxon S. (eds.) *Scour and erosion: Proceedings of the 8th international conference on scour and erosion*, Oxford, UK, 12–15 September, CRC Press: Boca Raton, FL., 179–189.

Frostick, L.E., McLelland, S.J. & T.G. Mercer (eds.) (2011) Users guide to physical modelling and experimentation: Experience of the HYDRALAB network. CRC Press/Balkema: Boca Raton, FL., Leiden, The Netherlands.

Froude, M.J., Alexander, J., Barclay, J. & Cole, P. (2017) Interpreting flash flood palaeoflow parameters from antidunes and gravel lenses: An example from Montserrat, West Indies. *Sedimentology* 64(7), 1817–1845.

Fu, H., Rockwell, D. (2005) Shallow flow past a cylinder: Transition phenomena at low Reynolds number. *Journal of Fluid Mechanics* 540(1), 75–97.

Garlan T, Marches E, Brenon E (2015) A classification of scouring marks in macrotidal environments from analysis of long-term wreck marks. In: Wang, P., Rosati, J.D. & Zheng, R. (eds.) *The proceedings of the coastal sediments 2015*, 11 – 15 May 2015, San Diego, USA. World Scientific: Singapore, 14–27.

Gazi, A.H. & Afzal, M.S. (2020) A review on hydrodynamics of horseshoe vortex at a vertical cylinder mounted on a flat bed and its implication to scour at a cylinder. *Acta Geophysica* 68(3), 861–875.

Ghilardi, T., Franca, M.J. & Schleiss, A.J. (2014a) Bed load fluctuations in a steep channel. *Water Resources Research* 50(8), 6557–6576.

Ghilardi, T., Franca, M.J. & Schleiss, A.J. (2014b) Period and amplitude of bedload pulses in a macro-rough channel. *Geomorphology* 221, 95–103.

Golpira, A., Baki, A.B.M., Ghamry, H., Katopodis, C., Withers, J. & Minkoff, D. (2022) An experimental study: effects of boulder placement on hydraulic metrics of instream habitat complexity. *Scientific Reports* 12(1), 13156.

Golpira, A., Baki, A.B.M., Ghamry, H. & Katopodis, C. (2023) Influence of boulder submergence ratio on local flow field: Implications for sediment and fish instream habitat. *Ecological Engineering* 193, 106997.

Goring, D.G. & Nikora, V.I. (2002) Despiking Acoustic Doppler Velocimeter Data. J*ournal of Hydraulic Engineering* 128(1), 117–126.

Graf, W.H. & Istiarto, I. (2002) Flow pattern in the scour hole around a cylinder. *Journal of Hydraulic Research* 40(1), 13–20.

Grams, P.E., Buscombe, D., Topping, D.J., Kaplinski, M. & Hazel, J.E. (2019) How many measurements are required to construct an accurate sand budget in a large river? Insights from analyses of signal and noise. *Earth Surface Processes and Landforms* 44(1), 160–178.

Grams, P.E., Topping, D.J., Schmidt, J.C., Hazel, J.E. & Kaplinski, M. (2013) Linking morphodynamic response with sediment mass balance on the Colorado River in marble canyon: Issues of scale, geomorphic setting, and sampling design. *Journal of Geophysical Research - Earth Surface* 118(2), 361–381.

Grant PF, Nickling WG. 1998. Direct field measurement of wind drag on vegetation for application to windbreak design and modelling. *Land Degradation & Development* 9(1), 57–66.
Greenbaum, N., Schwartz, U., Carling, P., Bergman, N., Mushkin, A. & Zituni, R. *et al*. (2020) Frequency of boulders transport during large floods in hyperarid areas using paleoflood analysis – An example from the Negev Desert, Israel. *Earth-Science Reviews* 202, 103086.
Gregory, S. V., Swanson, F. J., McKee, W. A., & Cummins, K. W. (1991) An ecosystem perspective of riparian zones. *BioScience* 41(8), 540–551.
Gu, J., Shan, Y., Liu, C., & Liu, X. (2019) Feedback of flow and bed morphology from a submerged dense vegetation patch without upstream sediment supply. *Environmental Fluid Mechanics* 19, 475–493.
Gurnell, A. (2014) Plants as river system engineers. *Earth Surface Processes and Landforms* 39(1), 4–25.
Gurnell, A. M., Petts, G. E., Hannah, D. M., Smith, B. P. G., Edwards, P. J. *et al*. (2001) Riparian vegetation and island formation along the gravel-bed Fiume Tagliamento, Italy. *Earth Surface Processes and Landforms* 26(1), 31–62.
Gurnell, A. M., Bertoldi, W., & Corenblit, D. (2012) Changing river channels: The roles of hydrological processes, plants and pioneer fluvial landforms in humid temperate, mixed load, gravel bed rivers. *Earth-Science Reviews* 111(1–2),129–141.
Gurnell, A. M., Bertoldi, W., Francis, R. A., Gurnell, J., & Mardhiah, U. (2019) Understanding processes of island development on an island braided river over timescales from days to decades. *Earth Surface Processes and Landforms* 44(2), 624–1640.
Gurnell, A. M., & Bertoldi, W. (2022) The impact of plants on fine sediment storage within the active channels of gravel-bed rivers: A preliminary assessment. *Hydrological Processes* 36(7), e14637.
Guan, D., Chiew, Y.M., Wei, M. & Hsieh, S.C. (2019) Characterization of horseshoe vortex in a developing scour hole at a cylindrical bridge pier. *International Journal of Sediment Research* 34(2), 118–124.
Guan, D., Xie, Y., Yao, Z.., Chiew, Y.M., Zhang, J. & Zheng, J. (2022) Local scour at offshore windfarm monopile foundations: A review. *Water Science and Engineering* 15(1), 29–39.
Gjunsburgs, B., Jaudzems, G., Govša, J. (2010) Hydrograph shape impact on the scour development with time at engineering structures in river flow. *Construction Science* 11, 6–12.
Hager, W.H. & Hutter, K. (1984) On pseudo-uniform flow in open channel hydraulics. *Acta Mechanica* 53(3–4), 183–200.
Hajimirzaie, S.M. (2023) Experimental observations on flow characteristics around a low-aspect-ratio wall-mounted circular and square cylinder. *Fluids* 8(1), 32.
Hajimirzaie, S.M., Wojcik, C.J. & Buchholz, J.H.J. (2012) The role of shape and relative submergence on the structure of wakes of low-aspect-ratio wall-mounted bodies. *Experiments in Fluids* 53(6), 1943–1962.
Hajimirzaie, S.M. & Buchholz, J.H.J. (2013) Flow dynamics in the wakes of low-aspect-ratio wall-mounted obstacles. *Experiments in Fluids* 54(11).
Hajimirzaie, S.M., Tsakiris, A.G., Buchholz, J.H.J. & Papanicolaou, A.N. (2014) Flow characteristics around a wall-mounted spherical obstacle in a thin boundary layer. *Experiments in Fluids* 55(6), 1762.
Hall, J.W., Boyce, S.A., Wang, Y., Dawson, R.J., Tarantola, S. & Saltelli, A. (2009) Sensitivity Analysis for Hydraulic Models. *Journal of Hydraulic Engineering* 135(11), 959–969.
Hargitai, H. (2014) Obstacle dunes and obstacle marks. In: Hargitai, H. & Kereszturi, A. (eds.) *Encyclopedia of Planetary Landforms*. Springer: Heidelberg, 1–5.
Hao, Y., Kopp, G. A., Wu, C.-H., & Gillmeier, S. (2020) A wind tunnel study of the aerodynamic characteristics of a scaled, aeroelastic, model tree. *Journal of Wind Engineering and Industrial Aerodynamics* 197, 104088.

Hassan, M.A. & Woodsmith, R.D. (2004) Bed load transport in an obstruction-formed pool in a forest, gravelbed stream. *Geomorphology* 58(1-4), 203–221.
Hazel, J.E., Topping, D.J., Schmidt, J.C. & Kaplinski, M. (2006) Influence of a dam on fine-sediment storage in a canyon river. *Journal of Geophysical Research* 111(F1), 919
Heller, V. (2011) Scale effects in physical hydraulic engineering models. *Journal of Hydraulic Research* 49(3), 293–306.
Henriques, M., McVicar, T. R., Holland, K. L., & Daly, E. (2022) Riparian vegetation and geomorphological interactions in anabranching rivers: A global review. *Ecohydrology* 15(2), e2370.
Herget, J. (2005) Reconstruction of Pleistocene ice-dammed lake outburst floods in the Altai Mountains, Siberia. Geological Society of America: Boulder, Colo.
Herget, J., Euler, T., Roggenkamp, T. & Zemke, J. (2013) Obstacle marks as palaeohydraulic indicators of Pleistocene megafloods. *Hydrology Research* 44(2), 300–317.
Herget, J., Roggenkamp, T. & Krell, M. (2014) Estimation of peak discharges of historical floods. *Hydrology and Earth System Sciences* 18(10), 4029–4037.
Herget, J., Schütte, F., Klosterhalfen, A. (2015) Empirical modelling of outburst flood hydrographs. Zeitschrift für Geomorphologie Supplementary issues 59(3), 177–198.
Hodge R.A., Hoey T.B., Sklar L.S. (2011) Bed load transport in bedrock rivers: the role of sediment cover in grain entrainment, translation, and deposition. *Journal of Geophysical Research* 116, F04028.
Hoffmans, G.J.C.M. & Verheij, H.J. (1997) *Scour Manual*. CRC Press: Rotterdam.
Hoffmans, G.J.C.M. (1993) A hydraulic and morphologic criterion for upstream slopes in local-scour hole: Report W-DWW-93.255, Rijkswaterstaat: Delft.
Høgaas, F. & Longva, O. (2016) Mega deposits and erosive features related to the glacial lake Nedre Glomsjø outburst flood, southeastern Norway. *Quaternary Science Reviews* 151, 273–291.
Hong J-H, Chiew Y-M, Yeh P-H, Chan H-C. 2017. Evolution of local pier-scour depth with dune migration in subcritical flow conditions. *Journal of Hydraulic Engineering* 143(4): 4016098.
Hortobágyi, B., Corenblit, D., Steiger, J., & Peiry, J.-L. (2018) Niche construction within riparian corridors. Part I: Exploring biogeomorphic feedback windows of three pioneer riparian species (Allier River, France). *Geomorphology* 305, 94–111.
Hu, K., Bai, X. & Vaz, M.A. (2023) Numerical Simulation on the Local Scour Processing and Influencing Factors of Submarine Pipeline. *Journal of Marine Science and Engineering* 11(1), 234.
Huai, W.-x., Li, S., Katul, G. G., Liu, M.-y., & Yang, Z.-h. (2021) Flow dynamics and sediment transport in vegetated rivers: A review. *Journal of Hydrodynamics* 33(3), 400–420.
Huber, M.L., Lupker, M., Gallen, S.F., Christl, M. & Gajurel, A.P. (2020) Timing of exotic, far-traveled boulder emplacement and paleo-outburst flooding in the central Himalayas. *Earth Surface Dynamics* 8(3), 769–787.
Hunt, J.C.R., Abell, C.J., Peterka, J.A. & Woo, H. (1978) Kinematical studies of the flows around free or surface-mounted obstacles; applying topology to flow visualization. *Journal of Fluid Mechanics* 86(1), 179–200.
Hupp, C. R., & Osterkamp, W. R. (1996) Riparian vegetation and fluvial geomorphic processes. *Geomorphology* 14(4), 277–295.
Inman, D.L. & Jenkins, S.A. (2019) Scour and Burial of Objects in Shallow Water. In: Finkl, C.W. & Makowski, C. (eds.) *Encyclopedia of Coastal Science*, 2nd edition. Springer: Cham, 1474–1480.
James, M.R., Chandler, J.H., Eltner, A., Fraser, C., Miller, P.E., *et al*. (2020) Guidelines on the use of structure-from-motion photogrammetry in geomorphic research. *Earth Surface Processes and Landforms* 44, 2081–2084.
Javernick, L., Brasington, J., Caruso, B. (2014) Modeling the topography of shallow braided rivers using Structure-from-Motion photogrammetry. *Geomorphology* 213, 166–182.

Jiménez-Romero, R., Fernández-Salas, L.M., Palomino, D., Sánchez-Leal, R.F. & Vila, Y. (2022) Discovering the Fine-Scale Morphology of the Gulf of Cádiz: An Underwater Imaging Analysis. *Journal of Marine Science and Engineering* 10(5), 651

Johnson, P.A. (1995) Comparison of pier-scour equations using field data. *Journal of Hydraulic Engineering* 121(8), 626–629.

Johnson, P.A., Clopper, P.E., Zevenbergen, L.W. & Lagasse, P.F. (2015) Quantifying uncertainty and reliability in bridge scour estimations. *Journal of Hydraulic Engineering* 141(7), 04015013

Jomaa, S., Barry, D.A., Heng, B.C.P., Brovelli, A., Sander, G.C. *et al*. (2012) Influence of rock fragment coverage on soil erosion and hydrological response: Laboratory flume experiments and modeling. *Water Resources Research* 48(5), W05535.

Judd H.E., Peterson D.F. (1969) Hydraulics of large bed element channels. Report PRWG 17-6. Utah Water Research Laboratory: Logan, UT.

Karcz, I. (1968) Fluviatile obstacle marks from the wadis of the Negev (southern Israel). *SEPM Journal of Sedimentary Research* 38(4), 1000–1012.

Karcz, I. (1972) Sedimentary structures formed by flash floods in southern Israel. *Sedimentary Geology* 7(3), 161–182.

Kaplinski, M., Hazel, J.E. Jr, Grams, P.E., Kohl, K., Buscombe, D.D. & Tusso, R.B. (2017a) Channel Mapping River Miles 29–62 of the Colorado River in Grand Canyon National Park, Arizona, May 2009: U.S. Geological Survey Open-File Report 2017–1030. USGS: Reston, VA.

Kaplinski, M., Hazel J.E. Jr, Grams, P.E., Kohl, K., Buscombe, D.D. & Tusso, R.B. (2017b) Channel Mapping of the Colorado River in Grand Canyon National Park, Arizona, May 2009, River Miles 29 to 62—Data: U.S. Geological Survey data release. USGS: Reston, VA.

Kenney, W. A. (1987) A method for estimating windbreak porosity using digitized photographic silhouettes. *Agricultural and Forest Meteorology* 39(2–3), 91–94.

Kim, H.S., Kimura, I. & Shimizu, Y. (2015) Bed morphological changes around a finite patch of vegetation. *Earth Surface Processes and Landforms* 40(3), 375–388.

Kim S.C, Friedrichs C.T., Maa J.P.Y, Wright L.D. (2000) Estimating bottom stress in tidal boundary layer from acoustic Doppler velocimeter data. *Journal of Hydraulic Engineering* 126(6), 399–406.

Kirkil, G. & Constantinescu, G. (2015) Effects of cylinder Reynolds number on the turbulent horseshoe vortex system and near wake of a surface-mounted circular cylinder. *Physics of Fluids* 27(7), 75102.

Kirkil, G. & Constantinescu, G. (2010) Flow and turbulence structure around an in-stream rectangular cylinder with scour hole. *Water Resources Research* 46(11), W11549.

Kirkil, G., Constantinescu, S.G. & Ettema, R. (2008) Coherent Structures in the Flow Field around a Circular Cylinder with Scour Hole. *Journal of Hydraulic Engineering* 134(5), 572–587.

Kitsikoudis, V., Yagci, O., Kirca, O., & Kellecioglu, D. (2016) Flow field alteration due to permeability and subcanopy flow for emergent vegetation. In J. Chung, M. Muskulus, T. Kokkinis, & A. Wang (eds.) *Proceedings twenty-sixth international ocean and polar engineering conference*, June 26-July 1, 2016, Rhodes, Greece: Volumes 1-4, International Society of Offshore and Polar Engineers (ISOPE): Cupertino, CA, 1421–1427.

Kocurek, G., Ewing, R.C. & Mohrig, D. (2010) How do bedform patterns arise? New views on the role of bedform interactions within a set of boundary conditions. *Earth Surface Processes and Landforms* 35(1), 51–63.

Koken, M. & Constantinescu, G. (2023) Influence of submergence ratio on flow and drag forces generated by a long rectangular array of rigid cylinders at the sidewall of an open channel. *Journal of Fluid Mechanics*, 966, A5.

Kothyari, U.C., Garde, R.C.J. & Ranga Raju, K.G. (1992) Temporal Variation of Scour Around Circular Bridge Piers. *Journal of Hydraulic Engineering* 118(8), 1091–1106.

Kramer C.M., Papanicolaou A.N. (2006) The effects of relative submergence on flow patterns around large particles in a gravel bed river. In: Graham R (ed.) *Examining the Confluence of Environmental and Water Concerns: Proceedings of the 2006 World Environmental and Water Resources Congress*, Omaha, NE, 21–25 May, American Society of Civil Engineers: Reston, VA, 1–10.

Lacey, R.W.J. & Rennie, C.D. (2012) Laboratory Investigation of Turbulent Flow Structure around a Bed-Mounted Cube at Multiple Flow Stages. *Journal of Hydraulic Engineering* 138(1), 71–84.

Lança RM, Simarro G, Fael SCM, Cardoso AH. 2016. Effect of viscosity on the equilibrium scour depth at single cylindrical piers. *Journal of Hydraulic Engineering* 142(3), 6015022.

Lane, S.N.; James, T.D.; Crowell, M.D. (2000) Application of Digital Photogrammetry to Complex Topography for Geomorphological Research. *Photogrammetric Record* 16, 793–821.

Laronne, J.B., Garcia, C. & Reid, I. (2001) Mobility of patch sediment in gravel bed streams: patch character and its implications for bedload. In: Mosley, M.P. (ed.) *Gravel-bed rivers*. New Zealand Hydrological Society: Wellington, 249–289.

Launay, G., Mignot, E., Riviere, N. & Perkins, R. (2017) An experimental investigation of the laminar horseshoe vortex around an emerging obstacle. *Journal of Fluid Mechanics* 830, 257–299.

Lawless, M. & Robert, A. (2001) Three-dimensional flow structure around small-scale bedforms in a simulated gravel-bed environment. *Earth Surface Processes and Landforms* 26(5), 507–522.

Leary, K.C.P. & Buscombe, D. (2020) Estimating sand bed load in rivers by tracking dunes: A comparison of methods based on bed elevation time series. *Earth Surface Dynamics* 8(1), 161–172.

Lee C., Kim D., Kim S., Ji U, Dongwoo K. (2018) Flow structure around an actual willow patch under different depth conditions. *E3S Web of Conferences* 40(1), 02049.

Lee, S.O. & Sturm, T.W. (2009) Effect of Sediment Size Scaling on Physical Modeling of Bridge Pier Scour. *Journal of Hydraulic Engineering* 135(10), 793–802.

Leenders, J.K., van Boxel, J.H. & Sterk, G. (2007) The effect of single vegetation elements on wind speed and sediment transport in the Sahelian zone of Burkina Faso. *Earth Surface Processes and Landforms* 32(10), 1454–1474.

Li, J., Qi, M., Fuhrman, D.R. & Chen, Q. (2018) Influence of turbulent horseshoe vortex and associated bed shear stress on sediment transport in front of a cylinder. *Experimental Thermal and Fluid Science* 97, 444–457.

Li, Y., Xie, L., & Su, T. C. (2020) Profile of suspended sediment concentration in submerged vegetated shallow water flow. *Water Resources Research* 56(4), e2019WR025551.

Li, Q., Hao, Y., Zhang, P., Tan, H., Tian, W. & Chen, L. *et al*. (2023) Numerical study of the local scouring process and influencing factors of semi-exposed submarine cables. *Journal of Marine Science and Engineering* 11(7), 1349.

Liao, C.-T., Yeh, K.-C., Lan, Y.-C., Jhong, R.-K. & Jia, Y. (2021) Improving the 2D Numerical Simulations on Local Scour Hole around Spur Dikes. *Water* 13(11), 1462.

Link, O., Pfleger, F. & Zanke, U. (2008) Characteristics of developing scour-holes at a sand-embedded cylinder. *International Journal of Sediment Research* 23(3), 258–266.

Link, O., González, C., Maldonado, M. & Escauriaza, C. (2012) Coherent structure dynamics and sediment particle motion around a cylindrical pier in developing scour holes. *Acta Geophysica* 60(6), 1689–1719.

Link, O., Mignot, E., Roux, S., Camenen, B., Escauriaza, C., Chauchat, J. *et al*. (2019) Scour at bridge foundations in supercritical flows: An analysis of knowledge gaps. *Water* 11(8), 1656.

Link, O., García, M., Pizarro, A., Alcayaga, H., Palma, S. (2020) Local scour and sediment deposition at bridge piers during floods. *Journal of Hydraulic Engineering* 146, 4020003.

Lisle, T.E. (1981) Roughness elements, a key resource to improve anadromous fish habitat. In T. J. Hassler (ed.) *Proceedings of a symposium on propagation, enhancement, and rehabilitation of anadromous salmonid populations and habitat in the Pacific northwest*. Humboldt State University: Arcata, 93–98.
Liu, C., & Nepf, H. (2016) Sediment deposition within and around a finite patch of model vegetation over a range of channel velocity. *Water Resources Research* 52(1), 600–612.
Liu, C., Hu, Z., Lei, J., & Nepf, H. (2018). Vortex structure and sediment deposition in the wake behind a finite patch of model submerged vegetation. *Journal of Hydraulic Engineering* 144(2), 600–612.
Loeffler, A. E., Gordon, A. M., & Gillespie, T. J. (1992). Optical porosity and windspeed reduction by coniferous windbreaks in Southern Ontario. *Agroforestry Systems* 17(2), 119–133
López, G.; Teixeira, L.; Ortega-Sánchez, M.; Simarro, G. (2014) Estimating final scour depth under clear-water flood waves. *Journal of Hydraulic Engineering* 140, 328–332.
Lotsari, E.S., Calle, M., Benito, G., Kukko, A., Kaartinen, H. & Hyyppä, J. *et al*. (2018) Topographical change caused by moderate and small floods in a gravel bed ephemeral river – a depth-averaged morphodynamic simulation approach. *Earth Surface Dynamics* 6(1), 163–185.
Lu, J.Y., Shi, Z.Z., Hong, J.H., Lee, J.J. & Raikar, R.V. (2011) Temporal variation of scour depth at nonuniform cylindrical piers. *Journal of Hydraulic Engineering* 137(1), 45–56.
Luo, W., Dong, Z., Qian, G. & Lu, J. (2012) Wind tunnel simulation of the three-dimensional airflow patterns behind cuboid obstacles at different angles of wind incidence, and their significance for the formation of sand shadows. *Geomorphology* 139-140, 258–270.
Lança, R.M.M., Simarro, G., Fael, C.M.S. & Cardoso, A.H. (2016) Effect of viscosity on the equilibrium scour depth at single cylindrical piers. *Journal of Hydraulic Engineering* 142(3), 06015022.
Machado, M.J., Medialdea, A., Calle, M., Rico, M.T., Sánchez-Moya, Y. & Sopeña, A. *et al*. (2017) Historical palaeohydrology and landscape resilience of a Mediterranean rambla (Castellón, NE Spain): Floods and people. *Quaternary Science Reviews* 171, 182–198.
Maity H., Mazumder B.S. (2014) Experimental investigation of the impacts of coherent flow structures upon turbulence properties in regions of crescentic scour. *Earth Surface Processes and Landforms* 39(8), 995–1013.
Manes C, Coscarella F, Rogers A, Gaudio R, Paquier A, Rivière N. (2018) Viscosity effects on local scour around vertical structures in clear-water conditions. *E3S Web of Conferences* 40(1): 3038.
Manes, C. & Brocchini, M. (2015) Local scour around structures and the phenomenology of turbulence. *Journal of Fluid Mechanics* 779, 309–324.
Mao, L. (2012) The effect of hydrographs on bed load transport and bed sediment spatial arrangement. *Journal of Geophysical Research*, 117, F03024.
Marjoribanks, T. I., Hardy, R. J., & Lane, S. N. (2014) The hydraulic description of vegetated river channels: The weaknesses of existing formulations and emerging alternatives. *Wiley Interdisciplinary Reviews: Water* 1(6), 549–560.
Marjoribanks, T. I., Lague, D., Hardy, R. J., Boothroyd, R. J., Leroux, J., *et al*. (2019) Flexural rigidity and shoot reconfiguration determine wake length behind saltmarsh vegetation patches. *Journal of Geophysical Research: Earth Surface* 124(8), 2176–2196.
Mazumder BS, Maity H, Chadda T. 2011. Turbulent flow field over fluvial obstacle marks generated in a laboratory flume. *International Journal of Sediment Research* 26(1), 62–77.
McKenna Neuman, C., Sanderson, R.S. & Sutton, S. (2013) Vortex shedding and morphodynamic response of bed surfaces containing non-erodible roughness elements. *Geomorphology* 198, 45–56.
Melville, B.W. & Chiew, Y.-M. (1999) Time Scale for Local Scour at Bridge Piers. *Journal of Hydraulic Engineering* 125(1), 59–65.

Melville, B.W. & Coleman, S.E. (2000) *Bridge scour*. Water Resources Publications: Highlands Ranch, Colo.
Melville, B.W. & Sutherland, A.J. (1988) Design method for local scour at bridge piers. *Journal of Hydraulic Engineering* 114(10), 1210–1226.
Merritt, D. M. (2022). Reciprocal relations between riparian vegetation, fluvial landforms and channel processes. In: Shroder, J.F. (ed.) *Treatise on Geomorphology*, Elsevier: Amsterdam 269–297.
Mia, M.F. & Nago, H. (2003) Design method of time-dependent local scour at circular bridge pier. *Journal of Hydraulic Engineering* 129(6), 420–427.
Mohammadpour, R., Ab. Ghani, A., Zakaria, N.A. & Mohammed Ali, T.A. (2017) Predicting scour at river bridge abutments over time. *Proceedings of the Institution of Civil Engineers: Water Management* 170(1), 15–30.
Montakhab A., bt.Yusuf B., Ghazali A.H., Mohamed T.A. (2013) Estimation of vegetation porosity in vegetated waterways. *Proceedings of the Institution of Civil Engineers – Water Management* 166(6), 333–340.
Morgan, J.A., Brogan, D.J. & Nelson, P.A. (2017) Application of Structure-from-Motion photogrammetry in laboratory flumes. *Geomorphology* 276, 125–143.
Mueller, D.S. & Wagner, C.R. (2005) Field observations and evaluations of streambed scour at bridges: Publication no. FHWA-RD-03-052. U.S. Department of Transportation: Washington, D.C.
Murray, A. B., Knaapen, M. A. F., Tal, M., & Kirwan, M. L. (2008). Biomorphodynamics: Physical-biological feedbacks that shape landscapes. *Water Resources Research* 44(11), W11301.
Murray, A.B., Coco, G. & Goldstein, E.B. (2014) Cause and effect in geomorphic systems: Complex systems perspectives. *Geomorphology* 214, 1–9.
Muste, M. (ed.) (2017) *Experimental Hydraulics: Methods, Instrumentation, Data Processing and Management,* Two Volume Set. CRC Press Taylor & Francis Group: Boca Raton, London, New York, Leiden.
Muzzammil, M., Gangadharaiah, T. & Gupta, A.K. (2004) An experimental investigation of a horseshoe vortex induced by a bridge pier. *Proceedings of the Institution of Civil Engineers - Water Management* 157(2), 109–119.
Muzzammil, M. & Gangadhariah, T. (2003) The mean characteristics of horseshoe vortex at a cylindrical pier. *Journal of Hydraulic Research* 41(3), 285–297.
Nakayama, K., Fielding, C.R. & Alexander, J. (2002) Variations in character and preservation potential of vegetation-induced obstacle marks in the variable discharge Burdekin River of north Queensland, Australia. *Sedimentary Geology* 149(4), 199–218.
Nakayama, K. (1992) Fluvial gravel beds with superimposed boulders in the Seto Group, Japan. *Journal of Sedimentological Society of Japan* 37(3), 79–84.
Nepf, H. M. (1999). Drag, turbulence, and diffusion in flow through emergent vegetation. *Water Resources Research* 35(2), 479–489.
Nezu, I. & Nakagawa, H. (2017) *Turbulence in Open-Channel Flows*. Routledge: London.
Nikora (2010) Hydrodynamics of aquatic ecosystems: an interface between ecology, biomechanics and environmental fluid mechanics. *River Research and Applications* 26(4), 367–384.
Nikora V, Larned S, Nikora N, Debnath K, Cooper G, Reid M. (2008) Hydraulic resistance due to aquatic vegetation in small streams: field study. *Journal of Hydraulic Engineering* 134(9), 1326–1332.
Niu, Y., Gao, Z., Li, Y. & Luo, K. (2019) Effect of rock fragment content on erosion processes of disturbed soil accumulation under field scouring conditions. *Journal of Soils and Sediments* 19(4), 1708–1723.
Novak, P. & Čábelka, J. (1981) *Models in hydraulic engineering*. Pitman Publisher: Boston.
O'Briain, R., Shephard, S., McCollom, A., O'Leary, C., & Coghlan, B. (2022). Plants as agents of hydromorphological recovery in lowland streams. *Geomorphology* 400, 108090.

Okamoto T, Nezu I. (2010) Flow resistance law in open channel flows with rigid and flexible vegetation. In: Dittrich A (ed.() *River Flow 2010: Proceedings of the 5th International Conference on Fluvial Hydraulics*, Braunschweig, Germany, 8–10 June 2010, Bundesanstalt für Wasserbau: Karlsruhe, 261–268.
Okamoto, S. & Sunabashiri, Y. (1992) Vortex shedding from a circular cylinder of finite length placed on a ground plane. *Journal of Fluids Engineering* 114(4), 512–521.
Oliveto, G. & Hager, W.H. (2002) Temporal Evolution of Clear-Water Pier and Abutment Scour. *Journal of Hydraulic Engineering*, 128(9), 811–820.
Oliveto, G. & Hager, W.H. (2005) Further results to time-dependent local scour at bridge elements. Journal of Hydraulic Engineering 131(2), 97–105.
Oliveto, G. & Hager, W.H. (2014) Morphological evolution of dune-like bed forms generated by bridge scour. *Journal of Hydraulic Engineering* 140(5), 6014009.
Osterkamp, W.R. (1998) Processes of fluvial island formation, with examples from Plum Creek, Colorado and Snake River, Idaho. *Wetlands* 18, 530–545.
Pagliara, S. & Palermo, M. (2008) Scour control and surface sediment distribution downstream of block ramps. *Journal of Hydraulic Research* 46(3), 334–343.
Pagliara, S. & Palermo, M. (2018) Equilibrium scour morphology downstream of rock sills under unsteady flow conditions. *E3S Web of Conferences* 40, 3004.
Paik, J., Escauriaza, C. & Sotiropoulos, F. (2007) On the bimodal dynamics of the turbulent horseshoe vortex system in a wing-body junction. *Physics of Fluids* 19(4), 45107.
Paola, C., Gust, G. & Southard, J.B. (1986) Skin friction behind isolated hemispheres and the formation of obstacle marks. *Sedimentology* 33(2), 279–293.
Paola, C., Straub, K., Mohrig, D. & Reinhardt, L. (2009) The "unreasonable effectiveness" of stratigraphic and geomorphic experiments. *Earth-Science Reviews* 97(1-4), 1–43.
Papanicolaou A.N., Kramer C. (2006) Flow and sediment laboratory measurements over unsubmerged roughness elements. In: Graham R (ed.) *Examining the Confluence of Environmental and Water Concerns: Proceedings of the 2006 World Environmental and Water Resources Congress*, May, 21–25, 2006, Omaha NE, American Society of Civil Engineers: Reston, VA; 1–8.
Papanicolaou, A.N. & Tsakiris A.G. & Kramer C.M. (2010) Effects of relative submergence on flow and sediment patterns around clasts. In: Dittrich, A. (Ed.) *River flow 2010: Proceedings of the [5th] International Conference on Fluvial Hydraulics*, Braunschweig, Germany, 8 - 10 June 2010. Bundesanst. für Wasserbau: Karlsruhe, 793–799
Papanicolaou, A.N., Dermisis, D.C. & Elhakeem, M. (2011) Investigating the role of clasts on the movement of sand in gravel bed rivers. *Journal of Hydraulic Engineering* 137(9), 871–883.
Papanicolaou, A.N., Kramer, C.M., Tsakiris, A.G., Stoesser, T., Bomminayuni, S. *et al*. (2012) Effects of a fully submerged boulder within a boulder array on the mean and turbulent flow fields: Implications to bedload transport. *Acta Geophysica* 60(6), 1502–1546.
Papanicolaou, A.N. & Tsakiris, A.G. (2017) Boulder effects on turbulence and bedload transport. In: Tsutsumi, D. & Laronne, J.B. (Eds.) *Gravel-bed rivers: processes and disasters*. Chichester: Wiley, pp. 33–72.
Papanicolaou, A.N., Tsakiris, A.G., Wyssmann, M.A. & Kramer, C.M. (2018) Boulder Array Effects on Bedload Pulses and Depositional Patches. *Journal of Geophysical Research: Earth Surface* 123(11), 2925–2953.
Pattenden, R.J., Turnock, S.R. & Zhang, X. (2005) Measurements of the flow over a low-aspect-ratio cylinder mounted on a ground plane. *Experiments in Fluid*s 39(1), 10–21.
Peabody, F.E. (1947) Current crescents in the Triassic Moenkopi Formation [Arizona]. *SEPM Journal of Sedimentary Research* 17(2), 73–76.
Peakall, J., Ashworth, P. & Best, J. (1996) Physical modelling in fluvial geomorphology: principles, applications and unresolved issues. In: Rhoads B.L. & C.E. Thorn (ed.) *The scientific nature of geomorphology*, 221–253.
Pfister, M. & Chanson, H. (2014) Two-phase air-water flows: Scale effects in physical modeling. *Journal of Hydrodynamics* 26(2), 291–298.

Phillips, J.D. (2002) Sources of nonlinear and complexity in geomorphic systems. *Progress in Physical Geography* 26(3), 339–361.
Pizarro, A., Ettmer, B., Manfreda, S., Rojas, A. & Link, O. (2017) Dimensionless effective flow work for estimation of pier scour caused by flood waves. *Journal of Hydraulic Engineering* 143(7), 6017006.
Pizarro, A. & Tubaldi, E. (2019) Quantification of Modelling Uncertainties in Bridge Scour Risk Assessment under Multiple Flood Events. *Geosciences* 9(10), 445.
Pizarro, A., Manfreda, S. & Tubaldi, E. (2020) The science behind scour at bridge foundations: A review. *Water* 12(2), 374.
Poesen, J.W., Torri, D. & Bunte, K. (1994) Effects of rock fragments on soil erosion by water at different spatial scales: a review. *CATENA* 23(1-2), 141–166.
Poggi D. & Kudryavtseva, N.O. (2019) Non-intrusive underwater measurement of local scour around a bridge pier. *Water* 11(10), 2063.
Polvi, L.E. (2021) Morphodynamics of boulder-bed semi-alluvial Streams in northern Fennoscandia: A flume experiment to determine sediment self-organization. *Water Resources Research* 57(3), e2020WR028859.
Powell, D.M. (2009) Dryland rivers: Processes and forms. In: Parsons, A.J., & Abrahams, A.D., (eds.) *Geomorphology of desert environments*, Springer: Dordrecht, The Netherlands, 333–373.
Qi, W.-G. & Gao, F.-P. (2020) Local scour around a monopile foundation for offshore wind turbines and scour effects on structural responses. In: Hemeda, S. & Barış Can Ülker, M. (eds.) *Geotechnical Engineering - Advances in Soil Mechanics and Foundation Engineering*, 88591.
Qi, W.-G., Liu, J., Gao, F.-P., Li, B. & Chen, Q.-G. (2022) Quantifying the spatiotemporal evolution of the turbulent horseshoe vortex in front of a vertical cylinder. *Physics of Fluids* 34(1), 015110.
Quinn, R. (2006) The role of scour in shipwreck site formation processes and the preservation of wreck-associated scour signatures in the sedimentary record – evidence from seabed and sub-surface data. *Journal of Archaeological Science* 33(10), 1419–1432.
Quinn, R. & Smyth, T.A.G. (2018) Processes and patterns of flow, erosion, and deposition at shipwreck sites: a computational fluid dynamic simulation. *Archaeological and Anthropological Sciences* 10(6), 1429–1442.
Radice, A., Porta, G. & Franzetti, S. (2009) Analysis of the time-averaged properties of sediment motion in a local scour process. *Water Resources Research*, 45(3), 1069.
Radice, A. & Tran, C.K. (2012) Study of sediment motion in scour hole of a circular pier. *Journal of Hydraulic Research* 50(1), 44–51.
Radspinner RR, Diplas P, Lightbody AF, Sotiropoulos F. (2010) River training and ecological enhancement potential using in-stream structures. *Journal of Hydraulic Engineering* 136(12), 967–980.
Raudkivi AJ, Ettema R. (1985) Scour at cylindrical bridge piers in armored beds. *Journal of Hydraulic Engineering* 111(4), 713–731.
Ravazzolo, D., Spreitzer, G., Tunnicliffe, J., & Friedrich, H. (2022). The effect of large wood accumulations with rootwads on local geomorphic changes. *Water Resources Research* 58(5), e2021WR031403.
Reid, I., Laronne, J.B., Powell, D.M. (1998) Flash-flood and bedload dynamics of desert gravel-bed streams. Hydrol. Process. 1998, 12, 543–557.
Rennie S.E., Brandt A., Friedrichs C.T. (2017) Initiation of motion and scour burial of objects underwater. *Ocean Engineering* 131, 282–294.
Richardson, K. & Carling, P.A. (2005) A typology of sculpted forms in open bedrock channels. In: Richardson, K. & Carling, P.A. (eds.) Special Paper 392: A typology of sculpted forms in open bedrock channels. Geological Society of America: Boulder, Colo.
Richardson, P.D. (1968) The generation of scour marks near obstacles. *SEPM Journal of Sedimentary Research* 38(4), 965–970.

Rodrigues, S., Bréhéret, J.-G., Macaire, J.-J., Moatar, F., Nistoran, D., & Jugé, P. (2006). Flow and sediment dynamics in the vegetated secondary channels of an anabranching river: The Loire River (France). *Sedimentary Geology* 186(1–2), 89–109.
Rodrigues S, Bréhéret J-G, Macaire J-J, Greulich S, Villar M. (2007) In channel woody vegetation controls on sedimentary processes and the sedimentary record within alluvial environments: a modern example of an anabranch of the River Loire, France. *Sedimentology* 54(1): 223–242.
Rogers, A., Manes, C. & Tsuzaki, T. (2020) Measuring the geometry of a developing scour hole in clear-water conditions using underwater sonar scanning. *International Journal of Sediment Research* 35(1), 105–114.
Russell, A.J. (1993) Obstacle marks produced by flow around stranded ice blocks during a glacier outburst flood (jokulhlaup) in west Greenland. *Sedimentology* 40(6), 1091–1111.
Russell, A.J., Roberts, M.J., Fay, H., Marren, P.M., Cassidy, N.J. & Tweed, F.S. *et al*. (2006) Icelandic jökulhlaup impacts: Implications for ice-sheet hydrology, sediment transfer and geomorphology. *Geomorphology* 75(1-2), 33–64.
Rygel, M.C., Gibling, M.R. & Calder, J.H. (2004) Vegetation-induced sedimentary structures from fossil forests in the Pennsylvanian Joggins Formation, Nova Scotia. *Sedimentology* 51(3), 531–552.
Sadeque, M.A., Rajaratnam, N. & Loewen, M.R. (2008) Flow around cylinders in open channels. *Journal of Engineering Mechanics* 134(1), 60–71.
Sadeque, M.A., Rajaratnam, N. & Loewen, M.R. (2009) Effects of bed roughness on flow around bed-mounted cylinders in open channels. *Journal of Engineering Mechanics* 135(2), 100–110.
Salamatian, S.A.; Tabarestani, M.K.; Zarrati, A.R. (2014) Local scour at cylindrical bridge pier under a flood wave. In: Schleiss, A.J., de Cesare, G., Franca, M.J., Pfister, M. (eds.) *River Flow 2014, Proceedings of the International Conference on Fluvial Hydraulics (River Flow 2014)*, Lausanne, Switzerland, 3–5 September 2014; CRC Press/Balkema: Boca Raton, FL, 1387–1391.
Sarkar, A. (2014) Scour and flow around submerged structures. *Proceedings of the Institution of Civil Engineers - Water Management* 167(2), 65–78.
Sarkar, K., Chakraborty, C. & Mazumder, B.S. (2015) Spacetime dynamics of bed forms due to turbulence around submerged bridge piers. *Stochastic Environmental Research and Risk Assessment* 29(3), 995–1017.
Schalko, I. & Nepf, H.M. (2024) Enhanced flow variability and morphological changes through individual wood placements on a gravel bed. *Geomorphology* 453, 109135.
Schalko, I.; Lageder, C.; Schmocker, L.; Weitbrecht, V.; Boes, R.M. (2019) Laboratory flume experiments on the formation of spanwise large wood accumulations part I. Effect on backwater rise. Water Resources Research 55(6), 4854–4870.
Schalko, I., Lageder, C., Schmocker, L., Weitbrecht, V. & Boes, R.M. (2019) Laboratory flume experiments on the formation of spanwise large wood accumulations part II: Effect on local scour. Water Resources Research 55(6), 4871–4885.
Schlömer O., Herget J. (2016) Physical modeling of fluvial obstacle marks at a sediment layer of limited thickness. In: Van Landeghem K.J.J., Garlan T., Baas J.H. (eds.) *MARID 2016: Fifth International Conference on Marine and River Dune Dynamics*, Caernafon, UK, 4–6 April, 159–162.
Schlömer, O. (2020) Morphometric relation of obstacle marks at boulder-like obstructions in time. In: Uijttewal, W., Blom, A. & Franca, M. (eds.) *River Flow 2020: Proceedings of the international Conference on fluvial hydraulic*s, Delft, Netherlands, 7–10 July. Rotterdam: CRC Press/Balkema, 719–727.
Schlömer, O., Herget, J. & Euler, T. (2020) Boundary condition control of fluvial obstacle mark formation – framework from a geoscientific perspective. *Earth Surface Processes and Landforms* 45(1), 189–206.
Schlömer, O., Grams, P. E., Buscombe, D. & Herget, J. (2021) Geometry of obstacle marks at instream boulders—integration of laboratory investigations and field observations. *Earth Surface Processes and Landforms* 46(3), 659–679.

Schlömer, O., & Reimann, A. (2021) Wenn Büsche Flussbaumeiste werden: Der Einfluss von Vegetation auf die Flussbettformung. *Geographische Rundschau* (7–8), 20–25 (in German).

Schlömer, O. & Herget, J. (2023) Geometry of Local Scour Holes at Boulder-like Obstacles during Unsteady Flow Conditions and Varying submergence. *Wate* 15(5), 958.

Schlömer, O., Luneau, S., Rodrigues, S. & Herget, J. (2024) Vegetation-induced sedimentary structures: porosity of riparian shrubs as control parameter of sedimentary processes during floods. *International Journal of Sediment Research* 39, 497–513.

*Schlömer, O. & Herget, J. (2025) Influence of submergence ratio on horseshoe vortex size at boulder obstacles. Submitted to *Journal of Hydraulic Research*.

*Schlömer, O., Herget, J., & Benito, G. (2025) On the usage of local scour holes at boulders for flow reconstruction in ephemeral streams. Submitted to *River*.

Schnauder I., Moggridge H.L. (2009) Vegetation and hydraulic–morphological interactions at the individual plant, patch and channel scale. *Aquatic Sciences* 71(3): 318–330.

Schulze, D., Jensen, K. & Nolte, S. (2022) Effects of small-scale patterns of vegetation structure on suspended sediment concentration and sediment deposition in a salt marsh. *Estuarine, Coastal and Shelf Science* 278, 108125.

Schumm, S.A., Mosley, M.P. & Weaver, W.E. (1987) *Experimental fluvial geomorphology*. Wiley: New York, NY.

Segura-Beltrán, F. & Sanchis-Ibor, C. (2013) Assessment of channel changes in a Mediterranean ephemeral stream since the early twentieth century. The Rambla de Cervera, eastern Spain. *Geomorphology* 201, 199–214.

Shahriar, A.R., Ortiz, A.C., Montoya, B.M. & Gabr, M.A. (2021) Bridge Pier Scour: An overview of factors affecting the phenomenon and comparative evaluation of selected models. *Transportation Geotechnics* 28, 100549.

Shamloo, H., Rajaratnam, N. & Katopodis, C. (2001) Hydraulics of simple habitat structures. *Journal of Hydraulic Research* 39(4), 351–366.

Sharpe, R. G., & James, C. S. (2007) Deposition of sediment from suspension in emergent vegetation. *Water SA*, 32(2) 211–218.

Shaw, J. & .Kellerhals, R. (1977) Paleohydraulic interpretation of antidune bedforms with applications to antidunes in gravel. *SEPM Journal of Sedimentary Research* 47(1),257-266.

Shugar, D., Kostachuk, R., Best, J. L., Parsons, D. R., Lane, S. N. *et al*. (2010). On the relationship between flow and suspended sediment transport over the crest of a sand dune, Rio Parana, Argentina. *Sedimentology* 57(1), 252–272.

Sheppard D.M., Miller W. (2006) Live-bed local pier scour experiments. *Journal of Hydraulic Engineering* 132(7): 635–642.

Sheppard, D.M., Melville, B. & Demir, H. (2014) Evaluation of existing equations for local scour at bridge piers. *Journal of Hydraulic Engineering* 140(1), 14–23.

Shobe, C.M., Turowski, J.M., Nativ, R., Glade, R.C., Bennett, G.L. & Dini, B. (2021) The role of infrequently mobile boulders in modulating landscape evolution and geomorphic hazards. *Earth-Science Reviews* 220, 103717

Simarro G., Teixeria L., Cardoso A.H. (2007) Flow intensity parameter in pier scour experiments. *Journal of Hydraulic Engineering* 133(11), 1261–1264.

Simarro, G., Fael, C.M.S .& Cardoso, A.H. (2011) Estimating equilibrium scour depth at cylindrical piers in experimental studies. *Journal of Hydraulic Engineering* 137(9), 1089–1093.

Simons D.B., Richardson E.V. (1966) Resistance to flow in alluvial channels. US Geological Survey Professional Paper 422-J: Washington, D.C.

Smith, M.W., Carrivick, J.L. & Quincey, D.J. (2016) Structure from motion photogrammetry in physical geography. *Progress in Physical Geography: Earth and Environment* 40(2), 247–275.

Sonia Devi, Y. & Barbhuiya, A.K. (2017) Bridge pier scour in cohesive soil: A review. *Sādhanā* 42(10), 1803–1819.

Sonin A.A. (2004) A generalization of the π-theorem and dimensional analysis. *PNAS* 101(23): 8525–8526.
Stolle, J., Takabatake, T., Nistor, I., Mikami, T., Nishizaki, S. *et al*. (2018) Experimental investigation of debris damming loads under transient supercritical flow conditions. *Coastal Engineering* 139, 16–31.
Straatsma, M. W., Warmink, J. J., & Middelkoop, H. (2008) Two novel methods for field measurements of hydrodynamic density of floodplain vegetation using terrestrial laser scanning and digital parallel photography. *International Journal of Remote Sensing* 29(5), 1595–1617.
Strom K.B, Papanicolaou A.N. (2008) Morphological characterization of cluster microforms. *Sedimentology* 55(1): 137–153.
Sumer B.M. (2004) Physical and mathematical modelling of scour. In: Chiew Y.M., Lim S.Y., Cheng N.S. (eds.) *Proceedings of the 2nd International conference on scour and erosion (ICSE-2)*, 14–17 November, Singapore, World Scientific: Singapore, 29–46.
Sui, J., Afzalimehr, H., Samani, A. K., & Maherani, M. (2010) Clear-water scour around semi-elliptical abutments with armored beds. *International Journal of Sediment Research* 25(3), 233–245.
Sukhodolova, T. A., & Sukhodolov, A. N. (2012) Vegetated mixing layer around a finite-size patch of submerged plants: 1. Theory and field experiments. *Water Resources Research* 48(10), W10533.
Sukhodolov, A. N., & Sukhodolova, T. A. (2012) Vegetated mixing layer around a finite-size patch of submerged plants: Part 2. Turbulence statistics and structures. *Water Resources Research* 48(12), W12506.
Sumer, B.M. & Fredsøe, J. (2005) *The mechanics of scour in the marine environment*. World Scientific Publ: New Jersey.
Sumner, D. (2013) Flow above the free end of a surface-mounted finite-height circular cylinder: A review. *Journal of Fluids and Structures* 43, 41–63.
Sumner, D., Heseltine, J.L. & Dansereau, O.J.P. (2004) Wake structure of a finite circular cylinder of small aspect ratio. *Experiments in Fluids* 37(5), 720–730.
Sutherland, J. & Soulsby, R. (2011) Sediment dynamics. In: Frostick, L.E., McLelland, S.J. & Mercer, T.G. (eds.) *Users guide to physical modelling and experimentation: Experience of the HYDRALAB Network*. CRC Press: Hoboken, NJ, 67–125.
Tabarestani, M.K. & Zarrati, A.R. (2017) Local scour calculation around bridge pier during flood event. *KSCE Journal of Civil Engineering* 21, 1462–1472.
Tanaka, N., & Yagisawa, J. (2010) Flow structures and sedimentation characteristics around clump-type vegetation. *Journal of Hydro Environment Research* 4(1), 15–25.
Thompson, D.M. (2008) The influence of lee sediment behind large bed elements on bedload transport rates in supply-limited channels. *Geomorphology* 99(1-4), 420–432.
Thomas, R.E., Johnson, M.F., Frostick, L.E., Parsons, D.R., Bouma, T.J. *et al*. (2014) Physical modelling of water, fauna and flora: knowledge gaps, avenues for future research and infrastructural needs. *Journal of Hydraulic Research* 52(3), 311–325.
Tinoco, R. O., & Coco, G. (2014) Observations of the effect of emergent vegetation on sediment resuspension under unidirectional currents and waves. *Earth Surface Dynamics* 2(1), 83–96.
Tinoco, R. O., & Coco, G. (2018) Turbulence as the main driver of resuspension in oscillatory flow through vegetation. *Journal of Geophysical Research: Earth Surface* 123(5), 891–904.
Tinoco, R. O., San Juan, J. E., & Mullarney, J. C. (2020) Simplification bias: Lessons from laboratory and field experiments on flow through aquatic vegetation. *Earth Surface Processes and Landforms* 45(1), 121–143.
Tominga A. (2014) Flow structure and bed deformation around a sphere on moveable bed. In: Schleiss A.J., de Cesare G., Franca M.J., Pfister M. (eds.) River Flow 2014: Proceedings of the international conference on fluvial hydraulics, Lausanne, Switzerland, 3–5 September, CRC Press/Balkema: Boca Raton, FL/Rotterdam, 1499–1507.

Tooth, S. & Nanson, G.C. (2000) The role of vegetation in the formation of anabranching channels in an ephemeral river, Northern plains, arid central Australia. *Hydrological Processes* 14(16-17), 3099–3117.
Tregnaghi, M.; Marion, A.; Coleman, S (2009) Scouring at Bed Sills as a Response to Flash Floods. *Journal of Hydraulic Engineering* 135, 466–475.
Tregnaghi, M., Marion, A. & Gaudio, R. (2007) Affinity and similarity of local scour holes at bed sills. *Water Resources Research* 43(11), W11417.
Tsakiris, A.G., Papanicolaou, A.N.T., Hajimirzaie, S.M. & Buchholz, J.H.J. (2014) Influence of collective boulder array on the surrounding time-averaged and turbulent flow fields. *Journal of Mountain Science* 11(6), 1420–1428.
Truelsen C, Sumer BM, Fredsøe J. (2005) Scour around spherical bodies and self-burial. *Journal of Waterway, Port, Coastal, and Ocean Engineering* 131(1), jwped5.
Tubaldi, E., Macorini, L., Izzuddin, B.A., Manes, C. & Laio, F. (2017) A framework for probabilistic assessment of clear-water scour around bridge piers. *Structural Safety* 69, 11–22.
Tubaldi, E., White, C.J., Patelli, E., Mitoulis, S.A., Almeida, G. de & Brown, J. *et al*. (2022) Invited perspectives: Challenges and future directions in improving bridge flood resilience. *Natural Hazards and Earth System Sciences* 22(3), 795–812.
Unger, J. & Hager, W.H. (2006) Down-flow and horseshoe vortex characteristics of sediment embedded bridge piers. *Experiments in Fluids* 42(1), 1–19.
USGS National Bridge Scour Database. (2020) http://water.usgs.gov/osw/techniques/bs/BSDMS/BSDMS_1.html [Accessed 10th September 2020].
van Dijk, T.A.G.P., Best, J. & Baas, A.C.W. (2021) Subaqueous and Subaerial Depositional Bedforms. In: Alderton, D. & Elias, S.A. (eds.) *Encyclopedia of Geology*, Elsevier: Amsterdam, 771–786.
Vigiak, O., Sterk, G., Warren, A., & Hagen, L. J. (2003) Spatial modeling of wind speed around windbreaks. *CATENA* 52(3–4), 273–288.
Vittal, N., Al-Muttair, F. & Abu-Sharekh, M.S. (1993) Hydraulic design of flume aqueducts. *Journal of Hydraulic Engineering* 119(2), 284–289.
Wahl T.L. (2000) Analyzing ADV data using WinADV. In: Hotchkiss RH (ed.) *Building Partnerships*, American Society of Civil Engineers: Reston, VA; 1–10.
Waters, K.A.; Curran, J.C. (2015) Linking bed morphology changes of two sediment mixtures to sediment transport predictions in unsteady flows. *Water Resources Research* 51, 2724–2741.
Wells, G.H., Dugmore, A.J., Beach, T., Baynes, E.R.C., Sæmundsson, Þ. Et als(2022) Reconstructing glacial outburst floods (jökulhlaups) from geomorphology: Challenges, solutions, and an enhanced interpretive framework. *Progress in Physical Geography: Earth and Environment* 46(3), 398–421.
Wentworth, C.K. (1922) A scale of grade and class terms for clastic sediments. *The Journal of Geology* 30(5), 377–392.
Werner, B.T. (1999) Complexity in natural landform patterns. *Science* 284(5411), 102–104.
Werner, B.T. (2010) Modeling landforms as self-organized, hierarchical dynamical systems. In: Wilcock, P.R., Iverson, R.M. & Iverson, R.M. (Eds.) *Prediction in geomorphology*. American Geophysical Union: Washington, D.C., 133–150.
Werner, F., Unsöld, G., Koopmann, B. & Stefanon, A. (1980) Field observations and flume experiments on the nature of comet marks. *Sedimentary Geology* 26(1-3), 233–262.
Westoby, M.J., Brasington, J., Glasser, N.F., Hambrey, M.J. & Reynolds, J.M. (2012) "Structure-from-Motion" photogrammetry: A low-cost, effective tool for geoscience applications. *Geomorphology* 179, 300–314.
Wheaton, J.M., Brasington, J., Darby, S.E. & Sear, D.A. (2010) Accounting for uncertainty in DEMs from repeat topographic surveys: Improved sediment budgets. *Earth Surface Processes and Landforms* 35, 136–156.
Williams, G.P. (1989) Sediment concentration versus water discharge during single hydrologic events in rivers. *Journal of Hydrology* 111, 89–106.

Williams, P., Bolisetti, T. & Balachandar, R. (2017) Evaluation of governing parameters on pier scour geometry. *Canadian Journal of Civil Engineering* 44(1), 48–58.
Williams, P., Balachandar, R. & Bolisetti, T. (2019) Examination of blockage effects on the progression of local scour around a circular cylinder. *Water* 11(12), 2631.
Wintenberger, C. L., Rodrigues, S., Bréhéret, J.-G., & Villar, M. (2015). Fluvial islands: First stage of development from nonmigrating (forced) bars and woody-vegetation interactions. *Geomorphology* 246, 305–320.
Wu, J., Fan, M., Zhang, H., Shaukat, M., Best, J. *et al*. (2024) Decadal evolution of fluvial islands and its controlling factors along the lower Yangtze River. *Frontiers in Environmental Science* 12, 1388854.
Wu, P. & Balachandar, R. (2016) Local scour around bridge abutments including effects of relative bed coarseness and blockage ratio. *Canadian Journal of Civil Engineering*, 43(1), 51–59.
Wu, Y. & Chiew, Y.M. (2012) Three-dimensional scour at submarine pipelines. *Journal of Hydraulic Engineering* 138(9), 788–795.
Wyssmann, M.A., Coder, J.G., Schwartz, J.S. & Papanicolaou, A.N.T. (2024) Turbulent junction flow characteristics upstream of boulders mounted atop a rough, permeable bed and the effects of submergence. *Experiments in Fluids* 65(9), 10.1007.
Xiong, X., Matsumoto, T., Shi, Z. & Zhang, F. (2022) Flume tests and corresponding numerical simulation of hydraulic/mechanical behavior of Tangjiashan landslide dam subjected to seepage loading. *Soils and Foundations* 62(5), 101200.
Yagci, O., Tschiesche, U., & Kabdasli, M. S. (2010) The role of different forms of natural riparian vegetation on turbulence and kinetic energy characteristics. *Advances in Water Resources* 33(5), 601–7614.
Yagci, O., Celik, M.F., Kitsikoudis, V., Ozgur Kirca, V.S., Hodoglu, C. & Valyrakis, M. *et al*. (2016) Scour patterns around isolated vegetation elements. *Advances in Water Resources* 97, 251–265.
Yagci, O., & Strom, K. (2022) Reach-scale experiments on deposition process in vegetated channel: Suspended sediment capturing ability and backwater effectof instream plants. *Journal of Hydrology* 608, 127612.
Yagci, O., Özgur Kirca, V.S., Kitsikoudis, V., Wilson, C.A.M.E., Celik, M.F. & Sertkan, C. (2024) Experimental study on influence of different patterns of an emergent vegetation patch on the flow field and scour/deposition processes in the wake region. *Water Resources Research*, 60(1).
Yager, E. M., & Schmeeckle, M. W. (2013). The influence of vegetation on turbulence and bed load transport. *Journal of Geophysical Research: Earth Surface* 118(3), 1585–1601.
Yalin, M.S. (1971) *Theory of Hydraulic Models*. Red Globe Press: London.
Yin, D., Peakall, J., Parsons, D., Chen, Z., Averill, H.M. & Wignall, P. *et al*. (2016) Bedform genesis in bedrock substrates: Insights into formative processes from a new experimental approach and the importance of suspension-dominated abrasion. *Geomorphology* 255, 26–38.
Yu, G.-A., Li, Z., Yang, H., Lu, J., Huang, H. Q., & Yi, Y. (2020) Effects of riparian plant roots on the unconsolidated bank stability of meandering channels in the Tarim River, China. *Geomorphology* 351, 106958.
Zhang, W., Uh Zapata, M., Bai, X., Pham-Van-Bang, D. & Nguyen, K.D. (2020) Three-dimensional simulation of horseshoe vortex and local scour around a vertical cylinder using an unstructured finite-volume technique. *International Journal of Sediment Research* 35(3), 295–306.
Zhao, M., & Fan, Z. (2017) Hydrodynamic characteristics of submerged vegetation flow with non-constant vertical porosity. *PLoS One* 12(4), e0176712.
Zhu, R., & Tsubaki, R. (2022). The role of riparian vegetation flexibility in a bio-hydro-morphodynamic simulation. *Earth Surface Processes and Landforms* 47(15), 3481–3496.
Zong, L., & Nepf, H. (2012) Vortex development behind a finite porous obstruction in a channel. *Journal of Fluid Mechanics* 691, 368–391.

Zuhr, A.M., Münch, T., Steen-Larsen, H.C., Hörhold, M. & Laepple, T. (2021) Local-scale deposition of surface snow on the Greenland ice sheet. *The Cryosphere* 15(10), 4873–4900.

*) Manuscripts were submitted during the course of the assessment of the thesis.